P2

C14

NASA TECHNICAL MEMORANDUM

NASA TM X-2719

NASA TM X-2719

(14)

SYMPOSIUM ON REUSABLE SURFACE INSULATION FOR SPACE SHUTTLE

Volume I - RSI Fabrication, Improvement, Morphology and Properties

Held at

Ames Research Center

Moffett Field, Calif.

November 1-3, 1972

NATIONAL AERONAUTICS AND SPACE ADMINISTRATION • WASHINGTON, D. C. • SEPTEMBER 1973

1. Report No. NASA TM X-2719	2. Government Accession No.	3. Recipient's Catalog No.
4. Title and Subtitle Symposium on Reusable Surface Insulation for Space Shuttle, Volume I - RSI Fabrication, Improvement, Morphology and Properties		5. Report Date September 1973
		6. Performing Organization Code
7. Author(s)		8. Performing Organization Report No. A-4725
		10. Work Unit No. 502-37-02
9. Performing Organization Name and Address NASA Ames Research Center Moffett Field, Calif. 94035		11. Contract or Grant No.
		13. Type of Report and Period Covered Technical Memorandum
12. Sponsoring Agency Name and Address National Aeronautics and Space Administration Washington, D. C. 20546		14. Sponsoring Agency Code

15. Supplementary Notes

Held at NASA Ames Research Center, November 1–3, 1972.

16. Abstract

The conference encompasses three technology efforts, each published as a separate volume.

Volume I - RSI Fabrication, Improvement, Morphology and Properties (NASA TM X-2719)
Volume II - Environmental Testing (NASA TM X-2720)
Volume III - Thermal Protection System Design and Optimization (NASA TM X-2721)

17. Key Words (Suggested by Author(s)) Thermal Protection System Reusable Surface Insulation Space Shuttle		18. Distribution Statement Unclassified — Unlimited	
19. Security Classif. (of this report) Unclassified	20. Security Classif. (of this page) Unclassified	21. No. of Pages 378	22. Price* $6.00

* For sale by the National Technical Information Service, Springfield, Virginia 22151

Page Intentionally Left Blank

FOREWORD

Howard K. Larson

One of the critical technology needs of the Space Shuttle is develop-
ment of a reusable thermal protection system (TPS). The baseline
material for a large part of the shuttle TPS is now reusable surface
insulation (RSI). Because of the rapid progress which has occurred
in this development effort during FY'72-'73, it was deemed appropriate
to review the state of RSI technology at this time. Therefore, Ames
Research Center, under the auspices of the Shuttle Thermal Protection
Systems and Materials Technology Working Group, hosted a three-day
symposium on Reusable Surface Insulation for Thermal Protection of
the Space Shuttle on November 1-3, 1972.

The objective of this symposium was to define the state-of-the-art
for RSI materials. The meeting was divided into five sequential half-
day sessions; each session addressing a specific technology area.

The first session "RSI Fabrication and Improvement" was chaired by
Howard E. Goldstein of NASA-Ames, and included papers discussing the
development of silica, mullite and alumino-silicate RSI materials.
Rigid and flexible RSI materials were described. The results reported
showed that mullite, silica and alumino-silicate rigid fibrous RSI
materials could be fabricated reproducibly. One paper described a
somewhat different RSI concept, a rigid closed pore alumino-silicate
insulation having good physical stability. Also described was a
silica non-rigid insulation which offers the possibility of minimizing
strain compatibility problems with the structure. While substantial
improvements have been made in the past two years, it was pointed out
by many of the papers that much effort is still required to optimize
the RSI materials. Substantial improvement in physical properties and
thermal stability should be expected with continued research.

The second session "RSI Morphology and Properties" was chaired by
Salvatore J. Grisaffe, NASA-Lewis, and included papers describing the
detailed mechanical and thermophysical properties of the rigid fibrous
RSI materials and their coatings. The mechanical properties as a
function of temperature for REI mullite and LI-1500 were presented.
One paper described a comparison of the mechanical and thermophysical
properties of HCF, REI mullite, and LI-1500. Radiant energy transmis-
sion through mullite RSI was discussed in one paper and the high
temperature surface optical properties of all the RSIs were discussed
in another paper. The final paper described the microstructure of
mullite fibers. This session demonstrated that the mechanical proper-
ties of the RSI materials are reasonably well understood, though the
precision of the reported values is still in doubt. Thermal conduc-
tivity, particularly radiant heat transfer effects, are not well
defined for the fibrous mullite materials. Emittances of the surface
coatings of all the RSI materials are still questionable and require
further study.

The third session "Environmental Testing I" was chaired by David H. Greenshields, NASA-MSC, and described the results of arc-plasma testing of the RSI materials. Most of these papers were concerned with both techniques for proper convective heating environment simulation and the response of the materials to the environment. Two papers described thermal response in gaps due to laminar and turbulent heating, respectively. In both studies, large panels simulating shuttle heat shield configurations were used. Other papers described the internal thermal response, catalytic wall effects and material response to cyclic heating. These studies were carried out on small models in uniform stagnation region heating regimes. Significantly higher thermal efficiency was reported for silica RSI compared with mullite RSI. Silica RSI coatings were also shown to be more chemically stable and less subject to cracking due to thermal shock.

The fourth session "Environmental Testing II" was chaired by John D. Buckley, NASA-Langley, and included papers that discussed the results of several diverse environmental testing programs. There were papers on the response of the RSI coatings in both convective and radiative heating environments. In these papers, emphasis was placed on the chemical and morphological changes that occur due to each heating environment. Significant differences were shown between the effects of radiant and convective heating. Convective heating was shown to have more severe effects. Other papers in the session described the effects of combined salt spray and cyclic radiant heating. It was shown that salt spray is more deleterious for silica than for mullite. Cold soak, acoustical rain erosion, and meteoroid impact tests were also described. The results of large panel tests in radiant heating and acoustic environments showed the silica RSI to be more stable. Mullite materials experienced thermostructural failures in these tests.

The fifth session "Thermal Protection System Design and Optimization" was chaired by George Strouhal, NASA-MSC, and included papers describing a number of specific design problems. Among these problems were the adhesive cold soak, the effect of optical properties on thermal design and techniques for mechanical attachment of RSI to the structure. The design concept of a non-rigid silica heat shield was described. Papers on mullite and silica RSI, respectively, contrasted the design philosophies and development maturities of the respective systems. Finally, a paper on thermostructural analysis of RSI application showed that mullite was much more subject to thermal stress failure than silica.

In conclusion, it is felt that the Symposium fulfilled its intended purpose in providing an "open forum" for Industry and Government to present, receive, and discuss the most recent results of a young, intensive technology program. NASA needed the results of this RSI technology program in order to make important decisions as to which of the RSI materials to choose for the shuttle heat shield. Early in 1973, NASA made the announcement that silica was chosen for the base material and that a coating with a ratio of solar absorbtance to room temperature emittance of 1.0 would be baselined.

CONTENTS

SYMPOSIUM CO-CHAIRMEN: Howard K. Larson,
Ames Research Center
David H. Greenshields,
Manned Spacecraft Center

VOLUME I. - RSI FABRICATION, IMPROVEMENT, MORPHOLOGY, AND PROPERTIES

Session I - RSI Fabrication and Improvement
Chairman: Howard E. Goldstein
Ames Research Center

Session II - RSI Morphology and Properties
Chairman: Salvatore J. Grisaffe
Lewis Research Center

VOLUME III. - THERMAL PROTECTION SYSTEM DESIGN AND OPTIMIZATION

Session V - Thermal Protection System Design and Optimization
Chairman: George Strouhal
Manned Spacecraft Center

x

FABRICATION AND IMPROVEMENT OF LMSC's ALL-SILICA RSI

R. M. Beasley, Y. D. Izu, H. N. Nakano, A. A. Ozolin, A. Pechman

LOCKHEED MISSILES & SPACE COMPANY. INC.

1

LI-1500 MATERIAL MANUFACTURING PROCESS AND CONTROLS

(Figure 1)

The LI-1500 and LI-900 RSI materials have made the transition from laboratory to manufacturing operation. Improvements in both quality and reproducibility have been achieved. The LI-1500 material has displayed superior reliability in evaluations conducted at various facilities. The dependable performance of the material may be attributed to the adherence to the stringent requirements of the numerous material, process, and product control evaluations and inspection points performed during manufacture. During the process span of raw fibers and materials to finished coated and bonded tiles, 140 control points are applied. Every production panel currently fabricated is subjected to these controls and analysis prior to acceptance and release for RSI utilization.

LI-1500 MATERIAL MANUFACTURING PROCESS AND CONTROLS *

RAW MATERIALS
- CHEMICAL
- THERMAL
- CRYSTALLINITY
- PROCESSABILITY
- MOISTURE

BINDER
- CHEMICAL
- CONSTITUENT
- PHYSICAL PROPERTIES
- CRYSTALLINITY
- THERMAL
- PROCESSABILITY

CASTING AND FORMING
- CONSTITUENT RATIOS
- DIMENSIONAL
- NDE (RADIOGRAPHIC)
- pH
- RESISTIVITY

DRYING AND SINTERING
- DIMENSIONAL
- CRYSTALLINITY
- THERMAL
- NDE (RADIOGRAPHIC)
- PHYSICAL PROPERTIES
- MECHANICAL PROPERTIES

MACHINING
- DIMENSIONAL
- PHYSICAL PROPERTIES

COATING MATERIALS
- CHEMICAL
- CONSTITUENT
- CRYSTALLINITY
- PROCESSABILITY

SURFACE COATING
- DIMENSIONAL
- PHYSICAL PROPERTIES
- THERMAL
- NDE (RADIOGRAPHIC)
- VISUAL

TPS ASSEMBLY
- DIMENSIONAL
- VISUAL
- NDE (RADIOGRAPHIC)

* A TOTAL OF 140 INDIVIDUAL CONTROL POINTS APPLIED.

Figure 1

3

LI-1500 RSI MATERIAL PRODUCTION ANALYSIS

(Figure 2)

Monitoring and analysis of the LI-1500 material produced for Contracts NAS 9-12083

and NAS 9-12137 verified the reproducibility of the production process in that 82 panels,

fabricated from 7 separate process lots, showed reproducibility within each lot and

between the separate lots. Sampling evaluations of each production panel by X-ray

diffraction showed all to be noncrystalline and that no phase change would occur for

any of the production material, even after additional isothermal exposures of four hours

at 1533°K (2300°F). Test specimens prepared from the LI-1500 material exhibited reproducibility

within each individual panel. Typical specimen density variation within a panel is exemplified

by: 65 specimens 224 ± 9.6 kg/m^3 (14.0 ± 0.6 pcf);   45 specimens 221 ± 6.4 kg/m^3

(13.8 ± 0.4 pcf); 42 specimens $\longrightarrow$ 228 ± 9.6 kg/m^3 (14.2 ± 0.6 pcf).

4

LI-1500 RSI MATERIAL PRODUCTION ANALYSIS

CONTRACTS NAS 9-12083 AND NAS 9-12137

PROCESS LOT NO.	2085	2087	2088	2091	2096	2097	2098	AVERAGE
FIBER ANALYSIS								
PERCENT SiO_2	99.54	99.62	99.54	99.50	99.33	99.55	99.49	99.51
PERCENT ASH	0.46	0.38	0.46	0.50	0.67	0.45	0.51	0.49
HOT STAGE X-RAY DIFFRACTION	CONDUCTED ON ALL LOTS							
LI-1500 PANEL								
DENSITY, kg/m^3	$228\ ^{+19.2}_{-1}$	$224\ ^{+8.0}_{-1}$	$208\ ^{+9.6}_{-1}$	$223\ ^{+8.0}_{-1}$	$236\ ^{+4.8}_{-1}$	$232\ ^{+6.4}_{-1}$	$236\ ^{+9.6}_{-1}$	$226\ ^{+9.6}_{-1}$
AVERAGE DENSITY OF 82 PANELS	$226\ kg/m^3$ (14.1 LB/FT^3)							
CRYSTALLINITY (A)	NONE							

(A) X-RAY DIFFRACTION ANALYSIS AFTER 4 HR AT $1533^\circ K$ ($2300^\circ F$) EXPOSURE

Figure 2

5

LI-1500 DEVELOPMENT

(Figure 3)

The LMSC silica RSI materials have resulted from development activities continuous since 1962. Historical test data have been accumulated and demonstrate the stability of the manufacturing process. LMSC participated with NASA/LaRC in the Pacemaker flight test in 1968. LMSC's confidence in the superiority of its silica RSI and process was demonstrated by the establishment of a major pilot plant during 1970. Material produced since that time and evaluated for NASA and by Battelle exhibits consistent property trends.

An initial expansion of the pilot plant was implemented in 1971 to attain a true manufacturing facility. A major production facility expansion has been initiated to meet the RSI material needs for the Shuttle TPS in 1973.

6

LI-1500 DEVELOPMENT

● LMSC HAS A DEVELOPED MATERIAL (LI-1500)

DEVELOPMENT INITIATED IN 1962
NASA FLIGHT TEST IN APRIL 1968
PILOT PLANT PRODUCTION SINCE MAY 1970
MATERIAL PRODUCED DURING PAST SIX YEARS SHOWS STABILITY OF PROCESS

IN-PLANE TENSILE STRENGTH

$N/m^2 \times 10^{-5}$

(LB/IN.^{2})

JUN 1966　　NOV 1966　　LMSC 1970　　BATTELLE 1971　　LMSC 1972　　BATTELLE 1972

Figure 3

7
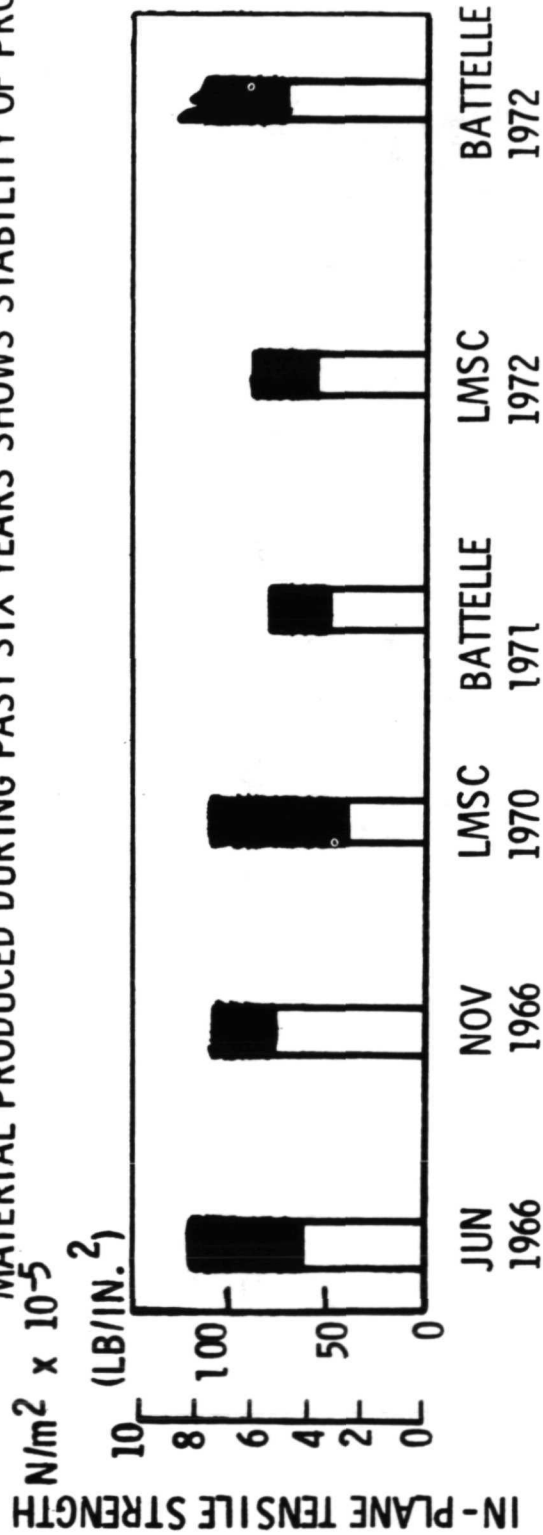
COMPARISON OF LI-1500 THERMAL CONDUCTIVITY DATA

(Figure 4)

In addition to the dependable mechanical characteristics just shown, a major design

factor for Shuttle TPS is reliable thermal conductivity characteristics. Reproducibility

and stability of the LI-1500 process is further substantiated by the extensive conductivity

evaluations of the silica RSI made over the last three years. These data have been

consistent as is shown with the two design sizing curves plotted in figure 4. The use of

LMSC's sizing conductivity curves has resulted in good correlation or slight over-

prediction of bondline temperatures.

Of particular interest, data from tests performed in 1964 agree closely with current

test values and the design curves. The latest data available (reported by Battelle) also

agree closely, except for the low temperature region where the variation was attributed

to suspect equipment/methods.

8

RSI MATERIAL IMPROVEMENT

SILICA MATERIAL SYSTEMS

    – CONTROL POLYMORPHIC CHARACTERISTICS TO INSURE RETENTION OF NONCRYSTALLINE STATE

MATERIAL SYSTEMS

    – VARYING DENSITY 96.2–1920 Kg/m^3 (6–120 PCF), MECHANICAL AND THERMOPHYSICAL PROPERTIES FOR CRITICAL AREAS

LI–900

    – RETAINED ATTRIBUTES OF LI–1500 WITH A REDUCTION OF BOTH DENSITY (30 PERCENT) AND MECHANICAL PROPERTY ANISOTROPY

FI–600

    – INCORPORATE RESILIENT FIBROUS MATERIAL WITH FUSED HIGH EMITTANCE BOROSILICATE SURFACE COATING FOR TOLERANCE TAKEUP TO SIMPLIFY TPS ASSEMBLY

LI–0042

    – HIGH EMITTANCE, IMPERVIOUS COATING WITH DEMONSTRATED USE TO 1644°K (2500°F)

Figure 5

LI-900 CONDUCTIVITY DATA

(Figure 6)

Thermal conductivity data measured to date show a retention of the superior character-istics established for LI-1500 and routinely used in successful TPS hardware design. Additional conductivity data for the LI-900 material are currently being generated as part of the NAS 9-12856 contractual effort.

12

LI-900 CONDUCTIVITY DATA

Figure 6

13
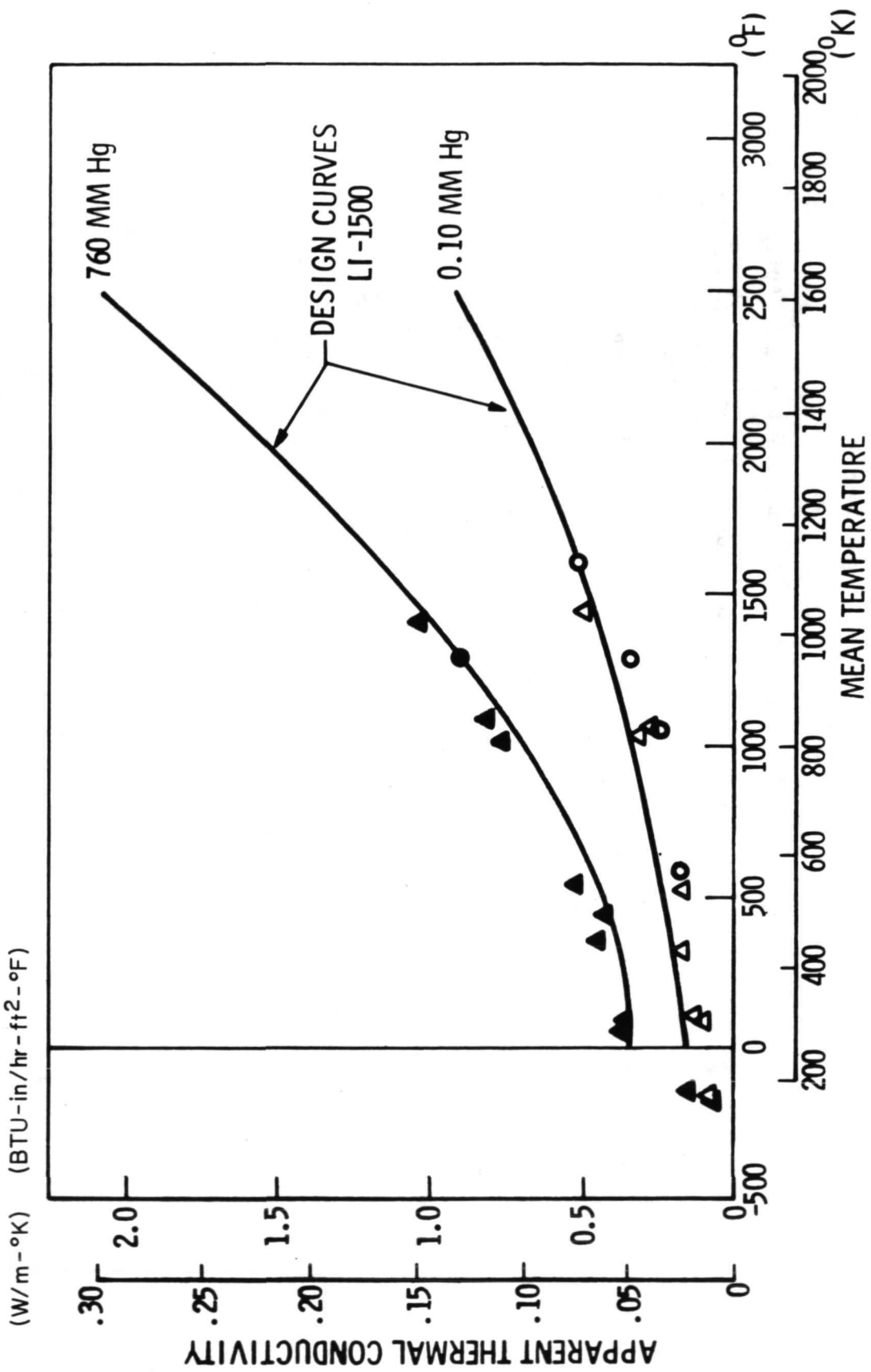
COATING DEVELOPMENT

(Figure 7)

Coating development resulted in a RSI surface coating system (identified as LI-0042), which provides environmental and handling, protection, high emittance (~0.9) at elevated temperatures 1644°K (2500°F), and capability to perform through repeated thermal at cycling at 1644°K (2500°F) temperature regime. The LI-0042 is of a refractory borosilicate formulation with silicon carbide as the emissivity agent. A major criterion in the development of this coating formulation was to match the extremely low thermal expansion of the silica RSI material systems. The data presented in the figure indicate the close match in expansion of the LI-1500, LI-900, and the coating material.

The LI-0042 coating system has performed successfully and reliably in various simulated Shuttle environmental exposures of both LI-1500 and LI-900 RSI materials.

14

COATING DEVELOPMENT

SILICA RSI THERMAL EXPANSION

TEMPERATURE ($^\circ$K) ($^\circ$F)		Δ L/L CM/CM (IN./IN.) x 10^{-5} LI-1500	LI-900
477	400	10.3 TO 13.6	10.0 TO 11.2
828	650	17.3 TO 19.6	19.6 TO 21.3
755	900	22.3 TO 25.9	28.7 TO 30.7
976	1300	37.7 TO 42.3	44.3 TO 46.0
1170	1650	50.4 TO 56.0	53.0 TO 55.2

0042 COATING THERMAL EXPANSION

TEMPERATURE ($^\circ$K) ($^\circ$F)		Δ L/L CM/CM (IN./IN.) x 10^{-5}
477	400	15.2 TO 18.1
700	800	36.6 TO 39.4
921	1200	57.7 TO 60.4
1143	1600	61.9 TO 65.6

Figure 7

PROCESSING OF RIGIDIZED REI-MULLITE INSULATIVE COMPOSITES

BY

J.J. GEBHARDT, P.D. GORSUCH, M.A. BRAUN

GENERAL ELECTRIC COMPANY
RE-ENTRY & ENVIRONMENTAL SYSTEMS DIVISION
PHILADELPHIA, PENNSYLVANIA

17

INTRODUCTION

The General Electric Company's Re-Entry and Environmental Systems Division (GE-RESD) has been developing and evaluating a series of high insulative efficiency, rigidized fibrous insulation materials for potential application to shuttle orbiter thermal protection systems (TPS). TPS based on these materials are lightweight and offer the potential for increasing the orbiter payload weight fractions. In addition, their refractory nature and high melting point temperatures suggest that they will have both (1) multimission capability without property or performance degradation, and (2) greater reserve margin than other candidate thermal protection systems during high surface temperature excursions such as might occur during a mission abort. The GE-RESD designation for this class of materials is Reusable External Insulations (REI).

The development and effective application of this lightweight, high performance surface insulative TPS has required an iterative procedure in which design, system, and mission requirements were defined and translated into material property and behavioral requirements and subsequently into specific test and evaluation criteria. With respect to design, REI materials offer both great flexibility and simplicity since the insulation thicknesses can be sized to achieve sufficiently low operational backface temperatures to permit the use of organic adhesive bonds for attaching the panels to the primary or support structures. However, the limited strength levels of the REI materials, i.e., about $6.9 \times 10^5 - 10.3 \times 10^5$ N/m^2 (100-150 psi) in tension and compression, mandate the use of finite thickness flexible adhesives to reduce both the stress concentrations and the shear and normal stress requirements of the adhesives and insulations. An additional advantage of the low operational backface temperatures is that they permit the use of state-of-the-art airframe structures fabricated from aluminum and titanium alloys, rather than the more costly superalloy and refractory metals.

The development programs at GE-RESD have included evaluation of an all silica system (REI-Silica), an all mullite system (REI-Mullite), and an all-zirconia based system (REI-Zirconia). Evaluation results indicated that the REI-Mullite material was the best compromise among TPS weight, insulation effectiveness, mechanical strength and structural integrity, and thermal and structural stability for a 100-mission life with the shuttle orbiter maximum surface temperature requirement of 1644°K (2500°F).

This paper summarizes the development and evaluation activities at GE-RESD on the REI-Mullite class of insulative materials. Much of the work described was supported through the use of General Electric Company discretionary funds. Studies concerned with the application of REI materials to the shuttle orbiter have been conducted under subcontract from the North American Rockwell Corporation (NR/SD) as part of their Space Shuttle Phase B contract. Other contract activities include (1) design application programs on rigidized reusable surface insulation TPS with the NASA Manned Spacecraft Center (NAS 9-12084 and NAS 9-12855), and (2) the development of insulation materials for the NASA Langley Research Center (NAS 1-10533). Data obtained in these contract activities are included wherever appropriate for completeness.

19

MOD IB REI-MULLITE INSULATIVE COMPOSITES

(Figure 1)

The material development program from which the Mod IB REI-Mullite evolved was guided by the principle that the fiber-binder interaction was extremely important in controlling the material properties and characteristics. In particular, maximizing the concentration of binder at fiber intersections was expected to minimize composite density for a given strength level and to maximize strength and strain-to-failure properties and insulation effectiveness at all density levels. This hypothesis has been verified both experimentally and analytically.

Three types of binder systems have been defined, developed, and evaluated in the study of the REI-Mullite class of materials. These are a mullite base binder system similar in composition to the mullite fibers (Mod O REI-Mullite), a silicone resin/organometallic system (Mod I REI-Mullite), and an aluminum-boria-silica glass (Mod IA and IB REI-Mullites). Much of the data presented here are on Mod IA REI-Mullite because it has undergone the most extensive characterization. However, Mod IA REI-Mullite and Mod IB REI-Mullite are similar except for a change in firing schedule, which has yielded a more effective distribution of binder with resulting superior mechanical properties and possibly insulative effectiveness.

Mod IB REI-Mullite consists of about 10 percent by volume of mullite fibers rigidized by bonding their points of contact with a refractory ceramic glass cement. The mullite fibers are alumina-rich near stoichiometric ($3 Al_2O_3 - 2 Si_2O_2$) materials supplied by the Babcock and Wilcox Company. Fiber diameters are typically in the 4 to 8 μm range. Although the rigidized composites can be made over a range of densities, the density level of about 192 Kg/m^3 (12 lbs/ft^3), selected to be near optimum for this material, reflects a compromise between mechanical properties including strength and strain-to-failure and insulative efficiency.

MOD I A AND I B REI-MULLITE INSULATIVE COMPOSITES
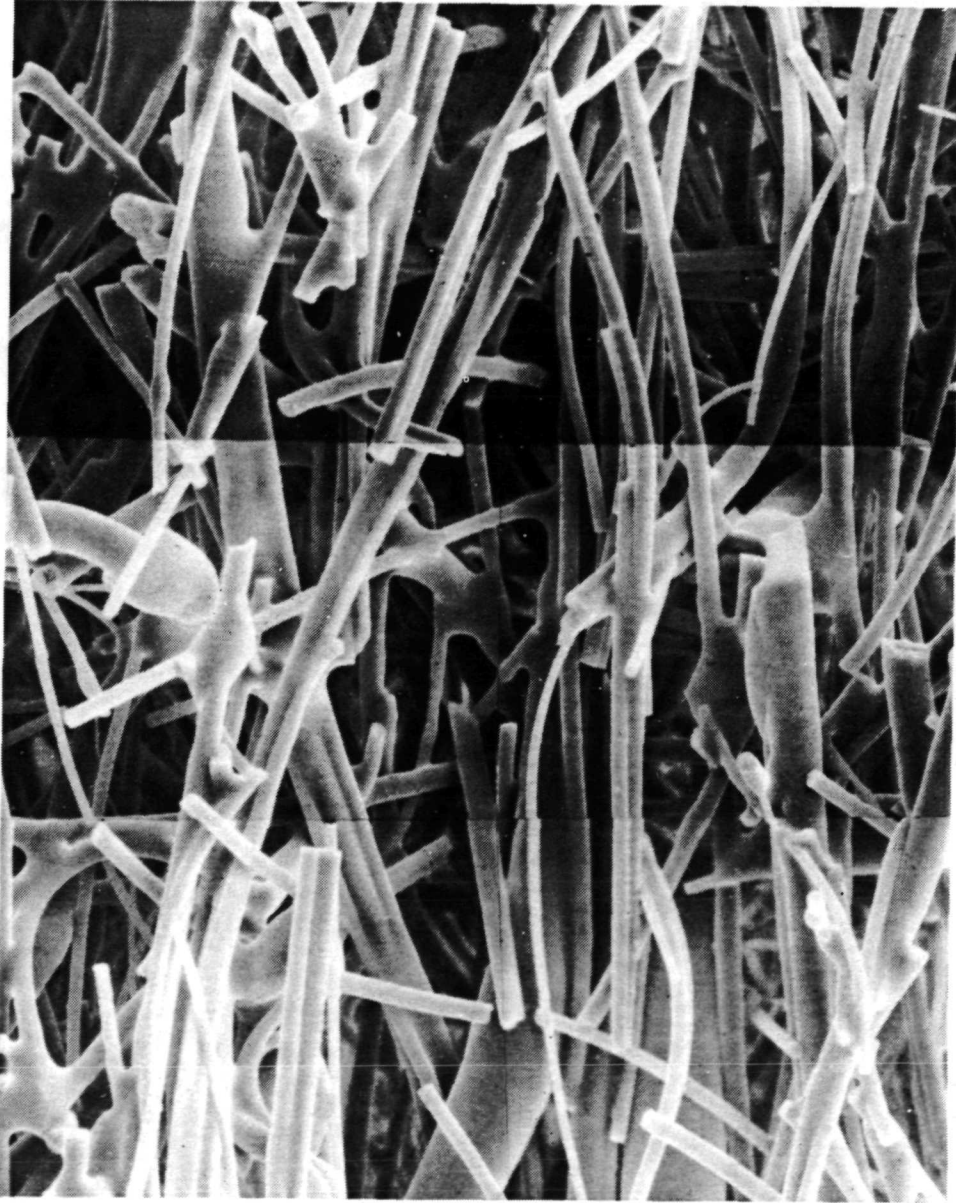
100 μm

Figure 1

21

MULLITE FIBER CHARACTERISTICS (AFTER FETTEROLF[1])

(Figure 2)

The mullite fibers are made by Babcock and Wilcox Company (B&W) by a salt decomposition process and, as manufactured, consist of a glassy mixture of oxides with a slight excess of γ-Al_2O_3. This oxide mixture, when fired to temperatures of at least 1450°K (2150°F), yields pure mullite ($3Al_2O_3 \cdot 2 SiO_2$). In some fibers, small amounts of aluminum borate ($9Al_2O_3 \cdot 2 B_2O_3$) are also present. These results are consistent with an initial nominal fiber composition of about 77 percent Al_2O_3, 17 percent SiO_2, 4.5 percent B_2O_3 and 1.5 percent P_2O_5.

The properties of the B & W mullite fibers are markedly dependent on firing temperature as indicated by the data of Fetterolf[1] shown in the figure. The degradation in strength properties at temperatures above 1422°K (2100°F) apparently results from a combination of factors including (1) vaporization of constituents such as B_2O_3 and P_2O_5, (2) mullite crystallite and grain formation, and (3) subsequent growth of the mullite grains in the fibers. X-ray diffraction studies at GE-RESD have confirmed the transformation of the initial oxide mixture into mullite in the 1553° to 1644°K (2300° to 2500°F) temperature range and the subsequent growth of the mullite grains, particularly for extended periods of exposure at temperatures of 1644°K (2500°F) or higher. The latter phenomenon has only been shown in a qualitative manner.

Because of this tendency for the oxide mixture in the fibers to crystallize to mullite and degrade the fiber properties, the firing schedule for coated Mod IB REI–Mullite composites has been adjusted to minimize time of exposure above 1533°K (2300°F). Also, the binder composition has been tailored to provide protection to the fibers and retard degradation. With these factors taken into consideration, the multimission use capability of the REI—Mullite thermal protection systems is maximized, and no significant performance degradation is observed for the temperature–time combinations to which the shuttle orbiter TPS is exposed.

22

MULLITE FIBER CHARACTERISTICS
(AFTER FETTEROLF)

Figure 2

23
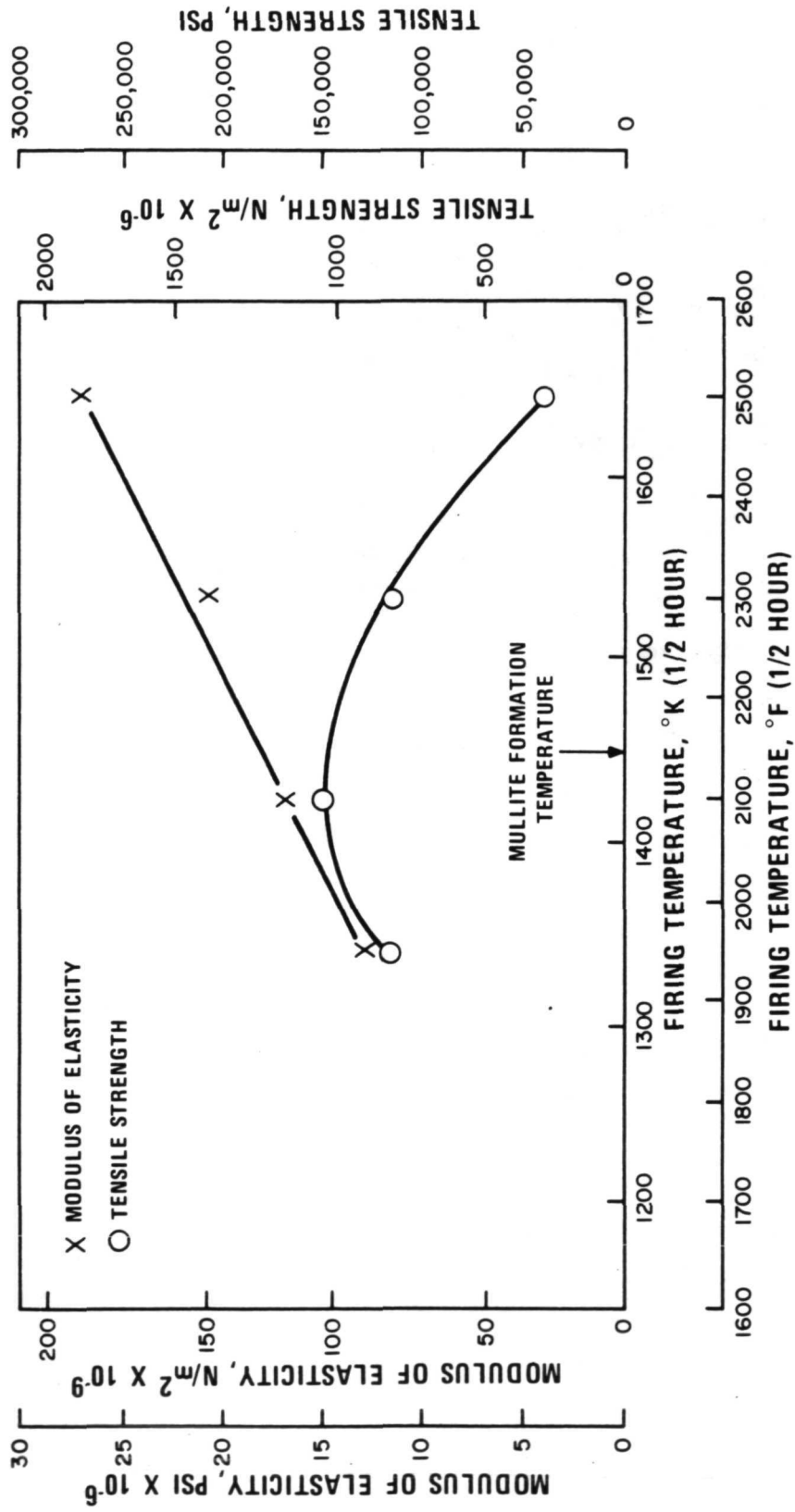
AS RECIEVED MULLITE FIBERS

(Figure 3)

The mullite fibers as received from B&W consist of long stable fibers in the form of batting or mats, the fiber axes being roughly parallel to the direction of the blanket. In certain batches, large quantities of powdered, unfiberized material are evident, while in other batches the fibers appear to contain significant quantities of thick, stiff material. Efforts were made to classify the raw material prior to use by cutting and water separation. Considerable dust and heavy material (~ 10 percent) was thus screened out, but it was also evident that a portion of the finer and presumably stronger material was also lost since the fiber diameter histogram for classified fibers indicated a larger average diameter, skewed toward the large diameter size (see Figure 4d). Consequently, fiber classification was dropped as a routine process step, and the fibers were used as received, with out-of-specification material eliminated by examination.

The degree of entanglement of the fibers made it necessary, however, to introduce a fiber cutting or separation step in the manufacture of the composites to achieve uniform and reproducible properties. This step is currently carried out in connection with the fiber-binder slurry preparation stage, and results in fiber lengths in the 200 to 400 μm range.

24

AS RECEIVED MULLITE FIBERS

10 μm

500X

20X

Figure 3

25
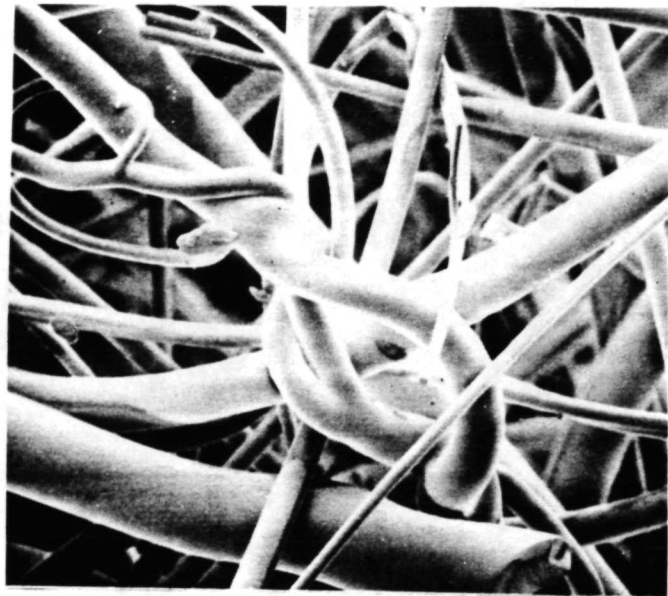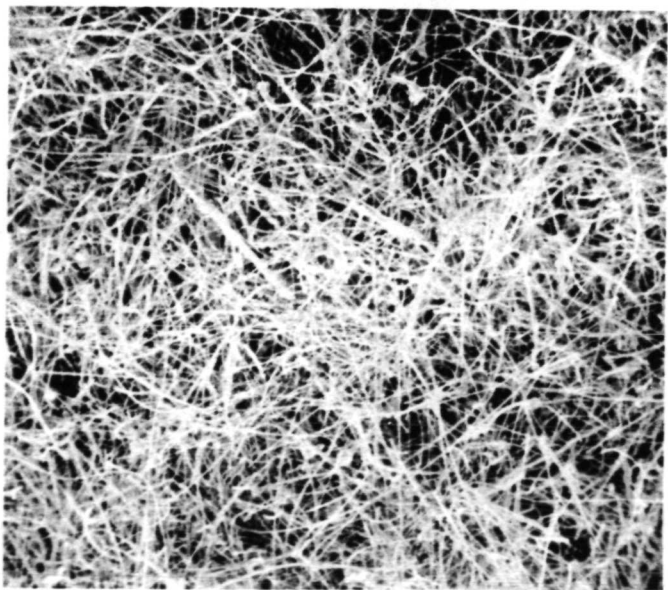
FIBER DIAMETER HISTOGRAMS OF B&W MULLITE FIBERS

(Figure 4)

Typical fiber diameter histograms are shown in Figure 4 for the 4, 4.7, and 6 μm classes of B & W mullite fibers. It is to be noted that the fiber diameter varies significantly within each class of material.

The mullite fibers used in Mod IA and IB REI-Mullite have a nominal 4.7 μm diameter. However, it was necessary to use larger diameter fibers (nominal 6 μm) for all of the Mod 0 and part of the Mod I REI-Mullite development and evaluation studies because of lack of availability of the smaller diameter fibers. Statistically, the smaller diameter fibers appear to produce insulative composites with higher strength and strain-to-failure capabilities. (See Figure 6.)

26

FIBER DIAMETER HISTOGRAM
OF B&W MULLITE FIBERS
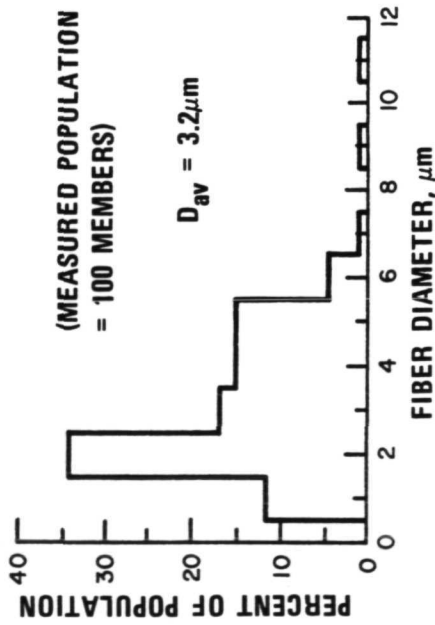
(a) DISTRIBUTION OF 4μm FIBER DIAMETERS

(b) DISTRIBUTION OF 4.7μm FIBER DIAMETERS
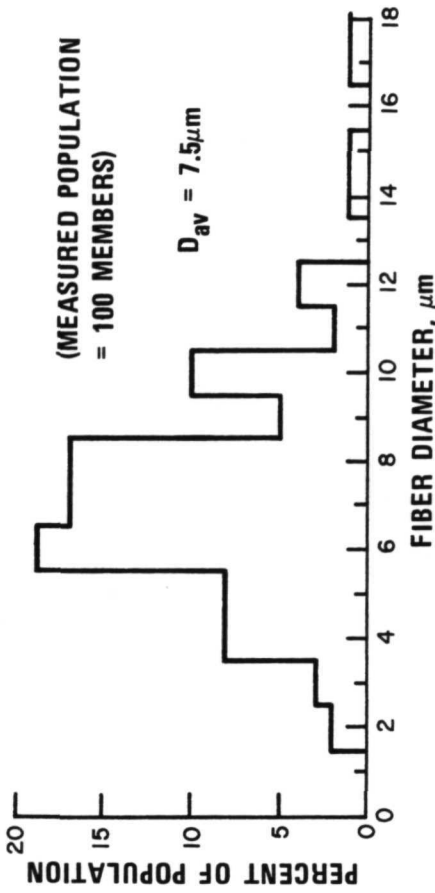
(c) DISTRIBUTION OF 6μm FIBER DIAMETERS
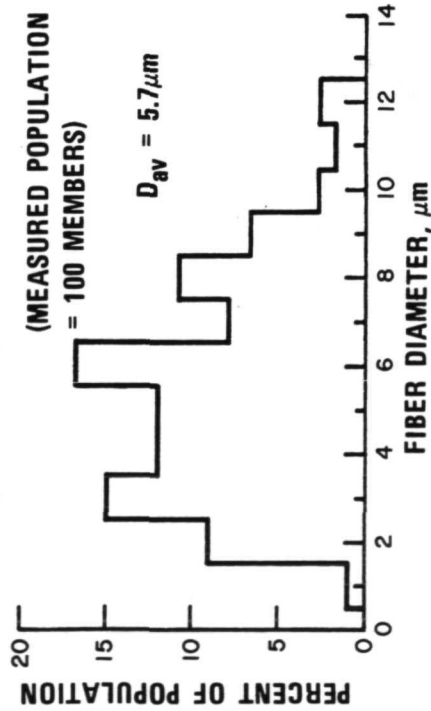
(d) DISTRIBUTION OF 6μm CLASSIFIED FIBER DIAMETERS

Figure 4

27
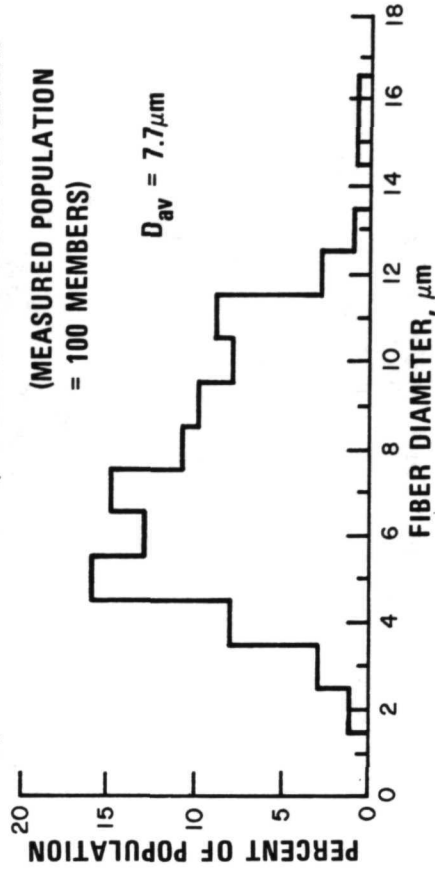
X-RAY DIFFRACTION PATTERNS

(Figure 5)

The as received mullite fibers typically consist of a low temperature γ-Al_2O_3 phase [strongest reflections at 1.40 and 1.98 $\times$ 10^{-10}m (1.40 and 1.98 A°) wavelengths], an amorphous phase and a nonstoichometric mullite phase. Upon heat treatment, the Al_2O_3 phase combines to form a stable mullite phase with some residual amorphous material.

28

X-RAY DIFFRACTION PATTERNS

B&W MULLITE FIBER
AS RECEIVED

B&W MULLITE FIBER
HEATED 4 HRS 1644°K (2500°F)

Figure 5

29
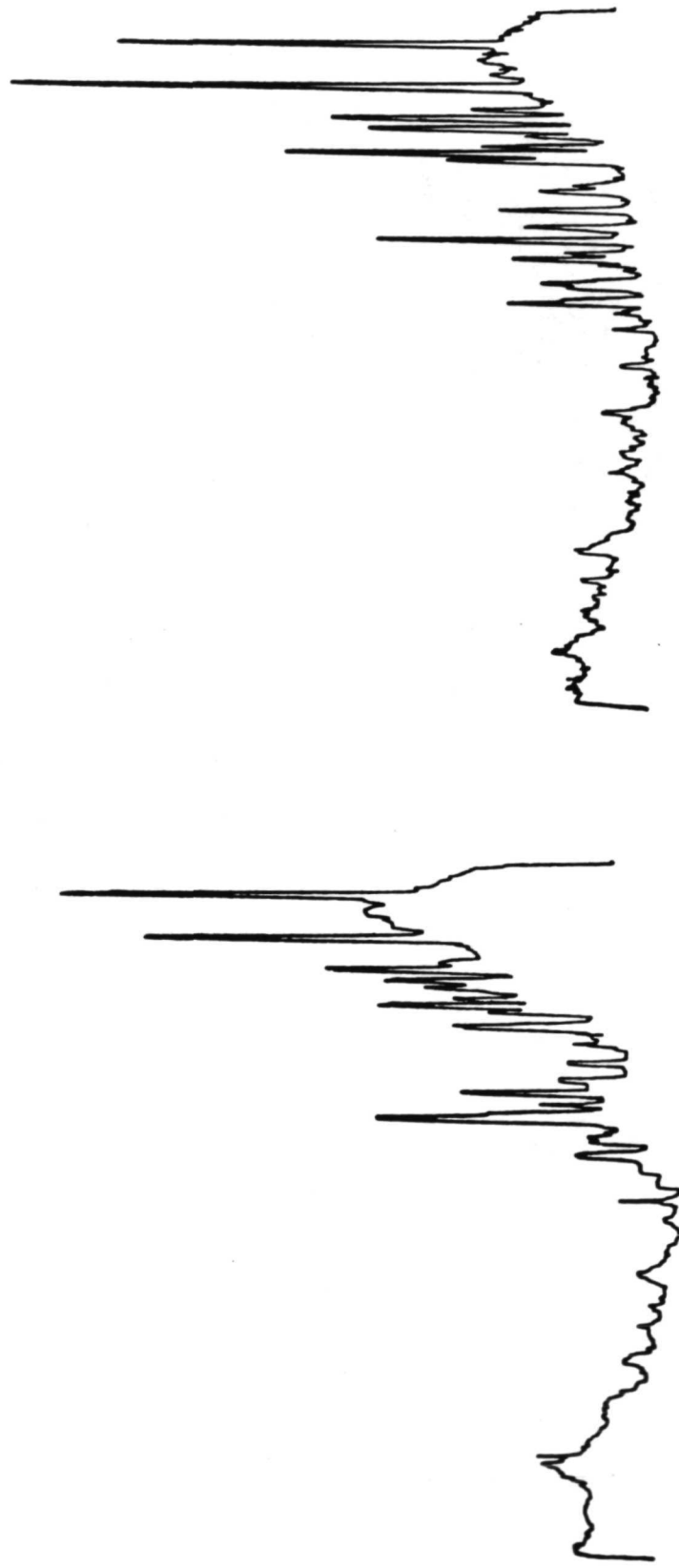
STRENGTH-FIBER SIZE DISTRIBUTION RELATIONSHIPS FOR MOD I AND IA REI-MULLITE

(Figure 6)

The strength of the REI-Mullite composites was expected to vary with the diameter of the fibers used in the fabrication of the composites. The smallest diameter fibers normally have intrinsically higher strength because of their lower surface areas and lesser degree of surface imperfections, and there are more fibers per unit weight incorporated into the composite compared with materials made with larger diameter fibers (potentially stronger and more flexible truss network).

The figure shows some experimental results for composites made with nominal 4 μm (actual average 3.2) and 6 μm (actual average 7.5) diameter fibers. The strength of the composite made with the finer fibers is about twice that for the composite made with the coarse fibers. Thus the emphasis in the REI-Mullite development program has been to use the smallest diameter mullite fibers available.

STRENGTH–FIBER SIZE DISTRIBUTION RELATIONSHIPS FOR MOD I AND IA REI-MULLITES

(A) SI UNITS

MOD I A

FIBER DIAMETER (μm)	TEST POINTS		TENSILE STRENGTH ($N/m^2 \times 10^{-3}$)	
	IN-PLANE	ACROSS PLANE	IN-PLANE	ACROSS PLANE
4	6	6	558.5	200.0
6	2	9	271.7	124.1

MOD I

FIBER DIAMETER (μm)	TEST POINTS		TENSILE STRENGTH ($N/m^2 \times 10^{-3}$)	
	IN-PLANE	ACROSS PLANE	IN-PLANE	ACROSS PLANE
4	2	4	379.2	213.0
6	2	3	326.8	157.2

(B) ENGLISH UNITS

MOD I A

FIBER DIAMETER (μm)	TEST POINTS		TENSILE STRENGTH (LB/IN^2)	
	IN-PLANE	ACROSS PLANE	IN-PLANE	ACROSS PLANE
4	6	6	81.0	29.0
6	2	9	39.4	18.0

MOD I

FIBER DIAMETER (μm)	TEST POINTS		TENSILE STRENGTH (LB/IN^2)	
	IN-PLANE	ACROSS PLANE	IN-PLANE	ACROSS PLANE
4	2	4	55.0	30.9
6	2	3	47.4	22.8

Figure 6

31

COMPARISON OF MOD 0, MOD I, MOD IA AND MOD IB REI-MULLITES

(Figure 7)

Three types of binder systems were evaluated in the fabrication studies on the REI-Mullite class of materials. They were compared as to cost effectiveness, reproducibility of manufacture, and level and uniformity of properties. Included were a mullite base binder system similar in composition to the mullite fibers (Mod 0), a silicone resin/organometallic system (Mod I), and an alumina-boria-silica glass (Mod IA and IB). Although Mod 0 REI-Mullite exhibited good stability during high temperature exposure, its properties were inadequate to meet design requirements because the binder phase was in the form of mud-like clumps adhering to the fibers and was not selectively attached to fiber/fiber intersection points. Thus primary emphasis in the program was shifted to Mod I, IA, and IB REI-Mullites.

The Mod I REI-Mullite system consists of mullite fibers bonded together with a binder system formed in a two-step process: rigidization by pyrolysis of a silicone resin followed by modification of the silica layer through addition of an alumina-silica-boria component obtained by hydrolysis and pyrolysis of specific organometallic precursors. The Mod I system has sufficiently high cross-plane and in-plane strength, as well as insulation capability and strength retention, to meet the TPS limit-load requirements (with zero factor of safety). The strain-to-failure level of the Mod I system, however, was found to be deficient with regards to the NASA established 1.5 factor-of-safety at ultimate load. The relatively low strain level is believed to be primarily the result of fiber changes brought on by the high firing temperature [1644° K, (2500° F)] required in order to stabilize the composite panel against dimensional changes at maximum operating temperatures. The Mod I process, although controllable on a laboratory-scale basis, was not easily applied in a pilot plant type operation because of the process complexity.

The simultaneous development of a wholly inorganic binder system (designated Mod IA REI-Mullite) consisting of an alumina-modified borosilicate glass mixture provided a binder that could be fired at a somewhat lower temperature 1533° K (2300° F) and still exhibit dimensional stability at 1644° K (2500° F). The higher tensile strain-to-failure levels and improved insulation efficiency of the Mod IA system coupled with its simpler, easily controlled, and less expensive process cycle (compared to the Mod I process), led to its incorporation into the GE-RESD REI pilot plant in November 1971. Mod IB REI-Mullite is similar to Mod IA except for firing procedure. The modified firing procedure results in a greater degree of optimization of binder distribution with resulting enhanced mechanical properties.

COMPARISON OF MOD 0, MOD I, MOD IA, AND MOD IB REI-MULLITES

	MOD 0	MOD I	MOD IA	MOD IB
FIBER	B&W 6 μm FIBER	B&W 6 μm FIBER	B&W 4.7 μm FIBER	B&W 4.7 μm FIBER
BINDER	MULLITE SYNTHESIS BASED UPON USE OF FIBER COMPOSITION BINDER	2 STEP PROCESS-SILICONE PYROLYSIS FOLLOWED BY MULLITE SYNTHESIS USING ORGANOMETALLIC A1$_2$O$_3$-SiO$_2$-B$_2$O$_3$ PRECURSORS	1 STEP PROCESS-TERNARY A1$_2$O$_3$-SiO$_2$-B$_2$O$_3$ GLASS COMPOSITION	1 STEP PROCESS-TERNARY A1$_2$O$_3$-SiO$_2$-B$_2$O$_3$ GLASS COMPOSITION
FORMING PROCESS	PRESSED	GRAVITY-DRAIN	GRAVITY-DRAIN	GRAVITY-DRAIN
MAXIMUM FIRING TEMPERATURE	1644°K (2500°F)	1644°K (2500°F)	1533°K (2300°F) 1644°K (2500°F WITH COATING CYCLE)	1533°K (2300°F) 1644°K (2500°F WITH COATING CYCLE)

Figure 7

33

MOD I, IA, AND IB REI-MULLITE PROCESS DESCRIPTIONS

(Figure 8)

The process flow diagrams for composite fabrication for each of the family of REI-Mullite materials are schematically shown in the figure. In panel fabrication, mullite fibers are blended into an aqueous binder solution using a high speed shear impeller, which chops them into desired lengths and disperses the fibers uniformly throughout the binder. The agitated fibrous slurry is transferred into a mold having a porous base that retains the fibers but allows passage of the excess binder solution. Rapid binder removal and fiber settling are necessary to maintain proper fiber orientation. The fibers are then compressed to the necessary height to produce the required panel density. After a short residence time in the mold, the panel is removed from the mold and dried in an air-circulating oven. The drying cycle removes binder water and rigidizes the mullite cake to permit subsequent handling and firing.

An important feature of the Mod IA and IB REI-Mullite process is the shear blade cutting of the fibers in the binder slurry. In this way, uniform mullite fiber lengths are obtained in the composites and the fibers are uniformly coated with binder. Density is controlled by pouring the slurry into a closed mold and pressing the panels to preselected thicknesses. This approach overcame difficulties encountered in early processing studies; that is, nonoptimum fiber lengths, distributions, and orientations led to the fabrication of panels containing fiber clumps, laminations, and voids. Thus effective utilization of the potential strengthening effects of the fibers in the composites was enhanced.

34

MOD I, IA, AND IB
REI-MULLITE PROCESS DESCRIPTIONS
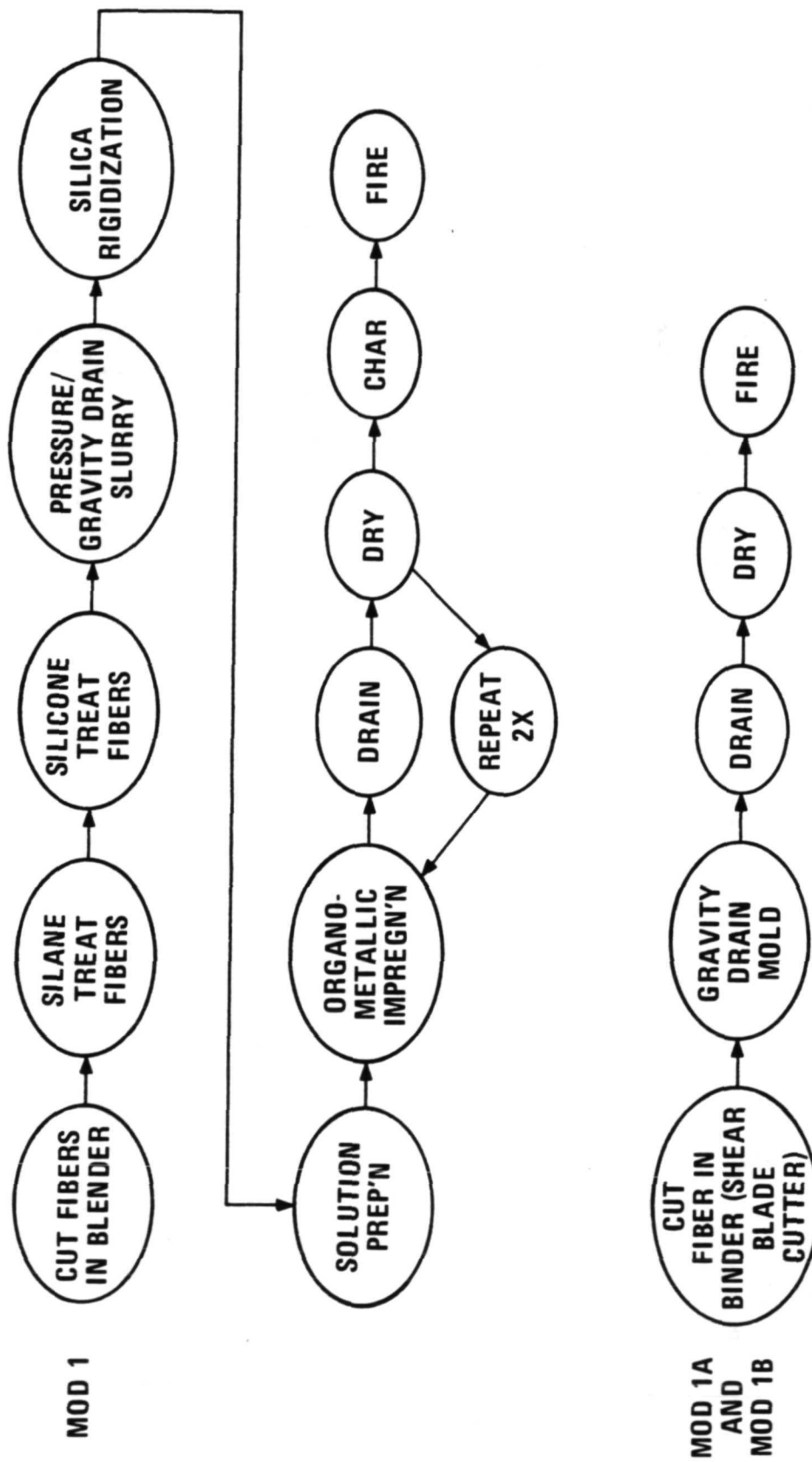
Figure 8

MOD 1B REI-MULLITE PROTOTYPE HARDWARE

(Figure 9)

The cast panels are fired in a high temperature kiln to rigidize the composites. The firing schedule is programmed to optimize binder flow to fiber intersections and its subsequent conversion to a refractory glass binder. After firing, the panels are machined into individual tiles or specimens as required. Uncoated material can be machined readily with conventional tooling.

36

MOD IB REI-MULLITE PROTOTYPE HARDWARE

TEST SPECIMENS

FABRICATED PANELS
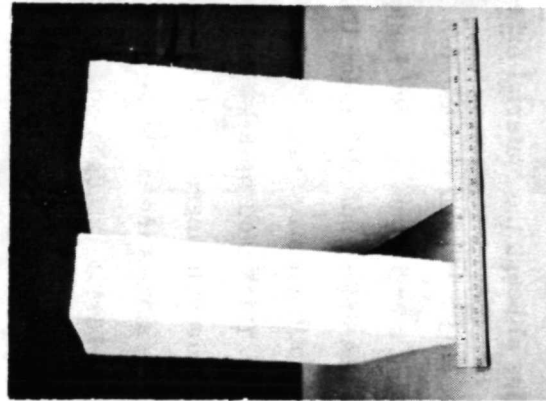
VARIETY OF TILES
AND TEST PIECES

Figure 9

37
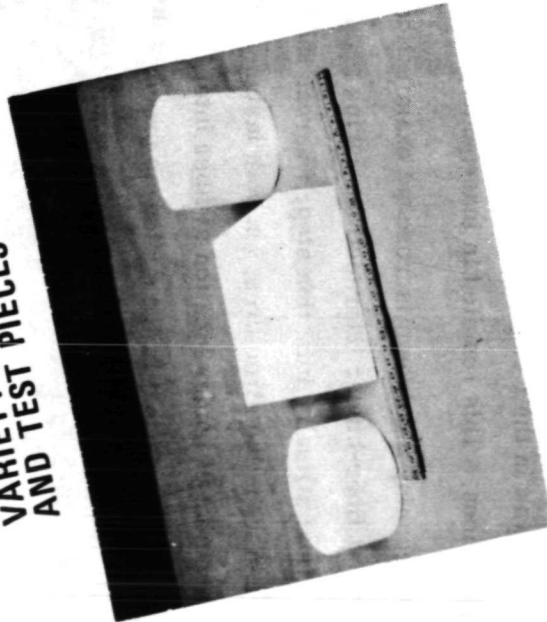
MICROSTRUCTURAL CHARACTERISTICS OF REI-MULLITES

(Figure 10)

The general improvement in binder distribution achieved with each step in progressing from Mod 0 to Mod IB binder systems is illustrated through the use of scanning electron micrographs (SEM) in this figure. The binder phase in Mod 0 was in the form of mud-like clumps adhering to the fibers and was not selectively attached to the fiber/fiber intersections. This resulted in inadequate properties although the material exhibited good thermal stability.

Scanning electron miscroscope examination of Mod I, IA, and IB REI-Mullite panels shows that fillet formation occurs at fiber-binder intersections during processing. In the case of Mod I material, filet formation occurred prior to the final silica rigidization step, whereas the Mod IA binder softens during the final firing and adheres to adjacent fibers in web-like structures. In both instances the optimum structure occurs with low binder contents and resulting enhancement of binder location at fiber intersections. Thick Mod I panels displayed increasing amounts of particulate binder indicating that in the scaled-up process a considerable degree of the desired binding mechanism was being lost, possibly because of the steeper silica gradient existing across the thickness. Inasmuch as the organometallic component added after rigidization does not soften and fuse at 1644° K (2500° F), it was essential that the fillets be formed prior to this step. With the advent of the simpler and more reproducible Mod IA system, further efforts to achieve maximum filleting in the Mod I system were dropped.

Correlation of the specimens displaying good mechanical strength with scanning electron microscope evidence showed that high tensile strengths were being achieved through the filleting action of the binder, and that highly refractory adobe-like binder systems did not contribute to strength in proportion to the amount of binder present.

38

MICROSTRUCTURAL CHARACTERISTICS OF REI-MULLITES

MOD 0 REI-MULLITE

MOD I REI-MULLITE

MOD I A REI-MULLITE

MOD I B REI-MULLITE

— INCREASING STRENGTH
— INCREASING STRAIN CAPABILITY
— DENSITY REDUCTION
— PROCESS SIMPLIFICATION

Figure 10

39
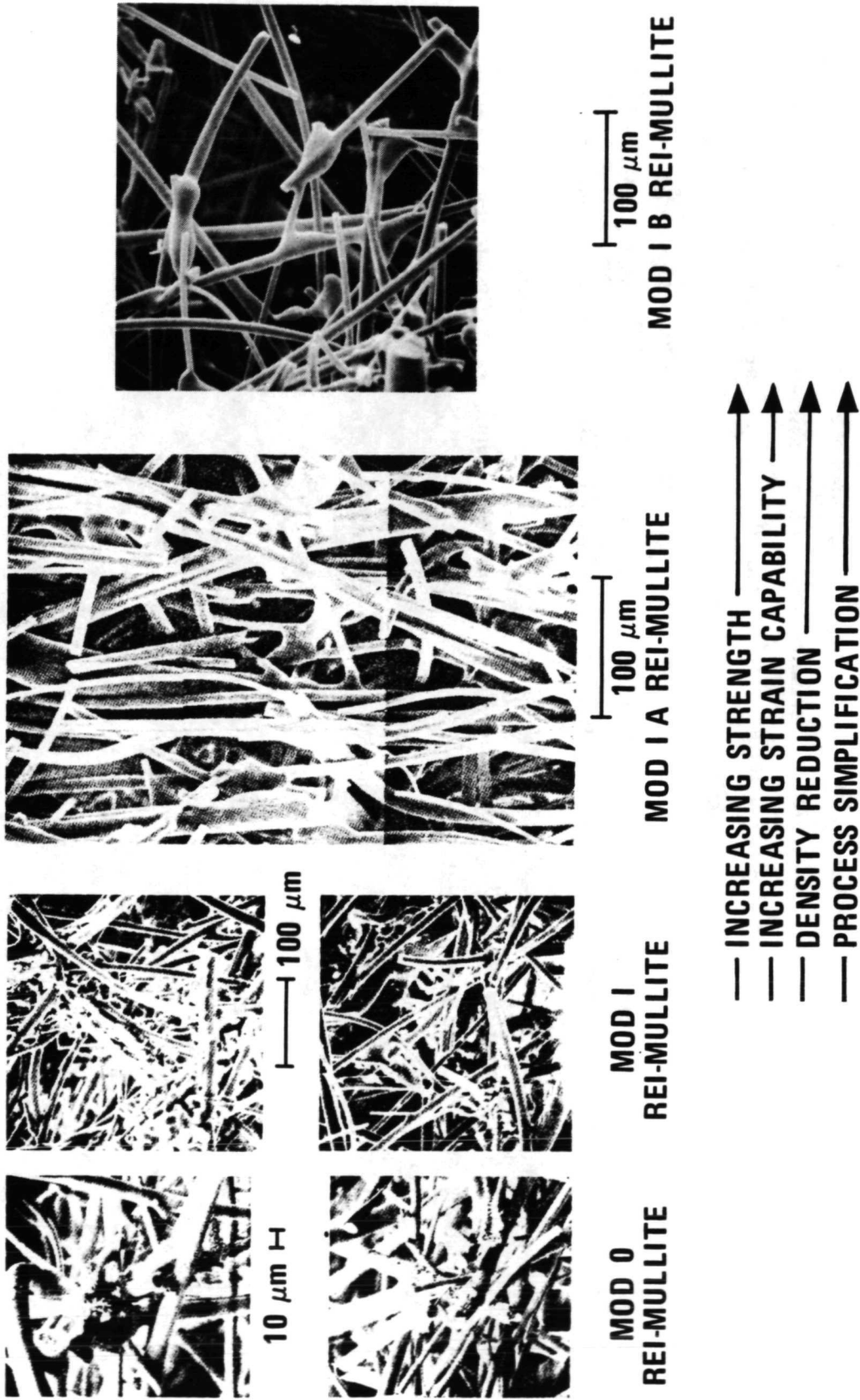
SBA BINDER SYSTEM FOR MOD IA AND IB REI-MULLITES

(Figure 11)

The SBA-10 binder system was evolved through a study of the softening points of a number of alumina-boria-silica glasses. In these studies, increasing quantities of alumina were added to a nonalumina containing borosilicate mixture until the desired high temperature flow characteristics were achieved. In particular, the formulation was selected which would wet the fibers as well as concentrate at the fiber intersections. The strength and strain-to-failure characteristics of these composites were improved without degrading the insulation effectiveness of the material. It was further found that the SBA-10 binder (74.8 percent SiO_2, 18.7 percent B_2O_3, and 6.5 percent Al_2O_3) selected from these studies was resistant to α-cristobalite formation for times up to six hours at $1644°$ K ($2500°$ F).

Figure 11 shows a plot of the composite of the SBA-10 on the $Al_2O_3 - B_2O_3 - SiO_2$ phase diagram proposed by Gielisse and Foster [2]. The estimated liquidus temperature for this composition from these data is about $1533°$ K ($2300°$ F). Reaction of the SBA-10 binder with the mullite-base fibers during exposure of the rigidized composites to temperatures of $1533°$ K ($2300°$ F) or higher increases the binder liquidus temperature. The direction in which the binder composition is expected to change due to the high temperature exposure is indicated.

40

SBA BINDER SYSTEM USED IN MOD IA AND IB REI-MULLITES
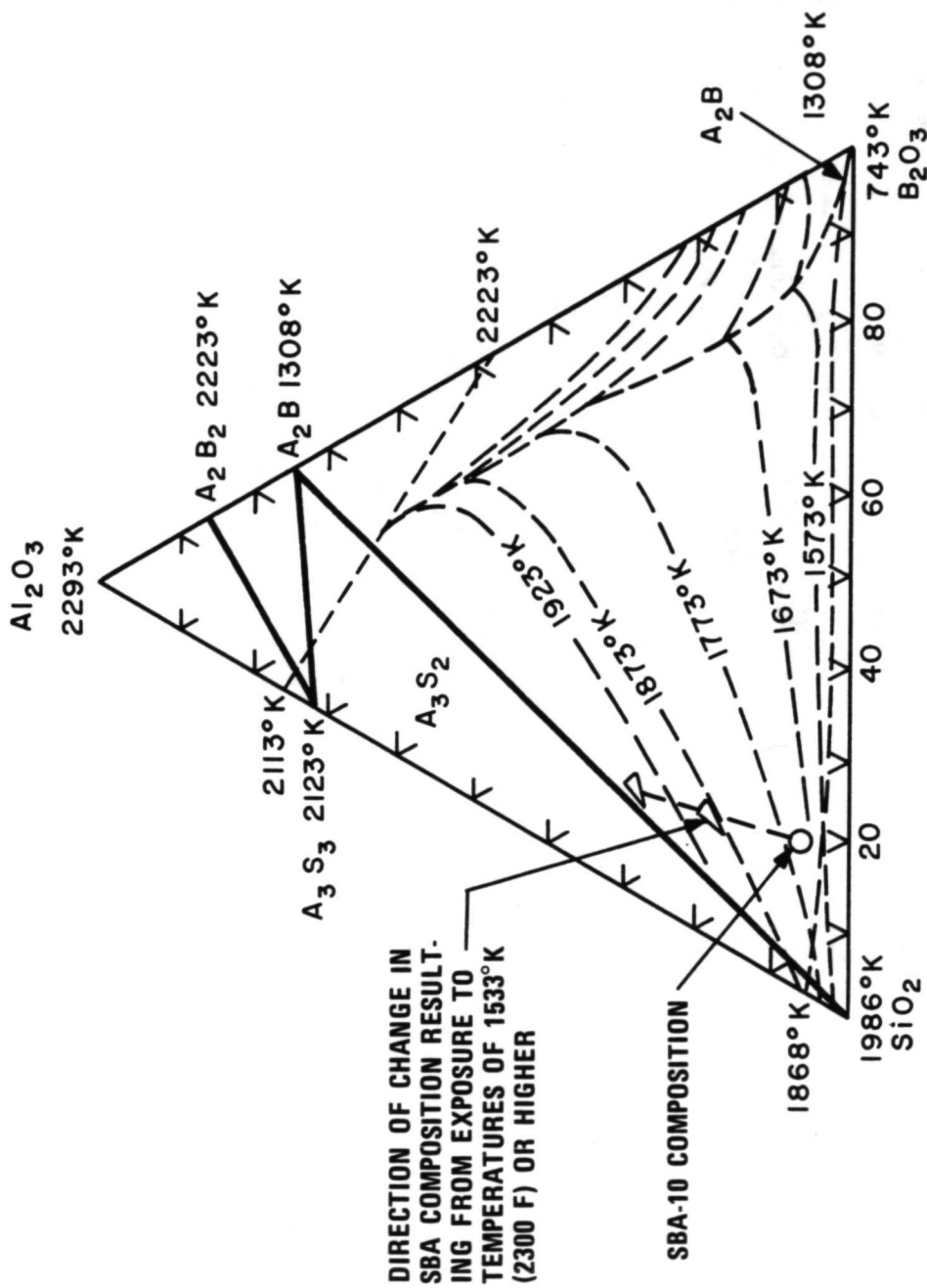
Figure 11

BINDER INFLUENCE OF MOD IA REI- MULLITE CHARACTERISTICS

(Figure 12)

Figure 12 illustrates a series of modulus of elasticity versus test temperature curves for 192 Kg/m^3 (12 pcf) rigidized Mod IA REI-Mullite composites. The general shape of the curves indicates that the composite properties are strongly influenced by the refractory glass binder system. The small rise in moduli up to about 1089° K (1500° F) and the sharp drop above 1366° K (2000° F) are typical of the behavior of refractory glasses. The peaks in the curves at temperatures of about 1200 to 1255° K (1700 to 1800° F) suggest that the glass binder is undergoing some crystallization. However, any crystallites that form are apparently redissolved at higher temperatures.

42

BINDER INFLUENCE ON MOD IA REI-MULLITE CHARACTERISTICS
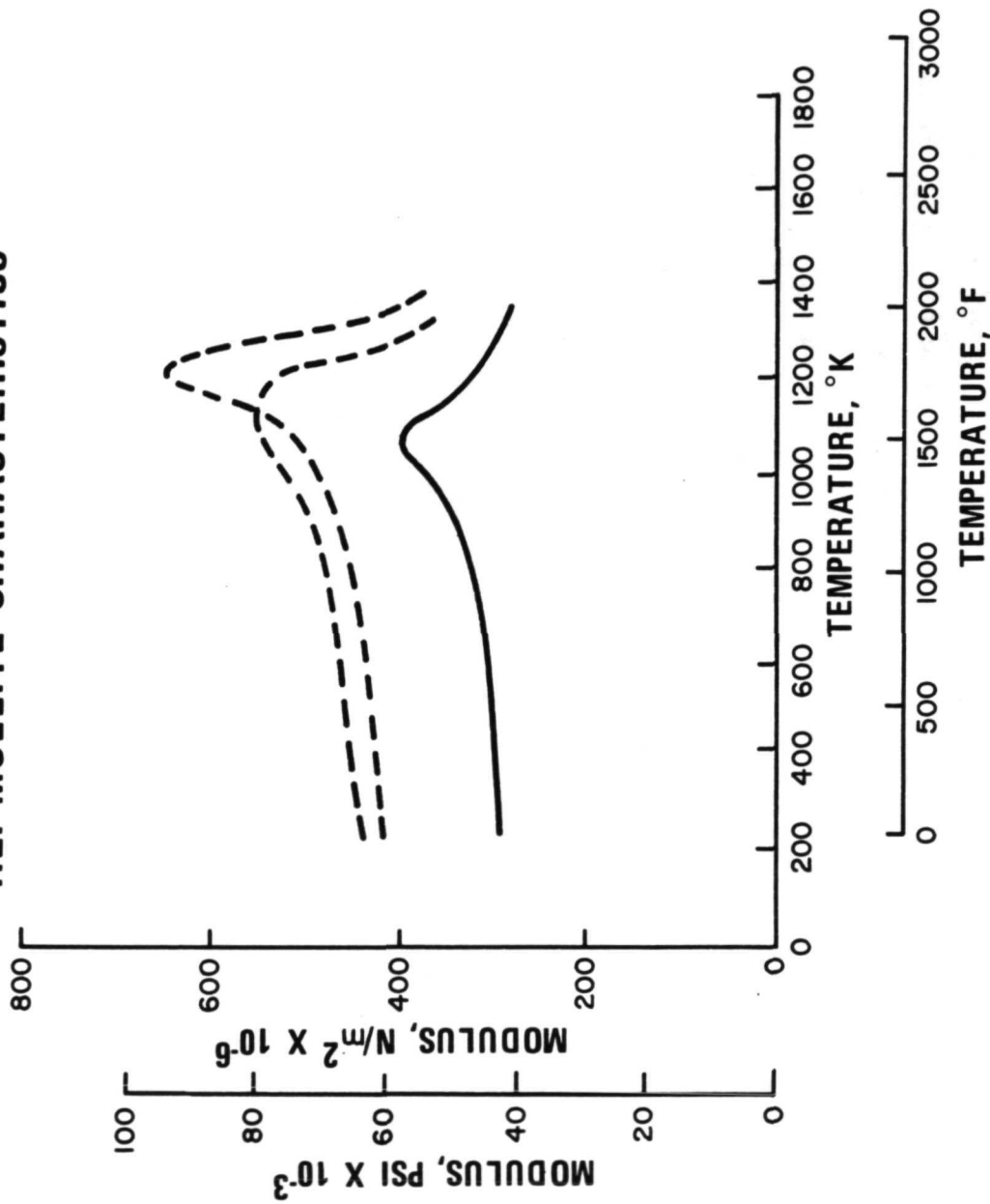
IN-PLANE TENSILE MODULUS VS TEMPERATURE FOR THREE PANELS OF MOD IA REI-MULLITE

Figure 12

43

SBA-10 BINDER STABILITY

(Figure 13)

The Mod IA and Mod IB REI-Mullite binder (SBA-10) is a silica-boria-alumina mixture; therefore, it was evaluated to determine whether the silica would tend to form cristobalite as a result of exposure to elevated temperatures during coating firing as well as during simulated entry heating. The binder was found to be resistant toward cristobalite formation except when the alumina content was low. Figure 13 illustrates that the SBA-10 binder is basically amorphous after 8 hours of heating to 1478° K (2200° F) with only a minimal tendency toward formation of mullite.

44

SBA-10 BINDER STABILITY

X-RAY DIFFRACTION PATTERN OF SBA-10 BINDER FUSED 2 HOURS AT
1561°K (2350°F) AND SUBSEQUENTLY HEAT TREATED FOR 8 HOURS AT
1478°K (2200°F). SOURCE RADIATION: Ni FILTERED CuKα.

Figure 13

45
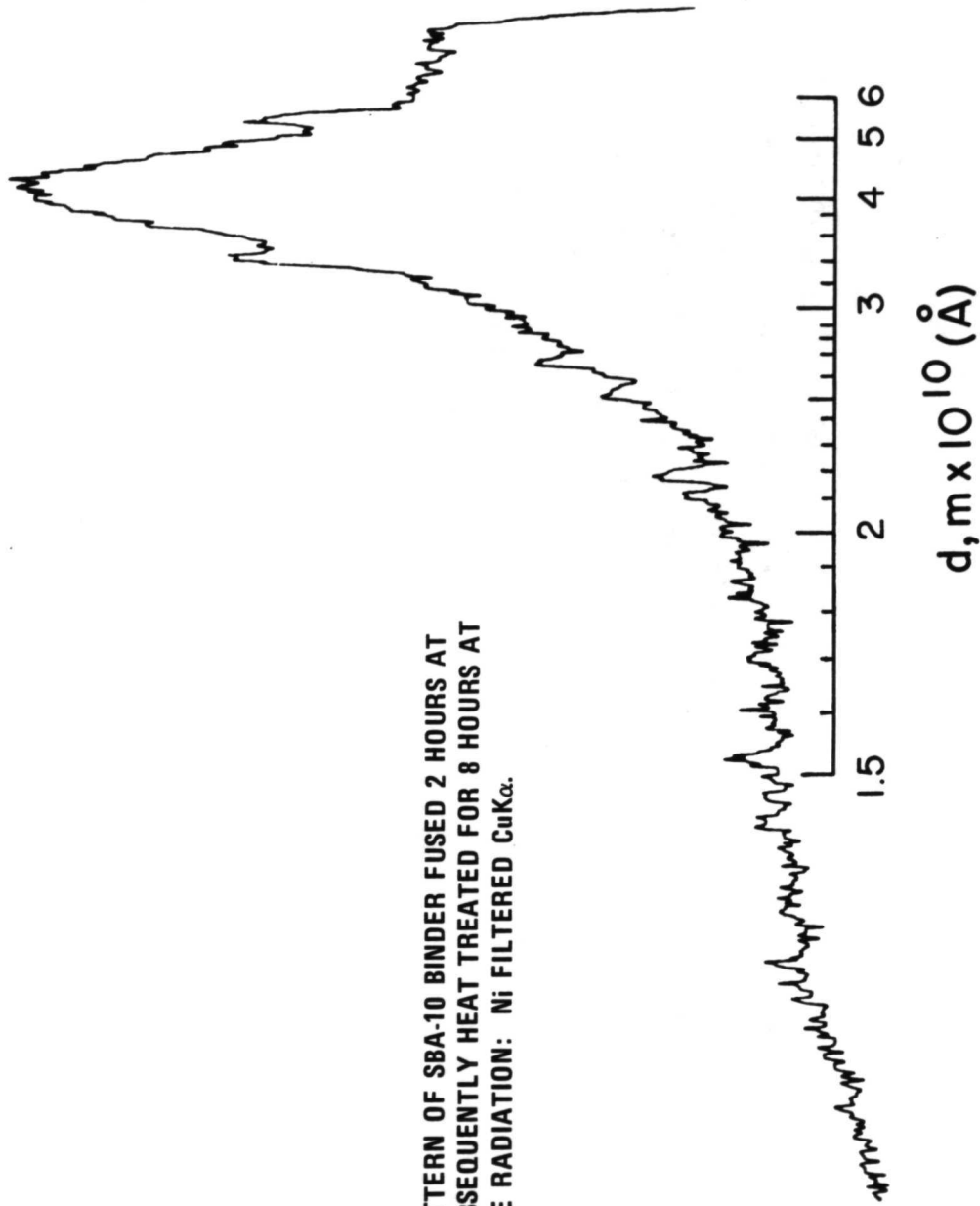
IN-PLANE DIMENSIONAL STABILITY OF MOD IA REI-MULLITE

(Figure 14)

The Larson–Miller parameter, which reduces the time and temperature of exposure to a single variable, has been shown to be an effective method for summarizing the kinetics of shrinkage of rigidized insulative composites [3]. This figure compares the in-plane shrinkage characteristics of several classes of RSI materials with Mod IA REI-Mullite. These results, which are based on data obtained by the Battelle Memorial Institute, show that Mod IA REI-Mullite is much more shape stable in the 1533 to 1644° K (2300 to 2500° F) range than any of the other candidate RSI's. [4] Similar characteristics are expected for Mod IB REI-Mullite.

46

IN-PLANE DIMENSIONAL STABILITY
OF MOD IA REI-MULLITE

Figure 14

47
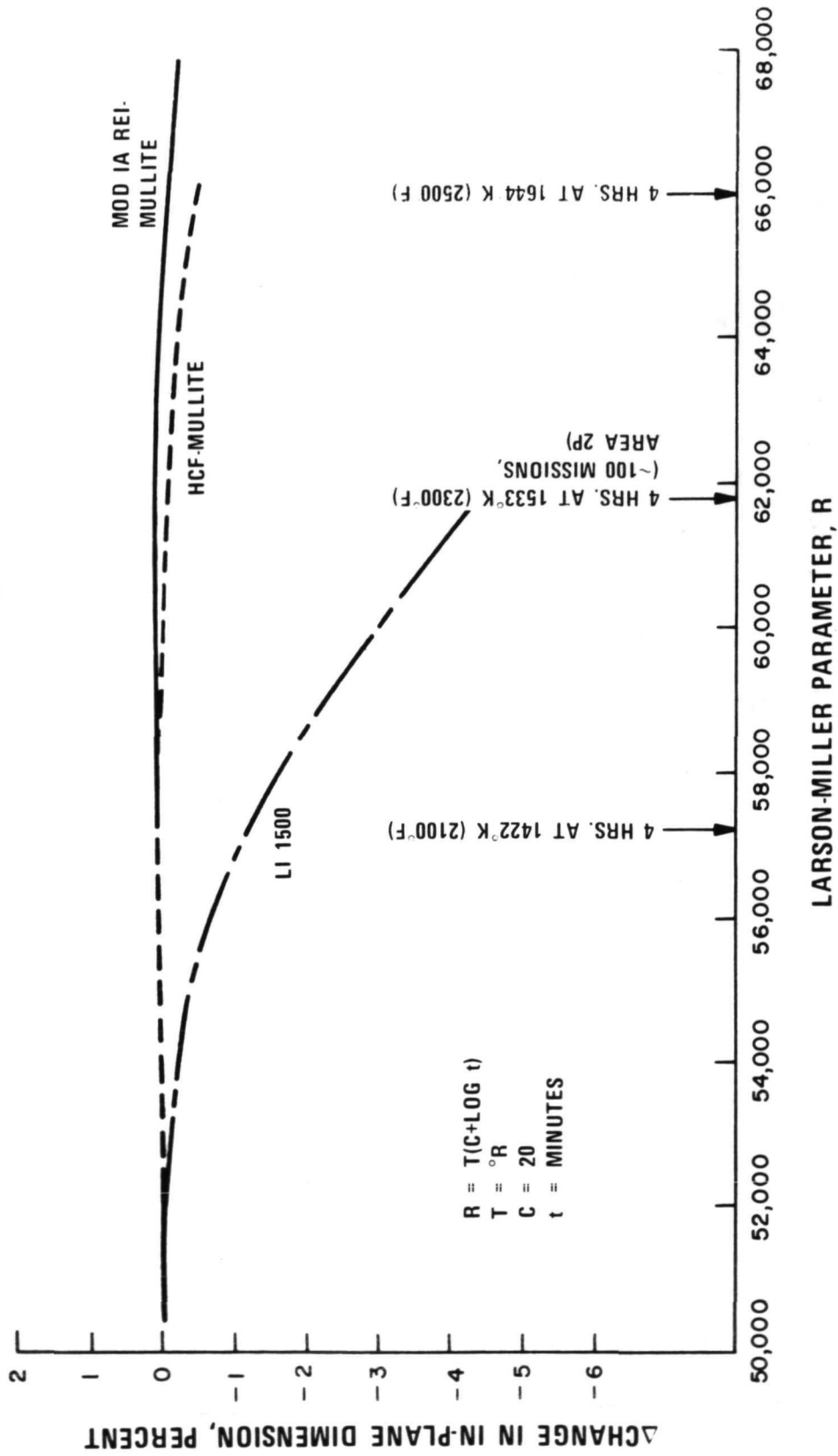
FIRING PROCESS CHANGE DOUBLES REI-MULLITE STRENGTH

(Figure 15)

Mod IB REI-Mullite is essentially identical in composition to Mod IA REI-Mullite except for firing procedure. In particular, the Mod IB REI-Mullite material is fired in an atmosphere that modifies the interfacial tension of the binder phase on the mullite fibers. As a result, the binder preferentially flows to the fiber intersections. Hence, more efficient use is made of the available binder and strength and strain-to-failure levels are increased.

FIRING PROCESS CHANGE DOUBLES
REI-MULLITE STRENGTH

PROPERTY DATA

PROPERTY	LABORATORY RESULTS FOR REI-MULLITE WITH MODIFIED FIRING PROCEDURES	MOD 1A REI-MULLITE,
STRENGTH X–Y, N/m^2 X 10^{-3}(PSI)	1241 (180)	662 (96)
STRAIN X–Y (%)	0.35	0.23
STRENGTH Z, N/m^2 X 10^{-3} (PSI)	276 (40)	186 (27)
STRAIN Z (%)	0.9	0.4

1,000 X

10,000 X

Figure 15

49
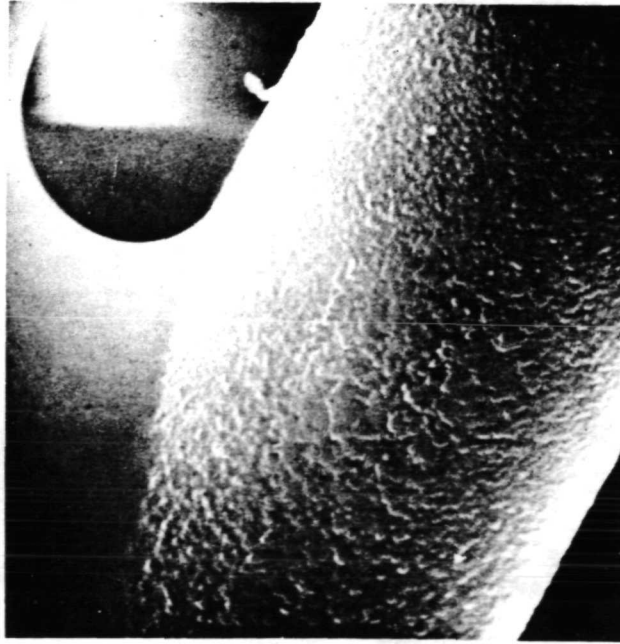
PROPERTY COMPARISONS FOR GE-RESD PILOT PLANT PRODUCED TILES

(Figure 16)

The technology for producing Mod IB REI-Mullite was transferred to the GE-RESD pilot plant and a number of panels were fabricated. Mechanical property data obtained for pilot plant produced panels show a marked improvement in properties similar to that obtained on a laboratory basis. Sufficient data were also generated to establish property minimums for the material: these are indicated in the figure.

50

COMPARISON OF TYPICAL PROPERTIES
FOR GE-RESD PILOT PLANT PRODUCED TILES

	MOD IA REI-MULLITE	MOD IB REI-MULLITE
DENSITY, Kg/m^3 (LBS/FT^3)	187 (11.7)	202 (12.6)
STRENGTH X-Y, N/m^2 X 10^{-3} (PSI)	662 (96)	931 (135)
STRAIN X-Y, %	0.23	0.30
STRENGTH Z, N/m^2 X 10^{-3} (PSI)	186 (27)	276 (40)
MODULUS X-Y, N/m^2 X 10^{-6} (PSI)	296 (43,000)	331 (48,000)
MODULUS Z, N/m^2 X 10^{-6} (PSI)	63 (9,100)	48 (7,000)

PROPERTY SPECIFICATION FOR MOD IB REI-MULLITE TO BE USED IN DELIVERABLES TO NASA-MSC	
• DENSITY RANGE	192 ± 16 Kg/m^3 (12.0 ± 1.0 LBS/FT^3)
• STRAIN X-Y, % MIN	0.25
• STRAIN Z, % MIN	0.5

Figure 16

51

IN-PLANE MECHANICAL PROPERTIES OF MOD IA REI-MULLITE

(Figure 17)

Figure 17 presents some typical mechanical properties for Mod IA REI-Mullite. Mod IB REI-Mullite panels are now undergoing a similar type of extensive characterization.

Although not shown here, the properties of both Mod IA and IB REI-Mullite are somewhat anisotropic. Application of pressure on the fiber/liquid slurry tends to force the fibers from random orientation to one in which a majority of the fibers are parallel to the plane of the panel or tile. This results, as indicated in Figure 15, in a lower through-the-thickness strength. The level of properties is still adequate, however, to meet shuttle orbiter TPS design requirements.

52

IN-PLANE MECHANICAL PROPERTIES
OF MOD IA REI-MULLITE

TENSILE MODULUS

TENSILE STRAIN

TENSILE STRENGTH

Figure 17

53
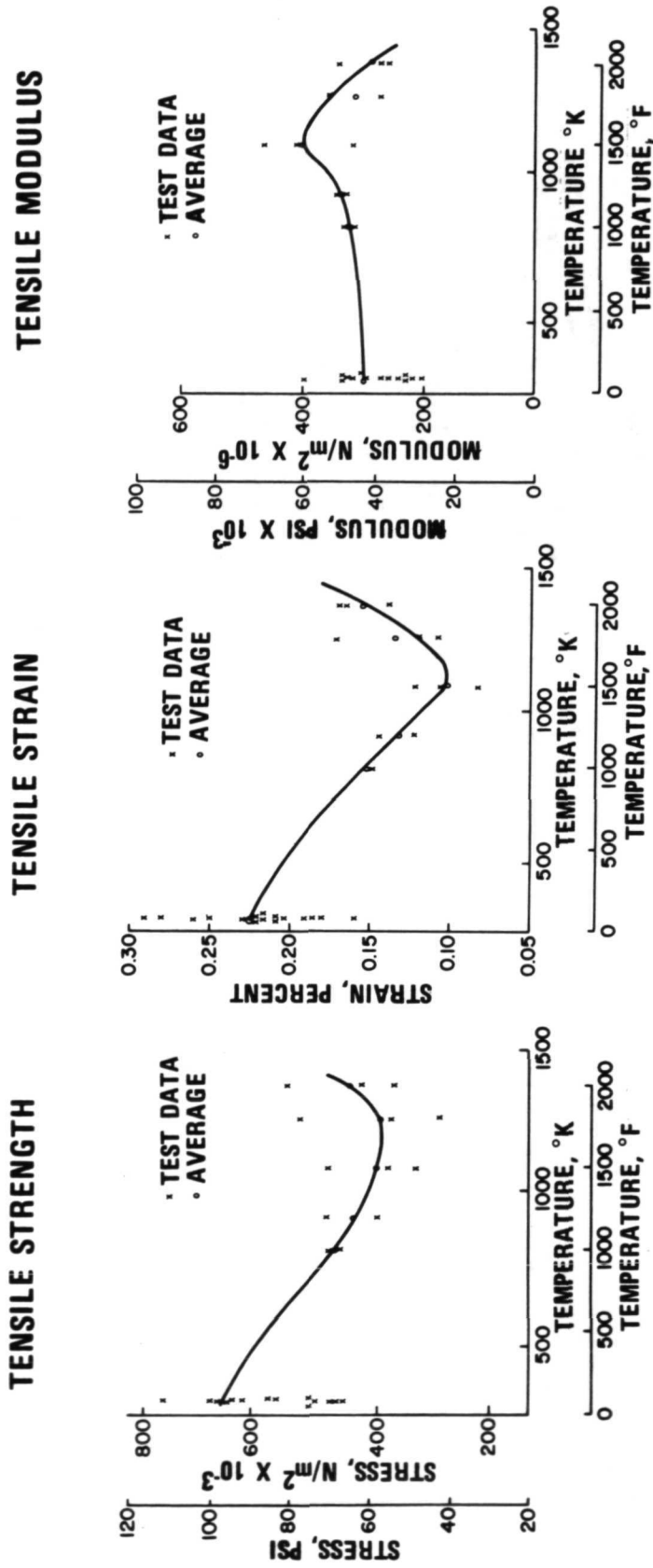
THERMOPHYSICAL PROPERTIES OF MOD IA REI-MULLITE

(Figure 18)

Typical thermophysical properties including coefficient of thermal expansion and thermal conductivity for Mod IA REI-Mullite are shown in this figure. Mod IB REI-Mullite has the same coefficient of thermal expansion as Mod IA, and is expected to have as much as a 20 percent lower thermal conductivity because of its smaller effective fiber diameter.

54

THERMOPHYSICAL PROPERTIES OF
MOD IA REI-MULLITE

Figure 18

55
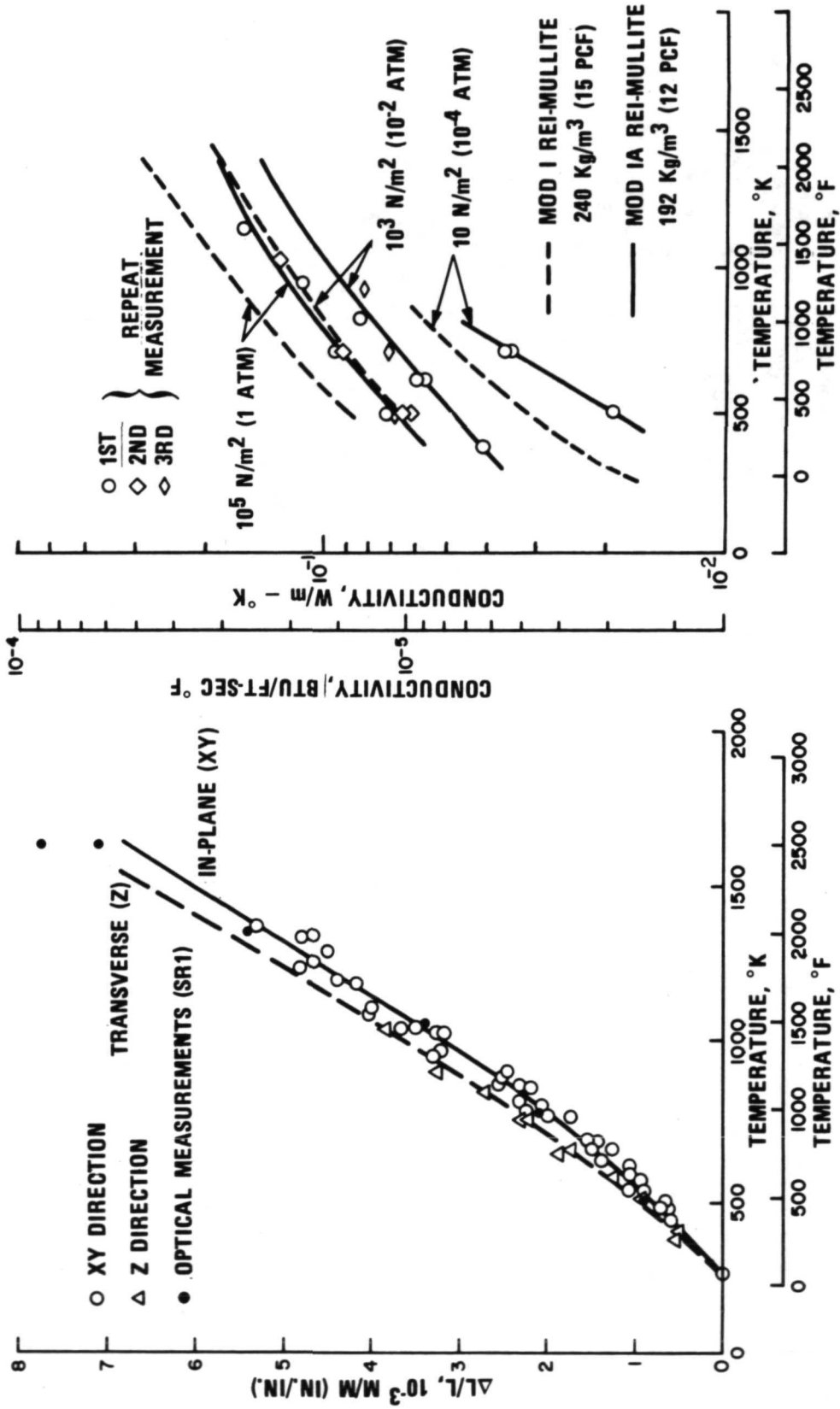
MECHANICAL PROPERTIES OF MOD IB REI-MULLITE

(Figure 19)

Figure 19 presents data obtained on experimental panels of Mod IB REI-Mullite produced in the GE–RESD pilot plant. As indicated in Figure 16, this material is now undergoing extensive characterization, but these data are adequate for indicating the magnitude of the property improvement achieved through modification of the firing cycle.

56

MECHANICAL PROPERTIES
OF MOD IB REI—MULLITE
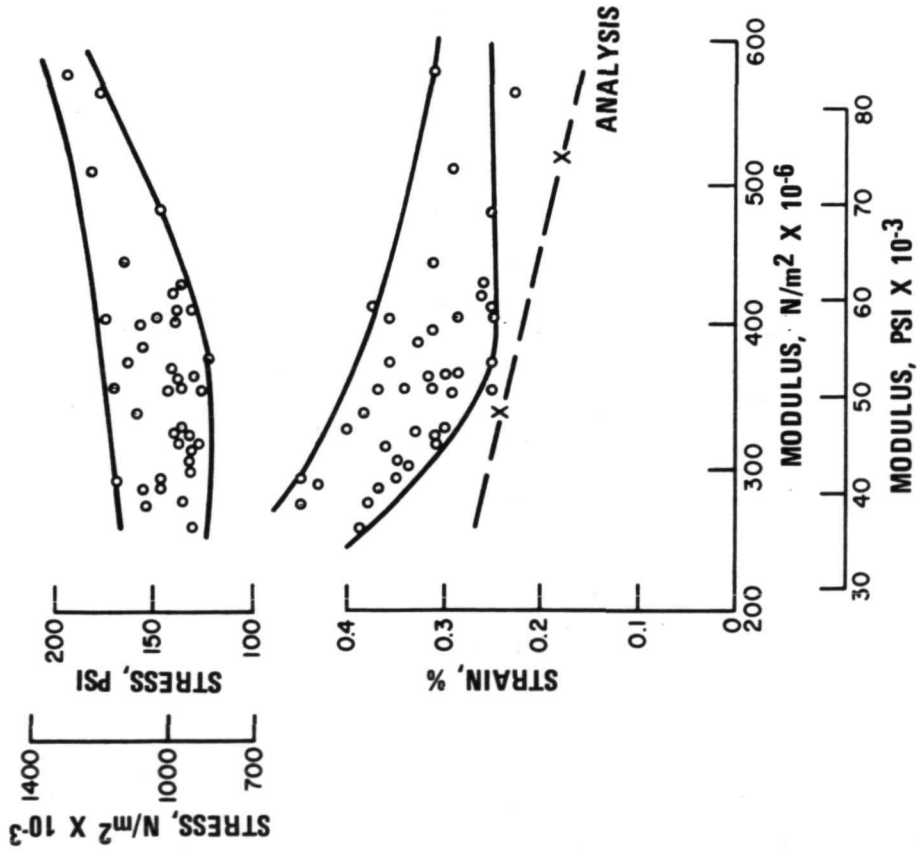
TRANSVERSE PROPERTIES

IN-PLANE PROPERTIES

Figure 19

57
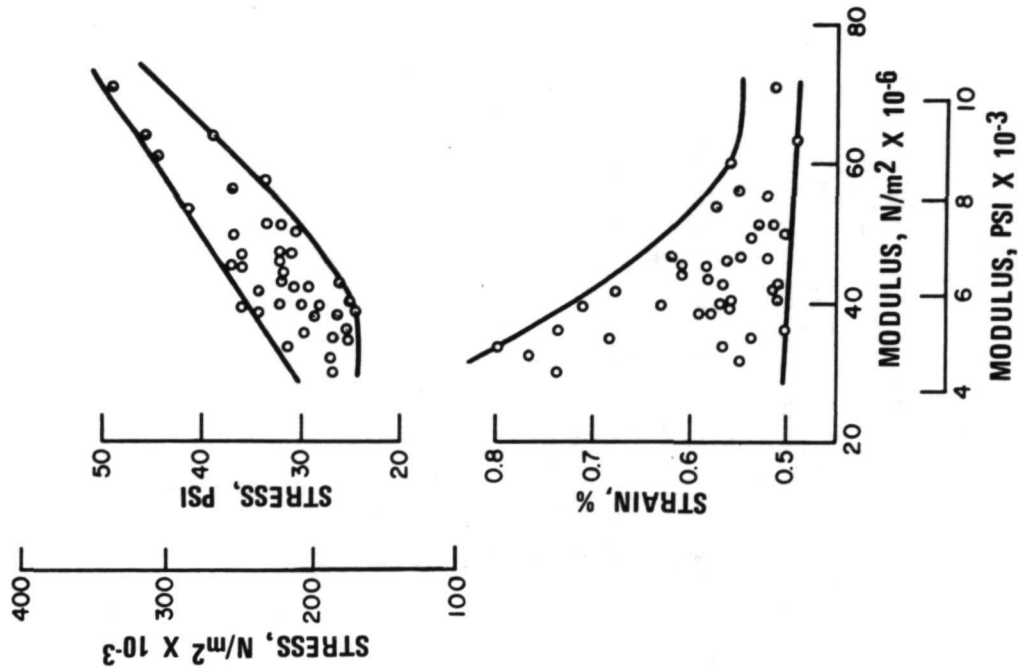
SUMMARY
(Figure 20)

The GE-RESD accomplishments in the systematic development and evaluation of REI-Mullite are summarized in this figure. Specifically:

1. Major reductions in TPS weight have been achieved by reducing the density and thermal conductivity of the insulation by 20 and 25 percent, respectively.

2. Already adequate structural margins-of-safety have been greatly enhanced by increasing the tensile strength and strain-to-failure capabilities of the insulation by factors of 3 and 2, respectively.

3. Cost effectiveness has been increased through the achievement of a high degree of uniformity and reproducibility of properties and through process simplification and binder modifications.

4. Maximization of multimission capability at surface temperatures of $1644°K$ ($2500°F$) has been achieved through firing cycle adjustments and the development of a material with high dimensional stability.

58

REI-MULLITE ACCOMPLISHMENTS SUMMARY

PROPERTIES

	MOD 0	MOD I	MOD IA	MOD IB
DESIGN TEMPERATURE, $°K$ ($°F$)	1644 (2500)	1644 (2500)	1644 (2500)	1644 (2500)
DENSITY, Kg/m^3 (LB/FT^3)	192 (12)	240 (15)	192 (12)	192 (12)
WEIGHT EFFICIENCY $(K/C_P)^{1/2} \rho$ 7/8	5.8×10^{-2}	6.86×10^{-2}	5.65×10^{-2}	5.1×10^{-2} (EST)
IN-PLANE STRENGTH/STRAIN, $N/m^2 \times 10^{-3}$ (PSI)/%	138 (20)/0.4%	269 (39)/0.17%	662 (96)/0.23%	827 (120)/0.25%
THRU-THE THICKNESS STRENGTH/STRAIN, N/m^2 (PSI)/%	34 (5) PSI/%	138 (20)/0.20%	186 (27)/0.3%	172 (25)/0.5%

PROCESSING PROCEDURES

- HIGH DEGREE OF UNIFORMITY AND REPRODUCIBILITY OF PROPERTIES.

- SIGNIFICANT COST REDUCTIONS THROUGH PROCESS SIMPLIFICATION AND BINDER MODIFICATION.

- FIRING CYCLE ADJUSTMENT TO MAXIMIZE MULTIMISSION LIFE.

MATERIAL CHARACTERISTICS

- HIGH DIMENSIONAL STABILITY TO SURFACE TEMPERATURES OF $1644°K$ ($2500°F$).

Figure 20

59

REFERENCES

1. R.M. Fetterolf, "Development of High Strength, High Modulus Fibers," AFML TR 70-197, p. 41, August 1970.

2. P.J. Gielisse and W.R. Foster, "Quarterly Progress Report 931-8", The Ohio State University Research Foundation, p. 6, October 1961.

3. "Final Report for Reusable Surface Insulation Thermal Protection Systems Development Program" GE-RESD Final Report to NASA-MSC on Contract NAS 9-12084 dated May 1972.

4. Battelle Memorial Institute, "Volume IV and V Evaluation of Non Metallic Thermal Protection Materials for the Manned Space Shuttle", July 1, 1971 and June 1, 1972.

DEVELOPMENT AND CHARACTERIZATION OF CPI SURFACE INSULATION

A. Tobin, C. Feldman, J. Reichman, M. Russak, and A. Varisco

Grumman Aerospace Corporation
Bethpage, New York

SUMMARY

This paper presents the results of IRAD and NASA sponsored programs designed to develop and characterize a new type of reusable surface material that could find application as a component of the Thermal Protection System of the Space Shuttle Orbiter.

These materials consist of 20-30% dense closed cell high emittance glass ceramic foams formulated by sintering an intimate mixture of fly ash cenospheres with 4-12 wt % cobalt oxide.

These unique ceramic foams exhibit: (1) high mechanical strengths compared to rigidized fibrous insulations; (2) no need for waterproof coating due to the non-interconnecting cell network; (3) high emissivities built into basic foam formulation; (4) ability to withstand Space Shuttle thermal environments with no loss of reuse capability; and (5) a machinable ceramic with capability of maintaining the close tolerances required of an integrated heat shield system.

Finally, the unique characteristics of the material allow design approaches which eliminate three major design constraints with RSI (1) elastomeric adhesives and all their associated problems; (2) complex brittle coatings; and (3) low strength rigidized fibrous insulations.

CPI PROCESS DEVELOPMENT

(Figure 1)

The class of closed pore insulation material being developed by Grumman uses low cost 9¢/kg (20¢/lb) fly ash cenospheres as the starting raw material. Cenospheres are a by-product of coal-burning power plants and consist of hollow alumino-silicate microspheres (50-150 micrometers diameter) with dense shell walls of 3 to 5 micrometers thickness. The spheres contain entrapped carbon dioxide and nitrogen gas at subatmospheric pressures. The as-received spheres are "decrepitated" at 755°K (900°F) to remove residual water dissolved in the glass. To extract the lowest density and highest quality (i.e., free of cloudy and carbonaceous material) spheres, a separation process was developed in which the spheres are placed on a low density fluid such as heptane and the "floating fraction" recovered. The lightweight cenospheres are mixed with a temporary organic binder and a high emittance additive (i.e., cobalt oxide) and pressed into a tile (23 cm x 23 cm x 2.5 cm) that is dried and fired to 1620-1680°K in a gas-fired or electric kiln in air. Standard ceramic fabrication procedures have been adopted at all times to reduce costs and to simplify scale-up problems.

It is estimated that CPI tiles could be produced for $1.80 to $2.70/kg ($4.00 to $6.00/lb) if full scale production procedures were adopted. Current production is 12 tiles/week.

62

CPI PROCESS DEVELOPMENT

```
┌──────────────┐        ┌──────────────────┐        ┌──────────────┐        ┌──────────────┐
│ REMOVE       │        │ SEPARATE         │        │ MIX          │        │ PRESS INTO A │
│ ABSORBED     │───────▶│ LIGHTWEIGHT      │───────▶│ CENOSPHERES  │───────▶│ SILICA       │
│ WATER        │        │ FRACTION IN      │        │ WITH ORGANIC │        │ MOLD         │
│              │        │ N-HEPTANE        │        │ & HIGH       │        │              │
│              │        │                  │        │ EMITTANCE    │        │              │
│              │        │                  │        │ BINDER       │        │              │
└──────────────┘        └──────────────────┘        └──────────────┘        └──────────────┘

                                                     ┌──────────────┐
                                                     │ FINISH FIRE  │
                                                     │ AT 1700°K    │
                                                     └──────────────┘
```
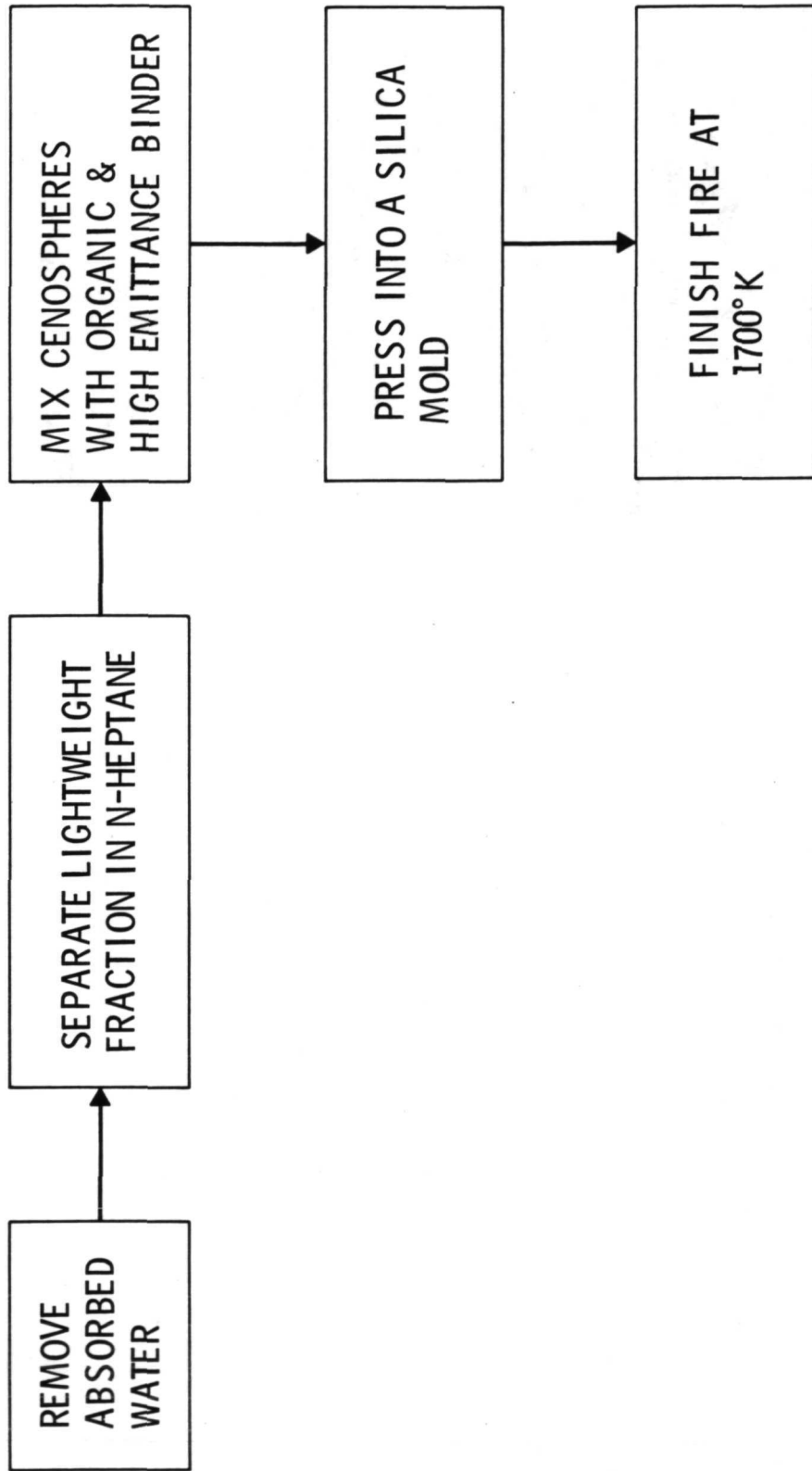
Figure 1

PHYSICAL PROPERTIES OF CPI

(Figure 2)

CPI materials are a class of rigid glass-ceramic cellular foams with a non-interconnecting network of cells rendering them impermeable to water. They are 20 to 30 percent dense, and are homogeneous and isotropic in physical properties. The cell size of the foam can be varied by changing the composition (cobalt oxide) or heat treatment in forming the foam. CPI materials are nonfriable and can be easily machined into any size and shape with conventional carbide tooling; however, the abrasive nature of the material reduces tool lifetime and tolerances and diamond tooling is the preferred drilling and cutting medium. CPI plates have good handleability; however, the brittle nature of the material requires some care, as with any glass body. The materials can be scaled up into larger and more complex components with minimum tooling problems.

64

PHYSICAL PROPERTIES OF CPI

PROPERTY	4% CoO	8% CoO	12% CoO
MICROSTRUCTURE	NETWORK OF CLOSED CELLS		
COLOR	BROWN-BLUE	DARK BLUE	NAVY BLUE
DENSITY (kg/m^3)	630-770	530-670	530-670
WT% WATER ABSORPTION	0.5-4	0.5-4	0.5-4
AVERAGE PORE SIZE	80 μm	170 μm	300 μm
AVAILABLE SIZES	23 cm x 23 cm x 3 cm	23 cm x 23 cm x 3 cm	23cm x 23cm x 3 cm
AVAILABLE SHAPES	FLAT TILE	FLAT TILE	FLAT TILE
MACHINABILITY	MACHINABLE CERAMIC WITHIN 0.005 cm TOLERANCE		

Figure 2

THERMAL AND CHEMICAL PROPERTIES OF CPI

(Figure 3)

CPI materials contain about 55-60 wt % SiO_2, 25-30 wt % Al_2O_3, 2-5 wt % Fe_2O_3, 4-12 wt % CoO, and small amounts of TiO_2, Na_2O, and K_2O. The materials composing the cell walls of CPI are mullite, cobalt aluminate, and a cobalt alumino-silicate glass. Although the equilibrium diagram predicts that mullite and cristobalite are the only phases that are stable, no cristobalite formation has ever been observed during any heat treatment, a fact that accounts for the thermal stability of CPI with regard to crystalline inversions. The high emittance of the foam is due to the cobalt in the cell walls, which is effective as a radiation absorber. The cobalt is also effective in reducing the thermal conductivity by increasing the absorption coefficient for radiative heat transfer. Although solid conduction comprises a significant component of the total heat transfer, the fine network of cells is effective in scattering and absorbing radiation and reduces the heat transfer at the elevated temperatures. As-fired tiles of CPI-4% CoO have been observed to show further crystallization of cobalt aluminate upon heat treatment in the 1200-1500°K range. This phenomenon is related to the increasing solubility of CoO in the glass phase at the "formation" temperature of the foam and the nucleation and growth of the "glass-ceramic" at the lower temperatures. The lowering of the softening point with increasing cobalt content is due to the well-known "fluxing" action of cobalt in the glassy matrix.

THERMAL AND CHEMICAL PROPERTIES OF CPI

PROPERTY	4% CoO	8% CoO	12% CoO
THERMAL EXPANSION (RT-1370K)	$5.2 \times 10^{-6}/°K$	$5.4 \times 10^{-6}/°K$	$5.8 \times 10^{-6}/°K$
HEAT CAPACITY RT-725K (JOULE/kg-K)	8-9	7.1-8.4	6.3-7.6
CRYSTALLOGRAPHY	MULLITE COBALT ALUMINATE GLASS		
DILATOMETRIC SOFTENING POINT	1300° K	1250° K	1180° K
TOTAL NORMAL EMISSIVITY RT-1500K	0.63-0.65	0.75-0.78	0.80-0.85
TOTAL NORMAL EMISSIVITY OF COATED SAMPLE	0.82-0.88		
THERMAL STABILITY (DTA)	FURTHER CRYSTALLIZATION OF COBALT ALUMINATE AT 1300°-1500°K	NO CHANGES	NO CHANGES
CHEMISTRY	Al_2O_3, SiO_2 Fe_2O_3, CoO, TiO_2Na_2O		
CHEMICAL RESISTANCE	NOT ATTACKED BY MOST ACIDS, ALKALIS OR ORGANIC MATERIALS		

Figure 3

67

SUMMARY OF THERMAL CYCLING RESULTS

(Figure 4)

A major problem with ceramic foam materials has been the thermal shock resistance and reuse capability during multiple exposure to reentry heating. We have undertaken an extensive program to study the thermal shock characteristics of CPI, using both radiant heat lamps and plasma arc jets. Initial failures were traced to poor processing procedures and lack of uniformity in heat treatment. Significant improvements in both areas has led to a newer generation of CPI materials with significantly improved thermal shock characteristics. CPI specimens have withstood up to 40 reentry cycles of Areas 2 and 2P with little or no change in appearance or properties. It is believed that CPI-12, CPI-8, and CPI-4 are capable of surviving with little change in Areas 1, 2, and 2P, respectively, of the Space Shuttle reentry heating in plate sizes of 23 cm x 23 cm x 1.25 cm. Convective heating environments have been simulated by using a "programmed" arc jet (7.6 cm x 0.96 cm diameter) in which the specimen is moved toward the jet (air exhaust) to simulate reentry heating. Specimens have survived 25 cycles with little change in appearance or evidence of failure.

Design integration schemes have focused on two approaches: (1) mechanical fasteners; and (2) bonded fibers. These approaches have required that a good bond be established between two separate pieces of CPI with a metallic fastener retained and direct bonding of CPI to rigidized fibrous insulation, i.e., mullite or Kaowool.

Successful CPI/CPI bonds have been achieved with inorganic cements such as ground-up CPI powders mixed with colloidal silica and Kaowool cement. These bonds have survived reentry cycling with no degradation of properties. CPI/mullite fiber bonds have been successfully achieved through a hot pressing technique in which the mating surfaces of CPI and mullite are heated to 1600°K for one hour at 1500 N/m² (0.2 psi) pressure. Successful CPI/Kaowool regidized fiber bonds have been achieved using commercially available Kaowool cement and bonding at 1300°K for one hour. These bonds have survived multiple reentry cycles with no evidence of failure.

68

SUMMARY OF THERMAL CYCLING RESULTS

SPECIMEN NO.	%CoO	SPECIMEN DIMENSIONS	HEATING CYCLE	NO. OF CYCLES	SPECIMEN CONDITION
1	8	17 cm x 17 cm x 0.32 cm	AREA 2	25	NO FAILURE SLIGHT BOW
2	8	17 cm x 17 cm x 0.37 cm	AREA 2	25	NO FAILURE SLIGHT BOW
3	8	17 cm x 17 cm x 0.8 cm	AREA 2	25	NO FAILURE SLIGHT BOW
4	8	17 cm x 17 cm x 0.32 cm	AREA 2P	40	NO FAILURE BOWED UP
5	8	19 cm x 19 cm x 0.95 cm	AREA 2	25	NO CHANGE
6	4	17 cm x 17 cm x 0.95 cm	AREA 2P	25	NO CHANGE
7	4	17 cm x 17 cm x 0.80 cm	AREA 2P	25	NO FAILURE SLIGHT BOW
8	4	BONDED CPI/KAOWOOL CEMENT/ KAOWOOL FIBERS	AREA 1	25	NO CHANGE
9	8	BONDED CPI/MULLITE	AREA 2	20	NO CHANGE
10	4	7.62 cm DIAMETER x 1.25 cm	AREA 1 (ARC JET)	25	UNCHANGED
11	4	7.62 cm DIAMETER x 0.85 cm	AREA 2P (ARC JET)	25	UNCHANGED

Figure 4

69

THERMAL CONDUCTIVITY (W/m-°K) OF CANDIDATE

TPS INSULATION MATERIALS VERSUS T (°K)*

(Figure 5)

A comparison of thermal conductivities for the various TPS candidates reveals the following conclusions with regard to design applications of CPI materials: (1) CPI must be used in conjunction with other low-density thermally efficient insulators, i.e., Kaowool or mullite or some flexible fibrous blanket, in order to be "thermally competitive"; (2) the higher density of CPI requires that it must be used as a thin plate, i.e., either as a coating on rigidized fibrous insulations or as an independently supported surface tile in order to be weight competitive with other candidate TPS. In both cases, weight competitive TPS designs are feasible; and (3) CPI must be considered an integral component of the composite TPS design that offers unique design advantages not available with other materials.

---

* Data obtained from Battelle Contract NAS 9-10853.

THERMAL CONDUCTIVITY (W/m-°K) OF CANDIDATE
TPS INSULATION MATERIALS vs T_λ(°K)*
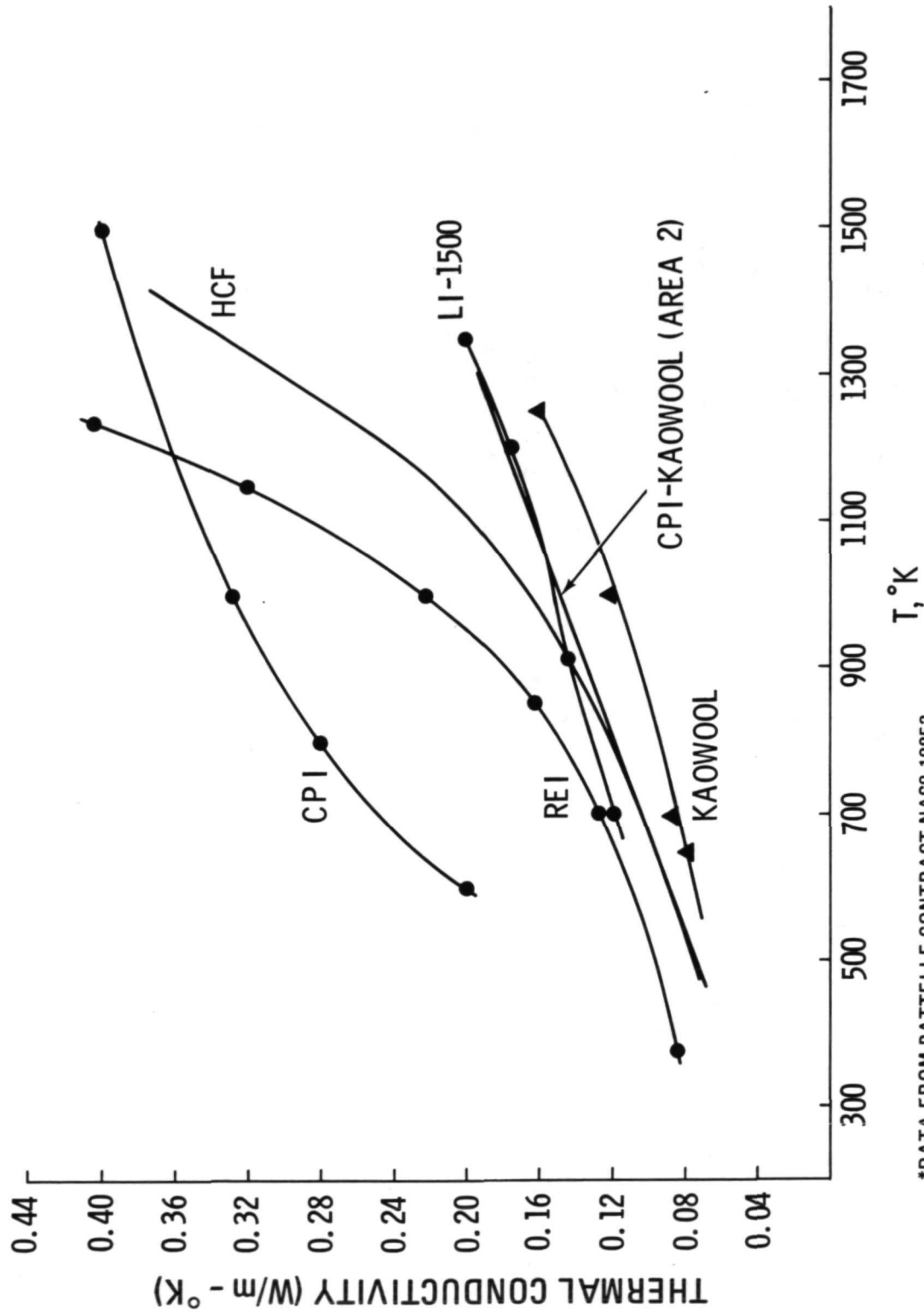
Figure 5

*DATA FROM BATTELLE CONTRACT NAS9-10853

71

COMPARISON OF ROOM TEMPERATURE MECHANICAL PROPERTIES OF CPI MATERIALS

(Figure 6)

An important feature of any design-integration activity is the knowledge of "design-allowables" of any material in which the mechanical properties of the heat shield material are known to vary within a certain range. These become critical to a design that permits mechanical attachments to the primary structure and that must survive a variety of loading conditions. Since CPI materials are homogeneous and isotropic in nature, and since processing improvements have been made to assure a uniform material, scatter of breaking strengths of CPI has been reduced to about 15 to 20 percent. This is a narrow range for a ceramic.

In all cases, the clear superiority of mechanical properties of CPI-4 over CPI-8 and CPI-12 has been observed. It is believed that the finer pore structure associated with the lower cobalt level reduces the critical flaw size required to initiate fracture. Also, stress concentration factors may be smaller in CPI due to the more "spherical" nature of the pores. These factors could account for the observed higher strengths of CPI-4.

72

COMPARISON OF ROOM TEMPERATURE
MECHANICAL PROPERTIES OF CPI MATERIALS

Figure 6

73

TENSILE STRENGTH OF CPI MATERIALS

(Figure 7)

Tensile properties of CPI materials have been measured at room and elevated temperatures, using a diametral compression test. In this test, a cylinderical specimen (3.2 cm diameter x 1.25 cm thick) is compression loaded along its diameter and a tensile force develops normal to the load axis causing a tensile fracture along the diameter, the fracture strength being computed from $\sigma = 2P/\pi Dt$, where P = applied load, D = diameter, and t = thickness. Tensile fractures are observed provided: (1) the specimen is uniform and isotropic; and (2) has a higher shear strength than tensile strength. These conditions are met with CPI. The same testing procedures used in the free standing compression test were used here (see figure 8). In all cases CPI-4 showed a significantly higher strength than CPI-8 or CPI-12 over the range investigated.

Results showed a general fall-off in strength above 1000°K with a more rapid fall-off as the softening point of the glassy matrix is approached. Again, no brittle failures were observed above the softening points, and a large decrease in modulus and increase in failure strain occurred. Finally, no tensile property degradation was found in CPI tiles that underwent 25 reentry cycles of Area 1 (CPI-12) or Area 2 (CPI-4 and CPI-8) of the Shuttle reentry profile.

74

TENSILE STRENGTH OF CPI MATERIALS
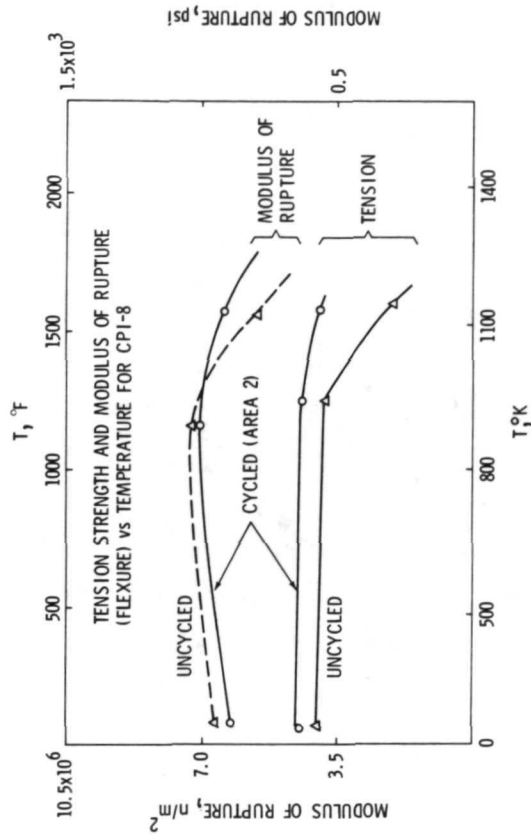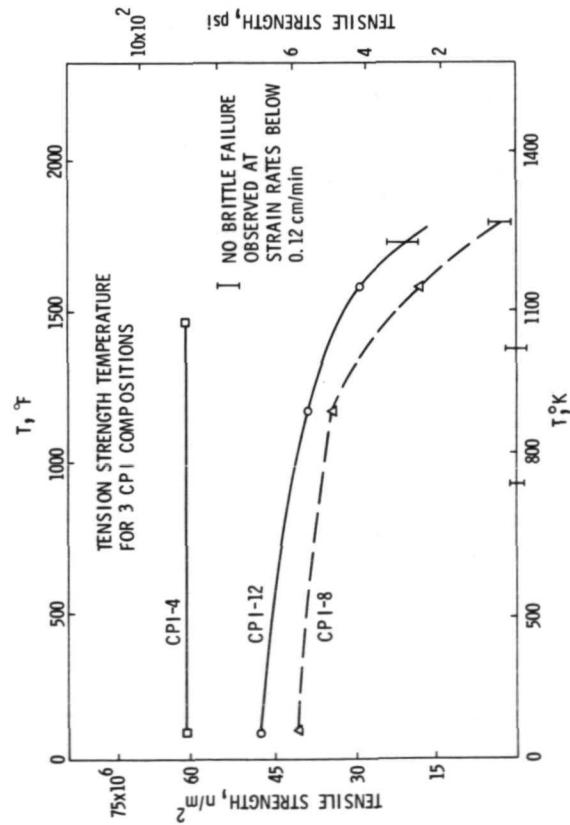
Figure 7

COMPRESSIVE STRENGTH OF CPI MATERIALS

(Figure 8)

Compressive properties of CPI materials have been measured at room and elevated temperatures in free-standing compression. Specimens consisted of rectangular parallelepipeds of dimension 0.96 cm x 0.96 cm x 2.54 cm. A universal test machine was used and strain rates were 0.3 cm/min. At the elevated temperatures, an alumina specimen support and alumina load rod were used. A platinum-wound tube furnace (at a pre-selected temperature) enclosed the specimen and fixtures and was raised or lowered onto the specimen using the loading train of the test machine. This technique permitted rapid specimen changes and minimized heat up and cool down operations with the furnace. As with other elevated temperature measurements, the failure of the material becomes strain rate sensitive at the temperatures indicated and no brittle failures were observed above these temperatures unless very large strain rates were applied (i.e., 5.5 cm/min). These temperatures correspond approximately to the measured softening points of the CPI glassy matrix. Room temperature failure strains varied from 0.002-0.003. In all cases, CPI-4 showed a significantly higher compressive strength than CPI-8 or CPI-12 over the temperature range studied.

Finally no compressive property degradation was found in CPI tiles that underwent 25 reentry cycles in Area 1 (CPI-12) and Area 2 (CPI-4 and CPI-8) of the Shuttle reentry profile.

76

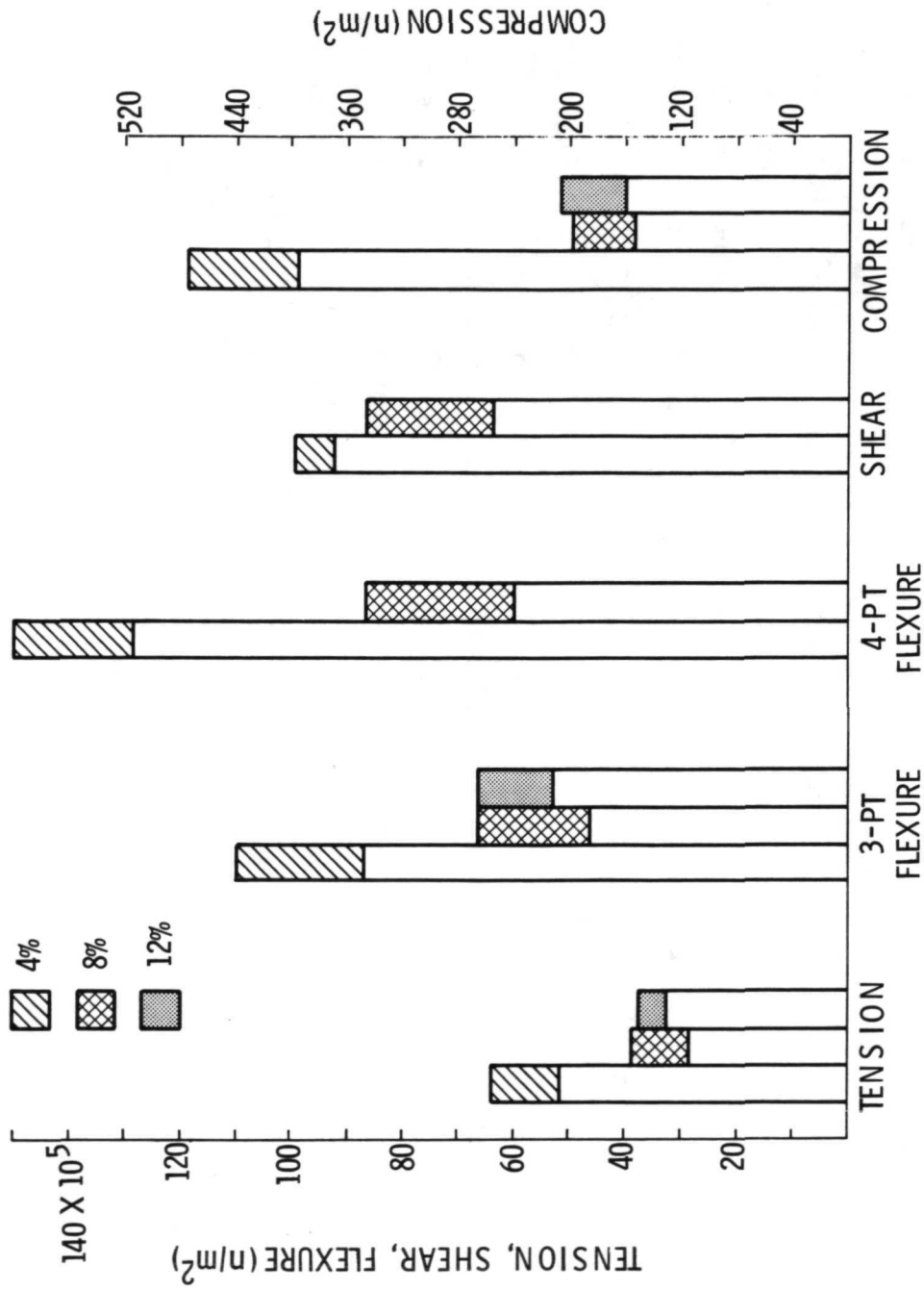# COMPRESSIVE STRENGTH OF CPI MATERIALS
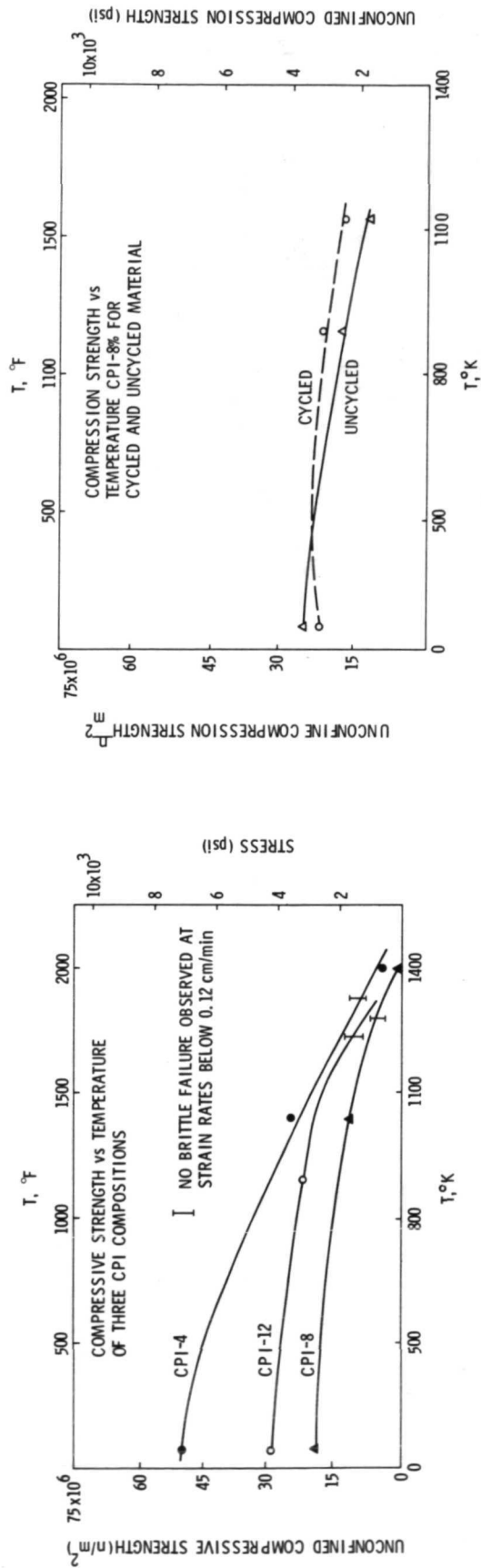
Figure 8

MODULUS OF RUPTURE (FLEXURE) VERSUS TEMPERATURE FOR CPI MATERIALS

(Figure 9)

Flexural properties of CPI materials have been measured at room and elevated temperatures using a three-point flexure test. In the test, a flexural bar 7.6 cm a 1.25 cm x 0.63 cm is loaded at its midpoint with an alumina rod having a V-shape at the load application point. The specimen was suspended on an alumina fixture consisting of a plate with an alumina "Dee" cemented at each end. A platinum-wound furnace (10-cm diameter) was raised or lowered over the specimen as described in figure 8. As with the tension and compression data, the failures became strain rate sensitive at the temperatures indicated and no brittle failures were observed from room temperature to 1100°K and then a fall-off in strength occurred as the softening point of the glassy matrix was approached. In all cases, CPI-4 showed significantly superior flexural strength than CPI-8 or CPI-12 over the temperature range.

Finally, no significant flexural property degradation was found in CPI tiles that underwent 25 reentry cycles of Area 1 (CPI-12) or Area 2 (CPI-4 and CPI-8) of the Shuttle reentry profile.

MODULUS OF RUPTURE (FLEXURE) vs TEMPERATURE FOR CPI MATERIALS
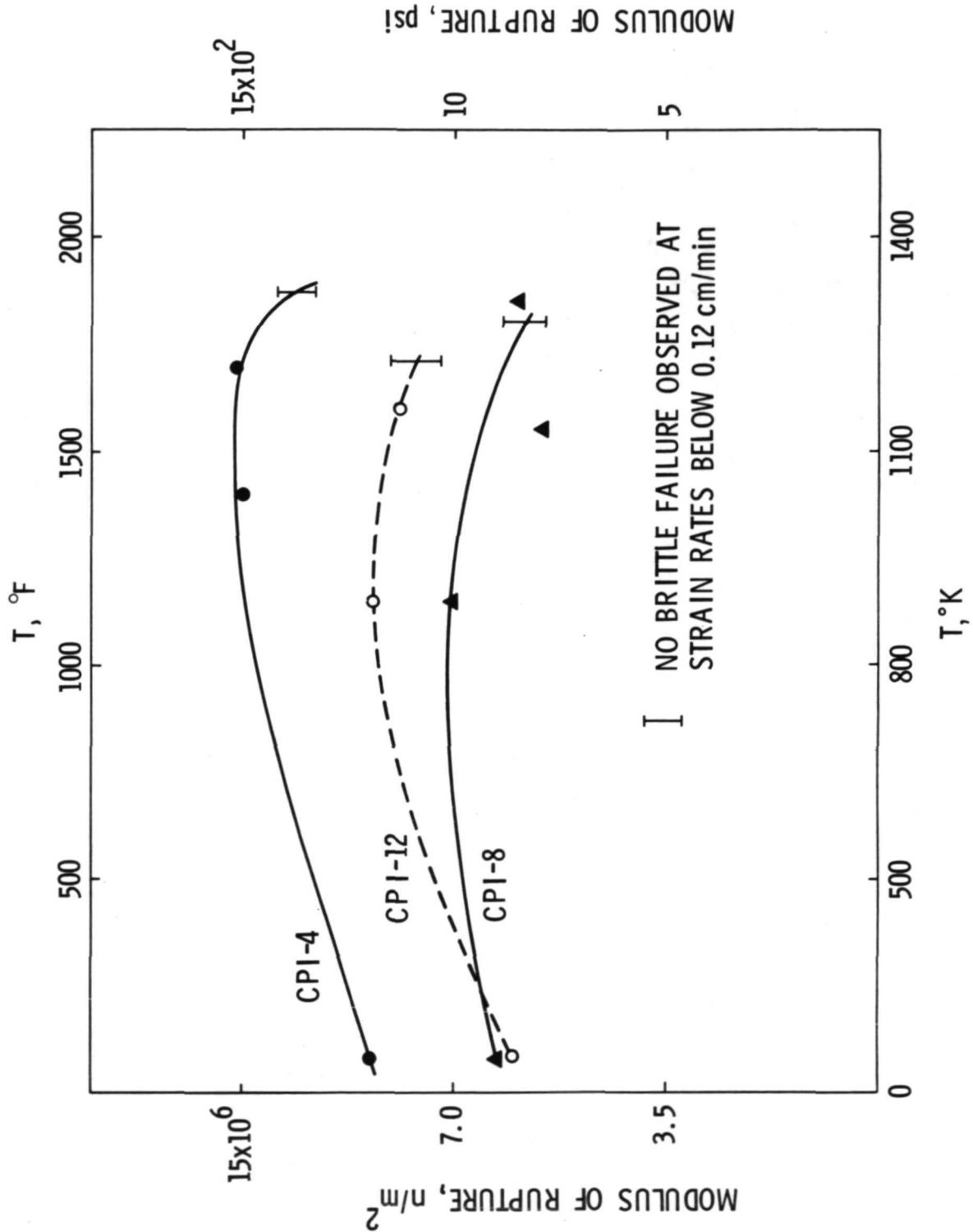
Figure 9

79

ELASTIC MODULUS VERSUS TEMPERATURE FOR CPI MATERIALS

(Figure 10)

Elastic modulus data were computed from the slope of the stress-strain curve. Significant fall-off in moduli for the three materials studied was found above 950°K. CPI-4 showed a higher modulus below 950°K, but the differences in the moduli of the three materials became small as the softening points were approached. Also, corresponding increases in failure strain were observed above 950°K until no failure could be induced. These data suggest that complex shapes of CPI can be fabricated by a "hot-forming" process above their respective softening points. Finally, no significant changes in modulus or failure strains were observed after 25 reentry cycles in Area 1 (CPI-12) and Area 2 (CPI-4 and CPI-8) of the Shuttle reentry profile.

ELASTIC MODULUS vs TEMPERATURE FOR CPI MATERIALS

Figure 10

81
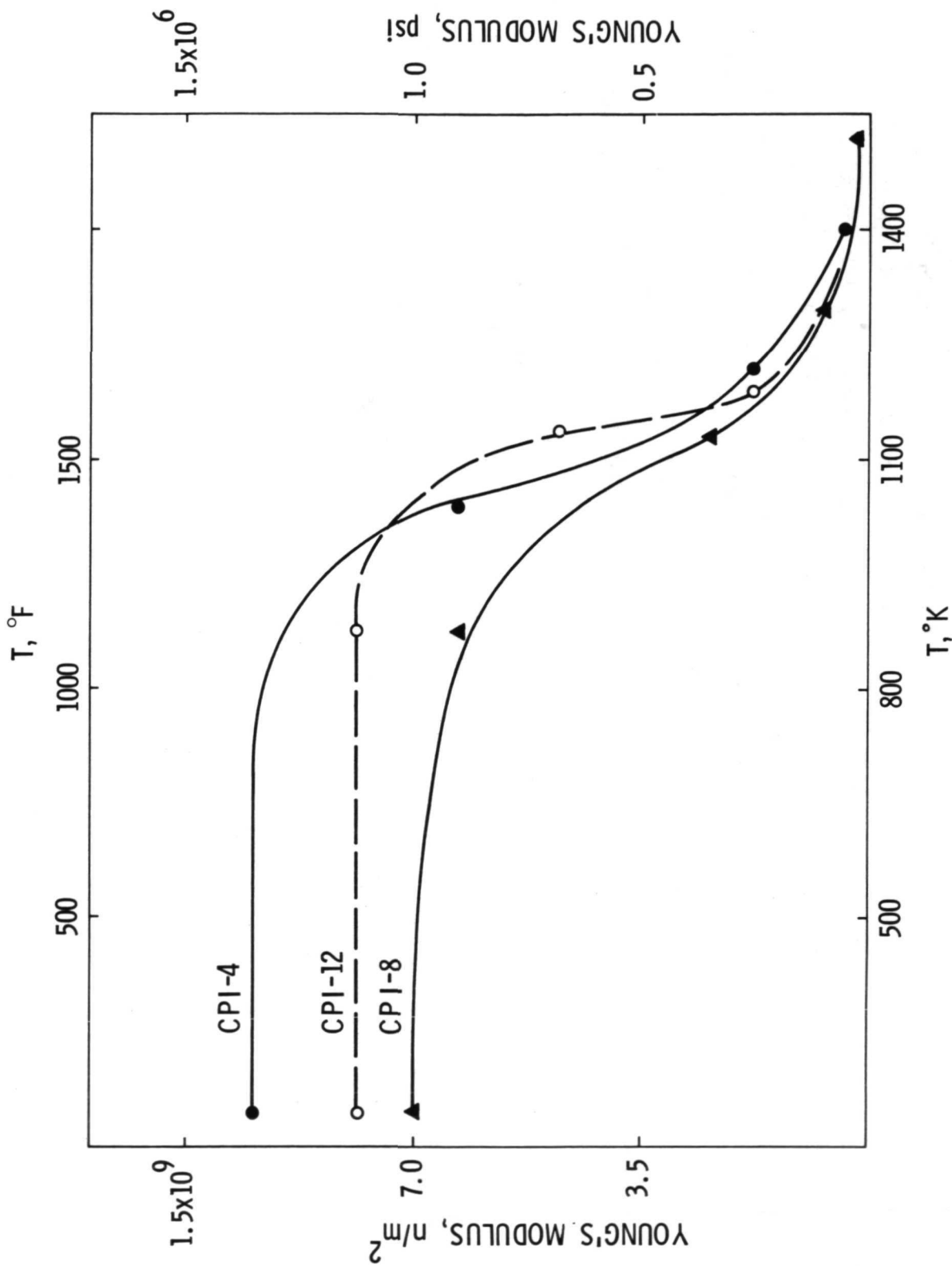
FLEXURAL CREEP PROPERTIES OF CPI MATERIALS

(Figure 11)

To assess the upper use temperature of CPI materials for use as an unsupported tile in the mechanically fastened concept, flexural creep studies were undertaken. Two different specimen dimensions were chosen: (1) 15.2 cm x 1.26 cm x 0.63 cm and; (2) 15.2 cm x 1.26 cm x 0.85 cm. Specimens were supported on a mullite shelf, and alumina weights corresponding to 700 N/m^2 "hot loading" were placed on the specimens. Specimen deflections were recorded in situ photographically as a function of time and temperature. In general, it was noted that increasing cobalt levels reduced the creep resistance as would be expected from the softening point data. It was observed that a 110°K increase in creep properties occurred for a 4 percent decrease in cobalt level and that no significant creep occurred in the 0.85-cm-thick CPI-4 samples below 1440°K. This behavior is typical of a glassy matrix containing increasing amounts of fluxing constituents.

The uniform loading of 700 N/m over the flexural bar of 0.63 cm depth corresponded to a 3 x 10^5 N/m^2 (43 psi) stress at the midpoint of the bar and the maximum deflection at the midpoint of the bar was measured. By increasing the "depth" of the bar to 0.85 cm (thus reducing the maximum stress to 1.4 x 10^5 N/m^2), it was observed that this lower stress level effectively raised the creep-deflection curve by an additional 110°K.

82

FLEXURAL CREEP PROPERTIES OF CPI MATERIALS

Figure 11

83
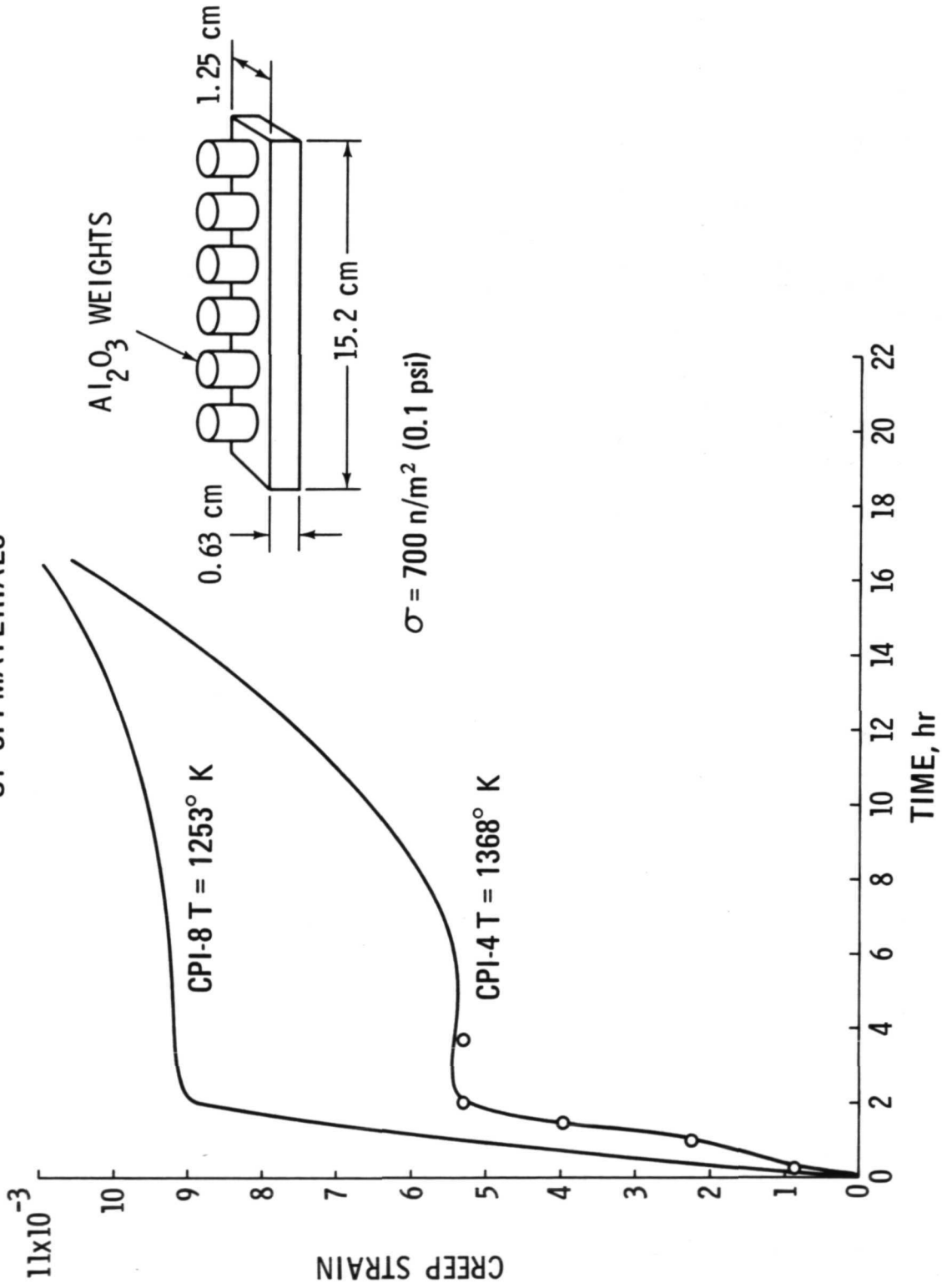
NDE INSPECTION OF CPI MATERIALS

(Figure 12)

NDE of candidate materials for heat shield applications becomes a major requirement where reliability and reusability are essential. We have found that X-ray radiography is a useful technique for inspection of CPI materials. This technique has successfully detected the presence of voids, visible and non-visible cracks on the surface, internal cracks, density variations, and cobalt-rich inclusions due to improper mixing procedures. Although no standards have yet been established as to what constitutes a "critical flaw," we have used the technique to reject any material that shows gross inhomogeneities due to poor mixing, and any voids or visible cracks. The figure shows typical (a) "good quality material," and (b) "flawed material" containing a crack and agglomerations. Off-center flexure failures and anomalously low strength values have been related to poor quality materials.

84

(a)

(b)

Figure 12

85
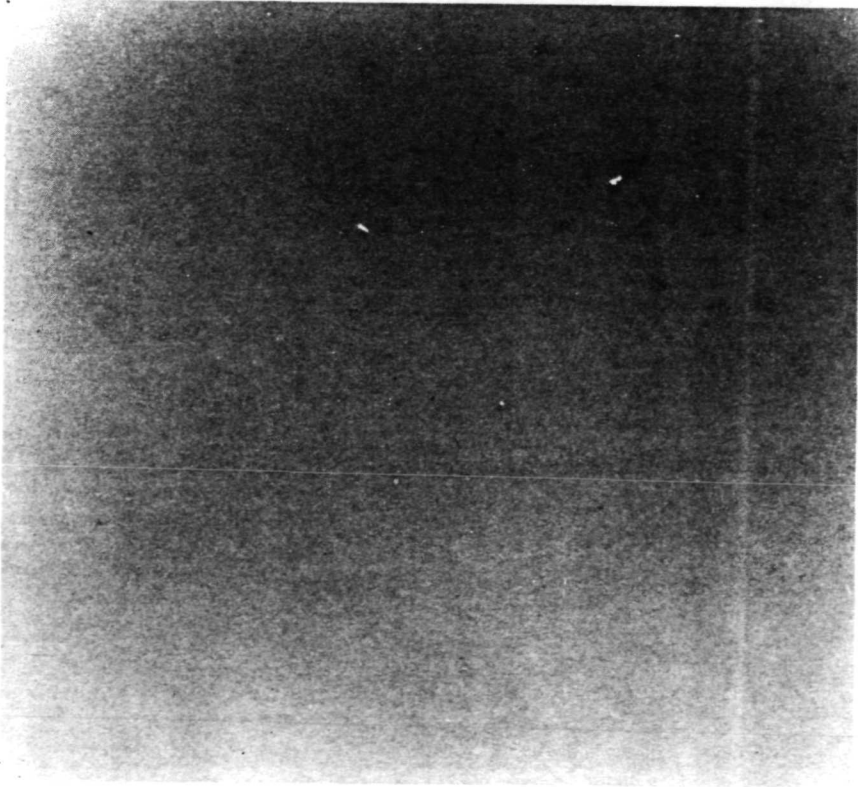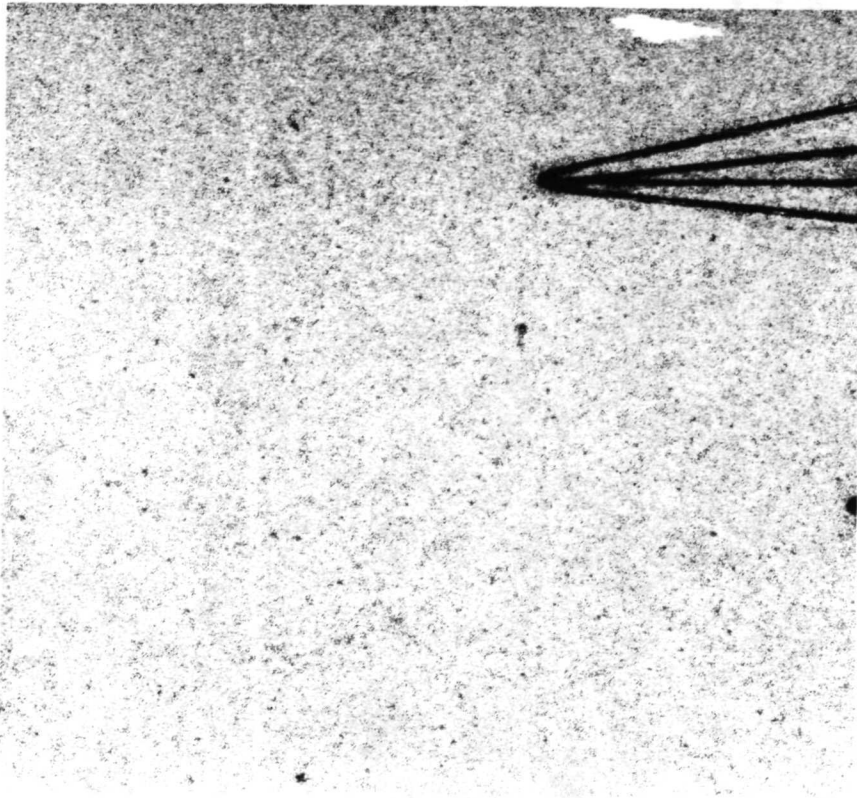
FUSED SILICA SURFACE COATING FOR A FLEXIBLE SILICA MAT INSULATION SYSTEM

W.H. Rhodes

AVCO Systems Division
Lowell, Massachusetts

INTRODUCTION

Impervious fused silica insulation coatings have been developed for application to a flexible mat insulation system designated 3DSX. The coating composition was selected from among the silica glass systems based on the criteria of maximum thermal-chemical stability, together with minimum thermal expansion coefficient. Based on an examination of the crystalline phase nucleation and growth kinetics, a 99+% SiO_2 glass was selected as the base composition. A coating was developed that incorporated the high emissivity phase $NiCr_2O_4$ as a two-phase coating with goals of high emittance and minimum change in thermal expansion. A second major coating classification has a plasma-sprayed emittance coating over a sealed pure amorphous SiO_2 layer. The processing of both coatings is quite different from usual concepts in insulation coating because of the 1720° C (3128° F) fusion temperature for pure SiO_2.

A third area of development centered on extremely thin amorphous SiO_2 coatings deposited by chemical vapor deposition. The coating characterization studies presented are mechanical testing of thin specimens extracted from the coatings, cyclic arc exposures, and emittance measurements before and after arc exposures.

SCHEMATIC OF 3DSX WOVEN MAT

(Figure 1)

The basic configuration of the 3DSX woven mat insulation is schematically illustrated. Silica felt mats are compressed to the desired density and held under compression by silica yarn laced perpendicular to the felt layers. An outer layer of silica fabric is used to sandwich the felt and provide a strong surface that prevents the vertical reinforcement yarn from tearing through the felt. Usually one outer layer of felt was provided to improve the bonding of the sealer coat to the mat system. The mat system could be produced in a variety of densities, but nominal 96.1 kg/m^3 (6 lb/ft^3) and 160 kg/m^3 (10 lb/ft^3) systems have been fabricated and tested.

SCHEMATIC OF 3DSX WOVEN MAT

SURFACE FABRIC WOVEN FROM CERAMIC YARNS

DENSE CERAMIC COATINGS PROVIDE MOISTURE BARRIER AND HIGH EMITTANCE

SURFACE FELT

MULTIPLE LAYERS OF COMPACTED CERAMIC FELTS 48.1-160 kg/m³ (3-10 lb/ft³) DENSITY RANGE

VERTICAL REINFORCEMENT CERAMIC YARN

INSULATOR THICKNESS

VERTICAL REINFORCEMENTS ON 2.54-12.7 mm (100-500 MIL) CENTERS

Figure 1

89
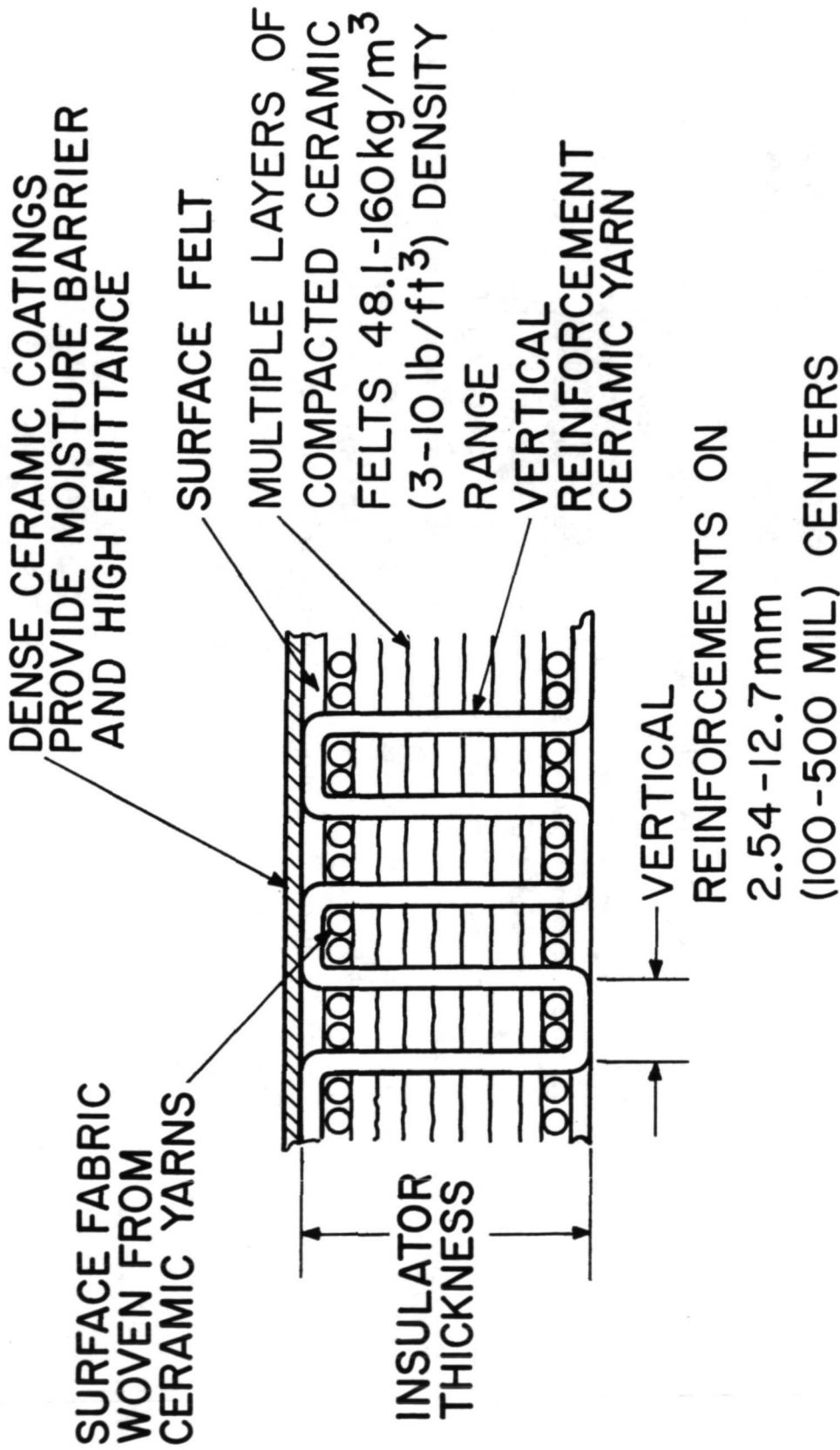
FEATURES OF 3DSX

(Figure 2)

The matrix shear modulus of approximately 6.55×10^5 N/m^2 (95 psi) gives the system the desirable feature of strain isolation. Strains transmitted into the matrix by the substructure are reduced by at least a factor of ten in terms of strain transmitted to the coating. Strain isolation operates favorably in the reverse situation also, in that coating thermal expansion or contraction strains are effectively restricted to the coating. The probability of failures in the coating is thereby reduced as only thermal gradients in the coating thickness or thermal strains resulting from end restraints can cause this type of failure.

The ability to readily fabricate the matrix in different densities having different thermal conductivity values gives the designer another variable to work with in designing the required insulation thickness for the various thermal environments over the vehicle.

The insulation system is based on an amorphous silica fiber insulation and a dense amorphous silica coating. A conservative estimate of the maximum use temperature is 1260° C (2300° F) without significant microstructural problems from devitrification. Since the coating and matrix are of the same phase, thermal expansion mismatch is never a problem. Some loss of adherence has been experienced between the NiCr$_2$O$_4$ emittance coat and the sealed SiO$_2$ coating. Increased thermal capability could be added by substituting mullite or zirconia surface felts with appropriate tie-down yarns and coatings.

Cracks in coatings have never been found to propagate deeply into the matrix due to crack blunting by the matrix. Because of the fact that cracks are restricted to the surface coating, it is possible to grind away the crack and repair the coating with the same constituent as the original coating.

90

FEATURES OF 3DSX

LOW SHEAR MODULUS OF WOVEN CERAMIC INSULATION PROVIDES EFFECTIVE STRAIN ISOLATION BETWEEN SURFACE COATING AND SUBSTRUCTURE.

LOW SHEAR MODULUS ALSO ISOLATES INSULATION FROM COATING THERMAL STRAINS.

INSULATIVE MATRIX CAN READILY BE FABRICATED IN VARIABLE DENSITIES AND AS LOW AS 96.1 Kg/m^3 (6 lb/ft^3)

DEMONSTRATED PURE AMORPHOUS SILICA SYSTEM WITH 1260°C (2300°F) CAPABILITY.

MATCHING THERMAL EXPANSION OF COATING AND SUBSTRUCTURE.

SYSTEM CAN INCORPORATE MORE REFRACTORY MATERIAL THAN SILICA.

SURFACE CRACKS CANNOT PROPAGATE THROUGH THE INSULATIVE MATRIX. CRACKING DOES NOT CAUSE CATASTROPHIC STRUCTURAL FAILURE.

MINOR SURFACE DAMAGE CAN BE READILY REPAIRED.

Figure 2

91

CRYSTAL GROWTH RATE AS A FUNCTION OF TEMPERATURE

(Figure 3)

Coating composition selection was based on achieving an impervious coating with the highest thermochemical stability. It was further decided that glass or glaze processing techniques based on SiO_2 containing glasses would be most applicable. It is well known that the thermochemical stability of the amorphous phase increases going from soda lime glass (72 SiO_2, 12 CaO, 16 Na_2O) to borosilicate glass (80.5 SiO_2 . 12.4 B_2O_3 . 4.6 Na_2O . 2.7 Al_2O_3) to fused silica (99.9 SiO_2).[1] These glasses are most useful while in the amorphous structural state; however, the amorphous phase is metastable at all peak temperatures contemplated for Space Shuttle application. Given the proper heterogeneous nucleation event and thermal cycle, all of the above glasses will crystallize into devitrite or cristobalite. A small percentage of crystalline phase probably would not compromise the coating performance, but high levels would crack the coating.

The nucleation event in crystallization starts the process and is sensitive to surface contamination,[2] as well as impurities in the glass.[3] These impurities can include OH ions as well as metal ions. Once the crystalline phase nucleates, the growth rate is, of course, important in governing the remaining useful life of the coating prior to cracking. The growth rate curves shown indicate that pure SiO_2 is very stable below 1400° C (2552° F), but that as little as 0.69% Na_2O will break up the network structure such that very large growth rates for SiO_2 will be observed to as low as 900° C (1652° F).[4] The borosilicate glass has a 1060° C (1940° F) liquidus and will devitrify between this temperature and 700° C (1292° F).[5] The scant data available indicate the kinetics are quite slow. The soda lime glass has the lowest liquidus of the three major glass compositions at 970° C (1778° F) and forms devitrite at an intermediate rate down to about 750° C (1382° F).

CRYSTAL GROWTH RATE AS A FUNCTION OF TEMPERATURE
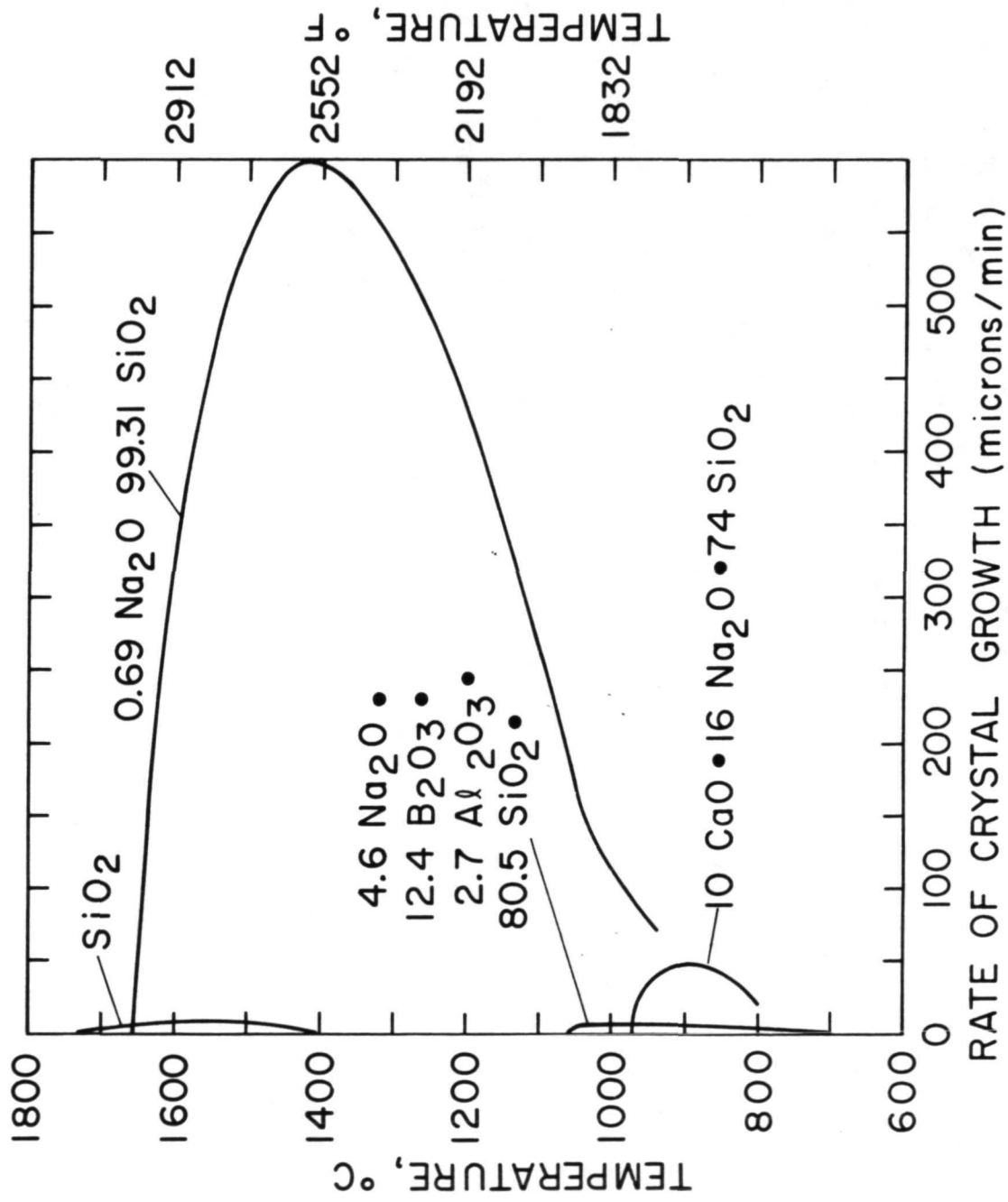
Figure 3

EXPANSION COEFFICIENT AS A FUNCTION OF PERCENT $NiCr_2O_4$

(Figure 4)

A second major criteria for coating selection was the coefficient of thermal expansion. The thermal shock resistance of a ceramic is known to be inversely proportional to the thermal expansion coefficient.[6] Also, in a tile configuration with a heated surface constrained by cooler side coatings, the thermally induced coating strain for a given ΔT and tile size will be directly proportional to the thermal expansion coefficient. This figure shows the thermal expansion coefficient of amorphous pure SiO_2 to be the lowest of the compositions considered. Several coatings were developed with physical mixtures of up to 30 weight percent $NiCr_2O_4$ to give high emittance. The solid line shows the calculation of the expected effect on the thermal expansion coefficient. The 30 weight percent $NiCr_2O_4$ concentration results in an expansion coefficient nearly equivalent to Corning's 7740 borosilicate glass. From recent work, as little as 2.5 weight percent $NiCr_2O_4$ gives a high emittance as well as a thermal expansion coefficient equivalent to Corning's 7900 high silica glass. The mixed phase coating may be more susceptible to devitrification than pure SiO_2. Both mixed and pure SiO_2 coatings have been developed and tested.

94

EXPANSION COEFFICIENT AS A FUNCTION OF percent
Ni Cr₂ O₄

Figure 4

95
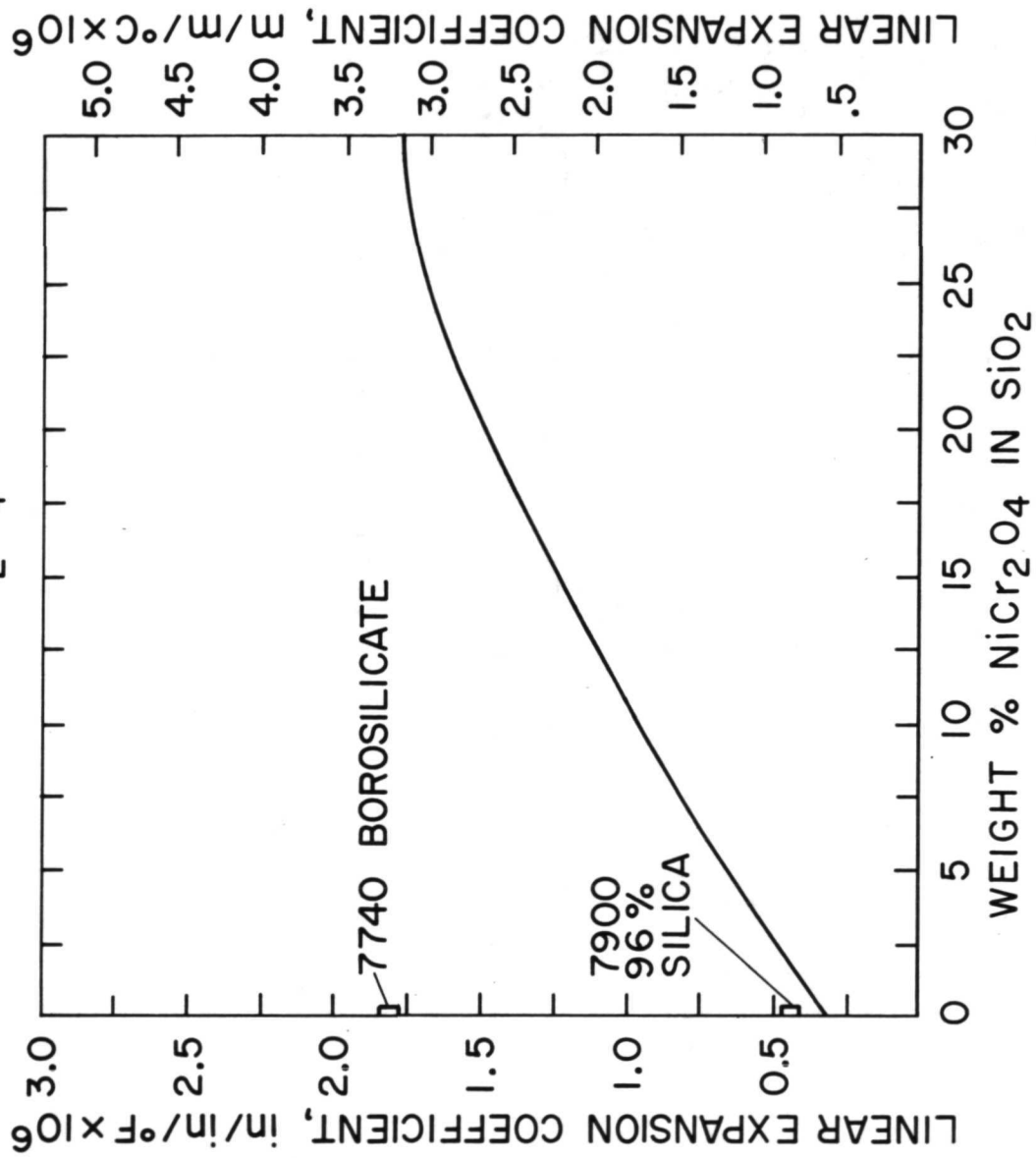
COATING DEVELOPMENT — PLASMA SPRAYING

(Figure 5)

Another boundary condition for the coating development was the desirability of not sintering the matrix during coating application as the shear modulus of the matrix rose with the development of fiber to fiber bonds.

One basic approach was to cold spray a water base slip of the desired oxide composition. The surface was then subjected to a steep thermal gradient densification process. The heat flux was achieved with either a plasma torch, radiant lamp, or oxyacetylene torch. The surface coating shown was densified with a plasma torch. The overall coating was judged to be 85 percent dense with the uppermost zone achieving the closed porosity impervious condition. The coating is sintered to the vertical yarns resulting in good adherence to the matrix. The $NiCr_2O_4$ emittance coating was applied by plasma spraying. The microstructures of the mixed coatings were quite similar except discrete particles of $NiCr_2O_4$ were uniformly mixed in the seal coat. Coatings sealed by the other techniques also appeared structurally similar except the overall coating density decreased in the order plasma, lamp, and oxyacetylene sealed.

96

COATING DEVELOPMENT - PLASMA SPRAYING

PLASTIC MOUNT

$NiCr_2O_4$

2.03 mm (80 mils)

SILICA COATING

VERTICAL SILICA YARN

TOP FELT

SILICA CLOTH

SILICA INSULATION
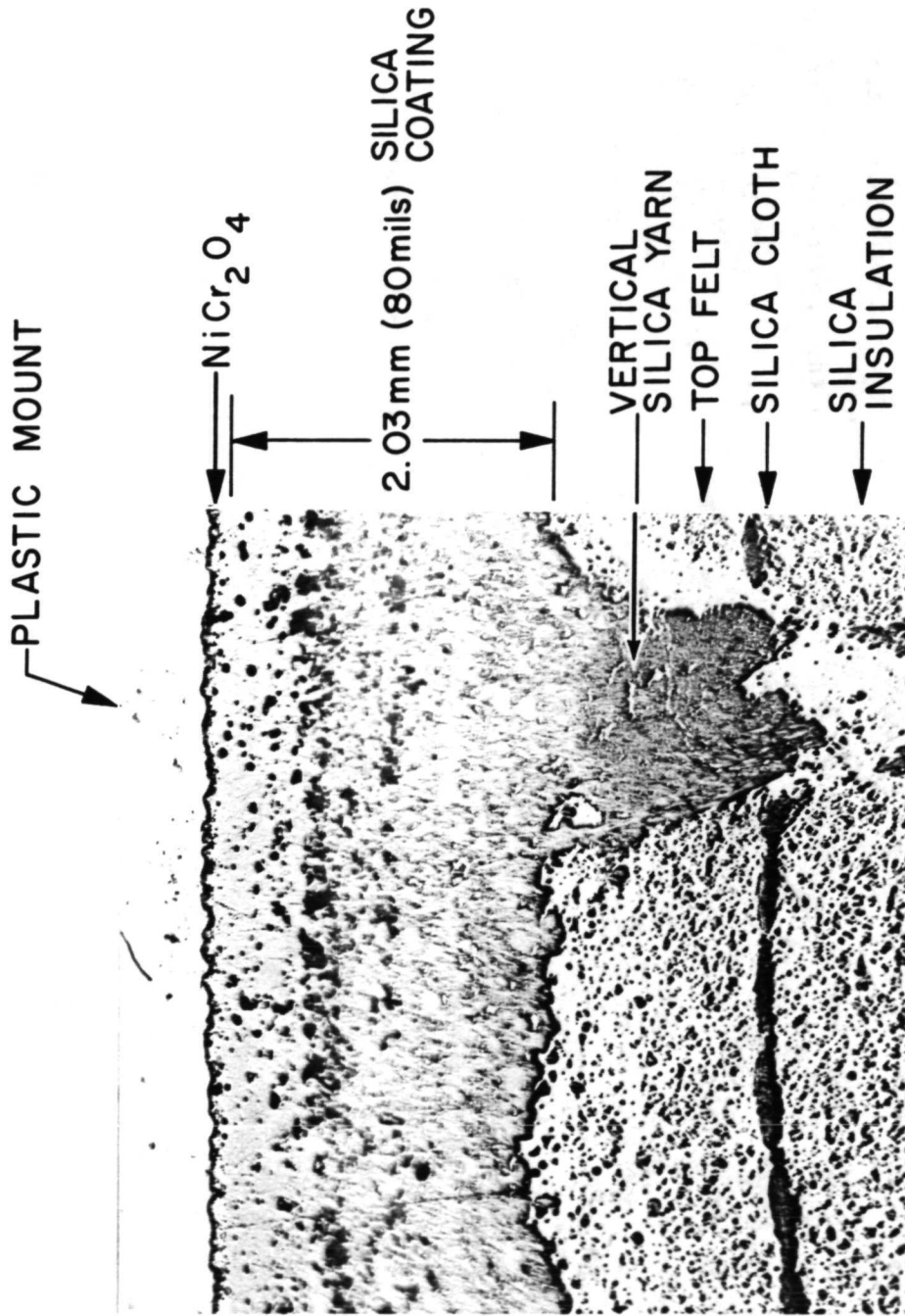
Figure 5

COATING DEVELOPMENT - CHEMICAL VAPOR DEPOSITION

(Figure 6)

Another major approach to coating application was based on the chemical vapor deposition process.*

A pure amorphous SiO_2 coating was deposited isothermally at about 700° C (1292° F) from an ethylsilicate source. The resulting coating is extremely dense and is fully impervious. The coating was extremely thin, which is desirable from the standpoint of weight and allowable substructure deflection. The coating has not yet been tested extensively; a problem remains in the prevention of deposition within the matrix. Progress has been made in solving this problem by application of this spray coating to nucleate the CVD deposit.

*A subcontract with Raytheon Co.

COATING DEVELOPMENT – CHEMICAL VAPOR DEPOSITION

PLASTIC MOUNT

.127 mm (5 mils) COATING

SILICA INSULATION

Figure 6

99
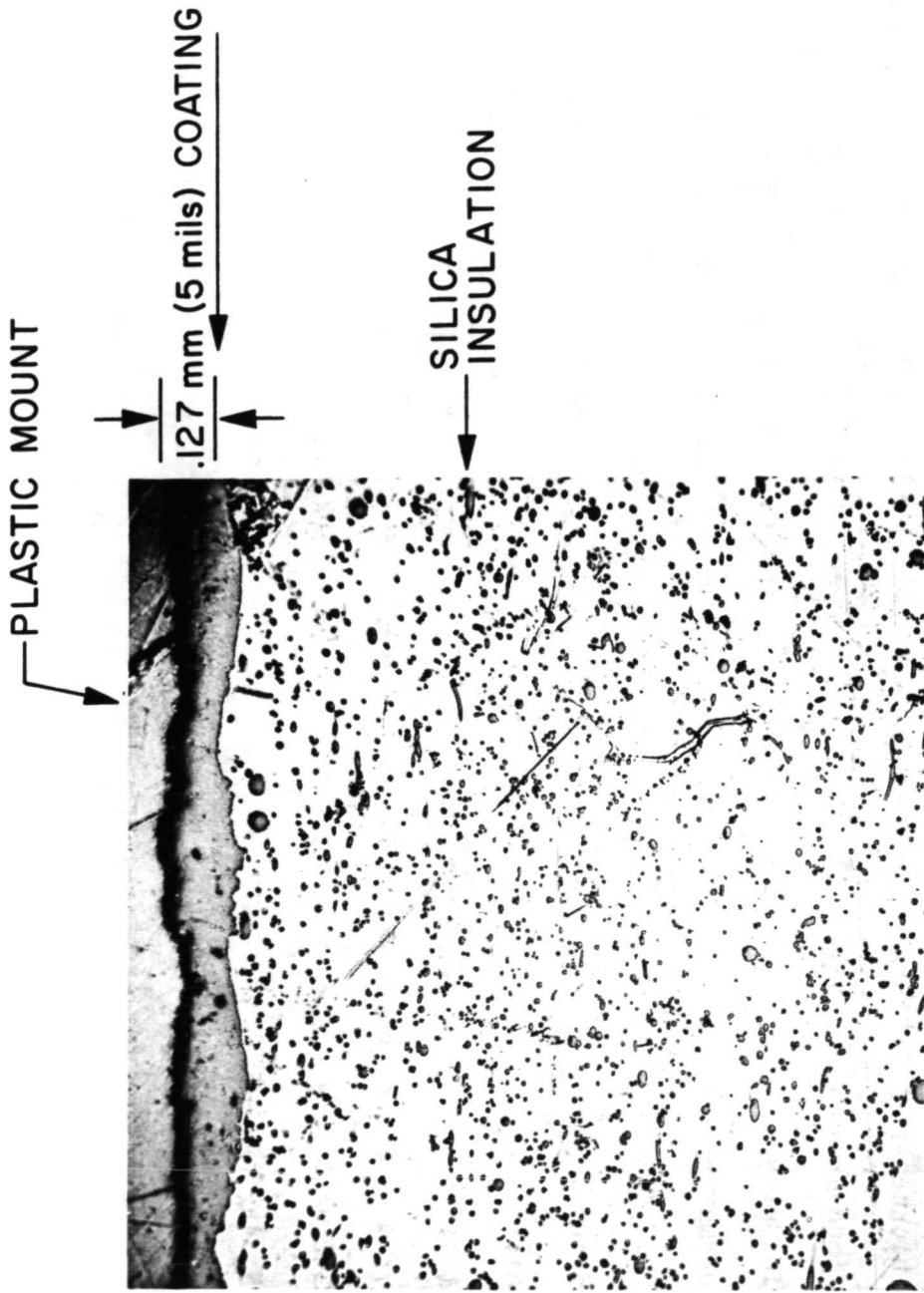
MECHANICAL PROPERTIES OF COATINGS

(Figure 7)

Metallographic sections demonstrated that the coating did not have a uniform microstructure through the thickness; therefore, the mechanical properties were not expected to be uniform through the thickness. Since ceramics normally fail in tension, it was decided to test four point bend specimens with the sealed side both in tension and compression. Surprisingly, the tests showed equivalent results, which may have been due to a shifting of the neutral axis part way into the denser zone due to the lower modulus of the higher porosity zone. In this case, the dense zone would be carrying the main load and the actual strength of the coating would be considerably higher than the reported strengths, which were calculated based on a homogeneous material and the standard elastic beam formula. Therefore, it is emphasized that the values reported are apparent mechanical properties and are useful mainly in comparing one coating to another. The double cold spray - double seal coating was fabricated with a goal of achieving a higher strength coating. The gains over a cold sprayed SiO_2 SiO_2 - oxyacetylene sealed coating were judged marginal. The mixed coatings did exhibit significant gains in strength. The elastic modulus was also increased leaving a net lower strain to failure for this coating compared to, for example, the cold sprayed - oxyacetylene sealed SiO_2. Thus, it becomes very much a design question whether or not the mixed coatings represent a desirable improvement in properties. It was judged that the high allowable strain of the pure SiO_2 coating was the more desirable feature.

100

MECHANICAL PROPERTIES OF COATINGS

COATING	APPARENT 4 Pt. BEND STRENGTH, 10^5 N/m² (psi)	APPARENT ELASTIC MODULUS, 10^8 N/m² (10^6 psi)	PERCENT STRAIN TO FAILURE
1. SiO_2 – OXYACETYLENE SEAL	104 (1500)	101 (1.47)	0.130
2. SiO_2 – DOUBLE OXYACETYLENE SEAL	130 (1880)	105 (1.52)	0.127
3. MIXED SiO_2 WITH $NiCr_2O_4$ – PLASMA SEAL	333 (4825)	369 (5.35)	0.091

Figure 7

101

ARC TEST RESULTS

(Figure 8)

Ten samples were subjected to simulated re-entry cycles in the Avco ROVERS arc facility to evaluate sealer coating and emittance coating performance. From one to five simulated cycles were conducted on each sample at approximately the same surface temperature. Peak surface temperatures were from 982° C (1800° F) to 1293° C (2360° F). Total normal emittance was measured before and after arc testing with a Barnes Radiometer. A summary of the major tests is given.

The coatings based on a pure SiO_2 sealer coat survived the arc exposures with little degradation. Some loss in both emittance and adherence of the plasma sprayed $NiCr_2O_4$ or CoO emittance coating was noted. The lowering of emittance value, while not judged serious, was due to a change in the oxidation states of the transition metal ions. The loss of adherence was undoubtedly due to the differential thermal expansion of the two phases. The mixed coating had a very high post test emittance and no loss of adherence. Cracks in the coating appeared on two of the mixed coating specimens tested, while one survived without cracking. The higher incidence of cracking was probably due to the higher thermal expansion coefficient of nominal 10% $NiCr_2O_4$ in SiO_2. Coatings have been fabricated with $2\frac{1}{2}$% $NiCr_2O_4$ in SiO_2, but these have not yet been arc tested.

102

ARC TEST RESULTS

COATING	EMITTANCE	PEAK TEMP. °C (°F)	NUMBER OF CYCLES	CRACK FORMATION	POST TEST EMITTANCE
1. SEPARATE SiO_2 – PLASMA SEALED – $NiCr_2O_4$	0.88	1271 (2320)	2	No	0.82
2. SEPARATE SiO_2 – PLASMA SEALED – $NiCr_2O_4$	—	1249 (2280)	5	No	—
3. SEPARATE SiO_2 – OXYACETYLENE SEALED – CoO	0.87	1077 (1970)	3	No	0.83
4. MIXED SiO_2 WITH $NiCr_2O_4$ – LAMP SEALED	—	1227 (2240)	5	No	0.86
5. MIXED SiO_2 WITH $NiCr_2O_4$ – PLASMA SEALED	—	1293 (2360)	1	Yes	—

Figure 8

103

CONCLUSIONS

An impervious amorphous silica coating for a flexible silica mat insulation system has been developed. High emittance is provided by plasma spraying a NiCr$_2$O$_4$ layer. The coating satisfies the main function of coating the insulation and has a number of attractive features including a low coefficient of thermal expansion. A partial loss of adherence of the emittance coating upon cyclic thermal exposure is the most serious problem remaining to be solved.

A second coating, which has reached the advanced development state, incorporates from 2 to 10 weight percent NiCr$_2$O$_4$ intimately mixed in amorphous SiO$_2$. This coating survives thermal cycling with no loss of adherence. The slightly higher thermal expansion coefficient appears to result in a higher incidence of cracking. This coating is not as fully developed or tested as the first coating.

A third basic coating approach is based on the deposition of a thin amorphous SiO$_2$ layer by chemical vapor deposition techniques. The coating is in a relatively early stage of development, but offers the potential for higher strength and much lower weight than the first two coatings.

These coating techniques are for the most part applicable to other insulation systems.

104

REFERENCES

1. H. Rawson, Inorganic Glass-Forming Systems, Academic Press, New York, p. 45, 1967.

2. N. G. Ainslie, C. R. Morelock, and D. Turnbull, in "Symposium on Nucleation and Crystallization in Glasses and Melts," M. K. Reser, G. Smith, and H. Insley, eds., American Ceramic Society, Columbus, Ohio, p. 97, 1962.

3. F.E. Wagstaff, S.D. Brown, and I.B. Cutter, "The Influence of H_2O and O_2 Atmospheres on the Crystallization of Vitreous Silica," Phys. and Chem. Glass, $\underline{5}$, 76, 1964.

4. A. Dietzel and H. Wickert, Glastech. Ber., $\underline{29}$, 1, 1956.

5. S.M. Cox and P.L. Kirby, Nature, $\underline{159}$, 162, 1947.

6. W.D. Kingery, INTRODUCTION TO CERAMICS, John Wiley & Sons, New York, p. 630, 1960.

105

PRECEDING PAGE BLANK NOT FILMED

5

MAR-SI, MARTIN SURFACE INSULATION

Authors:

P. Paul Plank
Arthur Feldman
William C. Müller
John F. Creedon
Joseph M. Toth, Jr.

MARTIN MARIETTA CORPORATION
DENVER DIVISION
Denver, Colorado 80201
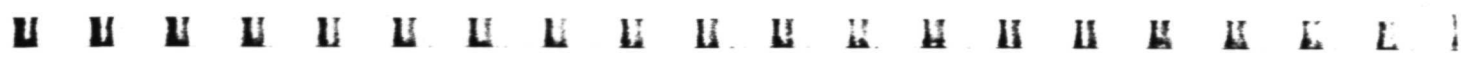
INTRODUCTION

(Figure 1)

The Space Shuttle reusable surface insulation (RSI), thermal protection system, must protect the basic structure (with low weight), provide 100 mission life (reuse, thermal stability, ability to withstand thermal shock), and be cost-effective for refurbishment and maintenance. Martin Marietta has developed a material, MAR-SI (Martin Surface Insulation) that satisfies these requirements. This paper describes the progress of the MAR-SI basic material and coating development, physical properties determination, environmental testing, design·and analysis, and projected costs.

MAR-SI, MARTIN SURFACE INSULATION - INTRODUCTION

Basic Material Development

Coating Development

Thermophysical and Mechanical Properties

Environmental Testing

Design and Analysis

Projected Costs

Figure 1

MAR-SI OBJECTIVE AND SUMMARY

(Figure 2)

The objective for developing MAR-SI was to provide a second generation RSI with the characteristics shown in figure 2. The most important characteristics are high thermal stability, low thermal conductivity, and the ability to satisfy thermal shock requirements. To satisfy these requirements, alumina silicate has been selected as the basic component of the material and coating. Property and environmental tests are being continually conducted, and analysis has been performed and compared with the test results. A pilot plant has been completed with a capability to produce 5000 kg (11,000 lb) per year of completed tile. This production capacity has been used to project the cost of coated tiles.

110

MAR-SI OBJECTIVE AND SUMMARY

Objective

Produce a Second Generation RSI to Provide:

240 kg/m^3 (15 lb/ft^3) Density or Less

High Thermal Stability of 1371 to 1427°C
(2500 to 2600°F)

Low Thermal Conductivity

Satisfy Thermal Shock Requirements

Low Cost

Maximum Reuse with Waterproof – High
Emissivity Coating

Construct Pilot Plant to Define Production
Requirements

Summary of Progress:

Selected Alumina Silicate

Thermal Property Tests (SRI)

Mechanical Property Tests

Developed Coating

Environmental Tests with Salt
and Acoustics (Quartz Lamp
and Plasma Arc)

Analysis and Design – Total
TPS System

Bonding Effort

Pilot Plant, 0.406 x 0.406 m
(16 x 16 in.) Billets, Capability
for Larger Billets (Projected Costs)

Figure 2

111

BASIC MATERIAL DEVELOPMENT

(Figure 3)

Considering the candidate fibrous materials available, alumina silicate was selected because

of its low fiber diameter (potentially low thermal conductivity), high thermal stability, and

low material cost. The felting process was selected because of prior experience and greater

potential for success. Process variables were evaluated, the most important of which are the

binder/fiber ratio (0.7 by weight) and the firing schedule of 1427°C (2600°F) for 0.5 hour.

The criteria for establishing the final process were an optimum combination of strength, ease

of fabrication, lack of cracking, uniformity, firing temperature higher than use temperature,

and low-cost raw materials.

112

BASIC MATERIAL DEVELOPMENT

	Candidates and Variations	Selections
Material	Alumina Silicate Mullite Silica	Alumina Silicate Fiber Diameter, 2.0-3.0 μm (low K) High Thermal Stability Low Material Cost
Process	Felting and Foaming	Felting
Process Variables		
Binder/Fiber Ratio	0.4 to 1.0 by Weight	0.7
Fiber Length	Chopped, Not Chopped	Not Chopped
Fillers	Silica Microspheres	Silica Microspheres
Additives	CoO or Cr2O3	Not Used
Firing Studies	1316°C to 1427°C (2400°F to 2600°F) (0.5 to 3.0 hr)	1427°C (2600°F) (0.5 hr)
Density Profile	Felting Density and Impregnation	4% (Variation)

Figure 3

113

PILOT PRODUCTION FLOW

(Figure 4)

Manufacturing procedures were established as shown, using the pilot plant facility. Of these procedures, it was found that the impregnation process has the greatest impact on the mechanical properties, and that thermal properties are primarily dependent on fiber composition, but are independent of process parameters and density. It was also found that mechanical properties are dependent on both material composition and process parameters.

114

PILOT PRODUCTION FLOW

Weigh Raw Materials → Mix with Binder → Felt → Dry → Impregnate → Dry → Sinter → Machine to Size → Apply Coating → Sinter → Ready for Application
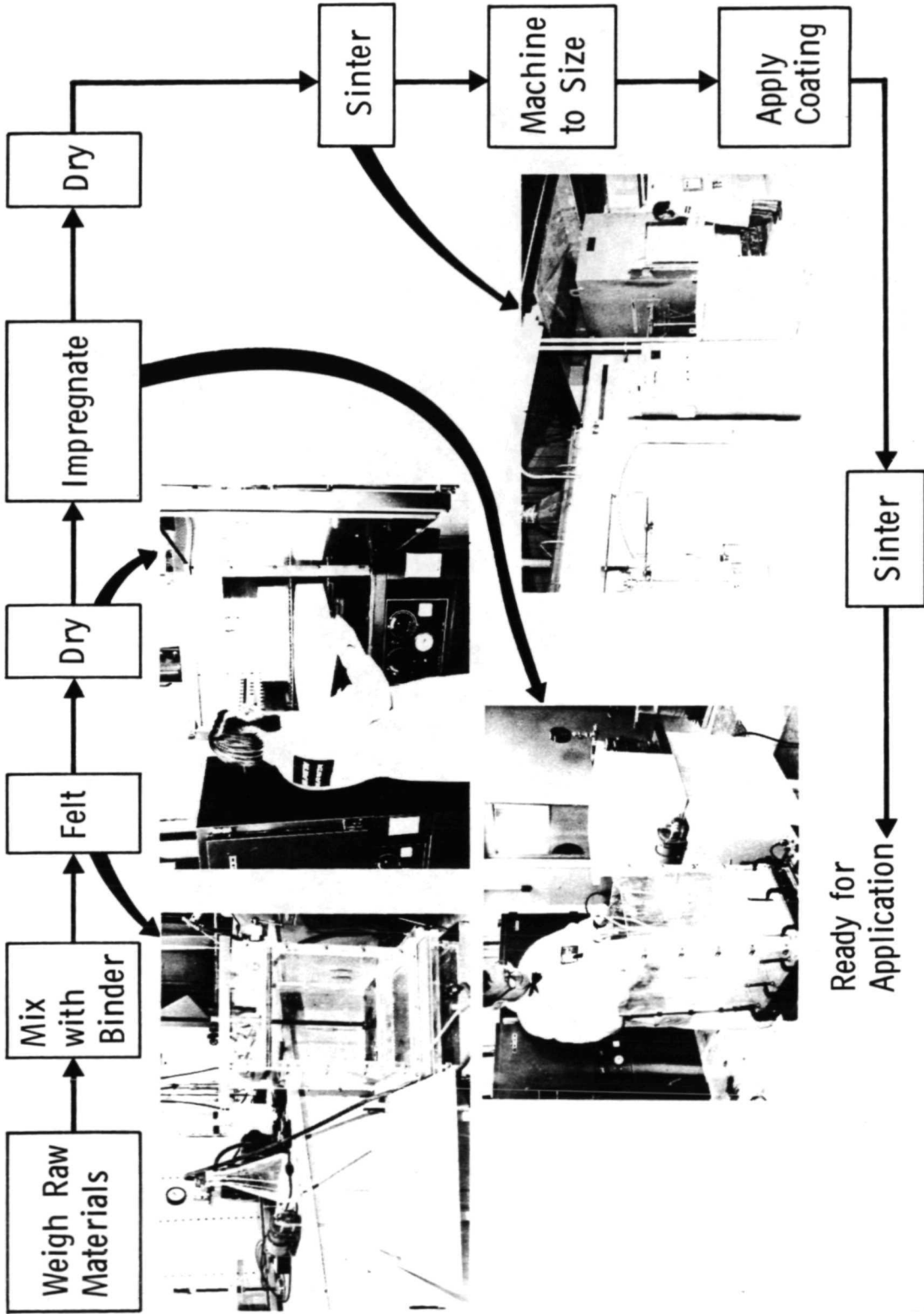
Pilot Plant Capacity – 11,000 lb/yr of Completed Tile

Figure 4

SCANNING ELECTRON MICROGRAPHS

(Figure 5)

Scanning electron micrographs of MAR-SI material are shown after being sintered at 1427°C (2600°F) for 0.5 hour. The micrographs indicate that good fusion and bonding are occurring between the fibers. Also, the 5000X micrograph shows that the fiber diameter is approximately 2.0 μm.

116

SCANNING ELECTRON MICROGRAPHS
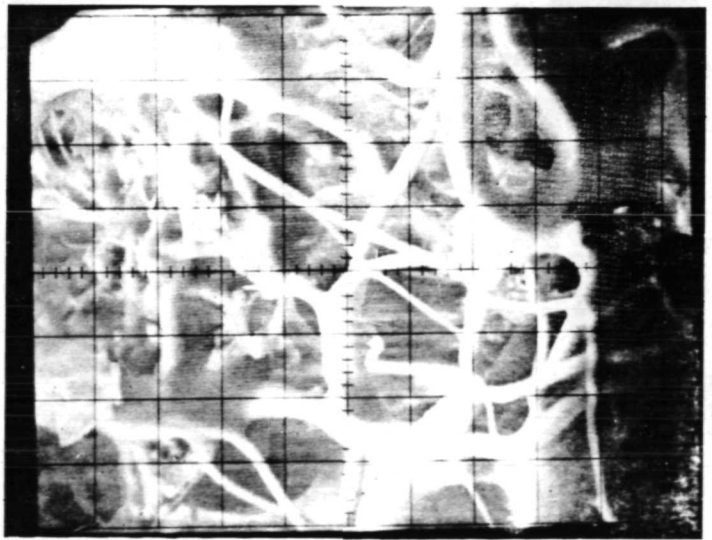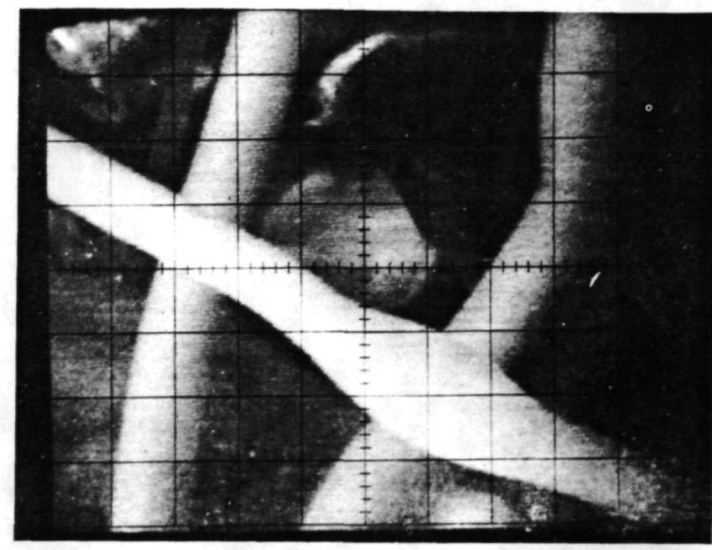
1000 X   2000 X   5000 X

Figure 5

COATING DEVELOPMENT

(Figure 6)

After examining the many candidate processes, a sprayed single application coating was selected. This type of coating is relatively easy to apply, provides a uniform thickness, and does not involve problems of compatibility between coating layers. Alumina silicate was selected as the filler material, and spodumene (series 50) and eucryptite (series 60) were selected as binders (glazes). It was found that the most important process variables are the binder/filler ratio (0.7 by weight) and the firing schedule [1371°C (2500°F) for 1 hr]. The coating formulations satisfy the requirement for being waterproof and having a high emissivity [ε = 0.75 to 0.82 at 1204°C (2200°F)]. Elevated temperature test results of these coatings are presented in Figures 11 and 12.

118

MAR-SI COATING DEVELOPMENT

	Candidates and Variations	Selections
Process	Single and Multiple Application Spray, Plasma Spray, Brush, Dip	Single Application Spray
Material		
Filler	Alumina Silicate, Mullite	Alumina Silicate
Binder (Glaze)	Alumina Phosphate Spodumene, Synthetic Petalite, Eucryptite	Spodumene (Series 50) Eucryptite (Series 60)
Process Variations		
Binder/Filler Ratio	0.4 to 1.2	0.7
Firing Studies	1316 to 1427°C (2400 to 2600°F) (0.5 to 1.0 hr)	1371°C (2500°F) (1.0 hr)
Additives	Alumina 1.0 to 5.0% Cerium Oxide, Samarium Oxide, Ferro #3794	Alumina 2.5% Ferro #3794 (Emissivity Control)

Figure 6

119

COATING COMPATIBILITY EVALUATION

(Figure 7)

In addition to being waterproof and satisfying emissivity requirements, the coating must be compatible with the basic material in terms of αE (coefficient of thermal expansion and modulus) to minimize cracking. To provide this αE and, therefore, good thermal shock capability, various candidate coatings were examined. The figure presents a coating compatibility evaluation for the series 50 and series 60 coatings, and shows that the better αE compatibility with the basic material occurs using the series 60 coating. The test results shown later also indicate that the series 60 coating is more compatible with the basic material. Thermal stress cracks did not appear on the sides of the tiles near the top surface as they had with other coatings.

120

COATING COMPATIBILITY EVALUATION

αE (Coefficient of Thermal Expansion and Modulus)

Material	Elastic Modulus, 10^8 N/m^2 (10^6 psi)	Tensile Strength, 10^5 N/m^2 (psi)	Tensile Strain to Failure, %	Coefficient of Thermal Expansion, 10^{-6} m/m/°C (10^{-6} in./in./°F)	Product of Coefficient of Thermal Expansion and Elastic Modulus, αE 10^2 N/m^2-°C (lb/in.^{2}-°F)
Series 50 Coating	448 (6.5)	41.3 (600)	0.0092	3.24 (1.8)	1450 (11.7)
Series 60 Coating	234 (3.4)	37.9 (550)	0.0162	0.57 (0.32)	133 (1.09)
Basic Material	2.37 (0.0343)	3.1 (45)	0.13	5.04 (2.8)	12 (0.096)

Figure 7

MAR-SI THERMOPHYSICAL PROPERTIES

(Figure 8)

Thermophysical properties were measured by Southern Research Institute. In addition to the thermal conductivity and thermal expansion values shown, enthalpy and heat capacity were also determined.

Two densities, 184.3 kg/m^3 (11.5 pcf) and 240.5 kg/m^3 (15 pcf), and two developmental process combinations were sent to Southern Research Institute for evaluation. The data indicate that the variation in densities and process parameters did not affect the thermal conductivity. Successful thermal conductivity measurements at 1454°C (2650°F) demonstrated the high thermal stability of the material. Also, the thermal stability was further established when thermal cycling to obtain thermal expansion data indicated only very small dimensional changes in the material, as shown in the figure.

MAR-SI THERMOPHYSICAL PROPERTIES

Thermal Expansion - XY Direction

Thermal Conductivity - Z Direction
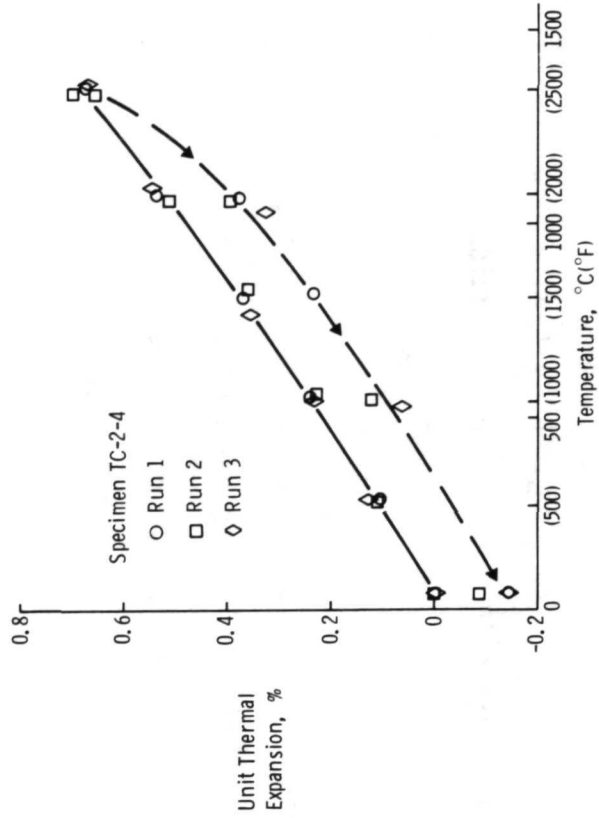
(Measured by Southern Research Institute)

Figure 8

123

MECHANICAL PROPERTIES

(Figure 9)

Mechanical properties were determined for the basic material as well as for the coatings. The resulting elastic modulus for the basic material is 2.37 x 10^8 N/m^2 (34,300 psi). As discussed earlier, the series 60 coating provides the lowest coating modulus and is more compatible with the basic material. Therefore, the series 60 is the leading candidate coating system.

Tensile strength, tensile strain, and elastic modulus of the basic material were measured on 0.0508x0.0508x0.0762 m (2x2x3 in.) specimens. Shear modulus was determined by flexure testing deep beams of varying length/depth ratios. Coating properties were measured on coated four-point-loading flexure specimens; 0.00953 m deep x 0.01907 m wide x 0.1143 m long (3/8x3/4x4½ in.).

124

MECHANICAL PROPERTIES

BASIC MATERIAL

Tensile Strength (X-Y)	3.1×10^5 N/m^2 (45 psi)
Elastic Modulus (X-Y)	2.37×10^8 N/m^2 (34,300 psi)
Tensile Strain to Failure (X-Y)	0.13%
Shear Modulus (X-Z)	0.689×10^7 N/m^2 (1000 psi)

COATING

Series 50:

Tensile Strength	41.3×10^5 N/m^2 (600 psi)
Elastic Modulus	448×10^8 N/m^2 (6.5×10^6 psi)
Tensile Strain to Failure	0.0092%

Series 60:

Tensile Strength	37.9×10^5 N/m^2 (550 psi)
Elastic Modulus	234×10^8 N/m^2 (3.4×10^6 psi)
Tensile Strain to Failure	0.0162%

Figure 9

HEATING TEST PROFILE

(Figure 10)

The Space Shuttle area 2P heating profile provided by NASA-MSC, has been used for both plasma arc and quartz lamp testing, as shown. The quartz lamp testing procedure can simulate the heating profile; however, as shown for the plasma arc testing, the profile must be modified. Quartz lamps are used for preheating to 56.7 kw/m^2 (5 Btu/ft^2-sec) during the plasma arc testing.

126

HEATING TEST PROFILE

Plasma Arc Tests

Cycle 1

Cycle 2

Cycle 3

Quartz Lamp Tests

Orbiter Area 2
(Perturbed Heating Rate)
MSC Environment 7/21/71

Local
Heating
Rate,
kw/m² 2
(Btu/ft²-sec)

Time, sec

Figure 10

127
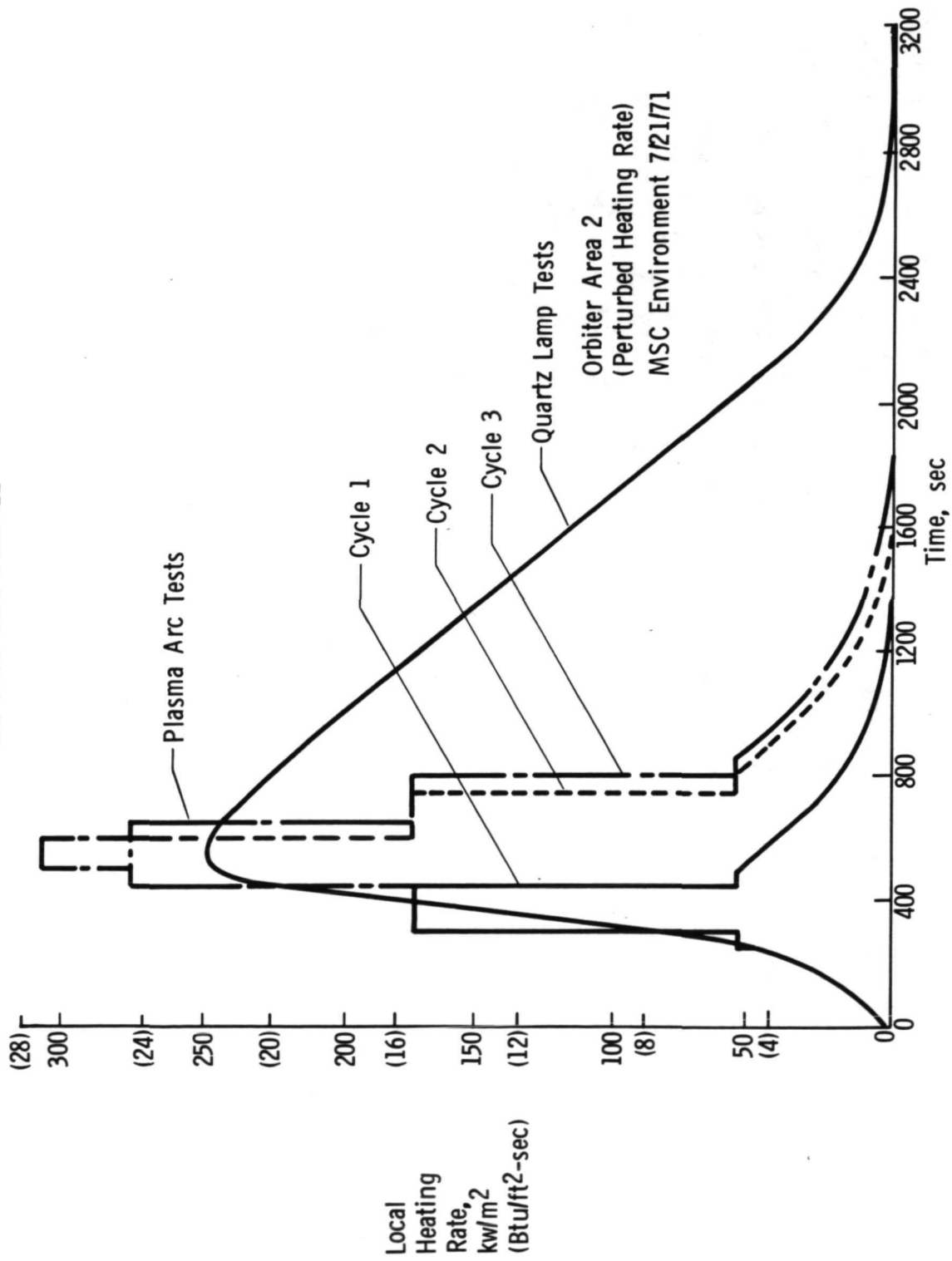
COATING SCREENING TESTS AND SELECTION (Radiant Heating Specimens)

Figure (11)

Using the previous heating profile, coating screening tests were conducted on 0.1524x0.0254x 0.0381 m (6x1x1.5 in.) and 0.1016x0.0508x0.0508 m (4x2x2 in.) coupons. While 104 cycles (3000 sec) to 1260°C (2300°F) and 1371°C (2500°F) were accomplished on the series 50 coating specimens and they were still waterproof, the series 60 coating specimens have shown more compatibility with the substrate material. Thermal cycling of both series of coatings with exposure to salt has shown no reaction.

128

COATING SCREENING TESTS AND SELECTION   (Radiant Heating Specimens)
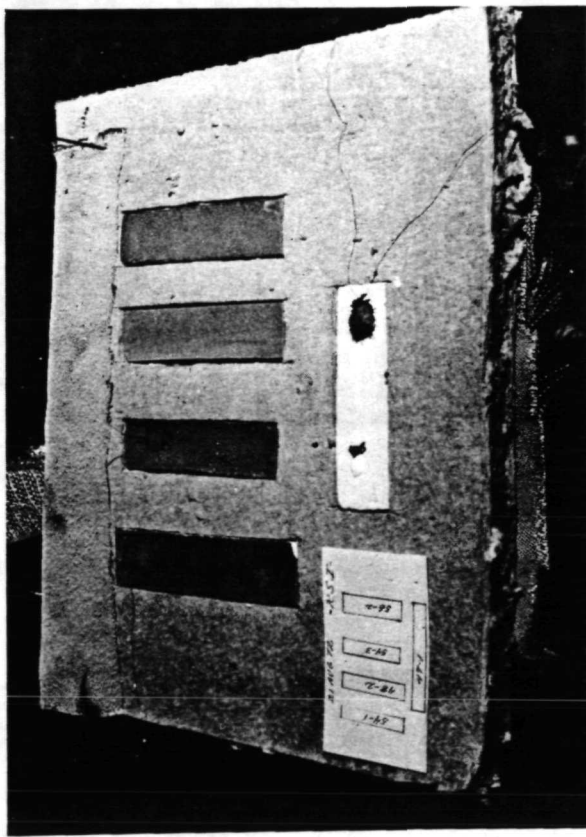
Numerous Tests
of 15.25 x 2.54 x
3.81 cm and 10.16
x 5.08 x 5.08 cm
(6 x 1 x 1 in. and
4 x 2 x 2 in.)
Coupons

Summary of Tests

Series 40 and 50 Specimens
Maximum of 104 Cycles, 1260
and 1371°C (2300 and 2500°F).
Still Waterproof. Thermal Cycling
with Exposure to Salt – No Reaction.

Series 60 Specimens – Still Testing
Maximum of Five Cycles, 1260
and 1371°C (2300 and 2500°F).
Thermal Cycling with Exposure
to Salt – No Reaction.

Remarks and Selection

αE of Coating and Basic
Material Not Compatible.

αE of Coating and Basic
Material Compatible;
Series 60 Coating Selected.

Figure 11

129

RADIANT HEAT AND ACOUSTIC TESTS

(Figure 12)

Panels have been tested with quartz lamps, as shown. The 0.1524x0.1524 m (6x6 in.) panel coated with the series 50 coating was cycled 20 times to 1413°C (2575°F) and was still water-proof. However, it had a crack on one side. The series 60 coating specimen, 0.1524x0.1524x 0.0508 m (6x6x2 in.), shown in the figure, is in the process of being cycled thermally and will be tested in an acoustic facility to 162 dB.

RADIANT HEATING AND ACOUSTIC TESTS

Series 60 Coating

Cycled to 1260°C
(2300°F)

Acoustic Test to 162 dB
(Still Testing)

Series 50 Coating

Cycled 20 Times
1413°C (2575°F)
(Still Waterproof)

[0.1524 m x 0.1524 m (6 in. x 6 in.) Panels (Coated on 5 Sides)]

Figure 12

131

PLASMA ARC TEST SPECIMEN BEFORE TEST

(Figure 13)

As shown, a 0.1016 m (4 in.) diameter, 0.0508 m (2 in.) thick specimen is used for plasma arc testing. A shield of the same MAR-SI material is used to protect the sides of the specimen during test, provide a more uniform temperature across the face of the specimen, and minimize heat flow through the sides of the specimen.

PLASMA ARC TEST SPECIMEN, BEFORE TEST

0.1016-m (4-in.) Diameter MAR-SI Test Specimen

MAR-SI Shield
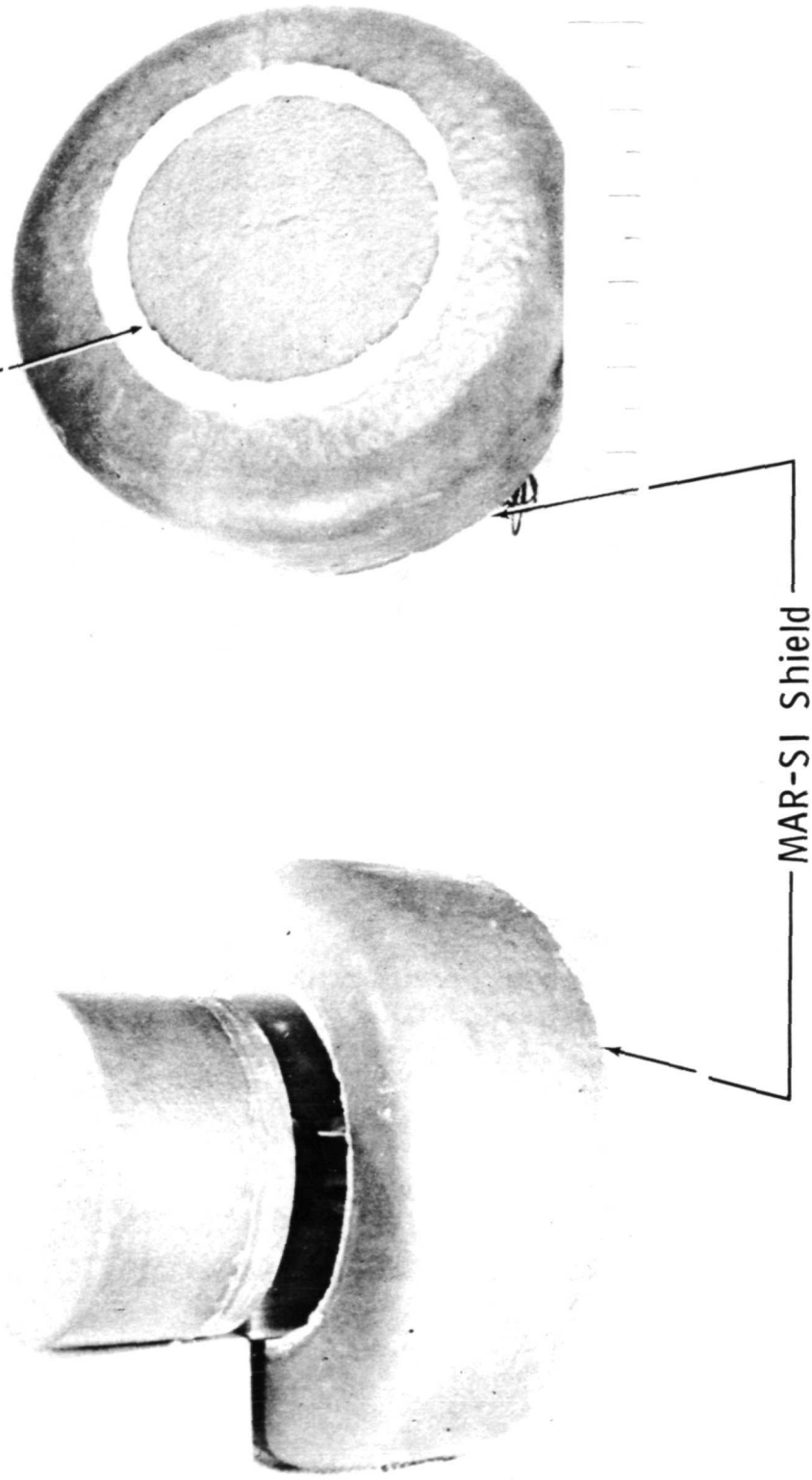
Figure 13

133

PLASMA ARC SPECIMEN DURING TESTING

(Figure 14)

This figure shows the shield and test specimen being preheated using a quartz lamp array and in the plasma stream. This testing was accomplished in our Plasma Arc Facility.

134

PLASMA ARC SPECIMEN DURING TESTING

In Plasma Arc

Preheating Using
Quartz Lamps

Figure 14

135
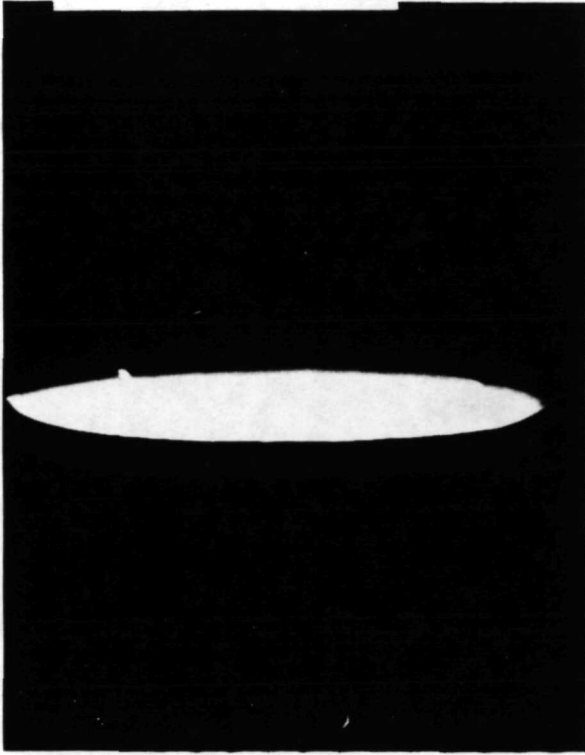
SUMMARY OF MAR-SI PLASMA ARC TESTS

(Figure 15)

Using the type of plasma arc specimen shown previously, six specimens were
tested for three different thermal cycles (Fig. 10). The test parameters and
results are summarized in figure 15. The peak hot wall heat rates ranged from
215 to 306 kw/m^2 (19 to 27 Btu/ft^{2}sec). For an emissivity value of 0.8, a peak
temperature of 1316°C (2400°F) was reached for the highest hot wall heating
rate condition. These results indicate that the coating is noncatalytic.

136

SUMMARY OF MAR-SI PLASMA ARC TESTS

TEST NO.	COATING SERIES	CYCLE NO. 1					CYCLE NO. 2					CYCLE NO. 3				
		q_{CW}*	H_T†	T_{PYRO}¶	q_{HW}§	T_{SURF}**	q_{CW}*	H_T†	T_{PYRO}¶	q_{HW}§	T_{SURF}**	q_{CW}*	H_T†	T_{PYRO}¶	q_{HW}§	T_{SURF}**
1	48-2	175 (15.4)	6.80 (2925)	1300 (1880)	145 (12.8)	1314 (1910)	278 (24.5)	9.01 (3875)	1476 (2200)	252 (22.2)	1511 (2260)	375 (33.0)	12.69 (5450)	1526 (2290)	279 (24.6)	1549 (2330)
2	59-1	286 (25.2)	9.19 (3950)	1433 (2120)	217 (19.1)	1455 (2160)	286 (25.2)	9.19 (3950)	1458 (2165)	231 (20.3)	1478 (2200)	286 (25.2)	9.19 (3950)	1444 (2140)	224 (19.7)	1466 (2180)
3	54-1	290 (25.5)	8.72 (3750)	1401 (2060)	196 (17.3)	1422 (2100)	290 (25.5)	8.72 (3750)	1444 (2140)	224 (19.7)	1466 (2180)	471 (41.5)	14.96 (6425)	1504 (2250)	262 (23.1)	1524 (2290)
4	54-3	290 (25.5)	8.72 (3750)	1398 (2055)	196 (17.3)	1422 (2100)	290 (25.5)	8.72 (3750)	1403 (2065)	201 (17.7)	1425 (2110)	471 (41.5)	14.96 (6425)	1523 (2280)	274 (24.1)	1544 (2320)
5	60-2	290 (25.5)	8.72 (3750)	1384 (2030)	190 (16.7)	1403 (2070)	290 (25.5)	8.72 (3750)	1414 (2090)	208 (18.3)	1437 (2130)	591 (52.0)	17.92 (7700)	1567 (2360)	308 (27.1)	1588 (2400)
6	54-1	290 (25.5)	8.72 (3750)	1421 (2095)	208 (18.3)	1437 (2130)	290 (25.5)	8.72 (3750)	1401 (2060)	196 (17.3)	1422 (2100)	591 (52.0)	17.92 (7700)	1567 (2360)	308 (27.1)	1588 (2400)

*MAXIMUM LEVEL IN CYCLE. COLD WALL HEATING RATE, 12.7 cm DIAMETER COPPER CALORIMETER, kw/m^2 (Btu/ft^2sec)

†CORRESPONDING STREAM ENTHALPY LEVEL, $10^6 J/kg$ (Btu/lb)

¶OPTICAL PYROMETER READING AT SPECIMEN ¢ (AT MAXIMUM LEVEL), °K (°F)

§APPARENT NONCATALYTIC SURFACE HOT WALL HEATING RATE, kw/m^2 (Btu/ft^2sec)

**CORRESPONDING TRUE MAXIMUM SURFACE TEMPERATURE (ϵ), °K (°F)

Figure 15

EFFECT OF SURFACE CATALYTIC ACTIVITY ON SURFACE TEMPERATURE OF MAR-SI

(Figure 16)

This figure illustrates the noncatalytic characteristics of the MAR-SI coatings. The theoretical curves are taken from "Reusable Surface Insulation Materials and Development" by H. E. Goldstein, et al. *NASA Space Shuttle Technology Conference* April 12-14, 1972, NASA TM X-2570. The surface temperature is plotted against the hot wall heating rate for the cases of the wall that are catalytic to the recombination of atoms of nitrogen and oxygen, and the cases that are noncatalytic to the recombination. The data obtained at our Plasma Arc Facility are superimposed on the theory curves. These data show that the coatings tend to be somewhat noncatalytic, which may be significant in the design of the Space Shuttle TPS, because of the lower surface temperature. Therefore, development of the most noncatalytic coating is a desirable goal.

138

EFFECT OF SURFACE CATALYTIC ACTIVITY ON SURFACE TEMPERATURE OF MAR-S1

Figure 16

139
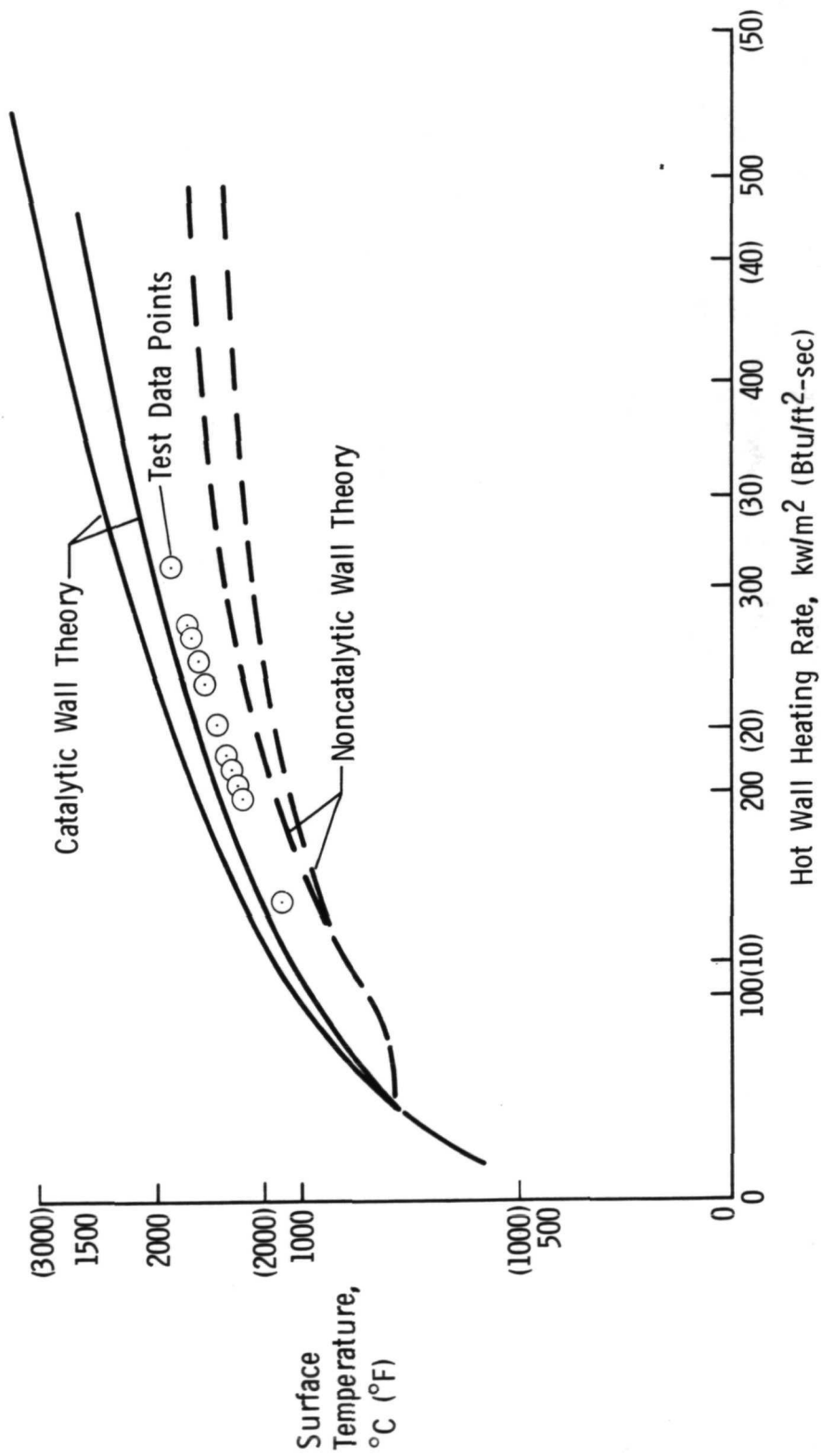
PLASMA ARC TESTING - HIGH TEMPERATURE DYNAMIC SEALS

(Figure 17)

Additional plasma arc testing is planned in the near future for the dynamic seal program shown in the figure. Coated MAR-SI will be bonded to the hinge and control surface as shown. The MAR-SI will be 0.1778 m (7 in.) wide. While the objective is to determine the adequacy of the seal for a defined gap width, the coated MAR-SI material will be evaluated during this test.

140

PLASMA ARC TESTING - HIGH TEMPERATURE DYNAMIC SEALS FOR AERODYNAMIC CONTROL
SURFACES ON THE SPACE SHUTTLE (NAS9-12883 (MSC)

MAR-SI to Be Bonded to Hinge and Control Surfaces   (To Be MAR-SI)

Internal Profile
View of Aluminum
Structure and Seal
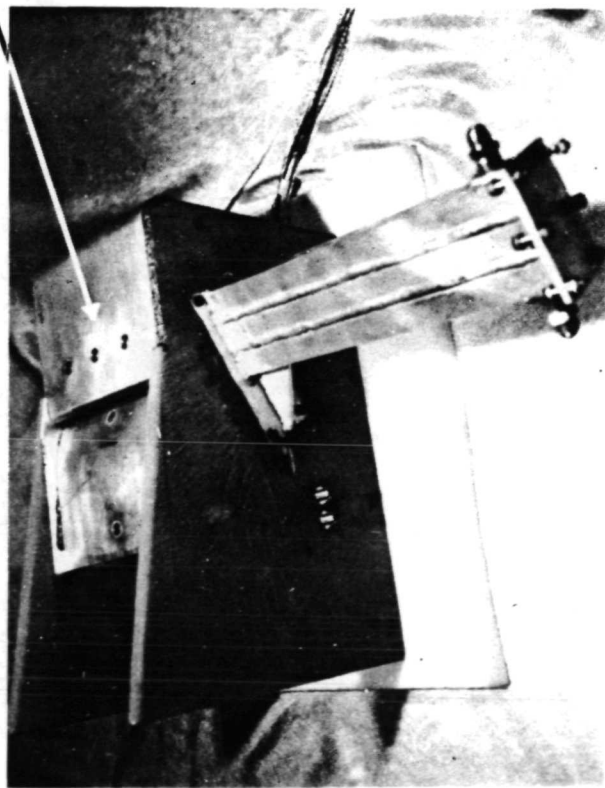
External View of
Aluminum Structure
(Plasma Arc Model)

Figure 17

DESIGN AND ANALYSIS (Typical TPS Configuration)

(Figure 18)

Using results of the previous material tests, a design and analysis effort has been conducted.

As shown in the figure, a coating, basic material strain isolator, and aluminum substrate

operating at a peak temperature of 149°C (300°F) were analyzed.

142

DESIGN AND ANALYSIS

Typical TPS Configuration

3-D Computer
Model Portion

Figure 18

143
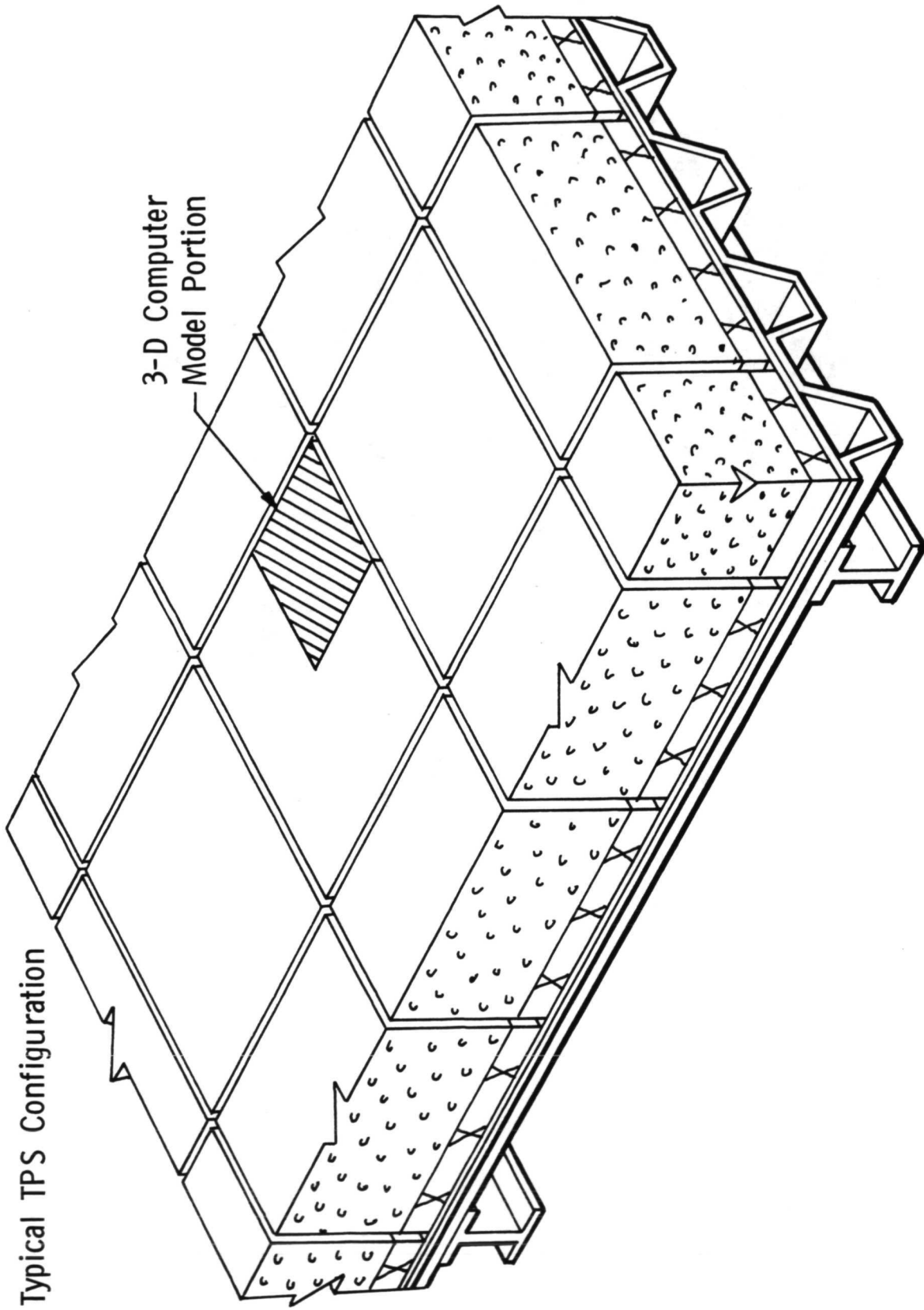
COMPUTER MODELS

(Figure 19)

Using the typical TPS configuration (Fig. 18), two-dimensional and three-dimensional finite element models have been constructed and used for analysis. As shown, the models include the coating, basic material, strain isolator, and the aluminum substructure. The characteristics of the current two-dimensional model are:

514	Node points
68	Axial and bending bars
899	Axial bars
52	Axial and shear plates
415	Shear plates

The three-dimensional model is constructed as follows:

Structural Element	Computer Finite Element	Number of Finite Elements
Coating	Isotropic plate	128
MAR-SI	Anisotropic tetrahedron	1280
Isolator	Anisotropic tetrahedron	320
Aluminum Skin	Isotropic plate	192
Aluminum Corrugations	Bending bars	72

144

COMPUTER MODELS

2-D Finite Element Computer Model
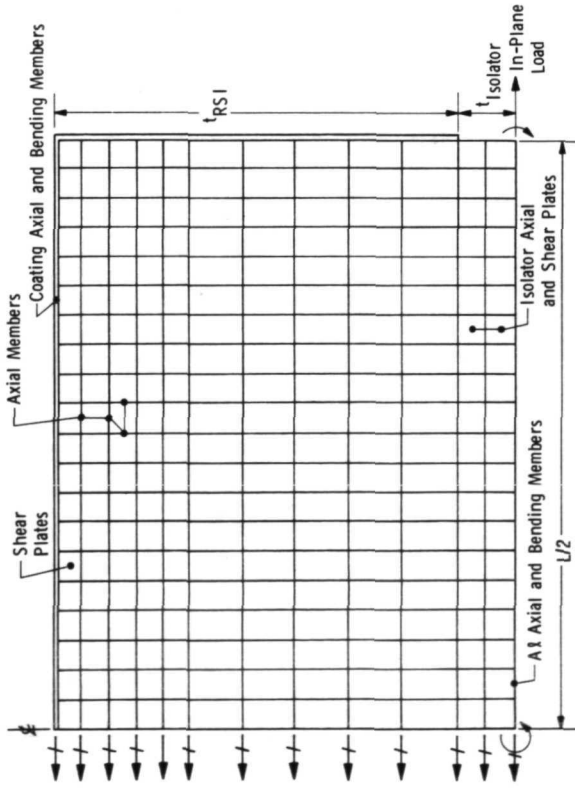
3-D Anisotropic Computer Model

Figure 19

145
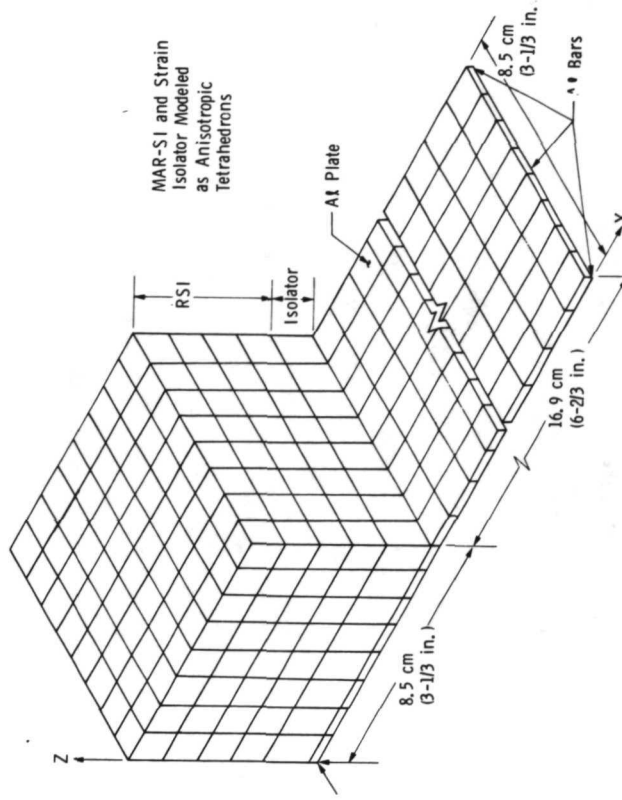
TILE TENSILE STRAIN vs ISOLATOR THICKNESS

(Figure 20)

Using the two-dimensional model, this figure is a plot of tensile strain vs isolator thickness for a tile 0.1695x0.1695x0.0508 m (6-2/3x6-2/3x2 in.). As shown in the figure, for a strain isolator thickness of 0.003175 m (1/8 in.), the strain in the tile is 0.11%.

TILE TENSILE STRAIN vs ISOLATOR THICKNESS

Thermal Loading
and Axial Loading -
- T_{Upper} = 1260°C (2300°F)
- T_{Lower} = 149°C (300°F)

Panel Thickness = 0.0508 m (2 in.)
Applied Aluminum Strain = 0.56%
Coating Properties:

E_c = 234x10^8 N/m^2 (3.4x10^6 psi)

α_c = 0.89x10^{-6} m/m/°C (0.5x10^{-6} in./in./°F)

0.1524x0.1524x0.0508 m
(6x6x2 in.) Tiles

MAR-SI ϵ_u

Tensile Strain, %

Isolator Thickness, m (in.)

Figure 20

147
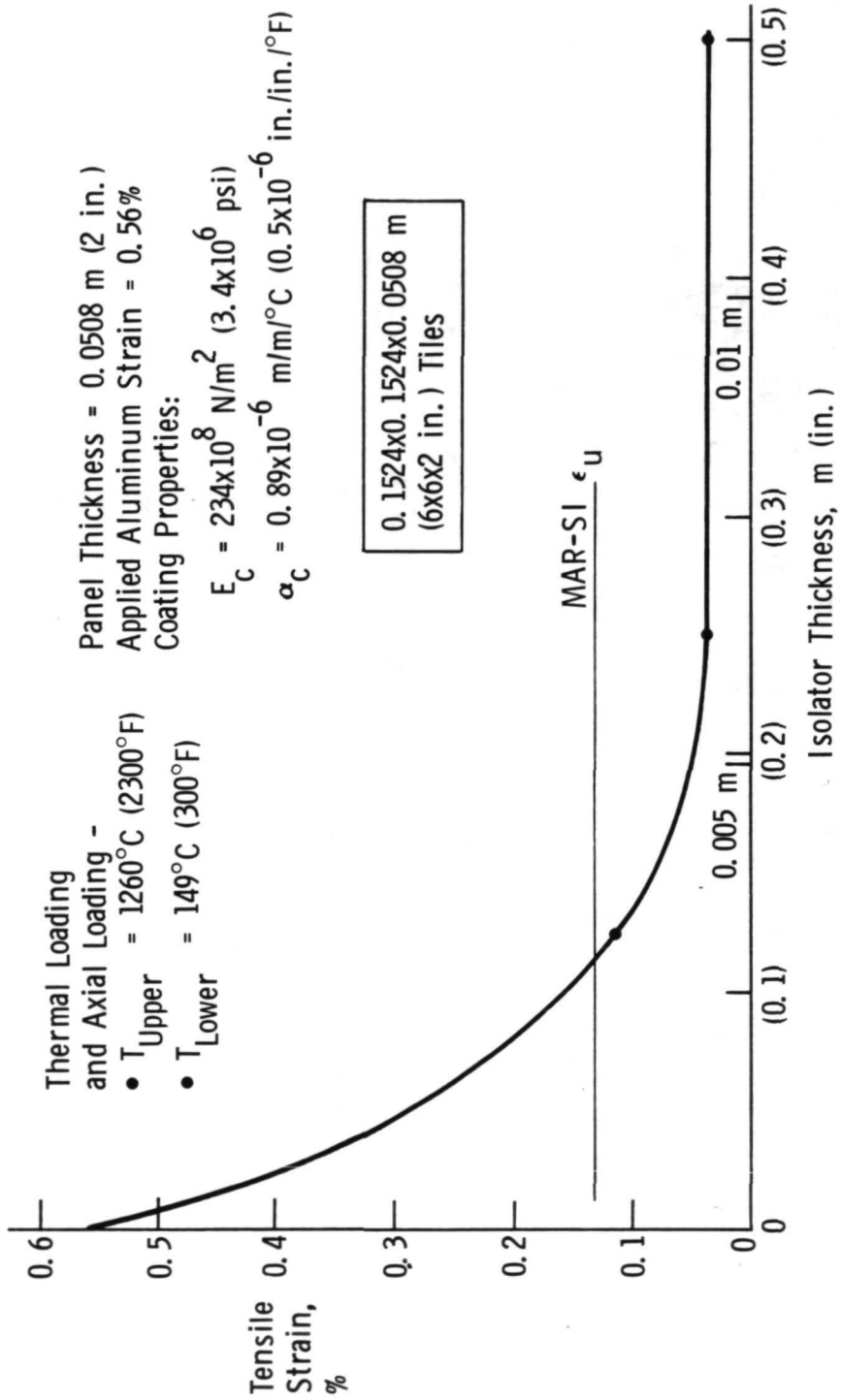
STRESSES ON SIDE OF 0.1524x0.1524x0.0508 m (6x6x2 in.) PANEL

(Figure 21)

The results of the analysis for the series 50 and 60 coatings indicate that the maximum stresses on the side of the MAR-SI tile are approximately equal for both coatings. As shown, a large amount of bending (and therefore a stress gradient) occurs in the series 50 coating (tension in one coating surface and compression in the other). There is essentially no bending or stress gradient in the series 60 coating at the location of maximum stress (tension in both coating surfaces).

As shown earlier, the αE of the series 60 coating is more compatible with the αE of the basic material; therefore, the tendency to crack due to thermal stresses on the side of the panels will be minimized. Also, test results presented earlier indicate that tiles with the series 60 coating do not have thermal stress cracks on the sides.

148

STRESSES ON SIDE OF 0.1524x0.1524x0.0508 m (6x6x2 in.) PANEL

Coating	E Modulus	Coefficient of Thermal Expansion	Maximum Stress on Panel Side	Remarks
Series 50	448×10^8 N/m^2 (6.5×10^6 psi)	3.24×10^{-6} m/m/°C (1.8×10^{-6} in./in./°F)	-34.5×10^5 N/m^2 (-500 psi) Inside Surface Coating 31.0×10^5 N/m^2 (450 psi) Outside Surface Coating	Bending
Series 60	234×10^8 N/m^2 (3.4×10^6 psi)	0.57×10^{-6} m/m/°C (0.32×10^{-6} in./in./°F)	31.0×10^5 N/m^2 (450 psi) Inside Surface Coating) 31.0×10^5 N/m^2 (450 psi) Outside Surface Coating	No Bending

Thermal Loading – Top Surface 1259°C (2300°F)
– Bottom Surface 149°C (300°F)

Figure 21

PROJECTED COST AND QUANTITY OF COATED MAR-SI TILES

(Figure 22)

Using the previously discussed material and coating developmental data for the production rates

of the present pilot plant, projected costs are defined. Cost and tile quantity are plotted

vs acceptance rates for uncoated and coated tiles. As shown, for a 90% acceptance rate, over

14,000 completed tiles can be produced in 1 year for a cost of approximately $3230/m^2 ($300/ft^2).

The same acceptance rate was applied to bare tiles before coating and to completed tiles. This

analysis permits using varying acceptance rates at each stage of production; such rates will

be used as additional production data become available.

150

PROJECTED COST AND QUANTITY OF COATED MAR-SI TILES

(Present Pilot Plant)

Figure 22

151
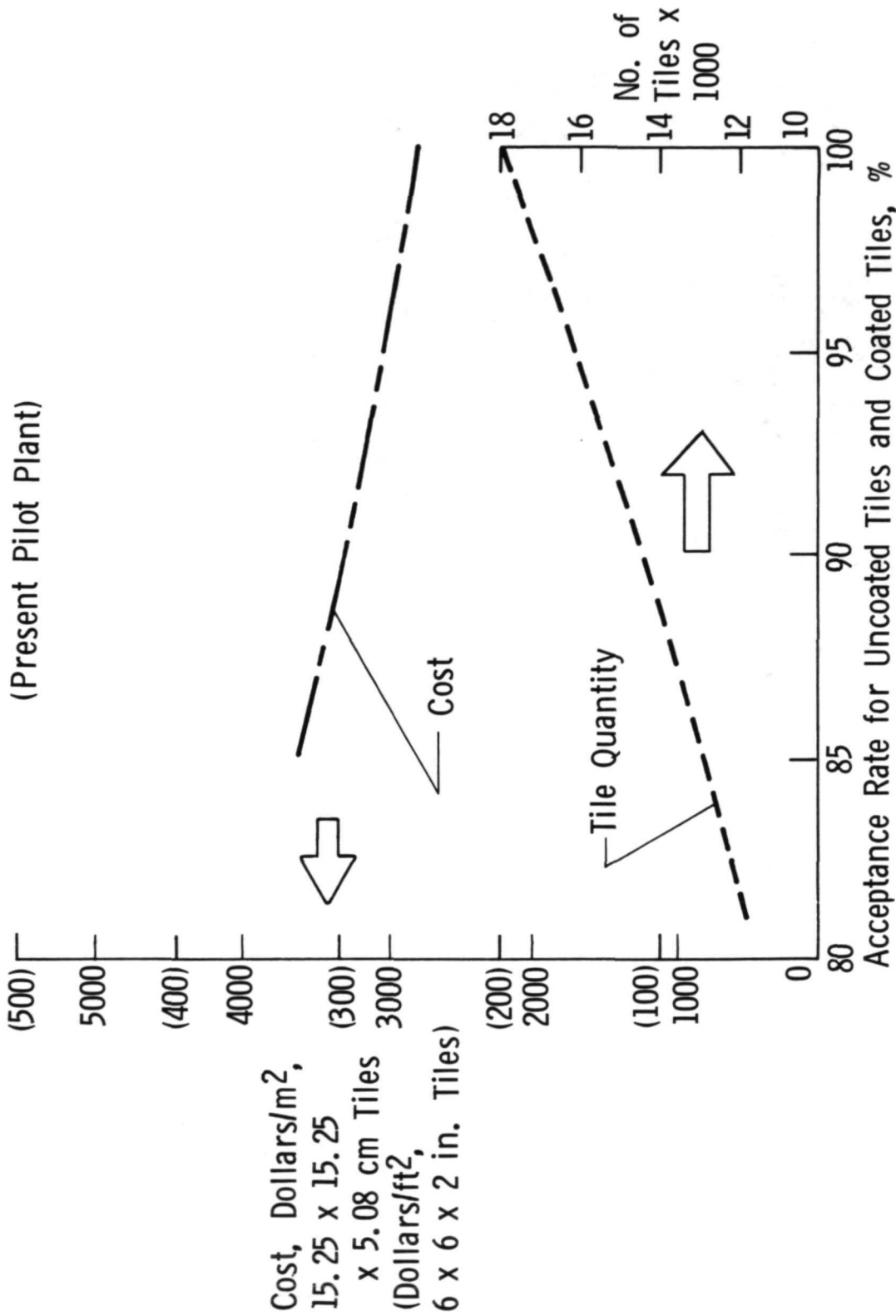
MAR-SI TECHNOLOGY STATUS

(Figure 23)

In conclusion, the MAR-SI technology status is presented. High thermal stability and low

thermal conductivity have been obtained, while providing a thermal shock stability with the

MAR-SI material and coating (series 60). The figure also shows the tests to be conducted at

the various NASA centers.

152

MAR-S1 TECHNOLOGY STATUS

High Thermal Stability - Measured Values of Thermal Conductivity to 1454°C (2650°F)

- Cyclic Tests to 1413°C (2575°F)

Low Thermal Conductivity

Thermal Shock Ability - with Series 60 Coating

Demonstrated Reuse - Waterproof and High Emissivity Coating - 104 cycles

Low Cost - Material ≈ $9.03/kg ($4.10/lb)

Pilot Plant Operation

Additional Test Evaluations

Dynamic Seal - Plasma Arc (MSC)

Salt Spray (LRC, KSC)

Plasma Arc Specimens - 10.16 cm (4 in.) Diameter (MSC, ARC)

Panels - Radiant and Acoustic (MSC)

Figure 23

153

6

SILICA REUSABLE SURFACE INSULATION IMPROVEMENT RESEARCH

by

H.E. Goldstein, M. Smith, D. Leiser, V. Katvala, and D. Stewart

Ames Research Center
Moffett Field, California
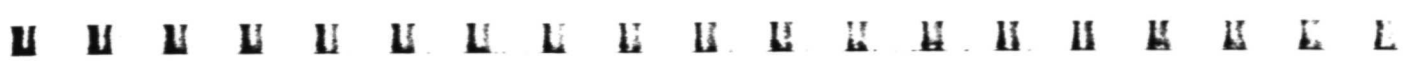
INTRODUCTION

(Figure 1)

Eighteen months ago, Ames Research Center began a research program to study means for improvement of Reusable Surface Insulation (RSI) materials under the auspices of the NASA Space Shuttle Materials Working Group. At the same time a fiber improvement program at Lewis Research Center and general RSI research programs at Langley Research Center and Marshall Space Flight Center were initiated. The Ames Research Center objectives were clearly defined at that time and they have not changed since. They are as follows:

· Gain an understanding of RSI fabrication to be better able to evaluate the manufacturer's RSI materials proposed for Space Shuttle.

· Develop RSI improvements that can be utilized by the manufacturers.

· Study the effects of process and composition variables on the response of RSI to convective heating environments.

Both mullite and silica materials have been investigated, but most of the effort has been concentrated on silica. This paper presents the results of the silica work conducted to date. Figure 1 outlines the subject areas that will be discussed.

156

SILICA REUSABLE SURFACE INSULATION IMPROVEMENT RESEARCH

- FIBER CHARACTERIZATION

- FABRICATION PROCESS

- PHYSICAL PROPERTIES

- THERMAL RESPONSE

Figure 1

157

SIGNIFICANT FIBER PROPERTIES

(Figure 2)

Early in this research program, it was determined that the critical RSI component raw material was the fiber. Initially, several silica fibers including Astroquartz (J.P. Stevens), AVCERAM CS (American Viscose), and Microquartz 108 (Johns Manville) were considered for use. The first two fibers devitrified below 1364°K (2000°F) and had relatively large diameters (5 µm). As a result of these factors, RSI tiles that were fabricated with these fibers were not acceptable. The Microquartz, however, could be utilized as shown by LMSC (reference 1) and GE (reference 2), although the results were variable Zaplatinsky (reference 3) and Mueller et al. (references 4-7) found that different lots of Microquartz fibers have distinctly different shrinkage and devitrification behavior. The better Microquartz fibers were stable up to 24 hours at 1533°K (2300°F) (references 3-5).

Attempts to determine how the fiber characteristics relate to the final tile properties have been considered in the Ames program. The studies have shown that the important fiber properties are those listed in this figure. They are listed in their order of significance relative to making acceptable tile by the Ames Process. The relative importance of these properties is dependent on the tile fabrication process. Chemical composition is the most critical property because the concentration of impurities in the fiber is the primary determinent of both fiber shrinkage and devitrification rates. The results have shown that fibers that exhibit significant devitrification at temperatures below 1478°K (2200°F) make tiles of poor quality. Shrinkage alone is not necessarily bad in terms of optimum tile properties. The major problem is that the amount of shrinkage may differ for each lot of acceptable fiber and, therefore, require variations in the process in order to obtain consistent tile properties. Surface chemical properties that appear to be important are the trace impurity levels on the surface which affect the devitrification and shrinkage rates. Other surface properties such as surface area and surface free energy may also be important. The wetting properties of the fiber affect slurry viscosity, pH, and other processing parameters important in fabrication of RSI tile. The amount of fiber chopping required and the mixing time are, of course, related to initial fiber length.

158

SIGNIFICANT FIBER PROPERTIES

- CHEMICAL COMPOSITION

- DEVITRIFICATION RATE

- SHRINKAGE

- SURFACE CHEMISTRY

- WETTING PROPERTIES

- FIBER LENGTH

Figure 2

159

SILICA FIBER CHARACTERIZATION

(Figure 3)

In order to characterize Microquartz 108, a number of methods were utilized including detailed chemical analysis, differential thermal analysis (DTA), thermal gravimetric analysis (TGA), surface area measurement by nitrogen absorption (BET Method), devitrification studies, shrinkage studies, etc. This table shows the results of some of these tests on a number of fiber lots.

The eight fiber lots listed are some of those with which Ames has had experience and are grouped into three different classifications. Other lots of fiber, not included, could be classified in the same manner. The old-type fibers, Lots 1437, 1466, and 1986, have on the order of a half percent alkali and a half percent of alkaline earth impurities. The Type C and Lot 2102 fibers, developed under contract to LeRC (reference 8), have little alkali, but still have over a quarter of a percent of alkaline earth impurities. The best fibers include Lots 2148, 2155, and 2083. Lot 2083 was used as a standard and is one of those used by Lockheed Missiles and Space Company to fabricate LI-1500 since May 1971. It was supplied to Ames by Mr. Robert Beasley of LMSC. Each of these better lots is low in alkali and alkaline earth impurities. As subsequent data will show, this is the most important difference between fiber lots. However, there are a number of other lot-to-lot variations that are also shown to be important.

An assessment of the overall quality of the RSI tiles that were fabricated from each fiber lot is listed in the last column in this figure. This assessment is based on stability to devitrification and shrinkage and the physical properties of the tile. The quality of the tile generally correlates with the bulk chemical composition of the fiber. Alkali or alkaline earth concentrations above 0.05 percent increase the devitrification rate significantly. Shrinkage is also related to impurity level and will be discussed in subsequent figures. DTA, TGA, and fiber surface area show no correlation with the tile quality. Very slight variations in surface chemistry, below the analysis detection limits, appear to have a significant effect on devitrification and shrinkage, and will be discussed subsequently.

160

SILICA FIBER CHARACTERIZATION

FIBER LOT	PERCENTAGE OF OXIDE			WEIGHT LOSS BY TGA AT 1273°K (1768°F)	SURFACE AREA M²/g	TIME TO 5% CRYSTALLINITY AT 1533°K (2300°F) HOURS	QUALITY OF FABRICATED TILE
	ALKALI Na₂O, K₂O	ALKALINE EARTH CaO, MgO, SrO	TOTAL IMPURITIES				
1437, 1466, [1986]	0.4–0.9	0.2–0.80	0.6–1.6	[5.0]	[3.0]	[<0.25]	[POOR]
TYPE C, (2102)	0.01–0.05	0.25–0.5	0.35–0.70	(9.0)	(2.4)	(1.0)	FAIR
2083	0–0.03	0.03	0.18	8.5	3.6	<16	STANDARD*
2148	0.04	0.04	0.30	6.0	32.1	16	COMPARABLE
2155	0.06	0.02	0.30	7.0	5.5	6.0, 16**	COMPARABLE

*LMSC LI 1500
**CLEANED FIBER
ND NOT DETECTED

Figure 3

161

CRYSTALLIZATION AND SHRINKAGE OF AS RECEIVED SILICA FIBER AT 1533°K (2300°F)

(Figure 4)

As previously stated, shrinkage, shrinkage and devitrification of Microquartz 108 fiber are both directly related to impurity level of the fiber. Ormiston et al. (reference 9) showed that for LI-1500, the tile shrinkage rate could be correlated with a simple equation showing that the change in fiber length is proportional to the ratio of surface tension to viscosity for a silica glass fiber. Mueller et al. (reference 7) showed that the apparent flow and devitrification rate of fibers increases with increasing impurity level. Zaplatinsky (reference 3) showed that once silica fiber devitrifies, no further flow occurs and, therefore, shrinkage essentially stops. The relationship between the above results and the stability of silica RSI tile is shown in this figure and subsequent data. The shrinkage and crystallinity versus time at 1533°K (2300°F) are plotted for a relatively pure fiber, Lot 2148, a less pure fiber, Lot 2102, and a very impure fiber, Lot 1986. Each fiber was water cast using deionized water, into a 15 x 15 x 7.5 cm (6 x 6 x 3 inch) block and then dried. Initial density of the dried compact was 192 kg/m^3 (12 lb/ft^3). Cubes 3.8 cm (1.5 inch) on a side were cut from each block and fired for from one to four hours. After firing, shrinkage was determined from dimensional change and crystallinity was determined by X-ray diffraction (XRD) using the technique described by Mueller et al. (reference 5). Other quantitive XRD techniques were tried (reference 5) and yielded essentially the same results. Sample size was found to have no effect on either shrinkage or devitrification.

The expected relationship between devitrification and impurity level is observed for the fibers tested. Lot 1986 devitrified most rapidly and Lot 2148 the least rapidly. Note that the shrinkage of Lot 1986 virtually stops after two hours, while Lot 2148 shrinkage continues up to 40 hours. Lot 2102 also shrinks rapidly at first and then very slowly when significant crystallinity is obtained at two hours. From these results, it is apparent that the purer fibers are most stable to devitrification but will continue to shrink due to viscous flow. This slow viscous flow is probably a significant factor in the binding obtained during fabrication of RSI tile utilizing good fiber. The least pure fibers shrink much more rapidly due to lower viscosity, but stop shrinking when significant devitrification has occurred.

These results coupled with the chemical analysis of figure 3 indicate that only fibers such as Lot 2148 with less than 0.06 percent alkali or alkaline earth impurity are stable enough to resist devitrification for times of the order of ten hours at 1533°K.

162

CRYSTALLIZATION AND SHRINKAGE OF AS RECEIVED SILICA FIBER AT 1533°K (2300°F)

Figure 4

163
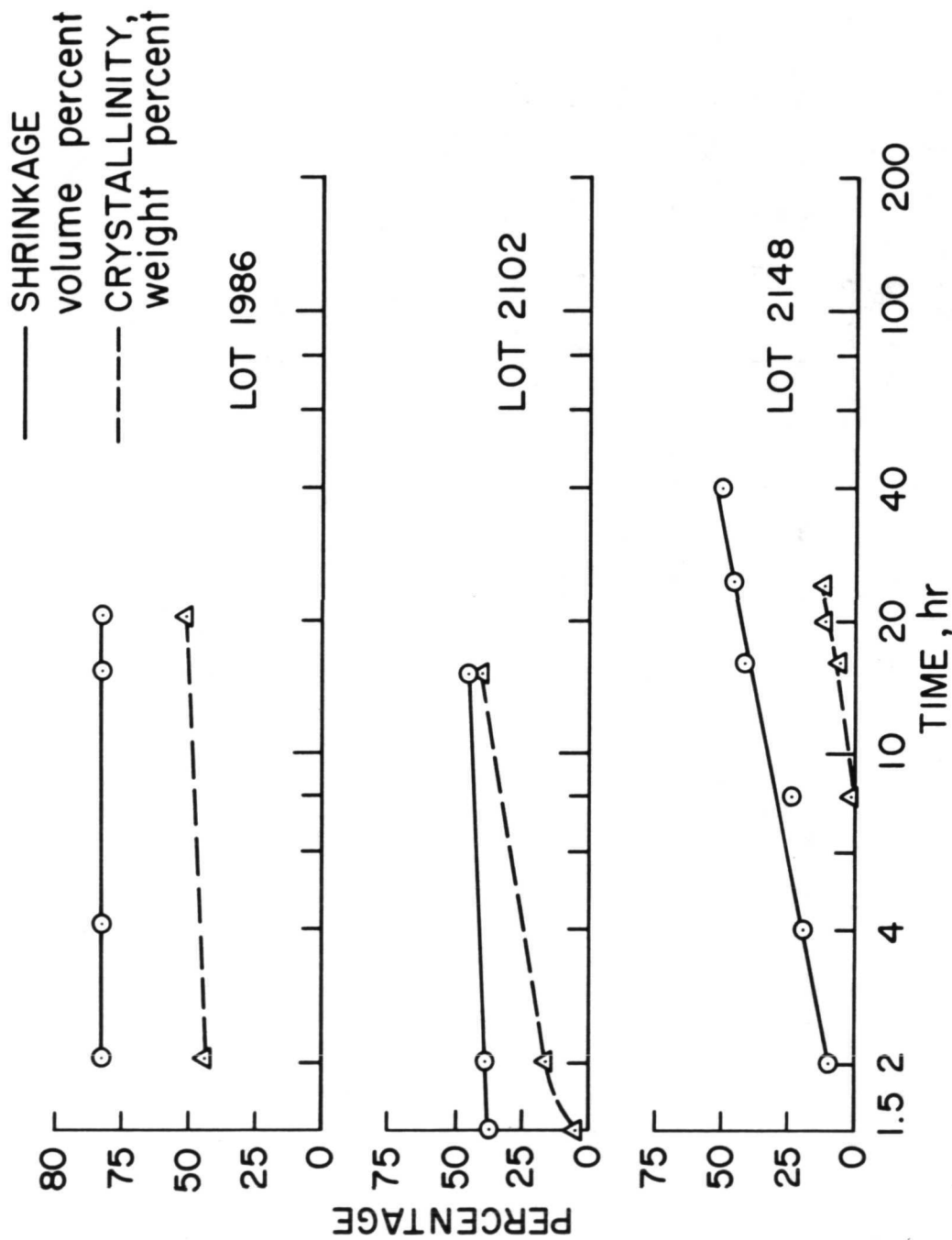
CRYSTALLIZATION AND SHRINKAGE OF LOT 2148 SILICA FIBER AS A FUNCTION OF TEMPERATURE

(Figure 5)

Both devitrification and shrinkage rates are functions of temperature. This figure shows percentages of devitrification and shrinkage at three different temperatures. This type of data is required to determine the exact molding procedure and firing cycle for each lot of fiber. At 1412°K (2100°F), little shrinkage or devitrification is measured after 200 hours at temperature. The shrinkage measured in this manner is not representative of the final tile stability. Once a tile has been bonded and fired, the shrinkage rate is much lower, as will be shown subsequently. The devitrification rate of fiber is generally about the same as the devitrification rate of the tile. If a fiber is not stable to measurable devitrification for at least eight hours at 1533°K (2300°F), it will probably not be stable in the tile with respect to the MSC Area 2P reentry environments for 100 flights.

164

CRYSTALLIZATION AND SHRINKAGE OF LOT 2148 SILICA FIBER AS A FUNCTION OF TEMPERATURE
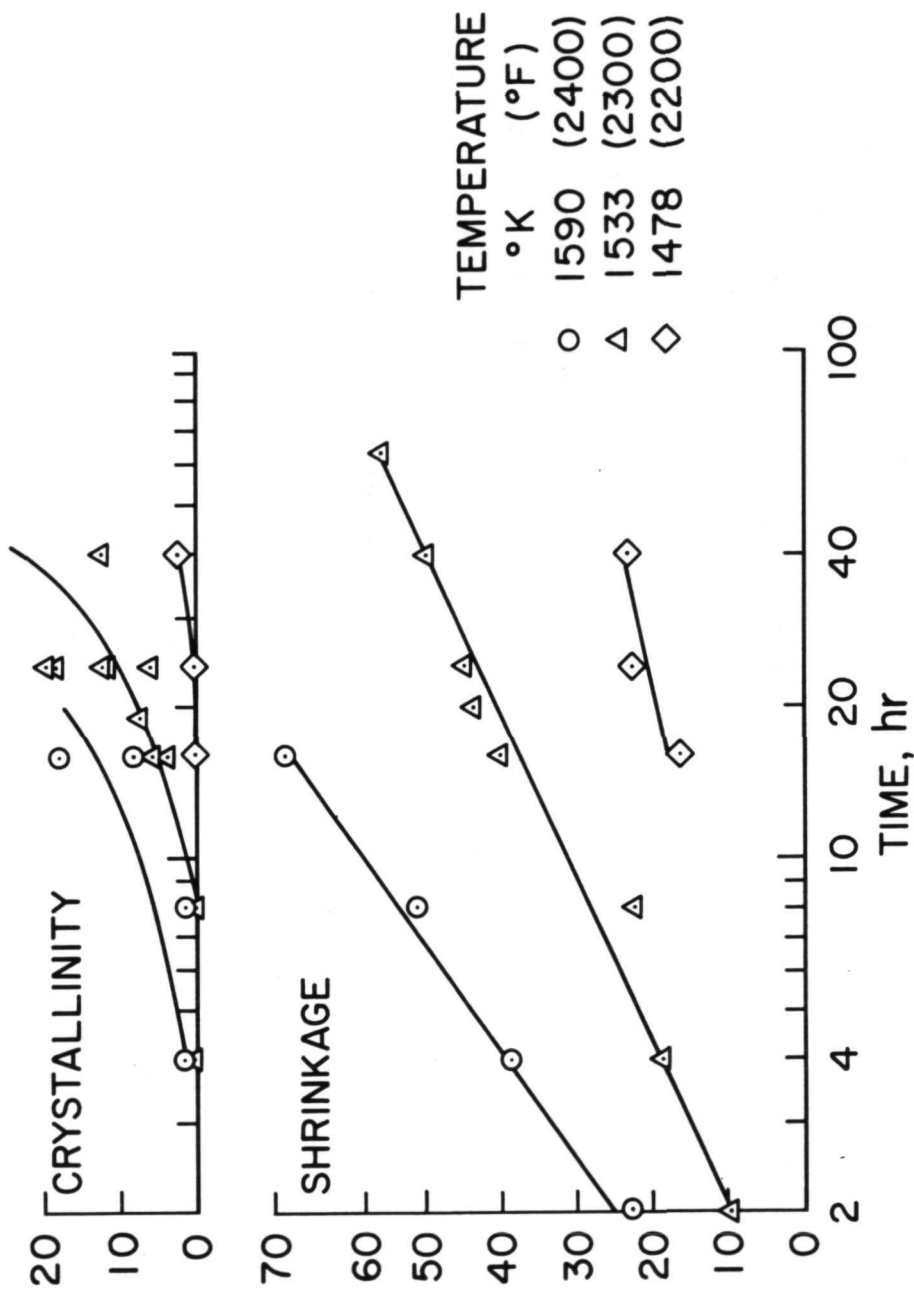
Figure 5

165

EFFECT OF WASHING ON CRYSTALLIZATION OF SILICA FIBERS AT 1533°K (2300°F)

(Figure 6)

The major cause of both high shrinkage and the high crystallization rate of fiber is the gross impurity level. A second somewhat lesser but still important effect on stability is the level of surface contamination of the fiber. Crystallization of amorphous materials generally starts from nucleation sites on the surface. Therefore, surface contamination can play an important role in the tendency toward devitrification. A series of experiments was performed in which acids and bases were used to wash the fiber and then the crystallization and shrinkage were measured as before. Based on these tests, a hydrochloric acid wash procedure for the fibers was adopted. It consists of alternate washes with HCl (pH = 3) and deionized water (pH = 6). The effects on fiber crystallization are shown in this figure.

The crystallization rate of even an impure fiber (Lot 2102) is decreased. Greater improvement is obtained with Lot 2155. The improvement is small for Lot 2148. Chemical analysis before and after washing showed no apparent change in fiber bulk composition for fiber Lots 2102 and 2155. These data indicate that even small amounts of impurities (not detectable by the analyses used) may provide nucleation sites for initiation of devitrification. Another possibility is that washing alters the surface chemistry or character of the fibers in such a way as to retard devitrification.

166

EFFECT OF WASHING ON CRYSTALLIZATION OF SILICA FIBERS
AT 1533°K (2300°F)

WASHED UNWASHED

LOT 2102

LOT 2155

LOT 2148

PERCENTAGE

TIME, hr

Figure 6

167
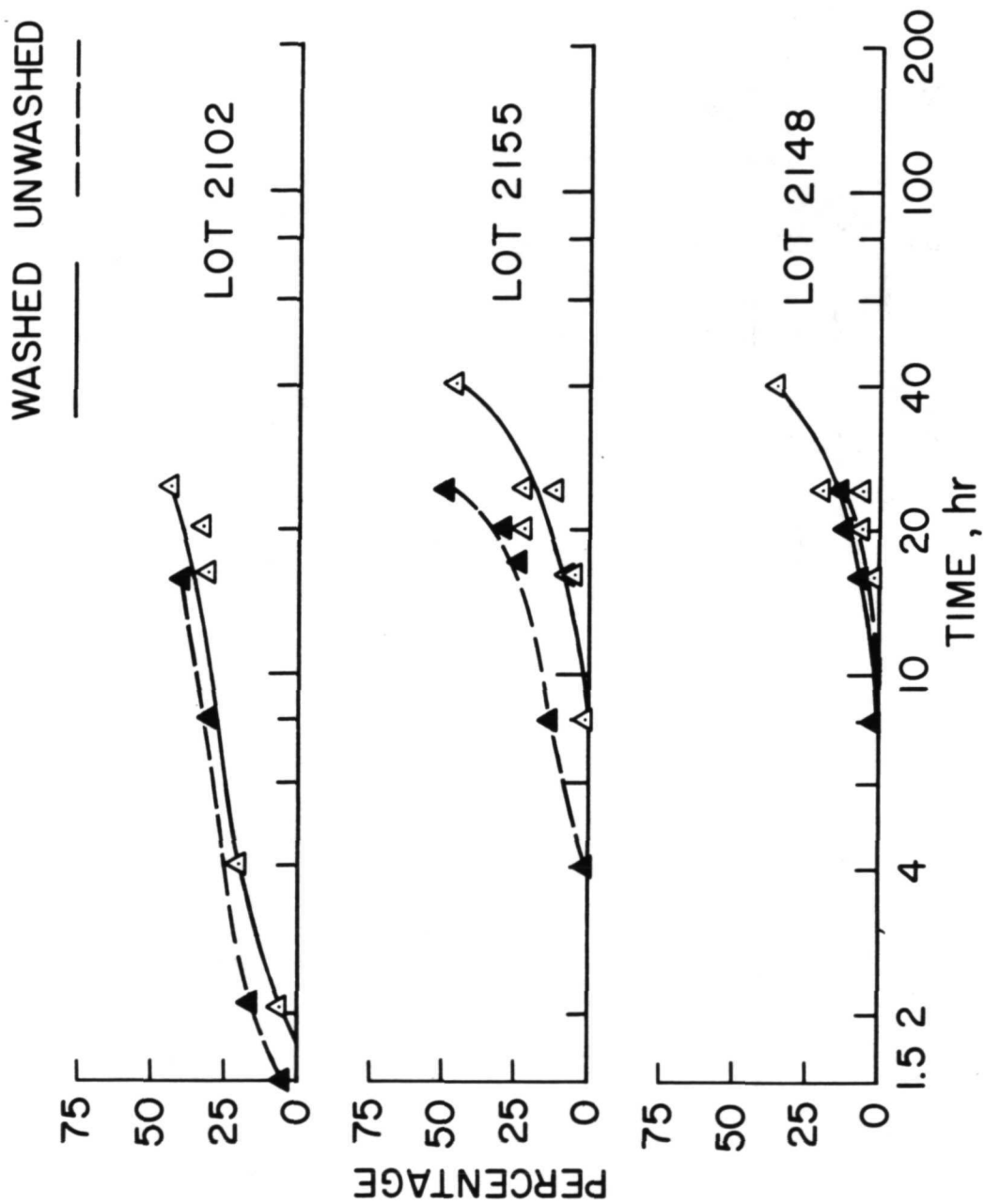
COMPARISON OF SILICA RSI TILES MADE WITH WASHED AND UNWASHED FIBER

(Figure 7)

This figure graphically illustrates the effect of washing on shrinkage for Lot 2155 fiber. The shrinkage of tile made with unwashed fiber was nearly twice that of tile made with washed fiber. The result was the same for Lot 2102. A possible explanation for this behavior is that removal of alkali and alkaline earth impurities from the surface causes a significant lowering of the fiber surface tension, thus decreasing the driving force to shrinkage. An increase in surface viscosity may also be significant, though bulk viscosity is probably more important. The results presented in figures 6 and 7 show that each lot of fiber responds differently to washing.

168

COMPARISON OF SILICA RSI TILES MADE WITH WASHED AND UNWASHED FIBER
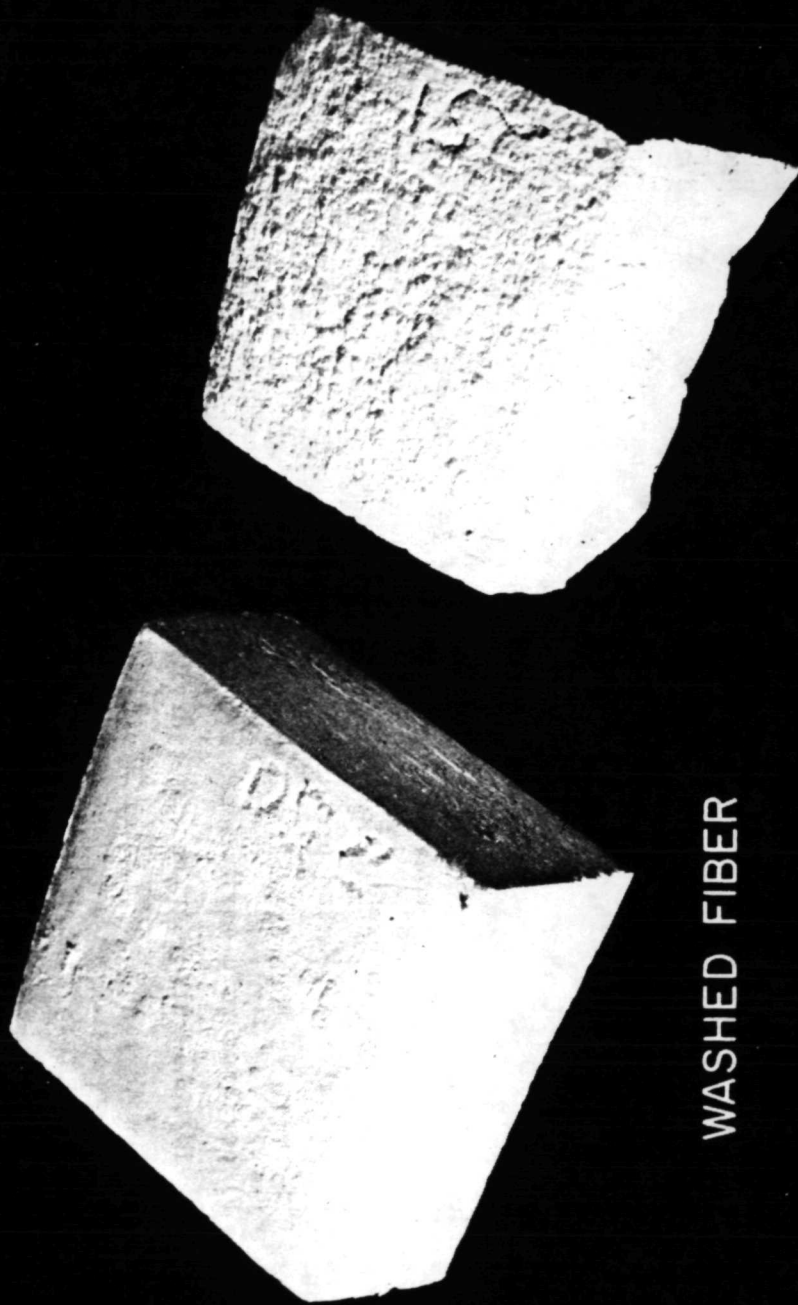
WASHED FIBER

UNWASHED FIBER

Figure 7

AMES SILICA RSI FABRICATION PROCESS

(Figure 8)

This figure is a schematic representation of the Ames silica RSI fabrication process. The process is inherently simple, and requires three days to fabricate a finished 15 x 15 x 7.5 cm tile ready for coating. Great care must be taken to avoid contamination of the raw materials during the process. All utensils and mixing vessels are polyethylene or stainless steel and only deionized water is used in any step of the process. The fibers are first washed in hydrochloric acid and then rinsed using pure nitrogen as the agitating agent. This may be done several times depending upon the fiber lot. The binder, which is usually 3 to 5 percent Cab-o-sil and 2 to 4 percent reagent grade starch and ammonia, is dispersed in a high speed mixer, then blended with the drained fibers and water in a V-blender where the pH is adjusted to 9.0 with ammonia. An intensifier bar in the V-blender is used to break up fiber clumps. The slurry is poured into a mold for either single direction or multi-direction pressing (to be discussed subsequently) and rapidly pressed into shape. The tile is then dried in an oven for 18 hours. The temperature is raised at the rate of 12°K (20°F) per hour to a maximum temperature of 457°K (300°F) and held for the remainder of the cycle. The tile is taken directly from the drying oven and placed in a firing furnace and fired using the cycle shown in figure 9. After firing, the tile is machined to final dimensions.

The process described in this figure is not fixed and is varied for different fibers as necessary. Among the possible process improvements being studied are variations in the fiber washing parameters such as acid type and concentration, and washing temperature; variations in the fabrication steps such as drying cycle and time, binder additives, opacifiers, fiber pretreatments, slurry viscosity, etc. Firing cycle variations are discussed with the next figure.

170

AMES SILICA RSI FABRICATION PROCESS

COLLOIDAL SILICA, ADDITIVES, DEIONIZED WATER

FIBER, DEIONIZED WATER AND ACID

BINDER MIXING

WASHING

BLENDING

MOLDING

DRYING

MACHINING
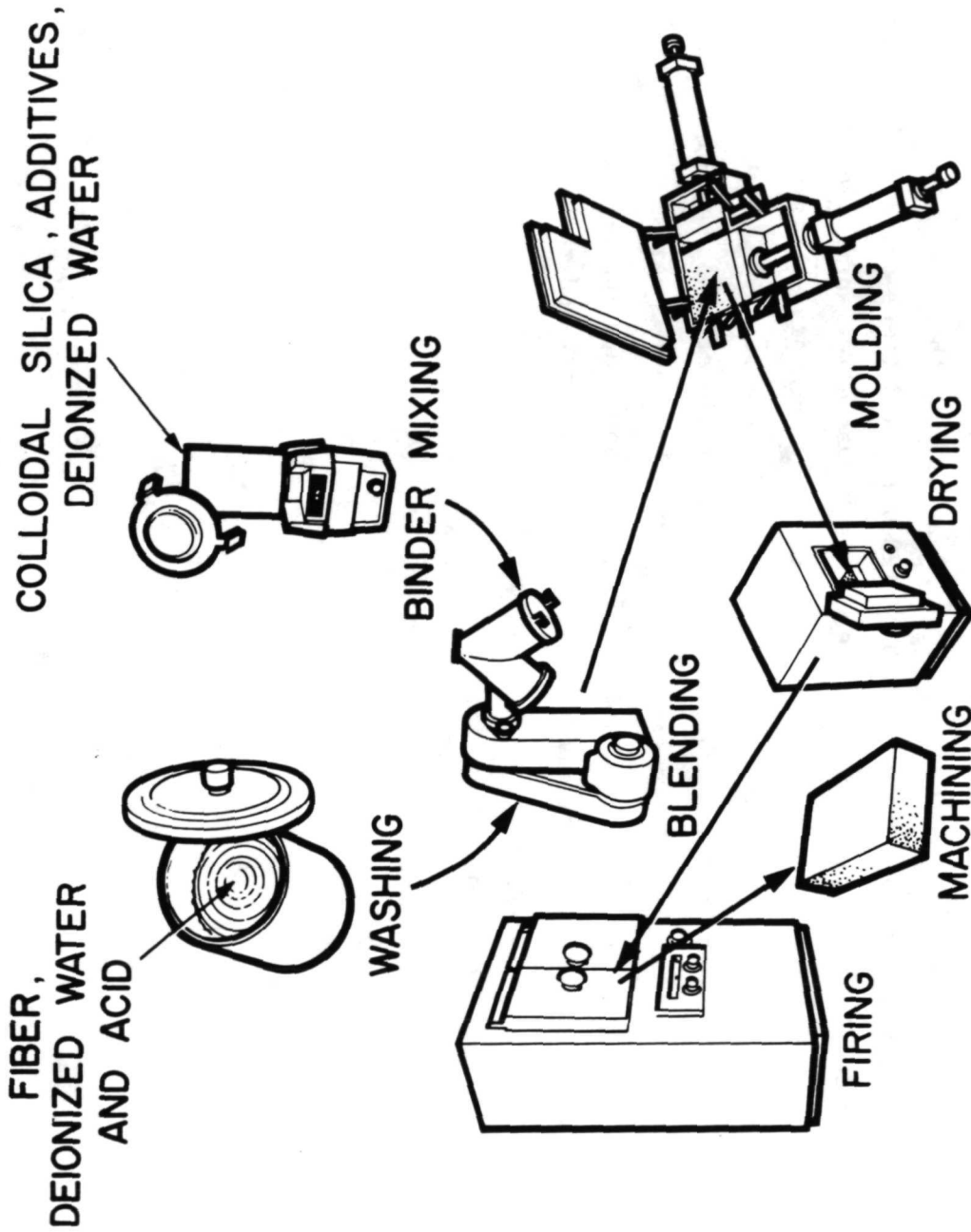
FIRING

Figure 8

FIRING CYCLE FOR SILICA RSI

(Figure 9)

This figure illustrates the range of firing cycles currently being used to cure silica RSI tiles. A temperature rise rate of 167°K (300°F)/hr or less is required to avoid cracking and warping the 15 x 15 x 7.5 cm tiles. For larger tiles, slower heating may be required. The time-at-temperature and the exact maximum firing temperature are dependent on the fiber used. For example, fiber Lot 2155 is fired for 1/2 hour at 1500°K (2250°F). The firing cycle for each fiber must allow sufficient time for sintering and stabilization relative to shrinkage while not allowing excessive shrinkage or any devitrification of the tile. The starch burns out at a temperature of about 800°K, leaving a pure silica unbonded structure. At about 1533°K (2300°F), fiber-to-fiber sintering occurs at a fairly rapid rate. It appears that the final tile properties are related to fiber-fiber sintering at least as much as they are to fiber-to-binder sintering. Shrinkage and sintering during firing are much more rapid with binder than without, allowing shorter firing times and thus, increasing long term stability of the tile. It appears from recent data that a substantial increase in tile strength can be obtained by optimization of the firing cycle.

172

FIRING CYCLE FOR SILICA RSI
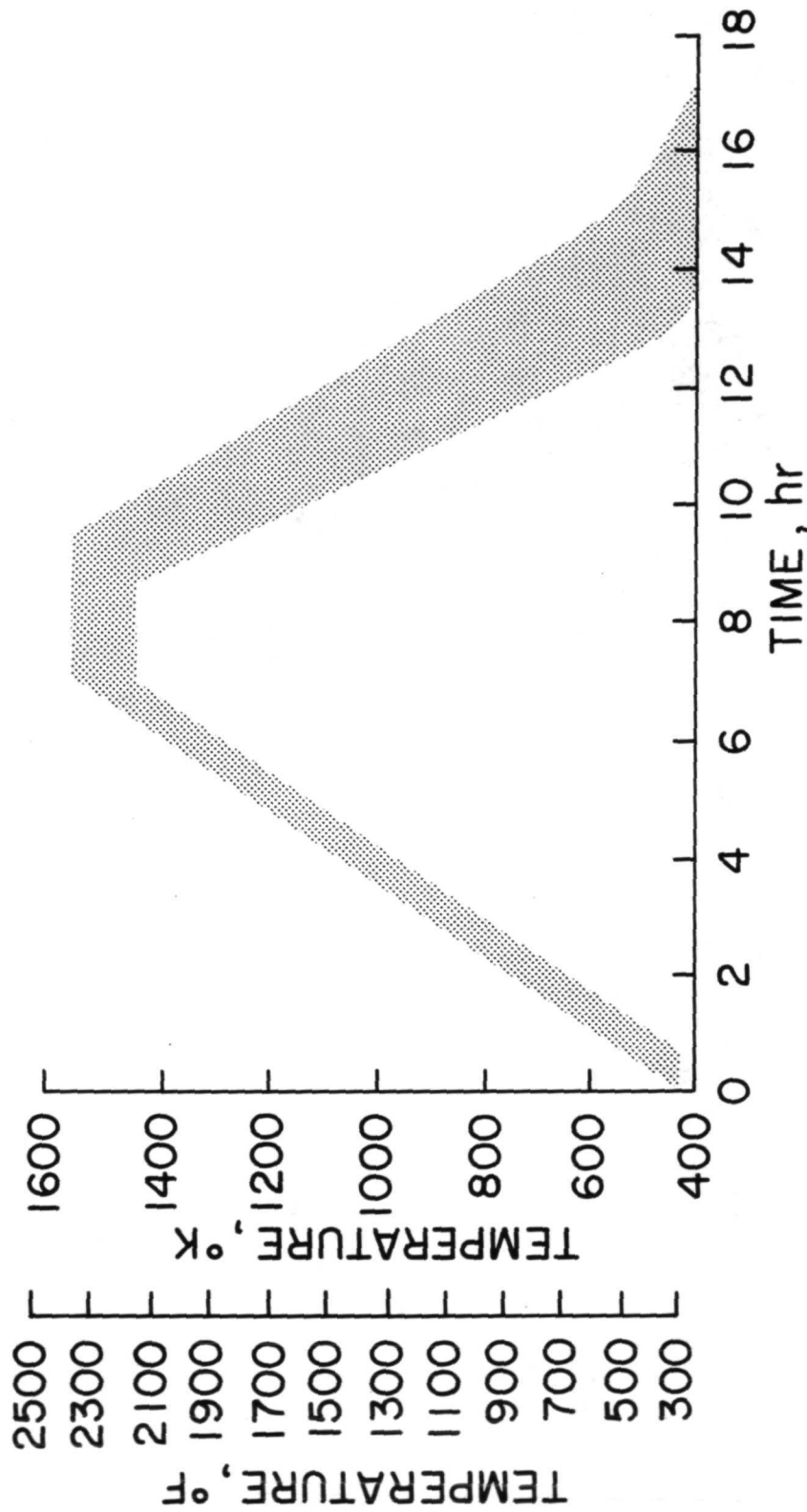
Figure 9

SILICA RSI TILE AT DIFFERENT STAGES OF FABRICATION

(Figure 10)

This figure shows a tile after drying, firing, and machining. In general, shrinkage during firing is 25-45 percent by volume. Approximately 0.5 cm of material is machined off the tile to obtain the finished size. The tile can be reimpregnated with binder to increase strength and refired with only a few percent of additional shrinkage. Warpage during firing can be a significant problem because the tile has essentially no strength at the firing temperature. Temperature gradients in the tile are likely to cause warping. Warping can also occur due to sagging of an unsupported tile during firing.

174

SILICA RSI TILE AT DIFFERENT STAGES OF FABRICATION

MOLDED AND DRIED

FIRED
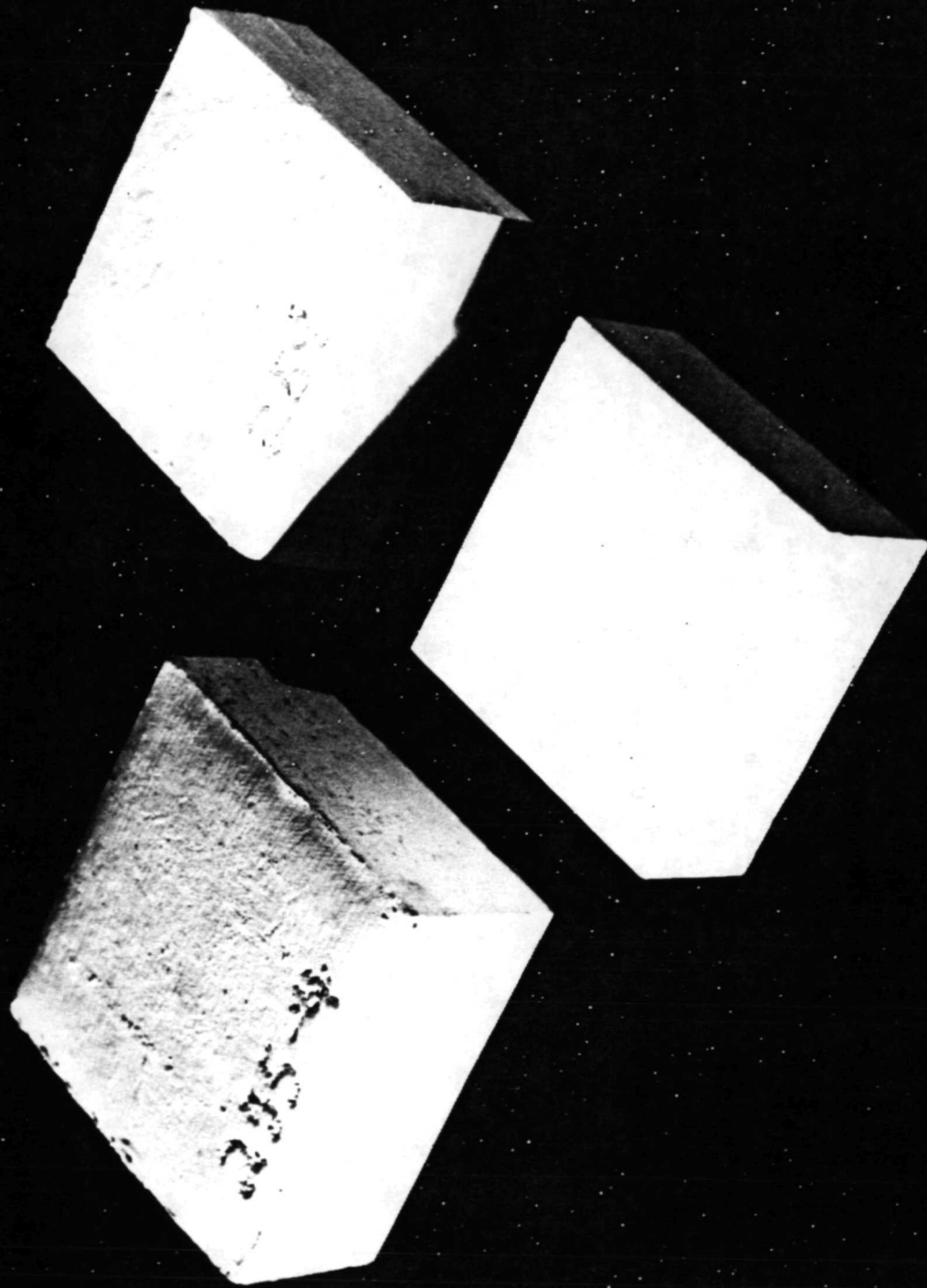
MACHINED TO FINAL DIMENSIONS

Figure 10
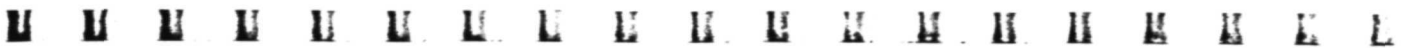
SILICA RSI TILES REIMPREGNATED WITH COLLOIDAL SILICA BINDERS AND FIRED

(Figure 11)

In order to increase tile strength, experiments have been performed using colloidal silica at varying percentages as a reimpregnant for the tile. A significant, but currently not understood result, is shown in this figure. Cab-o-sil tends to harden the tile and increase strength slightly. Ludox AS causes severe shrinkage and devitrification of the tile. Both materials are extremely pure colloidal silicas. Further studies are being carried out to determine the effect of reimpregnation with binder on strength and thermal stability of tile.

SILICA RSI TILES REIMPREGNATED WITH COLLOIDAL SILICA BINDERS AND FIRED
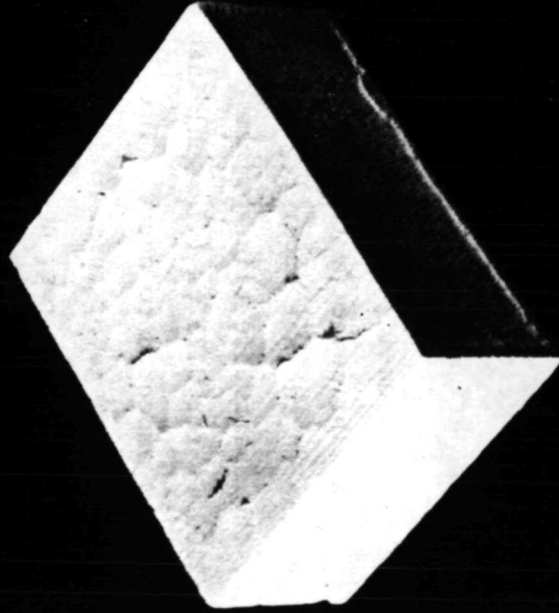
LUDOX AS
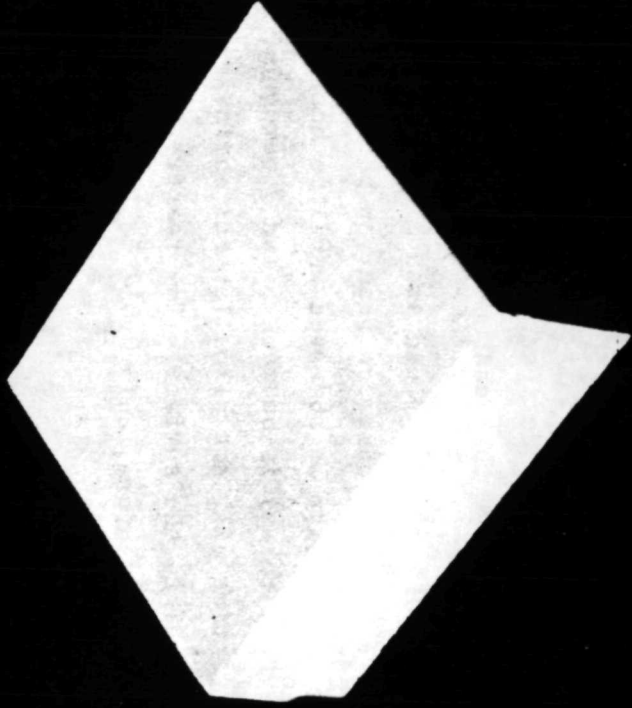
CAB-O-SIL

Figure 11

177
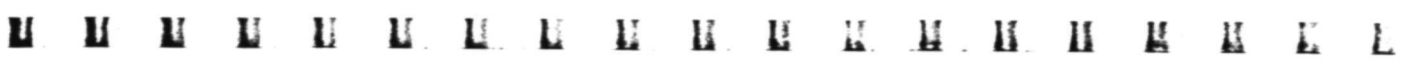
CRYSTALLIZATION AND SHRINKAGE OF SILICA RSI TILE AT 1533°K (2300°F)

(Figure 12)

This figure shows the volume percent shrinkage and percent crystallinity as a function of time for LI-1542 and Ames fabricated silica RSI at 1533°K (2300°F). The Ames tiles were made with fiber Lots 2148 and 2155, and the resulting materials are comparable to LI-1542. The Ames RSI shows somewhat less shrinkage, whereas the LI-1542 is more resistant to devitrification.

An arrow is shown at nine hours, which corresponds to the time in 100 flights that the surface of the shuttle heat shield will be above 1500°K (2250°F) in the NASA-MSC defined Area 2P trajectory. Using these data, the maximum amount of crystallinity and shrinkage that can occur on the shuttle in the area just below the coating can be estimated. No crystallinity is observed until 16 hours. At nine hours the linear shrinkage (volume shrinkage divided by three) is between 5 and 7 percent. Since the colder tile beneath the hot outer region and dense coating will not allow lateral shrinkage except at the corners, the observable tile shrinkage will be normal to the surface. The temperature is only above 1413°K (2100°F) for 0.25 cm (.1 inch) into the tile. Therefore, only 0.017 cm (.007 inch) dimensional change can be expected to occur. This amount of shrinkage is difficult to observe since the coating surface roughness is of this order. However, rounding of the corners is great enough to be observed. At higher temperatures, above 1561°K (2350°F) the effects of shrinkage may be more significant.

A set of experiments performed on early tiles fabricated with fiber Lot 2102 showed that in two hours at 1533°K (2300°F), no significant shrinkage occurred but the tile was 60 percent crystalline. In a few thermal cycles, the samples simply crumbled due to the alpha-beta cristobalite transformation. This result emphasizes the fact that stability relative to crystallization is the critical requirement for silica RSI. The exact amount of crystallinity that can be tolerated in processing and in the shuttle environment is not known, however, and must be determined.

178

CRYSTALLIZATION AND SHRINKAGE OF SILICA RSI TILE AT 1533°K (2300°F)
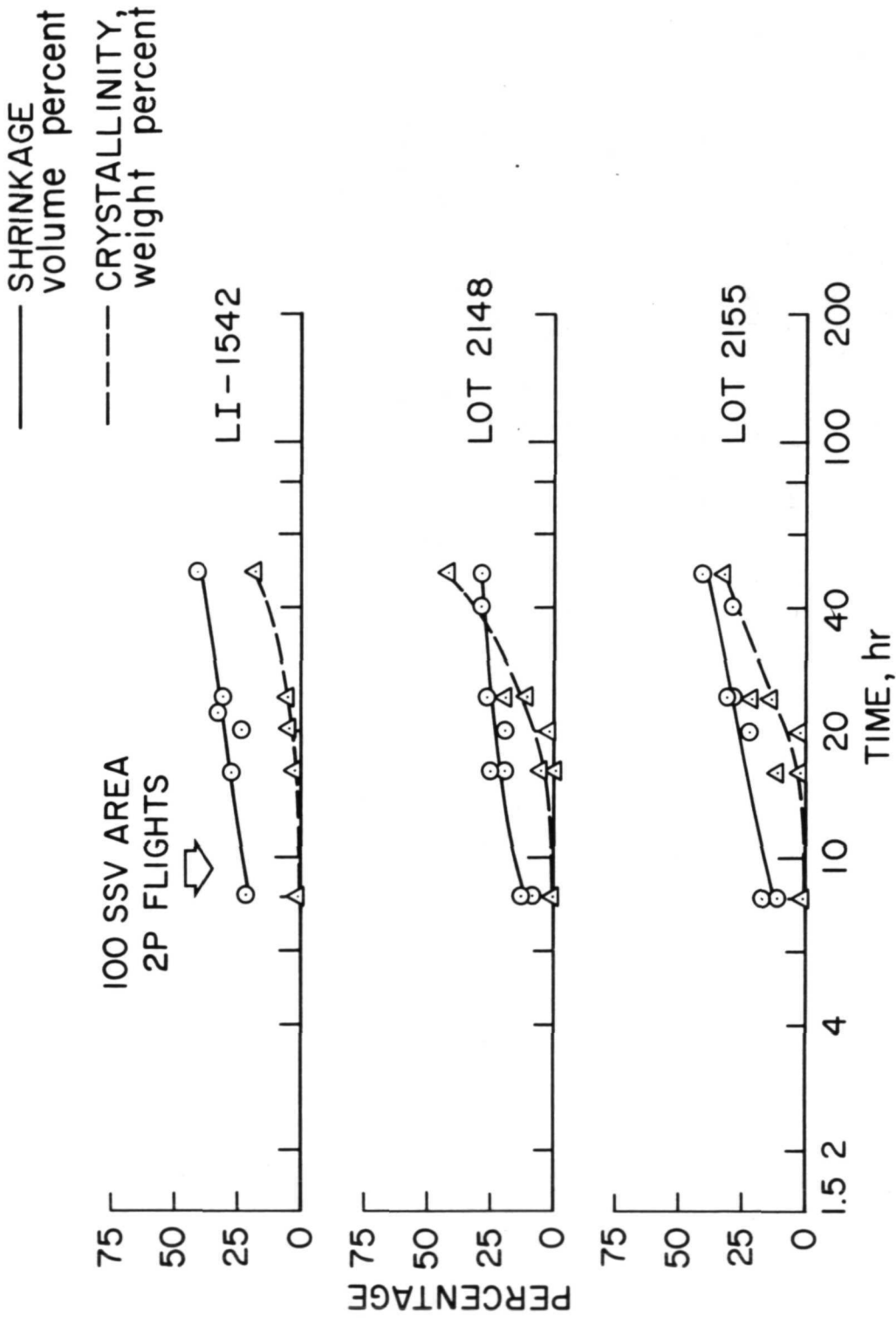
Figure 12

PROCESS VARIATIONS DUE TO FIBER LOT

(Figure 13)

This figure shows the variations in the process that are required for three lots of fiber. Lot 2102 is a less stable fiber and is fired for a shorter time and at a lower temperature than the other two, as previously noted. Shrinkage of the fibers differs during processing and requires different initial as-cast densities in order to obtain the same final tile density. The washing requirement varies for each fiber lot. Fiber Lot 2148 requires chopping because the initially longer fiber causes stratification during molding and cracking of the tile during the firing cycle.

Both Lots 2148 and 2155 make satisfactory stable RSI. However, only 50-60 kg of each lot is available because this is the normal lot size made by Johns-Manville. Therefore, a significant problem in silica RSI fabrication is lot-to-lot variation in fiber properties. If the RSI process must be varied for each fiber lot, then an added degree of complexity is added to the manufacturing procedure, resulting in increased cost. Johns-Manville is improving their process and expects to begin manufacturing fiber by a continuous process rather than a batch process in the next few months. As a result, fiber uniformity should be improved. At the present time, however, Ames is receiving small fiber lots that have significant differences between them.

PROCESS VARIATIONS DUE TO FIBER LOT

FIBER LOT	WASHING REQUIRED	CHOPPING REQUIRED	PERCENT SHRINKAGE		TOTAL FIRING TIME, HOURS	FIRING TEMPERATURE, °K (°F)	TENSILE STRENGTH $N/M^2 \times 10^5$ (psi)
			IN PROCESS	RAW FIBER IN 4 HOURS AT 1533° K (2300° F)			
2102	YES	NO	31	40	0.5	1500 (2250)	4.5 (65)
2148	NO	YES	43	19	2.5	1533 (2300)	5.9 (85)
2155	YES	NO	47	27	2.5	1533 (2300)	5.5 (80)

Figure 13

181

RSI MOLDS

(Figure 14)

All of the RSI materials currently being manufactured are quite anisotropic. From a structural standpoint it is desirable that these materials be isotropic if the strength is comparable to the strong direction strength of the anisotropic material. In order to make isotropic tiles, a two-directional mold, shown schematically in this figure, was developed. The slurry is placed in the mold, the top locked on, and the slurry rapidly pressed into shape using hydraulic pistons. The mold has screening on, and drainage from, all surfaces in contact with the tile. A conventional one-direction molding process is used to make the anisotropic tile. The slurry solids content, viscosity, and the molding pressure and rate were all found to be significant in determining the degree of anisotropy in terms of physical properties and density obtained with both processes.

182

RSI MOLDS
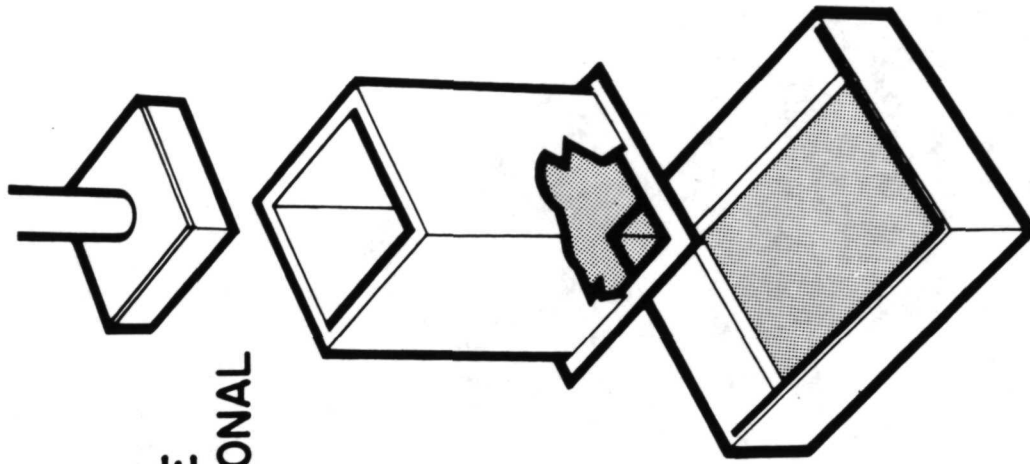
ONE DIRECTIONAL
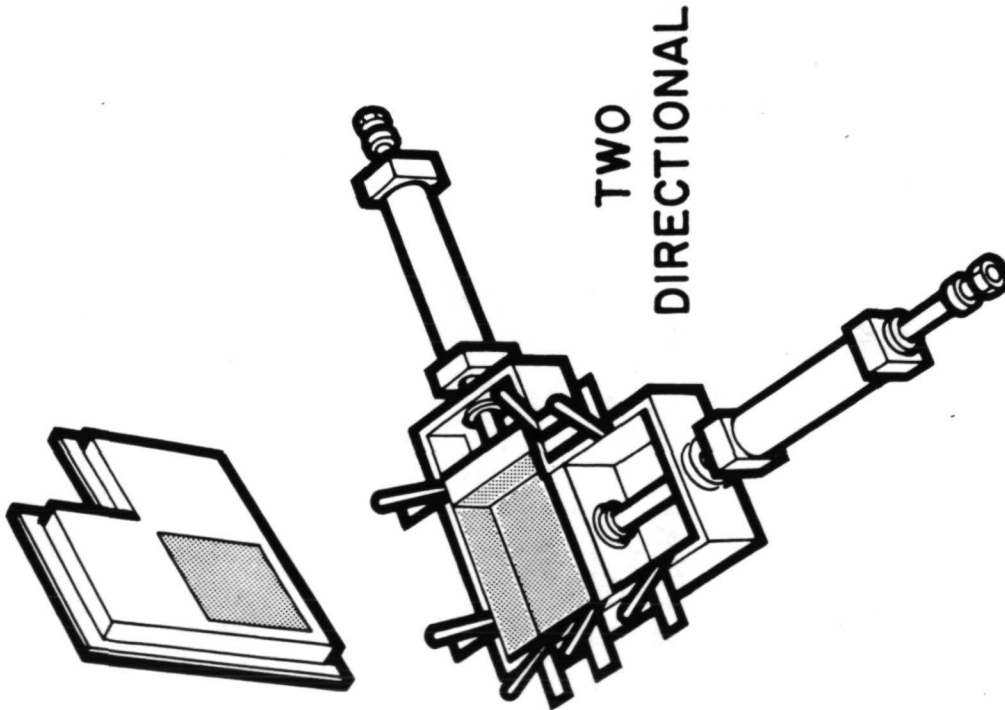
TWO DIRECTIONAL

Figure 14

MICROSTRUCTURE OF SILICA RSI

(Figure 15)

The figure shows the microstructure of LI-1542 and one-direction and two-direction press Ames silica RSI. LI-1542 shows a highly layered structure. The Ames one-direction press material shows layering, but is more uniform than the LI-1542 and apparently has a higher fiber density and less binder. The two-direction press material shows no fiber orientation but otherwise appears the same as the one-direction press material. The uniformity of the Ames fabricated material results from both the molding technique and the blending method. The relatively small amount of apparent bonding appears to result from the small percentage (less than five percent by weight) of binder in the tile. The strength of the materials is discussed in a subsequent figure.

MICROSTRUCTURE OF SILICA RSI

50X

500X

1000μ

100μ
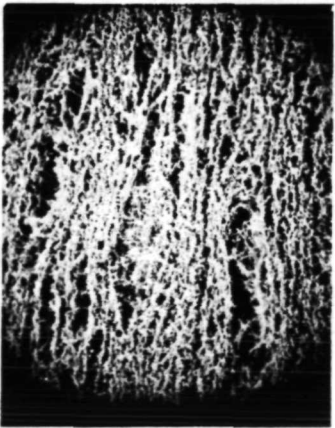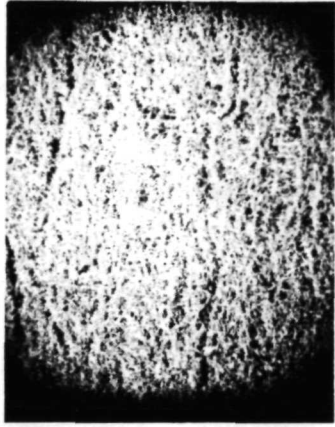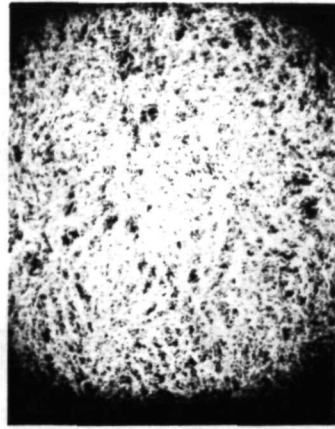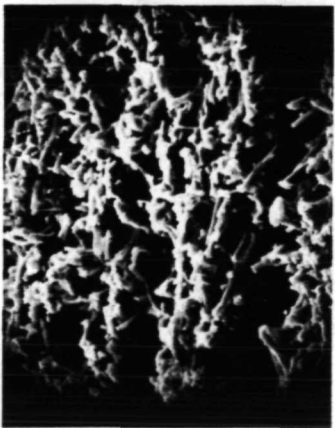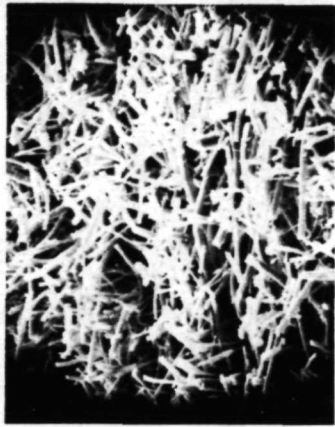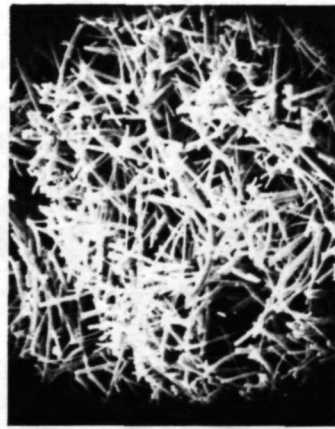
LI – 1542

ONE DIRECTION PRESS

TWO DIRECTION PRESS

AMES FABRICATED RSI

Figure 15

PHYSICAL PROPERTIES OF AMES FABRICATED SILICA RSI

(Figure 16)

This figure shows the room temperature tensile, compressive and shear strengths of the one-directional and two-directional pressed RSI tile. For the one-direction press RSI, an average of 40 data points is shown for each property. For the two-direction press material, an average of six points is shown. These data have been quite reproducible as shown by the 95 percent confidence limit. Using identical techniques, data in agreement with manufacturers measurements were obtained on LI-1500, REI, and HCF. The one-directional press properties are comparable to LI-1500 in the strong direction and superior in the weak direction. The two-directional press properties are nearly isotropic, and slightly lower than the one-direction press strong-direction properties. Strain-to-failure is quite high in both tensile and compression. This probably results from the relatively small amount of fiber bonding that was previously noted. The material is acting more like a fiber mat than a solid ceramic. As further improvement in strength is obtained, a decrease in the strain-to-failure and an increase in modulus is likely. It should also be noted that compressive strain was obtained using crosshead motion, which gives a high value for strain to failure. The high shear strength measured probably results from high fiber density and random orientation.

186

PHYSICAL PROPERTIES OF AMES FABRICATED SILICA RSI

PHYSICAL PROPERTY	ONE DIRECTIONAL PRESS*		TWO DIRECTIONAL PRESS**	
	LONGITUDINAL	TRANSVERSE	LONGITUDINAL	TRANSVERSE
DENSITY, KG/M^3 (lb/ft^3)	247 (15.4 ± 0.6)		247 (15.4)	
TENSILE STRENGTH, N/M^2 10^5 (psi)	5.7 (83±10)	2.2 (32±3)	4.2 (61)	4.1 (59)
TENSILE MODULUS, N/M^2 10^7 (psi 10^3)	32 (46±8)	6.8 (10±2)	12.3 (18)	27 (39)
STRAIN TO FAILURE, percent†	0.19 ± 0.03	0.32±0.05	0.34	0.15
COMPRESSIVE STRENGTH, N/M^2 10^5 (psi)	11 (166±25)	7.9 (115±20)	8.9 (130)	9.7 (139)
COMPRESSIVE MODULUS, N/M^2 10^7 (psi 10^3)***	12 (16±2)	4.8 (7±2)	9.8 (13)	12.8 (17)
STRAIN TO FAILURE, percent***	1.00 ± 0.25	1.5 ± 0.3	1.00	0.8
SHEAR STRENGTH, N/M^2 10^5 (psi)	4.8 (72)**		4.1 (60)	

*AVERAGE OF FORTY DATA POINTS FOR EACH VALUE ±95% CONFIDENCE LIMIT
**AVERAGE OF SIX DATA POINTS FOR EACH VALUE
***DETERMINED FROM CROSSHEAD MOTION

Figure 16

187

MICROSTRUCTURE OF SILICA RSI COATING CROSS SECTIONS

(Figure 17)

One of the critical aspects of RSI development is coating optimization. At Ames, the interaction of coatings with the convective heating environment are being studied as described in the papers by Leiser, et al. and Stewart in Volume II of these Proceedings. Among the significant coating properties that have been identified are: surface catalytic efficiency for recombination of atomic boundary layer species, spectral and total emittance, and solar absorptance (reference 10).

The changes in chemical composition of coatings that occur due to convective heating affects these properties. In order to study these coating changes, coating systems are being developed for the Ames silica RSI. Shown on this figure are cross sections of two recently prepared coatings. These coatings were made by blending pure boric acid with Corning 7900 glass (Vycor). The Vycor was chosen because of its low thermal expansion coefficient, which is very nearly the same as silica. The boron oxide serves to lower the viscosity of the Vycor allowing softening of the glass to occur at a lower temperature. An emittance pigment (3-10 percent solid weight) such as silicon carbide, chromium oxide, cobalt oxide, etc., is added when desired. The emittance pigment strongly affects the final coating physical properties. After ball milling for one hour, a 30 percent solids suspension in nitropropane is sprayed on the RSI tile. The coating thickness is controlled by the number of passes taken with the spray gun; if a two-layer coating is being applied, the second layer is sprayed while the first layer is still wet. The organic fluid is used because it has the proper combination of volatility and viscosity for successful spraying and the boric acid is insoluble in it. The coating is dried at 343°K (158°F) for at least 12 hours.

A number of firing techniques have been used. The coating cross sections shown in the figure were fired using an oxyacetylene torch. A one layer coating, having chromium oxide as the emittance pigment and a two-layered coating containing silicon carbide in the bottom layer are shown. As the figure illustrates, these coatings are very uniform. Coatings have also been furnace fired and radiantly fired at various temperatures. The primary problem in firing the coatings has been to obtain a uniform, fully fused coating without significant shrinkage of the tile. In order to obtain a fully fused coating requires firing above 1590°K (2400°F) for five minutes or more depending on the exact glass composition and pretreatment. If the firing time is too long, significant tile shrinkage will occur. A sintered coating can be obtained by firing for an hour at 1366°K (2000°F) with no measurable tile shrinkage. The allowable coating temperature and time-at-temperature are dependent on the fiber used in the tile. Tiles made with fiber Lot 2102 are so unstable that firing a coating on them at temperatures of 1533°K (2300°F) or above causes rapid devitrification and results in severe tile cracking. Tiles made with fiber Lot 1986 cannot be coated at all since they will crack after heating to 1366°K (2000°F). Tiles made with fiber Lots 2148 and 2155 can be successfully coated if they are not heated above 1653°K (2500°F) for more than five minutes, after which significant shrinkage occurs.

188

MICROSTRUCTURE OF SILICA RSI COATING CROSS SECTIONS

200 X

50 X

250 μ

1000 μ
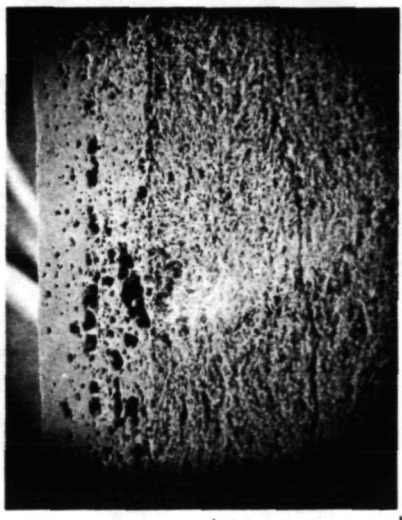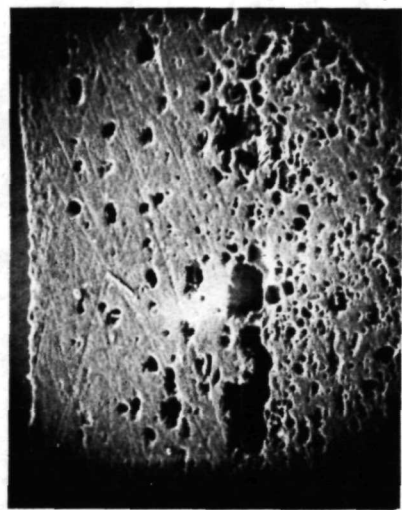
TWO LAYER

ONE LAYER

Figure 17

189
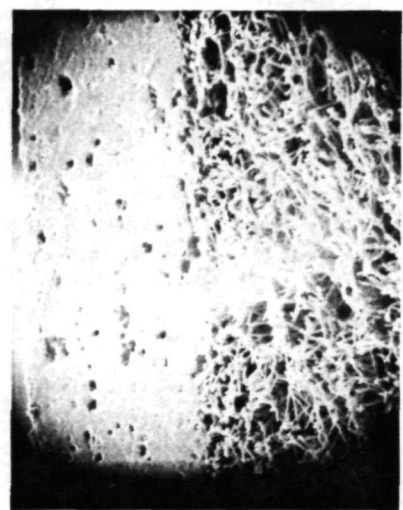
MICROSTRUCTURE OF SILICA RSI COATING SURFACE

(Figure 18)

This figure shows the outer surface of the two-layer coating containing silicon carbide described in the previous figure, before and after firing. The rod-like features in the coating before firing are boric acid crystals. After firing a glassy surface is obtained. The boron oxide has been fused with the Vycor glass. Elemental analysis after firing shows a slightly lower boron content in the coating than before firing. The coating was raised from room temperature to 1643°K (2500°F) in less than one minute and held there for several minutes. Apparently the rate of solution of the boron oxide with the Vycor glass was rapid enough so that little boron oxide was vaporized during firing. The two layer coatings have not been arc plasma tested.

For the arc plasma tests described in figure 19, a one layer, 0.5 mm (.020 inch) coating with silicon carbide as the emittance agent was used. One such coating has been tested for ten arc plasma cycles with no apparent deterioration. Additional tests are in progress.

190

MICROSTRUCTURE OF SILICA RSI COATING SURFACE

500X

100 μ

50X

1000 μ
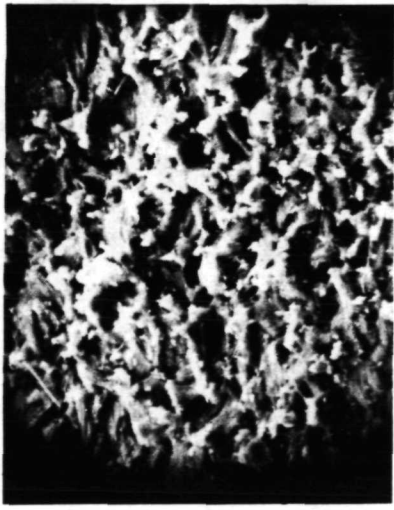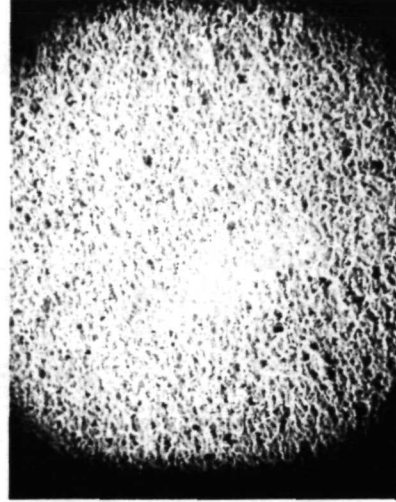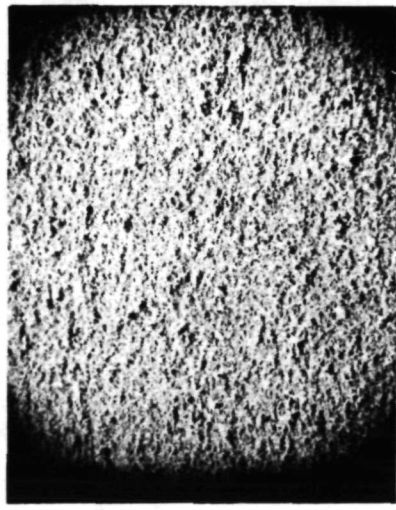
BEFORE FIRING

AFTER FIRING

Figure 18

TEMPERATURE HISTORY DURING ARC PLASMA TEST OF AMES SILICA RSI

(Figure 19)

In order to determine both the thermal stability and temperature response of the silica RSI, samples were tested in the Ames arc plasma facilities. The criteria for thermal stability were that the model showed no dimensional changes or visual cracks after test. The models tested were 10 cm (4 inch) diameter disks, approximately 4 cm (1.5 inches) thick. They were exposed to convective heating environments representative of the Area 2 shuttle environment. The experimental technique is described in the paper by Stewart (Volume II of these Proceedings).

Both one- and two-direction press materials were tested. This figure compares the internal temperature response of the two materials. Front surface temperatures were the same. The one-direction press material shows a significantly lower temperature response internally. Apparently, the thermal conductivity is higher when the fibers are randomly oriented to give isotropic strength properties than when they are less randomly oriented and give anisotropic strength properties. A comparison indicates that the one-direction press material gives the same temperature response as does LI-1542. Therefore, no weight penalty for the shuttle TPS is associated with the increased weak direction strength obtained in the Ames, one-direction press silica RSI. The isotropic material would result in a weight penalty, however. Further work is continuing in this area to determine the effect of both isotropy and fiber size on thermal conductivity. The one-directional press sample was exposed to ten arc-plasma test cycles and the two-directional press sample was run for three cycles. No sample degradation was noted. These samples will be further tested to determine their long term stability in a convective heating environment.

192

TEMPERATURE HISTORY DURING ARC PLASMA TEST OF AMES SILICA RSI

Figure 19

193
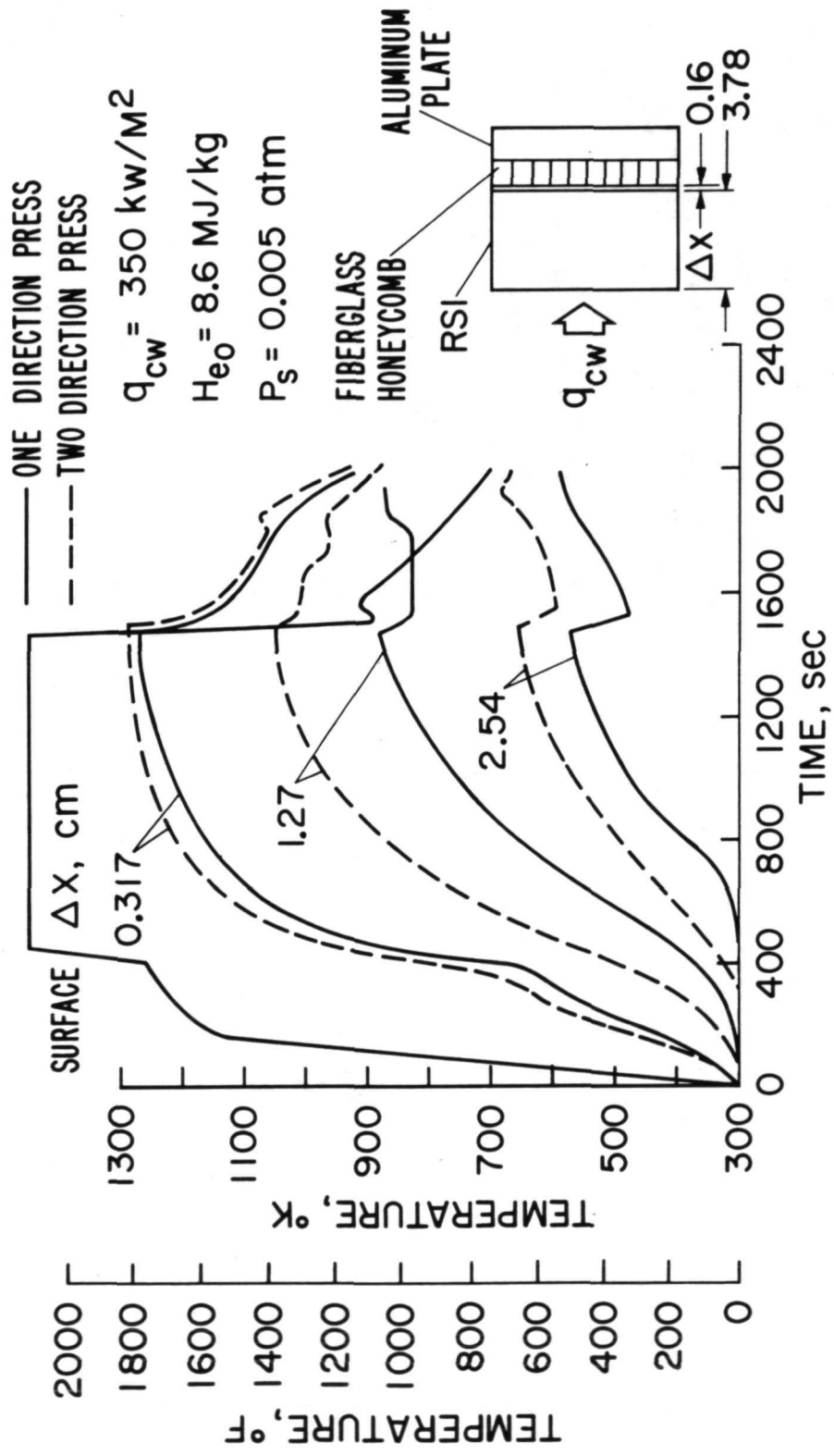
CONCLUSIONS

(Figure 20)

This study has shown that the devitrification and shrinkage of both the raw Microquartz 108 fiber and the finished tile correlate with the level and type of impurities in the fiber. As little as 0.1 percent alkali or alkaline earth impurities increase the devitrification rate substantially and result in the fibers being only marginally usable. Shrinkage is not as sensitive to impurity level but is still increased by the presence of alkali and alkaline earth impurities. Fiber cleaning can substantially improve resistance to devitrification and shrinkage though it does not measurably change bulk chemical composition. Large lot-to-lot variations in fiber chemistry and physical pro- perties exist and currently pose a significant problem in processing silica RSI that is thermally stable.

A simple process has been developed for fabricating silica RSI. The process requires three days. Resulting tiles have been demonstrated to be stable to both devitrification and shrinkage at 1533°K (2300°F) for a minimum of ten hours, which is equivalent to over 100 shuttle Area 2P trajectories. Both isotropic and anisotropic tile have been made. The anisotropic tile have slightly better physi- cal properties than LI-1500 in the strong direction and are stronger by over a factor of two in the weak direction. The isotropic tiles are slightly weaker in both directions than the anisotropic tiles are in the strong direction.

A coating process has been developed and coated tiles prepared. Cyclic arc plasma testing of coated tiles has demonstrated tile stability for ten shuttle Area 2 cycles in the convective heating. A comparison of isotropic and anisotropic tile temperature response to simulated entry environments shows that the isotropic tile has a substantially higher thermal conductivity.

194

CONCLUSIONS

- CRITERIA FOR FIBER SELECTION ON THE BASIS OF CHEMICAL COMPOSITION, SHRINKAGE AND DEVITRIFICATION HAVE BEEN DEFINED

- A SIMPLE PROCESS FOR FABRICATING SILICA RSI HAS BEEN DEVELOPED

- 5% LINEAR SHRINKAGE AND NO DEVITRIFICATION OF TILES ARE SHOWN AT 1533°K (2300°F) IN TEN HOURS

- ANISOTROPIC TILE WITH IMPROVED WEAK DIRECTION STRENGTH HAVE BEEN FABRICATED USING CONVENTIONAL MOLDING TECHNIQUES

- NEARLY ISOTROPIC TILE HAVE BEEN FABRICATED USING UNCONVENTIONAL MOLDING TECHNIQUES

- ISOTROPIC TILE SHOW INCREASED THERMAL CONDUCTIVITY IN ARC PLASMA TESTS

Figure 20

REFERENCES

1. Final Report "Space Shuttle Thermal Protection System Development," NASA Contract NAS9-12083, LMSC-D1527738, SS-1187, Lockheed Missiles and Space Company, Sunnyvale, California, January 17, 1972.

2. Thuss, R.C., Thibault, H.G., Hiltz, A.: "The Utilization of Silica Based Surface Insulation for the Space Shuttle Thermal Protection System," presented at the National SAMPE Technical Conference on Space Shuttle Materials, Huntsville, Alabama, October 5-7, 1971.

3. Zaplatinsky, Isidor: "Devitrification and Shrinkage Behavior of Silica Fibers," NASA TN D-6891, Lewis Research Center, 1972.

4. Mueller, J.I.: "Fundamental Research on the Nature and Properties of Ceramic Fiber Insulation," First Quarterly Report for the period June 30 to September 30, 1971, College of Engineering, Ceramic Engineering Department, University of Washington, Seattle, Washington, January 27, 1972.

5. Mueller, J.I., Leiser, D.B., Ormiston, T.J., Khandelwal, P., Whittemore, O.J., Scott, W.D., Miller, A.D., Garofalini, S.H.: "Fundamental Research on the Nature and Properties of Ceramic Fiber Insulation," Second Quarterly Report for the period October 1 to December 31, 1971, February 28, 1972.

6. Mueller, J.I., Smiser, L.W., Ormiston, T.J., Khandelwal, P., Whittemore, O.J., Scott, W.D., Miller, A.D., Garofalini, S.H.: "Fundamental Research on the Nature and Properties of Ceramic Fiber Insulation," Third Quarterly Report for the period January 1 to March 31, 1972, April 28, 1972.

7. Mueller, J.I., Smiser, L.W., Ormiston, T.J., Khandelwal, P., Whittemore, O.J., Scott, W.D., Miller, A.D., Garofalini, S.H.: "Fundamental Research on the Nature and Properties of Ceramic Fiber Insulation," Fourth Quarterly Report for the period April 1 to June 30, 1972, July 30, 1972.

8. Hurley, E.B., Smith, E.G.: Final Report: "Improved Silica Fibers," NASA Contract NAS3-15566, NASA CR-120987, Johns-Manville Products Corporation, Waterville, Ohio, March 30, 1972.

9. Ormiston, T.J., Whittemore, O.J.: "Sintering of Silica Fiber Compacts," presented at the Pacific Coast Regional Meeting of the American Ceramics Society in Portland, Oregon, October 25-27, 1972.

10. Goldstein, H.E., Buckley, J.D., King, H.M., Probst, H.B., Spiker, I.K.: "Reusable Surface Insulation (RSI) Materials Research and Development," presented at NASA Space Shuttle Technology Conference, April 12-13, 1972, NASA TM X-2570.

196

7

RADIANT HEAT TRANSFER IN

REUSABLE SURFACE INSULATION

by: T. A. HUGHES
R.M.F. LINFORD
R. J. SCHMITT
H. E. CHRISTENSEN

McDonnell Douglas Astronautics Company - East

St. Louis, Missouri

ABSTRACT

During radiant testing of HCF-TPS panels, temperatures in the insulation and support structure exceeded those predicted on the basis of guarded hot plate thermal conductivity tests. Similar results were obtained during arc tunnel tests of HCF specimens. To investigate the discrepancy between measured and predicted temperatures, HCF specimens were instrumented in depth, laterally shielded, and subjected to several time-temperature profiles in air at pressures corresponding to flight. The specimens were modeled on the MDAC-E General Heat Transfer computer program, and curves of the effective thermal conductivity obtained which minimized the differences between measured and predicted thermal response. The differences between effective conductivity and guarded hot plate values suggested that radiant transfer through the HCF was occurring. To study the radiant transport, measurements were made of the infrared transmission through various insulating materials and fibers of interest to the shuttle program, using black-body sources over the range of 780 to 2000°K. Experimental data was analyzed using a "two-flux" model for the radiation absorbed and scattered within the materials. Excellent correlation was obtained between theory and experiment, and scattering coefficients were derived for a variety of materials, fiber diameters, and source temperatures. Such coefficients have previously been shown to be directly relatable to infrared shinethrough.

198

INTRODUCTION*

During the development program on HCF-RSI**, MDAC-E conducted the usual guarded hot plate tests to measure the thermal conductivity of HCF as a function of pressure. In addition, to validate TPS designs, we conducted simulated mission tests under the expected shuttle orbiter entry conditions. Under the simulated mission tests, it was noted that the temperature response on the cool side of the HCF specimen was significantly different from that predicted using guarded hot plate thermal conductivity data. Because the thermal response of the insulation has a critical influence on the structural integrity of the shuttle orbiter during entry, and requires accurate design data to avoid severe weight penalties, it is imperative that accurate and reliable heat transfer data be available.

The guarded hot plate thermal conductivity data was inadequate due, not to inaccuracies, but to the effect of radiation transmittance or shinethrough, which is defined here as radiant energy, originating at the hot surface, transmitted through the insulation to the cool face, and which is not absorbed or scattered back to the originating surface. To resolve this problem, two approaches were used. One was the measurement of the effective conductivity under transient conditions, and the other was a basic study of radiation heat transfer through thermal insulations.

DYNAMIC EFFECTIVE THERMAL CONDUCTIVITY

(Figure 1)

The technique for measurement of effective conductivity under transient conditions employed highly instrumented test specimens subjected to a thermal pulse with a constant temperature source. The thermal pulse was provided by rapidly heating a coated columbium radiant panel to bring the adjacent surface of the HCF (which had an opaque, high emittance coating) to the desired temperature, 1533°K (2300°F), in about 300 seconds, and holding that temperature for an additional 500 seconds. The response of the thermocouples, precisely located within the test specimens, was recorded and used as the input for a general heat transfer thermal properties analyzer computer program. This program determined the effective thermal conductivity as a function of mean temperature, which minimized the difference between measured and computed response of all thermocouples.

The figure shows a group of seven test specimens ready for simultaneous testing. The test rack was installed directly over the coated columbium radiant panel of our graphite heater and the whole assembly mounted within a 1.68 m (5.5 ft) diameter space simulation chamber. This allowed the test to be conducted at a variety of subatmospheric pressures. The radiant panel and the space simulation chamber are described in references 1 and 2.

DYNAMIC EFFECTIVE THERMAL CONDUCTIVITY

THERMAL PERFORMANCE TEST SPECIMENS MOUNTED IN SPECIMEN HOLDER
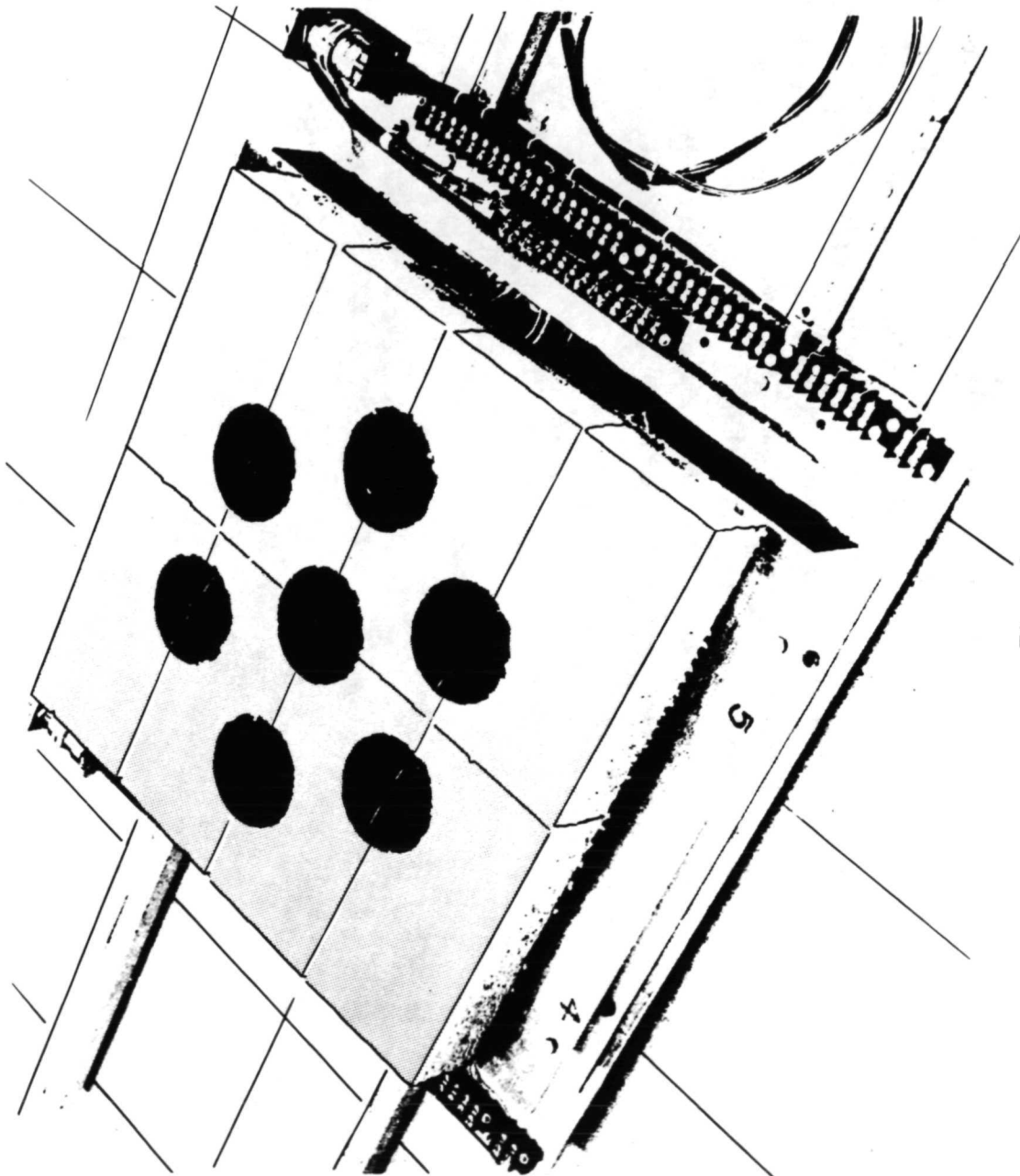
Figure 1

201

MEASURED VERSUS PREDICTED THERMAL RESPONSE

(Figure 2)

Figure 2 shows the improvement in predicting the temperature response of the more complex shuttle subscale panels .305 x .635 m (12 x 25 inch) using effective thermal conductivities obtained by the method described. This is an Area 2P structure incorporating an aluminum skin with a sponge interface for strain isolation. The critical elements in this structure are the temperatures at the HCF/sponge interface (channel 18), and at the aluminum skin (channel 44). The figure shows the comparison between measured thermal response at 10 torr [using the 2P thermal profile, which peaks at 1533°K (2300°F)]with those predicted from both effective thermal conductivity results, and from guarded hot plate conductivity. It can be seen that the effective conductivity technique predicted the measured response much more accurately than did the guarded hot plate conductivity values, the latter underestimating the temperature rise.

MEASURED VERSUS PREDICTED THERMAL RESPONSE

HALF-SIZE ALUMINUM AREA 2P PANEL,
CYCLE 4 TEST PRESSURE = 10 TORR

Figure 2

203
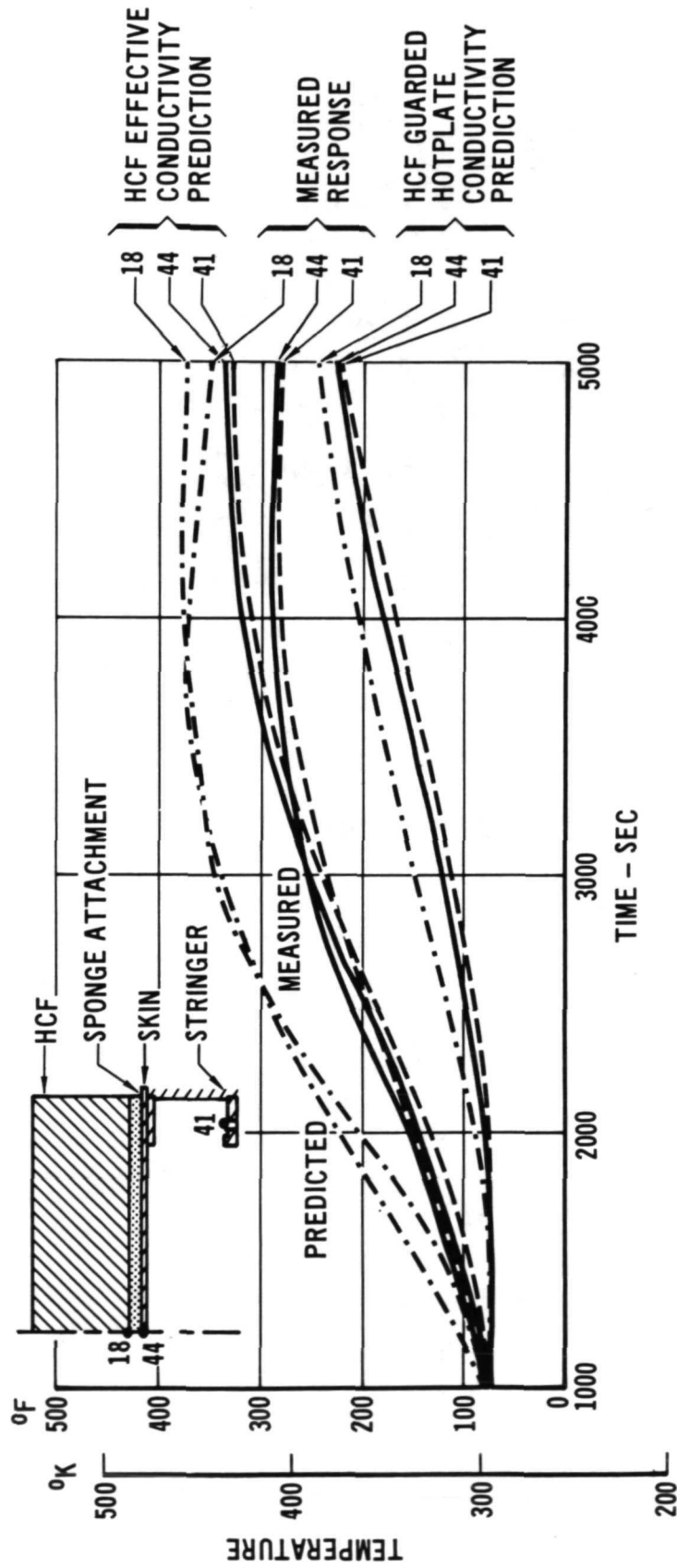
THERMAL CONDUCTIVITY COMPARISON

(Figure 3)

A potential shortcoming of the effective conductivity measurement technique is that a different conductivity curve is produced at different surface temperatures. This figure shows a comparison of effective conductivities of HCF determined for a 1533°K (2300°F) (Area 2P) and a 1033°K (1400°F), hot face (Area 1), and guarded hot plate results, all measured at 10 torr pressure. The effective conductivity determined with the surface temperature at 1533°K (2300°F) is about 0.8 MJ/m sec°K (0.45 Btu-in/hr-ft^2°F) higher than the guarded hot plate conductivity determined in accordance with ASTM-C-177. The guarded hot plate conductivity corresponds most closely to the effective conductivity measured with a 1033°K (1400°F) surface temperature. The disparity in effective conductivity results at different surface temperatures corresponds to expected increases in intensity of radiation transmittance with higher surface temperatures. The change in effective conductivity also explains the lessened correlation of subscale panel results shown in figure 2, after times in excess of about 3000 seconds. The Area 2P thermal profile has an early peak (at about 700 seconds) at 1533°K (2300°F) after which the surface temperature decays to about 466°K (380°F) at 3000 seconds.

204

THERMAL CONDUCTIVITY COMPARISON
240 kg/m³ (15 pcf) HCF

TEST PRESSURE = 10 TORR

Figure 3

205
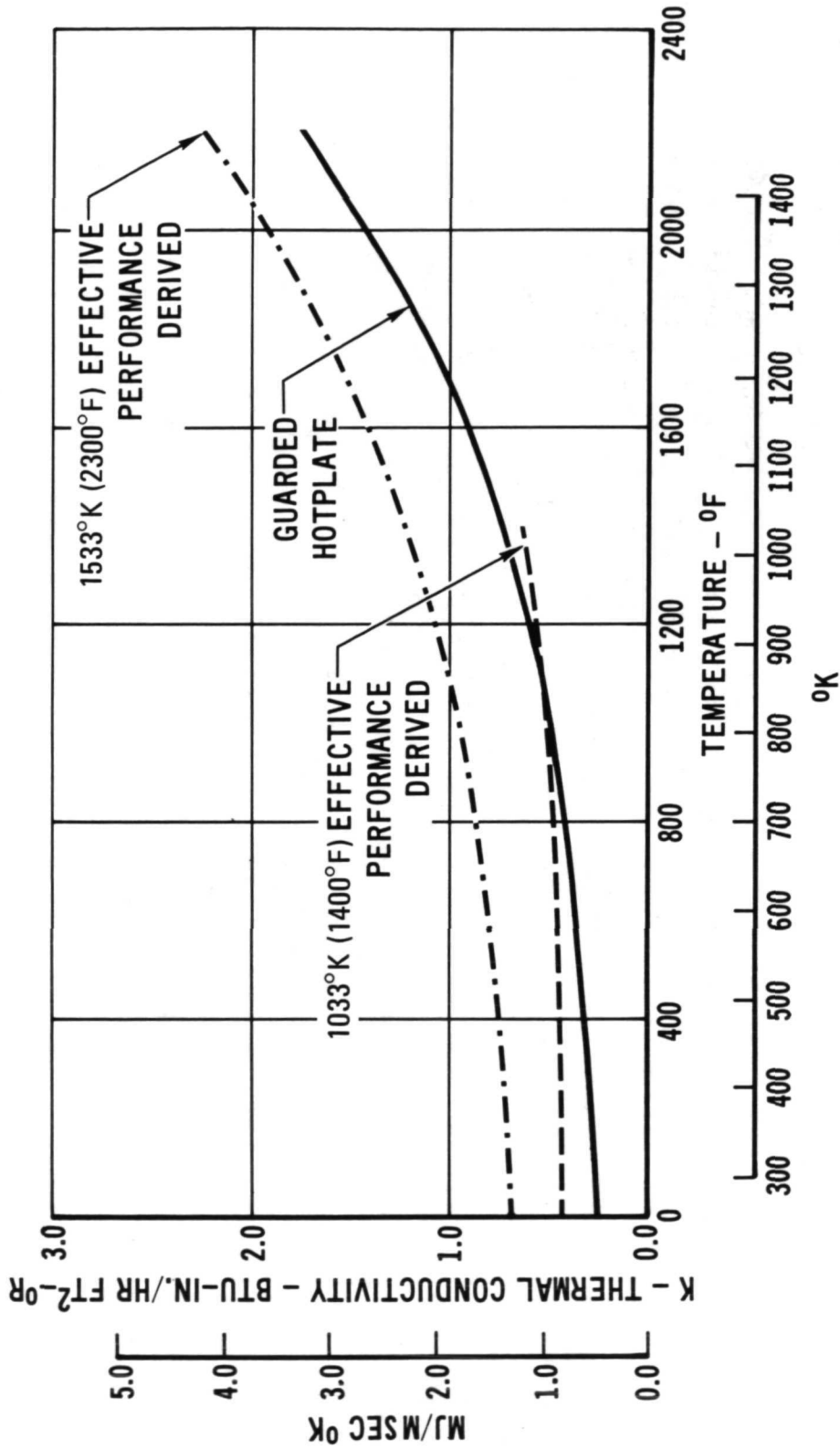
INFRARED TRANSMISSION MEASUREMENT

(Figure 4)

With considerable evidence indicating that radiation shinethrough had an appreciable effect on effective conductivity measurements and on mission performance, an extensive study was made of the infrared transmission characteristics of HCF and a number of other insulations and fibers.

The transmittance measuring equipment is shown opposite. Black-body radiation was generated by a cylindrical slug of oxidized Inconel, which was inductively heated by a 450 kHz RF generator. The emittance of oxidized Inconel is about 0.9 and is relatively independent of wavelength; the slug was, therefore, a good gray body, and the spectral distribution of the emitted radiation was essentially identical to that of a black body at the same temperature. A chromel-alumel thermocouple was spot welded to the slug for temperature measurement. The radiation from the Inconel slug was chopped at 13 Hz and focused on the entrance aperture of the integrating sphere. To provide a highly reflective, diffuse surface on the interior of the sphere, the inner wall was sprayed with a suspension of 180-grit silicon carbide powder in epoxy resin, followed by a vacuum deposition of gold. The radiation entering the sphere was measured by a thermistor detector connected to a lock-in amplifier tuned to the 13 Hz modulation frequency.

With the exception of the heated Inconel slug, all of the optical equipment was enclosed in a nitrogen-filled plastic tent to reduce absorption of the radiation at selected wavelengths by atmospheric moisture and carbon dioxide. To preserve the integrity of the purge during frequent sample changes, plastic gloves were installed in the wall of the enclosure for sample handling. All optical components in the system, including the silver chloride window, the mirrors, and the thermistor detector, were chosen for their uniform properties over the wavelength range of the experiment.

206

INFRARED TRANSMISSION MEASUREMENT
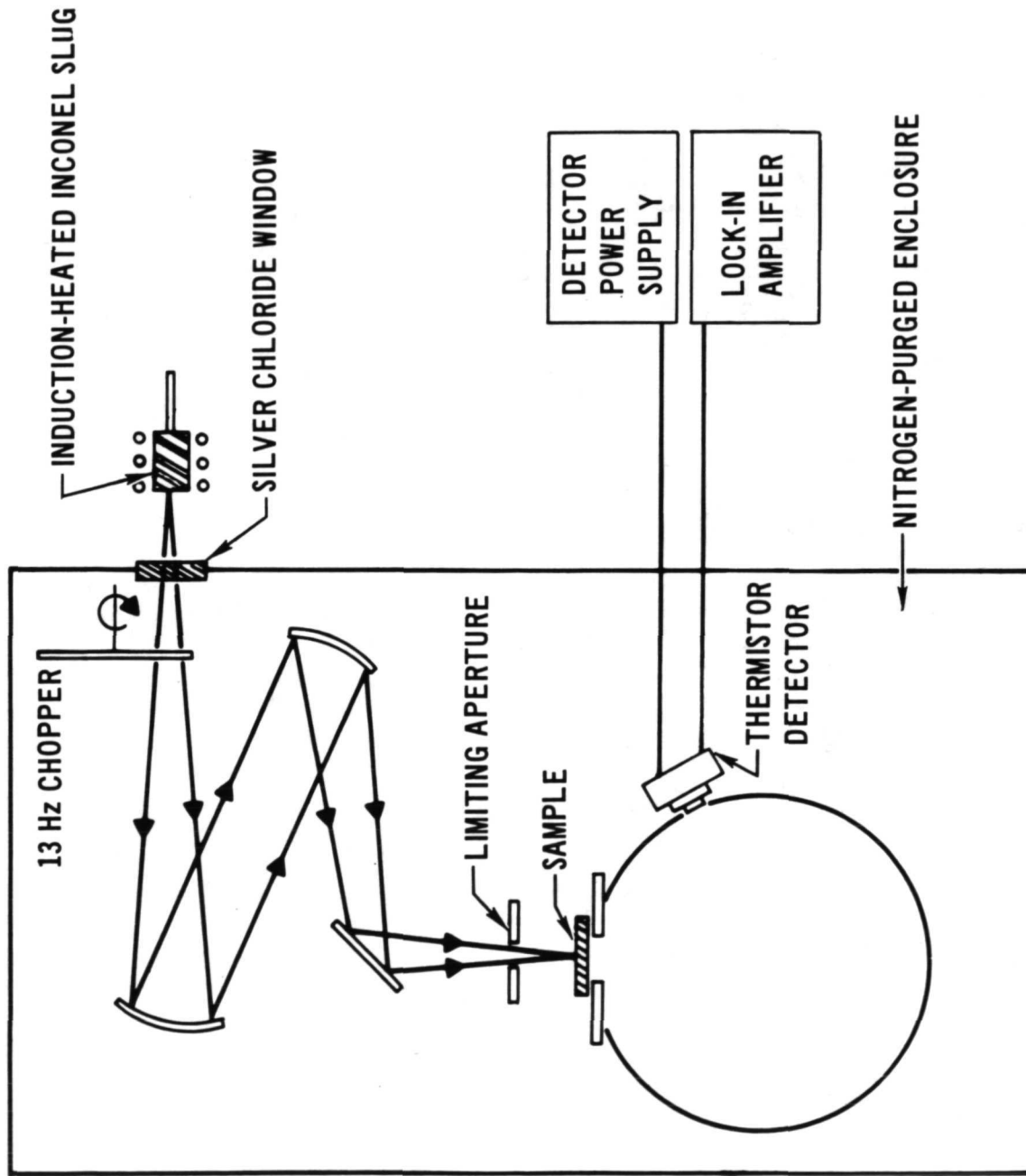
Figure 4

SPECTRAL TRANSMITTANCE OF DYNAQUARTZ

(Figure 5)

The present study recognized that radiant energy transmitted by the materials would emerge from the back surface scattered hemispherically. Measurements made with detection systems that accept radiation only from a narrow angle will generate transmittance data of doubtful accuracy. The errors that can be introduced by improper collection optics are illustrated in this figure, which shows the spectral transmission curves obtained with a 1.27 mm (.05 inch) thickness of Dynaquartz. The solid curve was obtained with a Perkin-Elmer Model 137 prism spectrometer with a narrow field of view detector, the dashed curve was generated from an ellipsoidal-mirror reflectometer. The collection angle of the prism spectrometer was less than 0.01 π steradians, while the detector in the ellipsoidal-mirror reflectometer collected radiation over a solid angle of about π steradians. It is apparent from these curves that radiation in the 2 to 6 micron wavelength band is scattered extensively as it is transmitted through Dynaquartz, and is only detected by wide acceptance angle detectors. In contrast, the narrow angle detector measured only the radiation in a narrow band centered about 7 microns.

The high transmittance peak at about 7.25 microns is typical of silica materials and is one of the Christiansen wavelengths for silica. According to theory, at the Christiansen wavelength, there is no scattering due to lack of a discontinuity in index of refraction between particle and surrounding mediums.

208

SPECTRAL TRANSMITTANCE OF DYNAQUARTZ
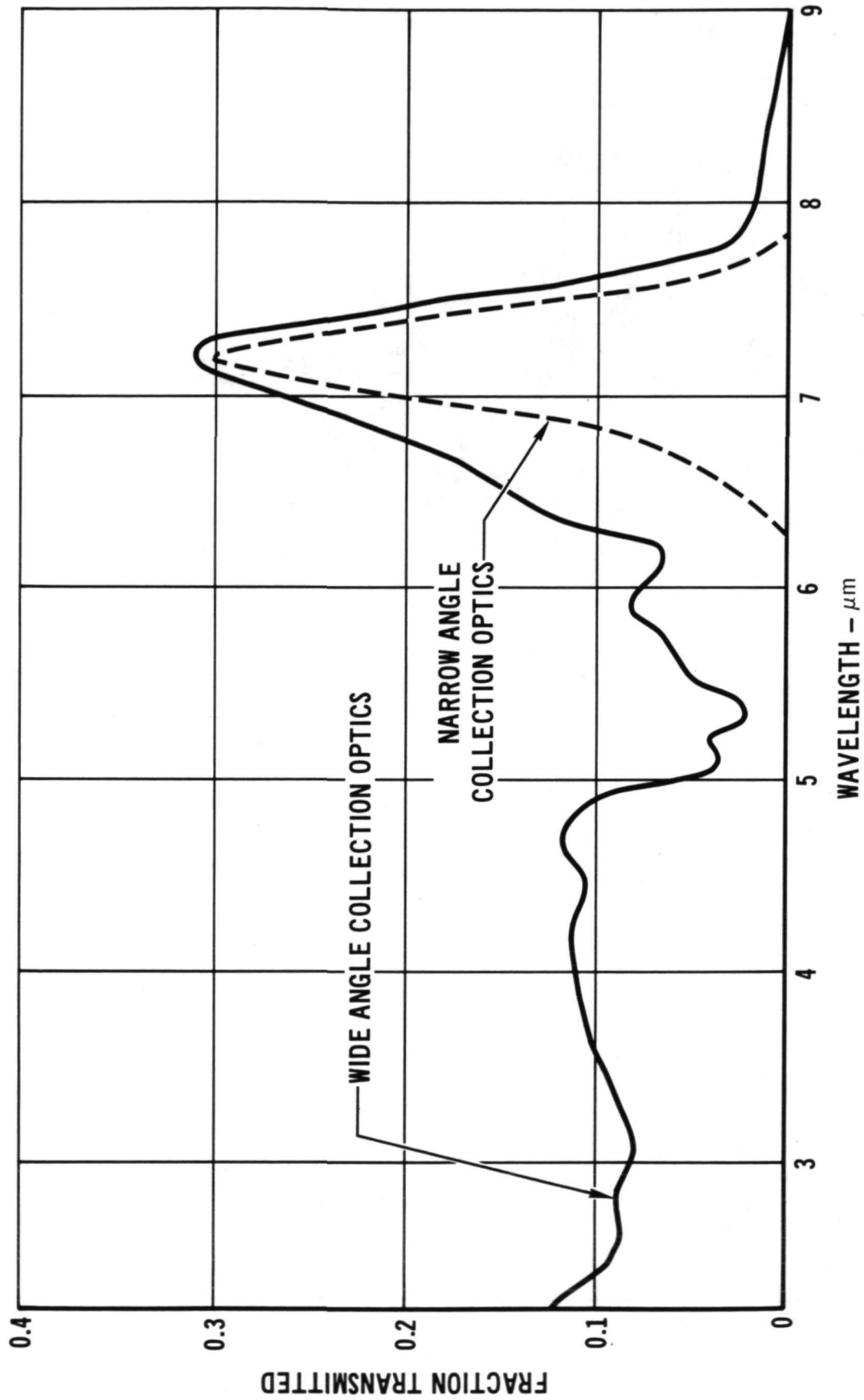
Figure 5

BLACK-BODY ENERGY DISTRIBUTION

(Figure 6)

The importance of measurements in the 2-6 micron wavelength range is illustrated by this figure, which shows the spectral distribution of black-body energy for the temperatures we are immediately concerned with. To assure maximum detection in this range, the measurements made in this program employed an integrating sphere with an acceptance angle of 2 π steradians.

BLACK BODY ENERGY DISTRIBUTION

Figure 6

1644° K
2500° F

1367° K
(2000° F)

1089° K
(1500° F)

811° K (1000° F)

WAVELENGTH – μm

INTENSITY 10^4 W/M^2 μm

211
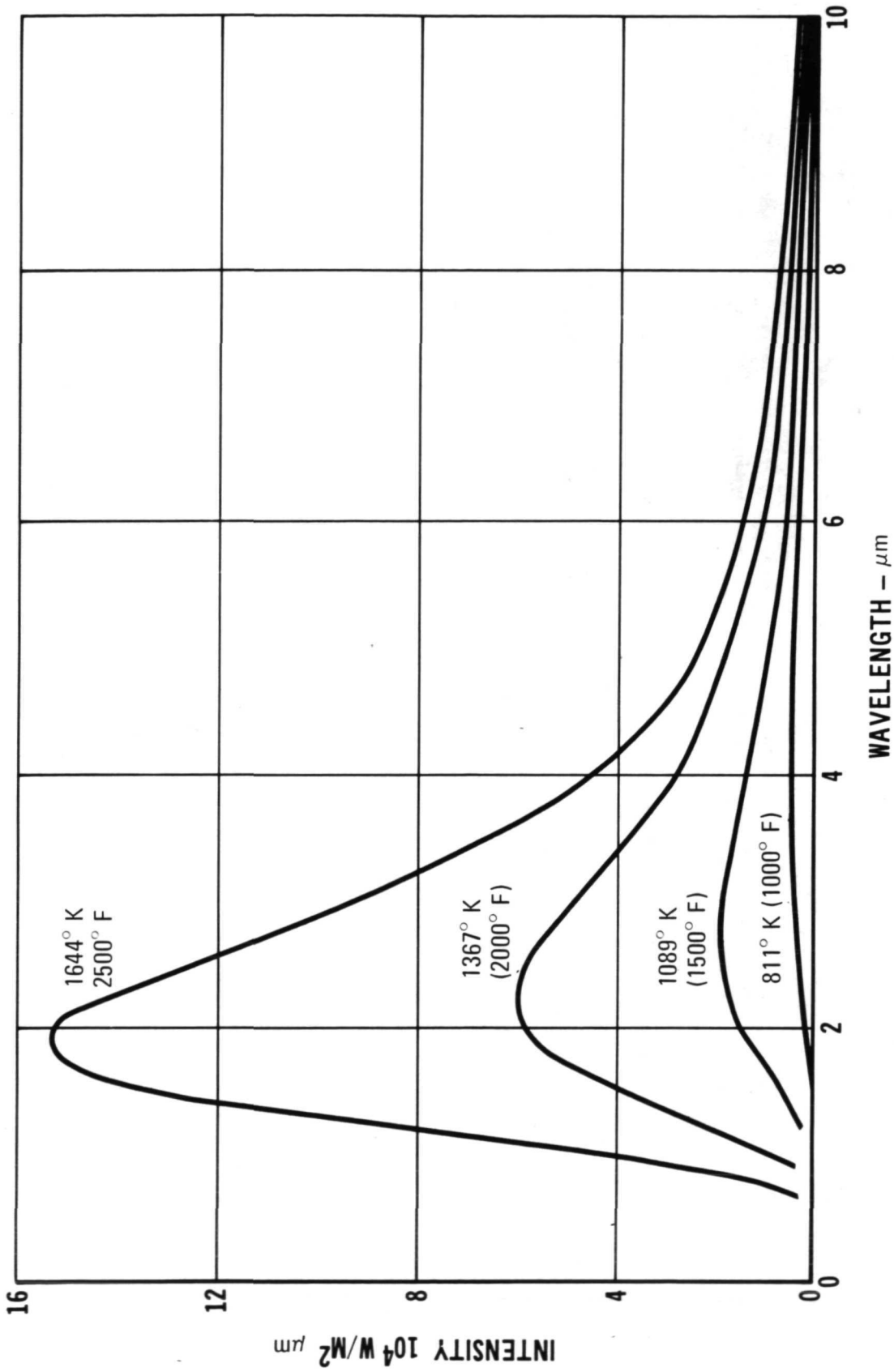
Transmittance was measured by the substitution method which, involved three measurements, and was calculated from:

$$T = \frac{V_S - V_{BG}}{V_{100} - V_{BG}} \, \eta$$

where T = fraction transmitted
V_S = signal voltage with the specimen covering the aperture
V_{100} = signal voltage with the sphere entrance aperture uncovered
V_{BG} = signal voltage from background noise, obtained by blocking the source input to the optical transfer system
η = sphere efficiency factor

If the detector in the sphere is not shielded from the aperture, a correction factor (η) is necessary to account for the change in reflective area of the integrating sphere when the specimen covers the aperture, and the reflectance of the surface of the sample facing the interior of the sphere. This was not recognized until late in this program, after most of the data had been accumulated, and the data have not been corrected for it. The transmission correction factor for our test equipment was found to be 0.88, which means that the reported interception (M) and backscattering (N) cross sections are slightly low.

212

The two-flux model formulated by Hamaker (Reference 3) and utilized by Larkin and Churchill (Reference 4), assumes that the interception and backscattering coefficients are independent of radiant energy spectral distribution (i.e., source temperature) and that radiant transport can be described by the two differential equations:

$$\frac{dI_1(x)}{dx} = -MI_1(x) + NI_2(x) + P\sigma T_x^4 \qquad (1)$$

$$-\frac{dI_2(x)}{dx} = -MI_2(x) + NI_1(x) + P\sigma T_x^4 \qquad (2)$$

where I_1 = flux in the direction of increasing distance (x), hot to cold surface
I_2 = flux in the opposite direction
M = interception cross section, unit area/unit volume = N + P
N = backscattering cross section, unit area/unit volume
P = absorption cross section, unit area/unit volume

The first equation states that in traversing a slice of material (dx), the intensity of the radiant flux in the forward direction (I_1) is decreased by the amount of forward flux intercepted, and increased both by the amount of backscattering of the flux from the reverse direction (I_2) and by reradiation. The second equation is the analogous balance for the flux in the reverse direction.

213

These equations were solved for the case where absorption is negligible.

$$P = M - N = 0$$

$$M = N$$

with appropriate boundary conditions, and an expression was derived for the energy transmitted through the slab for radiation under a linear temperature gradient:

$$q_r = \frac{\sigma[T_o^4 - T_L^4]}{\dfrac{1}{\varepsilon_o} + \dfrac{1}{\varepsilon_L} - 1 + NL} \qquad (3)$$

where ε_o and ε_L are the emittances of the hot and cold faces of the slab and L the thickness.

In experimentally measuring the transmission of infrared radiation through a specimen at room temperature, the $P\sigma T_x^4$ terms in the differential equations may be neglected, as the detector circuit responded only to radiation signals modulated at 13 Hz , and the solution of equations (1) and (2) is then:

$$\frac{I_1(L)}{I_1(0)} = \frac{2\sqrt{M^2 - N^2}}{M + \sqrt{M^2 - N^2}} e^{-L\sqrt{M^2 - N^2}} \left[\sum_{n=0}^{n=\infty} (-1)^n \left(\frac{M - \sqrt{M^2 - N^2}}{M + \sqrt{M^2 - N^2}} \right)^n e^{-2nL\sqrt{M^2 - N^2}} \right] \qquad (4)$$

where $\dfrac{I_1(L)}{I_1(0)}$ = relative intensity of forward scattered radiation at thickness (L)

214

To characterize the transmission properties of insulations, it was necessary to measure the percentage transmission for a series of specimens of varying thicknesses (L). The resultant data was analyzed by computer iteration to determine the constants M, N, and P that provided the best fit to equation (4).

When $L \sqrt{M^2 - N^2} > 2$, the series within the bracket approaches unity. For the materials and temperature we are concerned with, this is generally true for sample thicknesses greater than 1.27 cm (0.5 in). It is noteworthy that for those cases [thickness greater than 1.27 cm (0.5 in)] the Larkin and Churchill equation

$$I_{1(L)} = \frac{2 \sqrt{M^2 - N^2}}{M + \sqrt{M^2 - N^2}} e^{-L \sqrt{M^2 - N^2}}$$

takes the form of Lambert's Law:

$$I_{1(L)} = Ae^{-kL}$$

The Lambert absorption coefficient in terms of Larkin and Churchill constants is $k = \sqrt{M^2 - N^2}$, and:

$$A = \frac{2 \sqrt{M^2 - N^2}}{M + \sqrt{M^2 - N^2}}$$

A plot of the Larkin and Churchill equation should, therefore, be asymptotic to Lambert's Law for thicknesses greater than 0.762 cm (0.3 in) [~ 1.95 kg/m^2 at 240 kg/m^3 (~ 0.4 lb/ft^2 at 15 pcf)].

215

TRANSMITTANCE OF A 1477°K (2200°F) SOURCE BY HCF MOD III A

(Figure 7)

The units for M, N, and P are shown above as reciprocal length. For most of the experimental work, we used an equivalent term--the reciprocal of surface density. Measurements were made and are reported on the basis of mass per unit area as this method provided automatic compensation for variations in density of individual specimens of the same composition, and eliminated the problem of accurately measuring the thickness of soft, low-density felted products. For many applications where it is desired to compare materials on a thickness basis, or for use in the equations presented here, the preferred unit is reciprocal length. The data can be readily converted to reciprocal length by multiplying reciprocal surface density by the density of the insulation.

The transmittance of an IR source by various thicknesses of HCF MOD III is shown in this figure. This illustrates the correlation of experimental data with the Larkin and Churchill equation (Equation 4) and with Lambert's Law. The experimental data are seen to correlate well with the Larkin and Churchill equation, which indeed becomes asymptotic to a simple exponential function as postulated.

216

TRANSMITTANCE OF A 1477°K(2200°F) SOURCE BY HCF MOD IIIA

$$\frac{I_{1(L)}}{I_{1(0)}} = \frac{2\sqrt{M^2 - N^2}}{M + \sqrt{M^2 - N^2}} e^{-L\sqrt{M^2 - N^2}} \left[\sum_{n=0}^{n=\infty} (-1)^n \left(\frac{M - \sqrt{M^2 - N^2}}{M + \sqrt{M^2 - N^2}} \right)^n e^{-2 n L\sqrt{M^2 - N^2}} \right]$$

COMPARISON OF EXPERIMENTAL DATA WITH THEORY

LARKIN AND CHURCHILL EQUATION

$$M = [15.68 \ (kg/m^2)^{-1}] = [76.58 \ (LB/FT^2)^{-1}] = 37.63 \ cm^{-1} \ at \ 240 \ kg/m^3 \ [95.72 \ in.^{-1} \ at \ 15 \ LB/FT^3]$$

$$N = [15.66 \ (kg/m^2)^{-1}] = [76.46 \ (LB/FT^2)^{-1}] = 37.58 \ cm^{-1} \ at \ 240 \ kg/m^3 \ [95.57 \ in.^{-1} \ at \ 15 \ LB/FT^3]$$

LAMBERT'S LAW ASYMPTOTE

$$T = 0.106 e^{-0.878 \rho_S}$$
$$\rho_S = (kg/m^2)$$
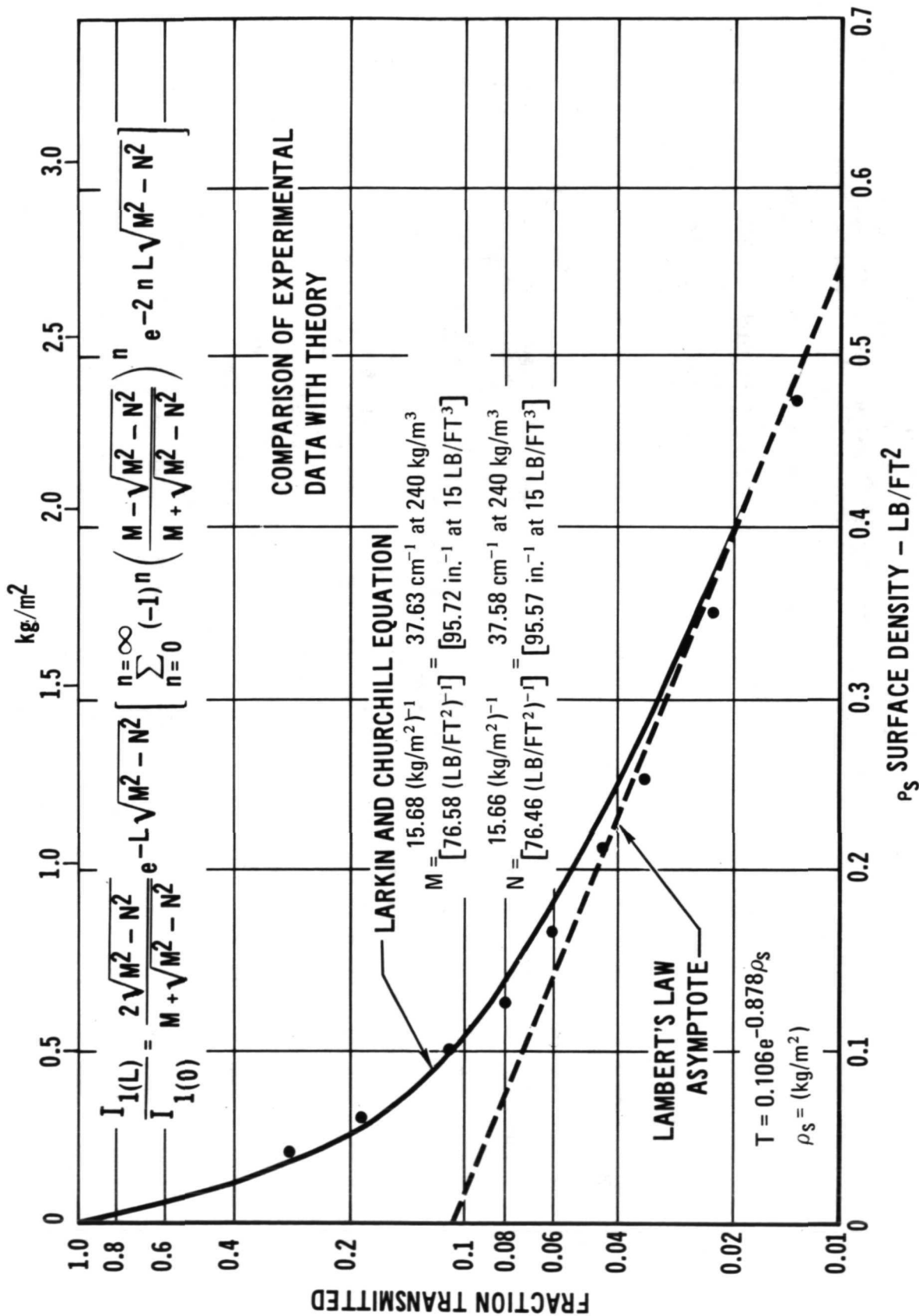
Figure 7

217

BACKSCATTERING CROSS SECTIONS OF SEVERAL CERAMIC FIBROUS INSULATIONS

(Figure 8)

Using the technique described, the backscattering coefficients for a number of insulations and raw fibers were determined as a function of source temperature, and are shown in this figure. It can be seen from these data that the backscattering of fibers (mullite, Microquartz, Refrasil A-100, and Astroquartz) is influenced mainly by fiber diameter, and to a lesser extent, by composition. The spectral distribution of the radiant energy (source temperature) also has a strong influence for mullite and aluminosilicate fibers/materials but much less influence for silica materials. The nominal diameters of these fibers are:

FIBER	COMPOSITION	NOMINAL AVERAGE DIAMETER (MICRONS)
Microquartz	Silica	1.3
Refrasil A-100	Silica	1.3
Astroquartz	Silica	7
Mullite, Coarse	Mullite	6
Mullite, Fine	Mullite	4
Mullite, Superfine	Mullite	2.5

The reason for the disparity in backscattering results between Microquartz and Refrasil A-100 is unknown. Both are silica fibers of the same average diameter and about the same purity, though their manufacturing techniques are radically different. Scanning electron micrographs of these two fibers at 3000X and 10,000X do not reveal any visually apparent differences in surface texture or flaws. Two factors that might account for the difference, but have not been measured, are the distribution of the fiber diameters, which make up the average diameter, and the average diameter of the specific materials tested.

RSI blocks made from these fibers, whether silica or mullite, all showed decreases in backscattering compared to the original fibers. This would be expected as much of the weight of these blocks is made up of binder, and in some cases, low-density coarse fillers, which would be expected to be relatively inefficient scatters. Comparison of the data on the fibers indicates how the transmission characteristics could be reduced. In the case of HCF, the substitution of 1.6 micron diameter SKX fiber (Al_2O_3. SiO_2) significantly increased the backscattering (this particular block also contained potassium titanate, which might also have contributed to the improvement). Also, the use of a blend of Microquartz with mullite fiber (4.7 micron) in the Mod V composition essentially doubled the backscattering. The ultimate refinement may come from an HCF made with the superfine mullite fibers (2.5 micron diameter). While this block has not yet been made, results with the fiber indicate that the backscattering would be comparable to Microquartz-based insulations. It could also have the advantage of the temperature resistance of mullite.

218

BACKSCATTERING CROSS SECTIONS OF SEVERAL CERAMIC FIBROUS INSULATIONS
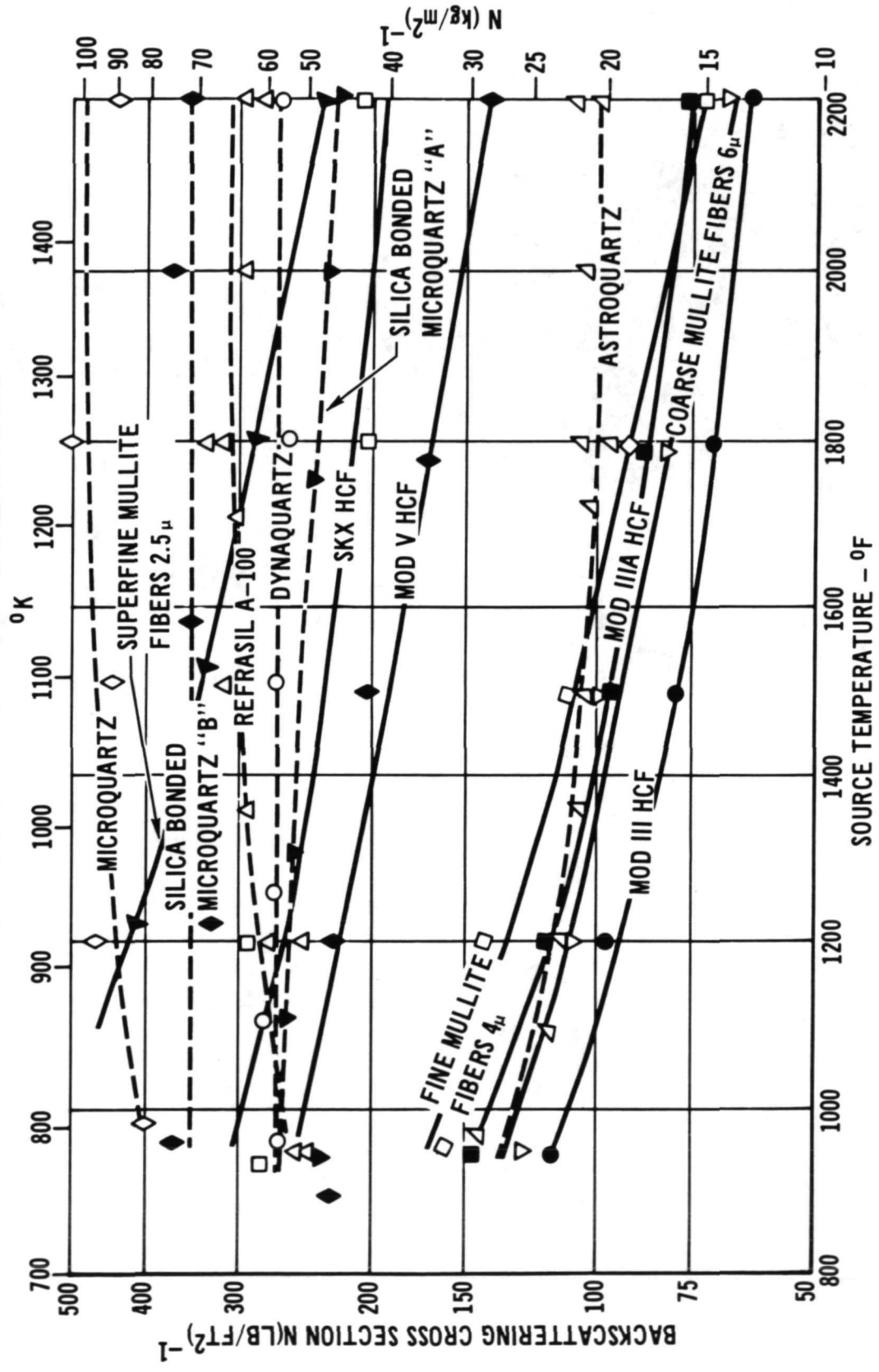
Figure 8

INFRARED SCATTERING CHARACTERISTICS OF VARIOUS INSULATIONS

(Figure 9)

Larkin and Churchill's data (reference 4) indicated that with glass fibers at lower source temperatures [366-700°K (200-800°F)] there is an optimum fiber diameter for maximum backscattering for each source temperature. Glass fibers, smaller or larger than the optimum, resulted in greater IR transmission (lower backscattering). For the temperatures and materials of concern here, we are not certain where the optimum lies, but we believe it to be somewhere in the range of 1.0 to 1.5μ diameter.

While the basic differential equations describing radiant heat transmission in insulations are relatively simple, their solution, except for steady-state conditions, are extremely complex. A common assumption made to simplify the solutions is that the absorption coefficient is negligible ($P \approx 0$). It can be seen from figure 9 that this assumption is generally a reasonable one. Only in the case of Astroquartz did the absorption cross section exceed 4% of the interception cross section, and in most cases was considerably less. The absorption cross section (P) is related to but not equal to α, the absorption coefficient (reference 5).

220

INFRARED SCATTERING CHARACTERISTICS OF VARIOUS INSULATIONS

CROSS SECTIONS (kg/m²)⁻¹ — SOURCE TEMPERATURE °K (°F)

MATERIAL		783 (950)	922 (1200)	1089 (1500)	1256 (1800)	1478 (2200)
HCF MOD III	M	23.43	19.74	16.41	13.97	12.70
	N	23.35	19.66	16.32	13.91	12.64
	P	0.08	0.08 (978°K 1300)	0.08	0.08	0.06
HCF MOD III A	M	29.72	25.81	21.40	18.08	15.68
	N	29.64	25.79	21.38	18.04	15.66
	P	0.08	0.02	0.02	0.04	0.02
HCF MOD V — EXPERIMENTAL – BLEND OF 4.7 µ MULLITE FIBERS AND MICROQUARTZ – NO FILLER	M	46.80	46.78	41.91	34.31	28.94
	N	46.74	46.76	41.88	34.29	28.92
	P	0.06	0.02	0.03	0.02	0.02
SKX – HCF — EXPERIMENTAL – SKX FIBERS 20% PKT	M	57.37	59.34 (867°K 1100)	50.94 (978°K 1300)	41.82 (1200°K 1700)	41.62
	N	57.27	59.27	50.90	41.78	41.58
	P	0.10	0.06	0.04	0.04	0.04
SILICA BONDED MICROQUARTZ "A" 261 kg/m³	M	51.27	54.44	52.66	49.46	45.74
	N	51.10	54.34	52.56	49.40	45.67
	P	0.16	0.10	0.10	0.06	0.06
SILICA BONDED MICROQUARTZ "B" 141 kg/m³	M	76.17	67.73	71.69	71.56	71.00
	N	76.03	67.59	71.58	71.48	70.95
	P	0.14	0.14	0.10	0.08	0.06

CROSS SECTIONS (kg/m²)⁻¹ — SOURCE TEMPERATURE °K (°F)

MATERIAL		783 (950)	922 (1200)	1089 (1500)	1256 (1800)	1478 (2200)
MICROQUARTZ FELT	M	84.32	96.76	94.17	103.60	92.13
	N	81.39	94.87	92.54	102.53	90.98
	P	2.93	1.88	1.64	1.07	1.15
DYNAQUARTZ	M	55.18	55.81	55.18	53.05	54.79
	N	54.77	55.53	54.93	52.82	54.62
	P	0.41	0.29	0.25	0.23	0.16
REFRASIL A-100	M	53.60	53.05	55.30	64.58	60.48
	N	52.06	51.61	54.21	63.88	59.85
	P	1.54	1.43	1.09	0.70	0.63
ASTROQUARTZ	M	31.54	26.81	24.95	25.34	23.90
	N	29.08	23.02	21.14	21.55	19.91
	P	2.46	3.79	3.81	3.79	3.99
COARSE MULLITE FIBERS – 6 µ	M	25.91	22.63	20.71	16.82	13.35
	N	25.81	22.55	20.65	16.73	13.27
	P	0.10	0.08	0.06	0.08	0.08
FINE MULLITE FIBERS – 4µ	M	32.89	28.74	22.43	18.35	14.97
	N	32.85	28.69	22.39	18.31	14.93
	P	0.04	0.04	0.04	0.04	0.04
SUPERFINE MULLITE FIBERS – 2.5 µ	M		83.63	69.13	59.17	48.86
	N		83.61	69.10	59.15	48.84
	P		0.02	0.02	0.02	0.02

M = INTERCEPTION CROSS SECTION
N = BACKSCATTERING CROSS SECTION
P = ABSORPTION CROSS SECTION

Figure 9

TRANSMITTANCE AS A FUNCTION OF SPECIMEN TEMPERATURE

(Figure 10)

The possibility that the backscattering characteristics might change with a change in specimen temperature was also investigated. The transmission equipment previously described was modified by enclosing the specimen in a small furnace and rotating the specimen in and out of the radiation beam. As the detector output was fed through a lock-in amplifier tuned to the beam chopper frequency, only the radiation transmitted through the sample from the heated Inconel slug was measured. The transmittance of two materials (HCF and a silica-bonded Microquartz) as a function of specimen temperature is shown in this figure. A constant source temperature of 1255°K (1800°F) was used in this test. The figure shows a very slight increase in transmission for both materials as the specimens were heated from room temperature to about 1144°K (1600°F). In the case of the silica-bonded Microquartz, the transmission was again measured when the specimen cooled to room temperature, and showed essentially no change from the elevated temperature values. It is believed that, initially, the presence of absorbed atmospheric moisture in the specimen altered the scattering properties slightly, with the moisture being driven out as the specimen was heated. This assumption is based on the scattering occurring partly as a result of change in index of refraction between particles and the surrounding medium. The presence of a water film, with a different index of refraction, could be expected to be responsible for this difference. We have concluded, therefore, that the specimen temperature has no significant effect on the backscattering coefficients.

222

TRANSMITTANCE AS A FUNCTION OF SPECIMEN TEMPERATURE
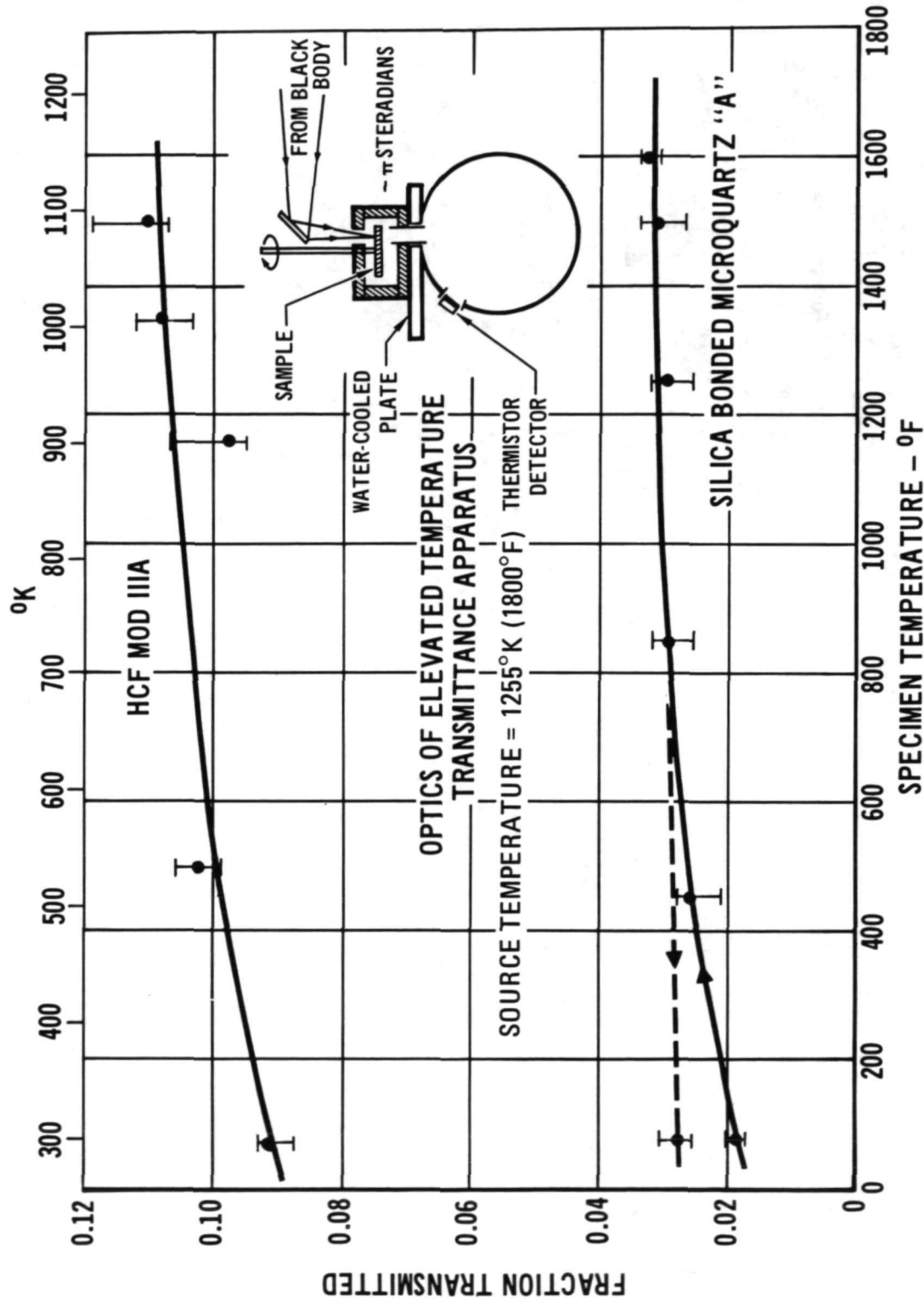
Figure 10

SUMMARY AND CONCLUSIONS

(Figure 11)

The use of the normal guarded hot plate conductivity data provided inaccurate predictions of thermal response of mullite fiber based RSI panels in mission simulation tests. Effective conductivity values, measured under transient thermal conditions, have provided more accurate predictions, and the data indicated that significant radiation shinethrough was occurring. Independent optical measurements have confirmed the existence of radiant transmission, and have allowed calculation of the backscattering coefficients for the infrared energy. Data have been presented for the interception, backscattering, and absorption coefficients as a function of source temperature for silica and mullite fibers of various diameters, and of insulation compositions containing those fibers. Generally, the interception and backscattering cross-sections of mullite fibers varied more as a function of source temperature than did the silica fibers. In limited testing, the temperature of the insulation itself was found to have little effect on infrared transmission, and the small change that did occur was likely due to the presence of a thin film of moisture in the initial low temperature tests.

224

SUMMARY AND CONCLUSIONS

- CLASSICAL GUARDED HOT PLATE THERMAL CONDUCTIVITY MEASUREMENTS HAVE NOT BEEN ADEQUATE TO DESCRIBE THE THERMAL RESPONSE OF CURRENT MULLITE FIBER BASED INSULATIONS IN THE SHUTTLE THERMAL ENVIRONMENT

- THE PRESENCE OF RADIANT TRANSMISSION THROUGH BOTH SILICA AND MULLITE FIBER BASED INSULATIONS HAS BEEN POSITIVELY IDENTIFIED BY OPTICAL METHODS.

- THE OPTICAL TECHNIQUE HAS PROVIDED A TOOL TO MEASURE THE INTERCEPTION, BACKSCATTERING AND ABSORPTION CROSS-SECTIONS OF INSULATIONS TO INFRARED RADIATION.

- BACKSCATTERING COEFFICIENTS OF MULLITE FIBERS WERE FOUND TO VARY WITH SOURCE TEMPERATURE SILICA FIBERS WERE FOUND TO BE LESS SENSITIVE TO SOURCE TEMPERATURE.

- BACKSCATTERING COEFFICIENTS WERE RELATIVELY INDEPENDENT OF INSULATION TEMPERATURE

- WITHIN THE RANGE OF FIBER DIAMETERS TESTED (1.3–7 μ), THE RADIANT TRANSMISSION WAS MARKEDLY REDUCED BY THE FINER DIAMETER FIBERS.

Figure 11

REFERENCES

1. Cox, B.G., "Thermal Testing Techniques for Space Shuttle Thermal Protection System Panels," presented at IES/AIAA/ASTM Sixth Space Simulation Conference, New York, N.Y., 1-3 May 1972. NASA SP-298, pp. 881-897.

2. Hughes, T.A., "High Temperature Insulation Materials for a Reradiative Thermal Protection System," Year-End Summary Report, MDAC-E Report MDC EO-449, 10 August 1971, Contract NAS 8-26115.

3. Hamaker, H.C., Phillips Research Reports 2, 55, 103, 112, 420, (1947).

4. Larkin, B.K. and Churchill, S.W., "Heat Transfer by Radiation Through Porous Insulations," AIChE - Journal, 5 (4), 467 (1959).

5. Folweiler, R.C., "Thermal Radiation Characteristics of Transparent, Semitransparent and Translucent Materials Under Nonisothermal Conditions,"ASD-TDR-62-719, April 1964.

6. Hughes, T.A., "High Temperature Insulation Materials for Reradiative Thermal Protection Systems," Final Report, MDAC-E Report MDC EO-666, 19 July 1972, Contract NAS 8-26115.

OPTIMIZATION OF REI-MULLITE PHYSICAL PROPERTIES

BY

R. A. TANZILLI, S. MUSIKANT, P. N. BOLINGER, J. P. BRAZEL

GENERAL ELECTRIC COMPANY
RE-ENTRY AND ENVIRONMENTAL SYSTEMS DIVISION
PHILADELPHIA, PENNSYLVANIA

INTRODUCTION

In order to provide quantitative approaches to REI-Mullite material improvements, micromechanical and thermal modeling studies of the basic insulation have been performed that provide considerable insight into the mechanical and thermal behavior of low-density, rigidized, fibrous insulation. These models have aided in the development of the present Mod-1B system. The intrinsic phase and dimensional stability of the all-mullite insulation at temperatures of 1644°K (2500°F) and above have clearly established this RSI candidate as the best material system for meeting the total Orbiter TPS requirements. Micromechanical modeling predictions, for example, indicate that at least a factor two increase in critical mechanical properties (e.g., in-plane tensile strain) should be achievable. Such improvement was effected in the Mod-1B REI-Mullite by an increase in the population of fiber junction bonds. Also, experimental thermal conductivity data have confirmed thermal modeling predictions that a factor of two reduction may be achieved by the use of small diameter mullite fibers (1-2 microns). The original Babcock and Wilcox mullite fiber was supplied in 6-8 μm nominal diameter. Current production comprises 4.7 μm nominal diameter, and further developments to finer fibers are now taking place.

Another problem area recently addressed has been the development of a reusable surface coating that meets both the orbital and entry thermal radiative requirements without recourse to refurbishment between flights. This system modification has been achieved through the use of a high purity hafnia pigment. Improved surface-coating phase and dimensional stability have been achieved through this surface coating change while still retaining its original noncatalytic behavior in a hypersonic flow environment.

8

PHASE DIAGRAM FOR THE MOD-1B REI-MULLITE SYSTEM

(Figure 1)

The Babcock and Wilcox Company (B&W) fiber is a quaternary oxide system whose mean composition lies within the phase equilibria tetrahedron as shown in Figure 1. As pointed out by Fetterolf in Reference 1, considerable variations in fiber properties may be achieved by adjustment of the relative proportions of the four oxide phases. For example, the presence of boric oxide and phosphorous pentoxide have been shown to result in improved fiber properties (strength, strain capability) as a result of grain growth inhibition.

This particular quaternary system has been studied by General Electric Company for solid ceramic applications and regions of phase stability have been identified. Also shown in Figure 1 is the SBA-10 binder system whose mean composition lies on the ternary silica-alumina-boria triangle (cross-hatched). The binder composition has resulted in near optimum fillet formation (Figure 4), and the studies on regions of phase stability were considered in the selection of the SBA-10 composition.

228

PHASE DIAGRAM
FOR THE MOD-1B REI-MULLITE SYSTEM

QUATERNARY SYSTEM

$Al_2O_3 - SiO_2 - B_2O_3 - P_2O_5$

SiO_2 (1996°K)

P_2O_5 (842°K)

$2S \cdot P$ (1393°K)

$S \cdot P$ (1563°K)

$A \cdot 3P$

$A \cdot P$

$B \cdot P$ (1723°K)

$3A \cdot 2S$ (2123°K)

Al_2O_3 (2323°K)

SBA-10 BINDER (TERNARY SURFACE)

FIBER COMPOSITION (WITHIN TETRAHEDRON)

(1308°K) $2A \cdot B$

(2225°K) $9A \cdot 2B$

B_2O_3 (723°K)

$A = Al_2O_3$ $B = B_2O_3$ $S = SiO_2$ $P = P_2O_5$

Figure 1

229
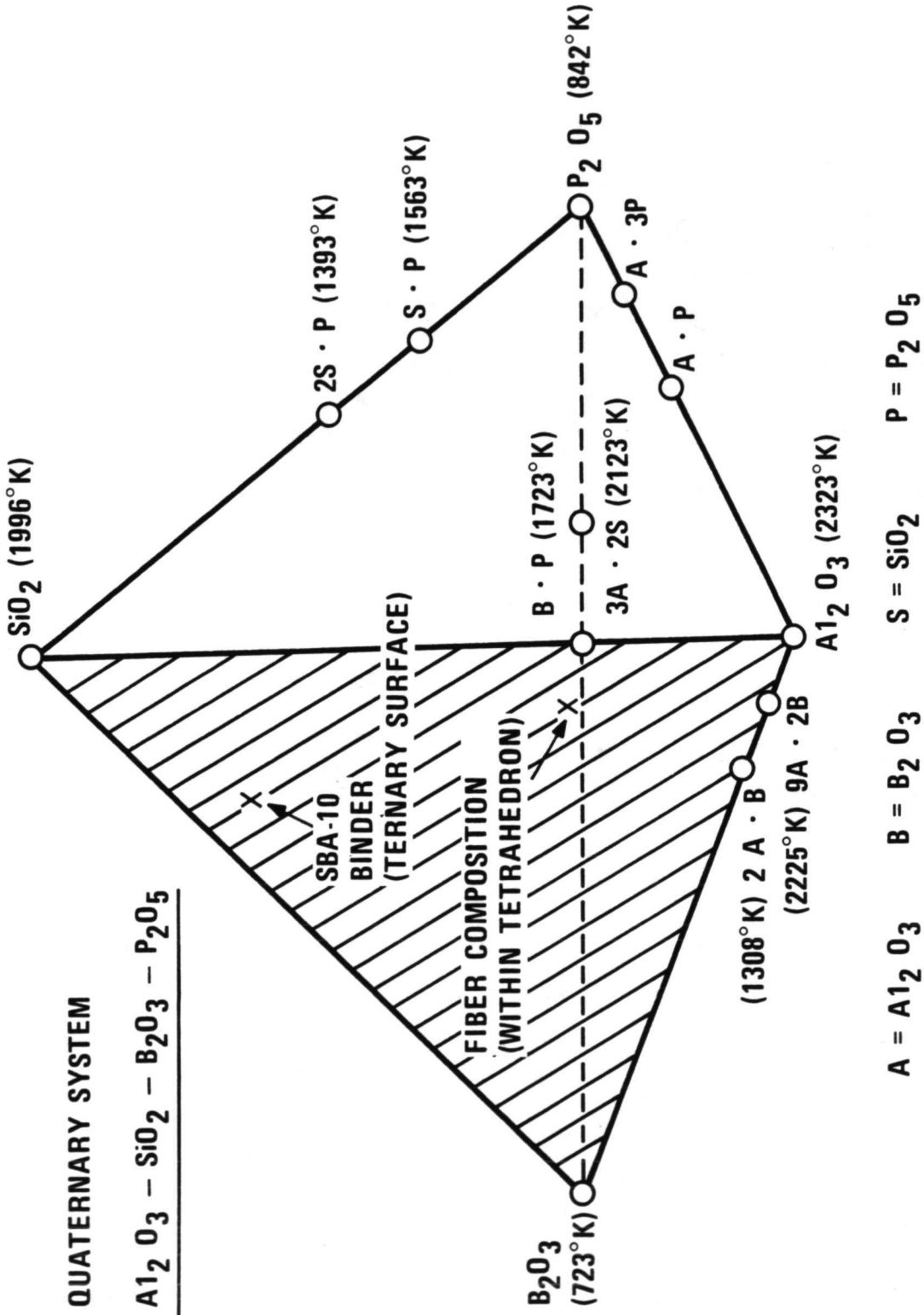
PHASE STABILITY OF MOD-1B REI-MULLITE

(Figure 2)

One of the major attributes of the REI-Mullite system is its phase stability at temperatures of 1644°K (2500°F) and above. The basic insulation has a relatively low and well-behaved thermal expansion and is refractory up to its melting point [2089°K (3300°F)]. Figure 2 shows x-ray diffraction patterns of a panel (a) as fabricated and (b) after an extended heat treatment at 1644°K (2500°F). In both instances, the major phase is mullite. Minor phases include aluminum borate and an amorphous glassy phase. It should be noted that the amorphous content of the composite is reduced slightly after the extended heat treatment.

All the REI-Mullites studied to date (Mod-0, 1, 1A, and 1B) have had the common feature of dimensional and crystallographic thermal stability when exposed to peak temperature of 1644°K (2500°F) for times equivalent to 100 mission exposure.

230

PHASE STABILITY OF MOD-1B REI-MULLITE

AS FABRICATED
UNMARKED LINES — MULLITE
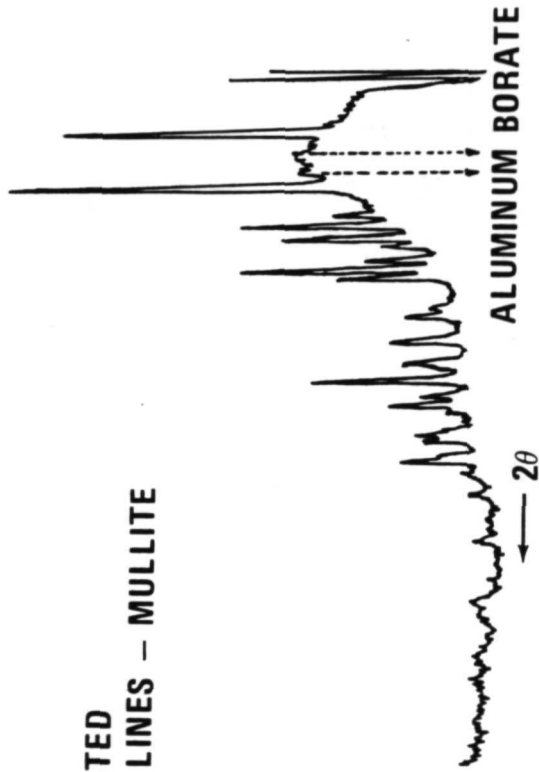
12 HR AT 1644°K (2500°F) IN AIR
UNMARKED LINES — MULLITE
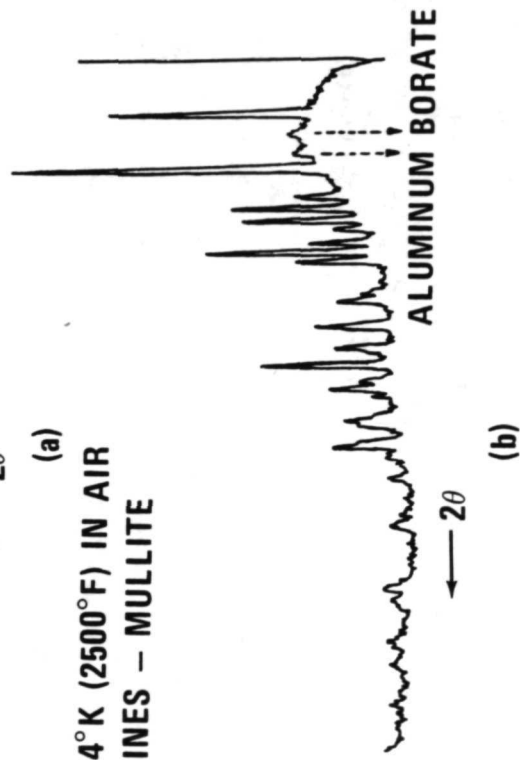
Figure 2

DIMENSIONAL STABILITY AFTER 5 HR EXPOSURE AT 1644°K AS A FUNCTION OF FIBER COMPOSITION

(Figure 3)

Dimensional stability (which is closely related to phase stability) is an important attribute of the REI-Mullite system. The major parameter controlling shrinkage appears to be the mullite/silica ratio of the fiber. For example, Figure 3 shows the volume shrinkage for three rigidized composites using the SBA-10 binder. Each composite was isothermally heat-treated at 1644° K (2500°F) for five hours. In order to ensure dimensional stability at 164° K (2500°F), the Al_2O_3/SiO_2 ratio should exceed the stoichiometric mullite ratio of 2.7 (based upon weight percent). Free silica rapidly transforms to cristobolite under this environmental exposure with severe dimensional discontinuity. Hence, even a relatively small fraction of free silica in the fiber can cause substantial disruption of the fiber structure. As shown in Figure 3, an order of magnitude reduction in shrinkage is achieved when the stoichiometric mullite ratio is exceeded. Needless to say, the lack of dimensional stability manifests itself in the development of tensile residual strains which severely limit system capability. In the worst instance, complete loss of the TPS due to severe distortion could occur if an over-temperature situation arises.

DIMENSIONAL STABILITY AFTER 5 HR EXPOSURE
AT 1644°K AS A FUNCTION OF FIBER COMPOSITION

FIBER	PANEL DENSITY		FIBER COMPOSITION[1]		SHRINKAGE VOL. (%)
	Kg/m³	pcf	W/O MULLITE	W/O SILICA	
BABCOCK & WILCOX 4.7 μm MULLITE	192	12.0	~ 100%		0.5
CARBORUNDUM FIBERFRAX H	192	12.0	~ 87%	~ 13%	4.5
J.M. MICROQUARTZ (HIGH PURITY)	272	17.0		~ 100%	5.8

(1) ESTIMATED FROM PHASE EQUILIBRIUM DIAGRAM.

Figure 3

THREE-DIMENSIONAL ALTERNATE CUBE SPACE FRAME MODEL

(Figure 4)

In an attempt to establish strength and strain goals for the fibrous composites with low fiber volume fractions, a mathematical model has been developed that idealizes REI in terms of a three-dimensional truss. Figure illustrates the alternate-cube space frame array utilized in the modeling study. The sectional views are in the directions of the positive axes. Fitting the truss-sections A1, C1, E1, normal to truss-section A2, C2, E2, and also to subsequent truss sections, forms an alternating-cube arrangement of truss elements in three dimensional space. The cube face diagonals form the plane of isotropy. Thus, small θ angles yield results representative of across-plane (or Z direction) properties while large θ angles yield results representative of in-plane (or XY direction) properties.

The photomicrograph shown in Figure 4 illustrates a typical XY plane (assumed to be the plane of isotropy). Typical joint spacings (ℓ) vary from 50 to 100 microns while total fiber lengths average in the 200 to 400 micron range. Fibers have been studied in the laboratory with diameters ranging from 3 to 8 μm.

The implications of this model suggested modifications in the fabrication procedures leading to significantly enhanced mechanical properties in the Mod 1B REI-Mullite.

234

THREE-DIMENSIONAL ALTERNATE CUBE SPACE
FRAME MODEL

TRUSS A2, C2, E2, ETC.

TRUSS A1, C1, E1, ETC.

LOADING DIRECTION
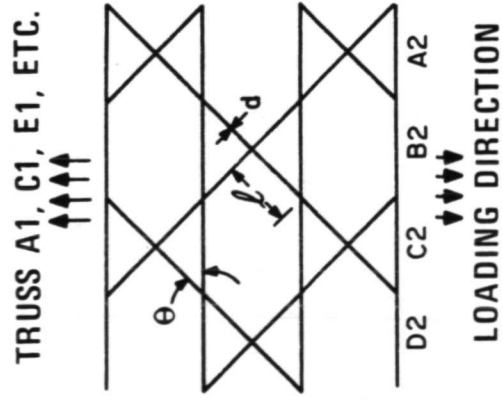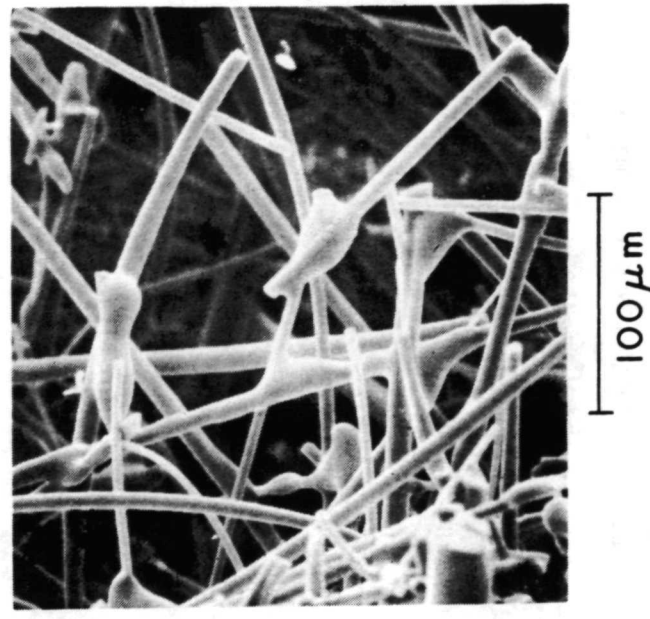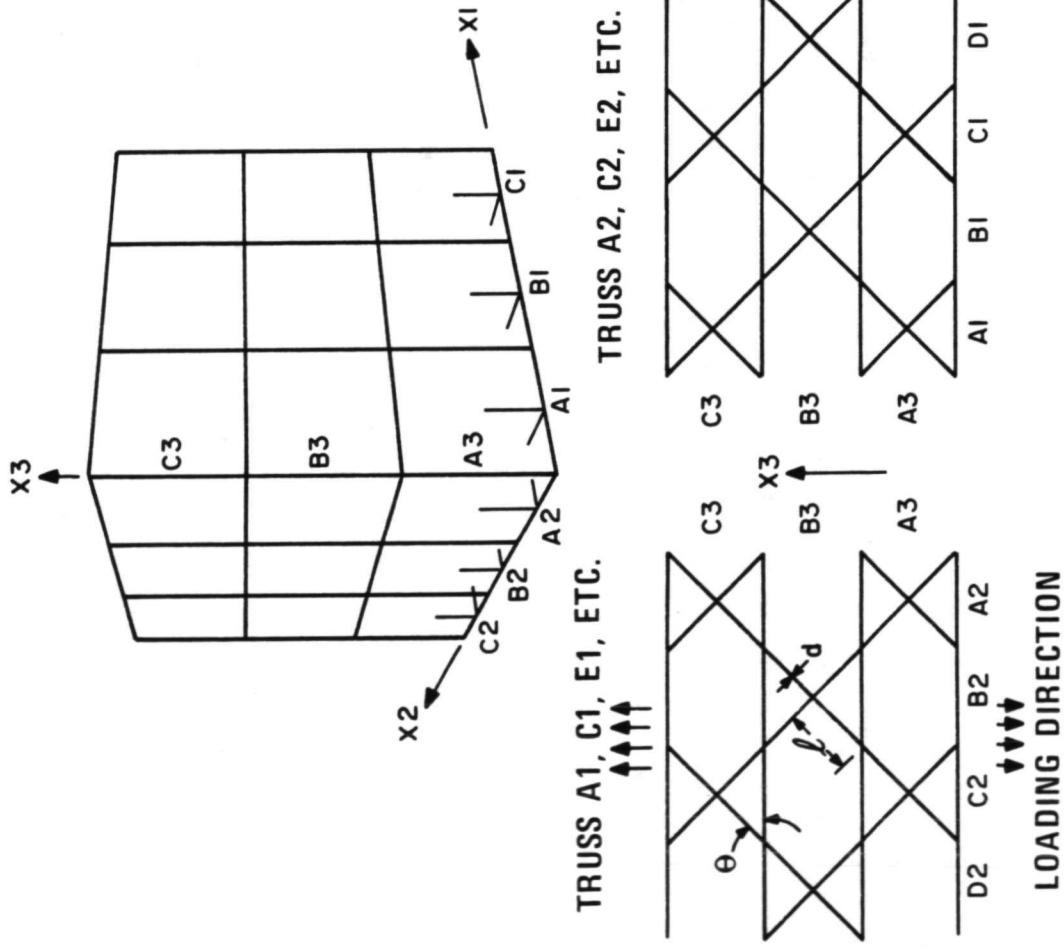
Figure 4

STRESS COMPONENTS ASSUMED IN MATHEMATICAL MODEL

(Figure 5)

The stresses in the space frame may be viewed as resulting from three principal effects, as described in Figure 5. First, there are direct axial stresses in the members, which are the type of stresses that would result from a given geometry with all joints pin-ended (i.e., no restraint against rotation). Second, there are the bending stresses resulting from joint fixity. (Note typical fixed joint in accompanying photomicrograph.) Finally, there are the bending stresses resulting from the fact that the frame members were not initially straight.

Additional model assumptions used in the derivation of the governing equations for the evaluation of these stresses include the following:

1. Fiber diameter (d) is the same for all the truss members.

2. The inclined diagonals are all of the same length (joint spacing, ℓ).

3. The modulus of elasticity (E) and the initial out-of-straightness (a) are the same for all members.

4. Fiber eccentricity (e) is defined as the ratio of out-of-straightness (a) to fiber diameter (d).

236

STRESS COMPONENTS ASSUMED
IN MATHEMATICAL MODEL

TOTAL STRESS WITHIN FIBER IS A COMBINED EFFECT
OF THREE STRESS COMPONENTS

AXIAL STRESS

+

BENDING STRESS
DUE TO FIXITY
OF JOINT

+

BENDING STRESS
DUE TO INITIAL
CURVATURE

237
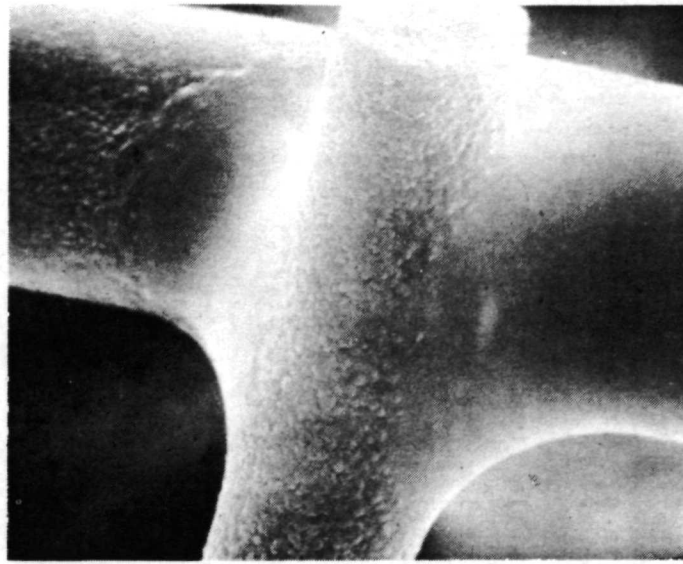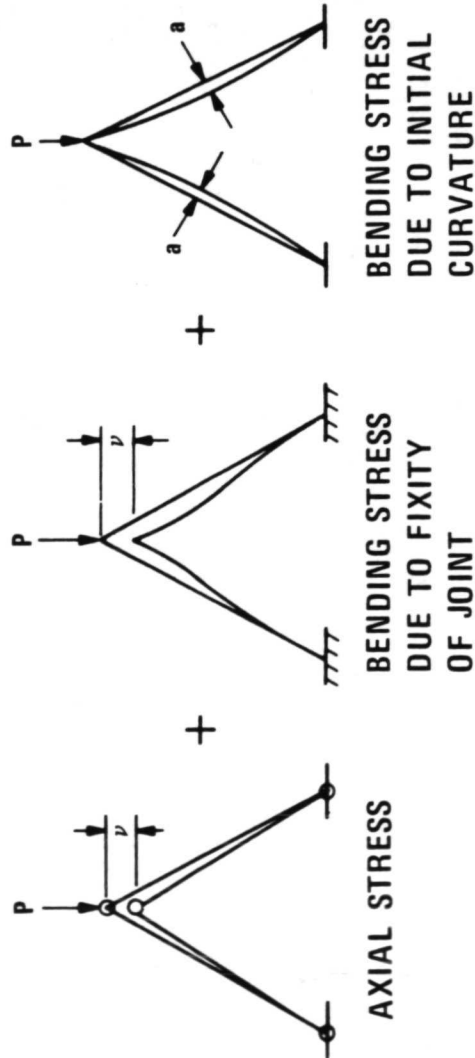
Figure 5

TYPICAL MECHANICAL BEHAVIOR PREDICTIONS OF THE MICROMECHANICAL MODEL

(Figure 6)

Numberical results have been obtained showing the variation of ultimate strength, strain and modulus of elasticity as functions of fiber eccentricity, e, the truss angle, θ, the ratio of joint spacing to fiber diameter, ℓ/d, and the allowable failure stress in the fiber. Fiber strength values of 344.8 MN/m² (50 ksi) and 689.5 MN/m² (100 ksi) were used along with a Young's modulus of 137.9 GN/m² (20 × 10⁶ psi).

Figure 6 shows the effect of truss variables on the ultimate tensile strain capability. As verified experimentally, the highest strain levels are associated with the low θ (Z direction) orientation. Higher strain levels are associated with the highest degrees of eccentricity. Also, the larger the joint spacing, the larger the ultimate strain capability, especially for low θ (Z direction) orientations. Measured in-plane tensile strain capability of Mod-1B REI-Mullite matches the value predicted by the model for the parameters indicated, although the predicted strain in the Z direction is higher than measured.

The developmental fabrication procedures being evaluated for REI-Mullite are designed to decrease θ and enhance the strain in the XY plane. In addition, heat treating techniques have been devised for this material to increase the population and quality of the fiber-to-fiber joints (Mod 1B REI-Mullite). An extensive discussion of the micromechanical modeling research is described in the communication noted below and in Reference 2.

238

B. W. Rosen and D. K. Bagchi, "Materials Sciences Corp.," Blue Bell, Pa. Private communication to R. A. Tanzilli.

TYPICAL MECHANICAL BEHAVIOR PREDICTIONS
OF THE MICROMECHANICAL MODEL

VARIATION OF ULTIMATE·STRAIN WITH ANGLE, θ
(VOL. FRACTION = 0.05)
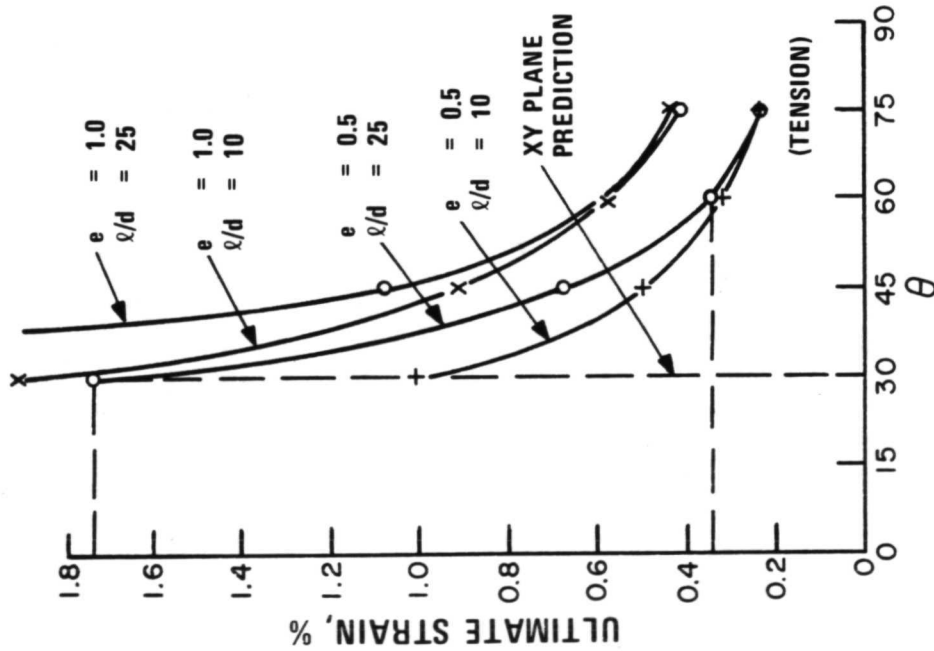
- MOD 1-B REI-MULLITE XY STRAIN DATA $\sim$ $\left[\dfrac{0.35\%}{0.50\%}\right]$
  Z STRAIN DATA $\sim$

- FOR $\ell/d \sim 25$, $\ell = 0.5$, $\theta \sim 60°$ (TYPICAL X-Y
  PARAMETERS DEDUCED BY SEM)
  ULTIMATE STRAIN PREDICTION

  XY $\sim$ $\left[\dfrac{0.35\%}{1.7\%}\right]$
  Z $\sim$

Figure 6

239

EFFECT OF FIBER DIAMETER VARIATIONS ON THERMAL CONDUCTIVITY
(Figure 7)

For fibrous insulations, the principal mode of heat transfer at elevated temperatures is by thermal radiation. In general the radiative contribution can be estimated from an empirical fit of the data with an equation of the form:

$$k_r = CT^m$$

where

C and m = Empirical constants determined by experiment

In order to proceed with a systematic optimization program, it is necessary to define the material variables that affect radiative transfer. Several theoretical models have been proposed which interpret these variables theoretically and thus provide the basis for a systematic experimental evaluation. For example, Larkin and Churchill (Reference 3) developed the following expression:

$$k_r = \frac{8\sigma T^3}{A + 2S}$$

where:

A = Absorption cross-section of the fibrous insulation

S = Back scattering cross-section of the fibrous insulation.

The coefficients A and S are readily determined experimentally from spectral transmission measurements. Their study identified fiber diameter as a major variable effecting the backscattering cross-section and fiber: void volume opacity as the variable effecting the absorption cross-section.

Recent experimental evaluations of fiber diameter effects on thermal conductivity have demonstrated that a rather dramatic reduction in thermal conductivity is achieved through the use of small diameter mullite fibers. Figure 7 compares the total thermal conductivity function of the current Mod IB REI-Mullite with a similar density panel fabricated using a 1.7 μm alumina-silica fiber and the SBA-10 binder. A thermal conductivity reduction greater than a factor of two has been measured over typical orbiter re-entry pressure and temperature regimes. It should be noted that Babcock and Wilcox Company is producing, on an experimental basis, mullite fibers with the majority of the fibers below 2 μm under NASA-Lewis sponsorship (Contract No. NAS 3-16764). At the conclusion of the contract activities, B&W will make a decision regarding higher production quantities.

It should be noted that, on the basis of a recently developed TPS weight correlation parameter, $W \sim (k/C_p)^{1/2} (\rho)^{7/8}$, the project flight insulation weight (using 1.7 μm diameter mullite fibers) will be 30% less than the current Mod IB REI-Mullite insulation weight.

EFFECT OF FIBER DIAMETER VARIATIONS ON THERMAL CONDUCTIVITY
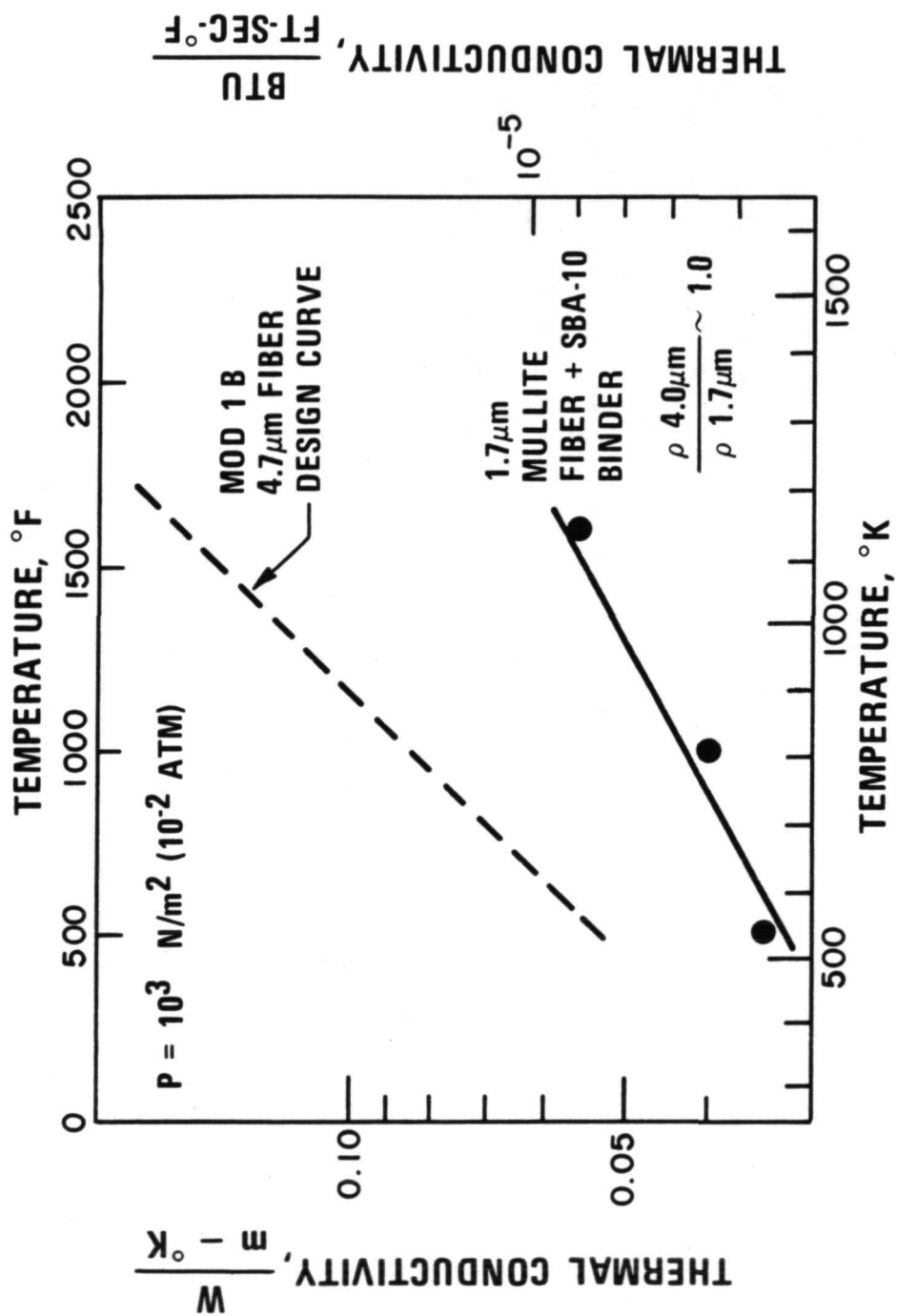
Figure 7

EFFECT OF Cr₂O₃ FIBER: VOID OPACIFICATION ON THERMAL CONDUCTIVITY

(Figure 8)

Additional reductions in thermal conductivity can be achieved through the utilization of opacification techniques to attenuate thermal radiation transfer through fibrous insulations. The development of a novel technique for applying a near-continuous fiber coating of chromia platelets on mullite fibers (Figure 8 (a)) has enabled a direct quantitative assessment of this heat transfer attenuation mechanism to be made.

Figure 8(b) compares the thermal conductivity function for chromia opacificied REI-Mullite with that of unopaci-fied REI-Mullite. Above temperatures of 1100°K, a significant reduction in thermal conductivity has been achieved (approaching a factor of 2) at 1644°K (2500°F). Another advantage of the fiber coating is that it acts as a direct thermal radiation barrier to any transmitted component as illustrated by the comparative transmission measurements in Figure 8(c).

Although void opacification has not been incorporated into the current production of REI-Mullite, such imple-mentation will yield a substantial TPS weight reduction.

The combined effect of small diameter fibers and fiber: void opacification when implemented into the REI-Mullite system should lead to TPS weight reductions approaching a factor of two.
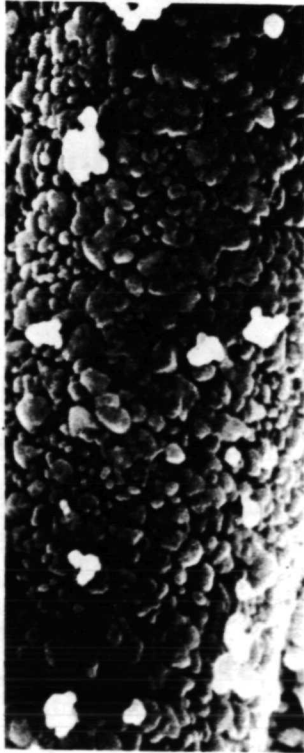
242

EFFECT OF Cr₂O₃ FIBER: VOID OPACIFICATION
ON THERMAL CONDUCTIVITY
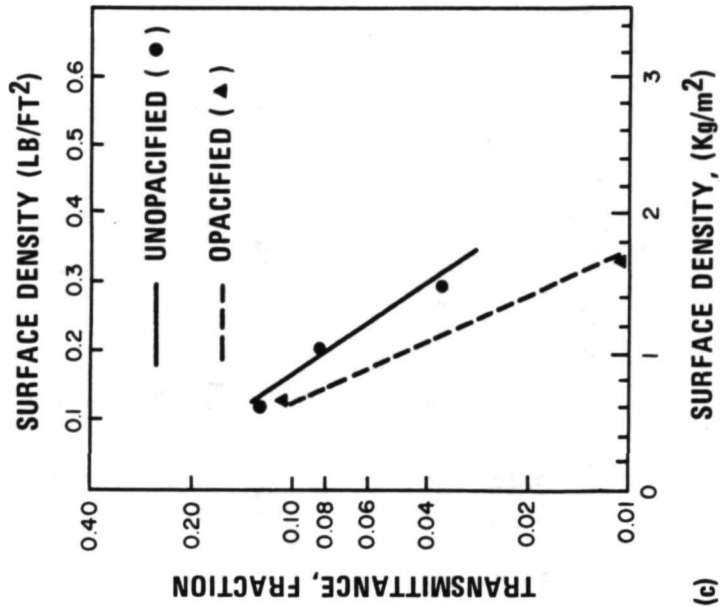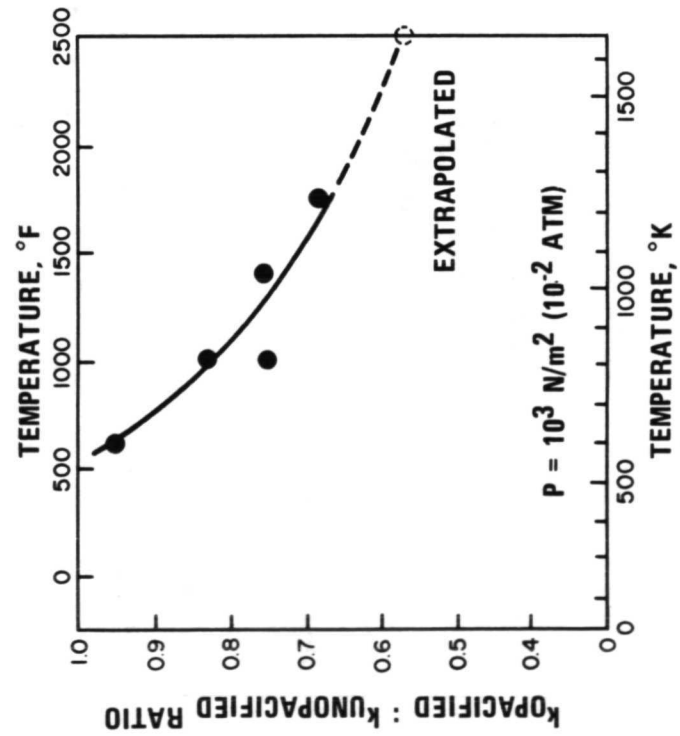
Figure 8

GUARDED HOT PLATE METHOD FOR HIGH TEMPERATURE
THERMAL CONDUCTIVITY MEASUREMENTS

(Figure 9)

Thermal conductivity measurements illustrated in Figures 7 and 8 were made utilizing a guarded hot plate thermal conductivity apparatus. This instrument is capable of making high accuracy thermal conductivity measurements from cryogenic temperatures to 1273°K and is designed to be operated in accordance with ASTM specification C-177 (Revision 1). The principles of operation are illustrated in Figure 9. In order to ensure one-dimensional heat transfer the main heater is guarded by a sensitive electronic proportional controller through sensing action of an eight junction thermopile.

Also shown in Figure 9 is an error analysis for this conservative measurement technique. Substantial errors may be introduced if the guarding criteria, $|T_M - T_G/\Delta T| \leq 0.1$ is exceeded. Because this conservative measurement is sensitive to guarding errors, one must be especially concerned about errors introduced in far less conservative heat transfer tests (e.g., comparator techniques, entry simulation testing) where provisions for appropriate geometry and guarding to insure one dimensional heat transfer may be compromised in terms of expediency or facility limitations.

244

GUARDED HOT PLATE METHOD
FOR THERMAL CONDUCTIVITY

- APPLICABLE TO INSULATIVE MATERIALS WITH $k < 17.3 \, \frac{W}{m \, ^{\circ}K}$ $\left(10 \, \frac{BTU}{ft\text{-}hr - ^{\circ}F}\right)$

- PRINCIPLE: ELECTRICAL HEAT IN CENTRAL HEATER (D.C.) GUARDED BY ANNULAR GUARD RING HEATER TO ELIMINATE RADIAL TEMPERATURE GRADIENT

$$\therefore \quad \dot{Q} = 2k \frac{(T_{HOT} - T_{COLD})}{\Delta X} [AREA]$$

VXI ← TWO SPECIMENS

ΔX ← SPECIMEN THICKNESS

[AREA] ← AREA OF CENTRAL HEATER

ASTM C177 (1971 REVISION) REQUIRES

$$\left| \frac{T_M - T_G}{\Delta T} \right| \leq 0.1$$

$T_M - T_G$ – GUARD ERROR

ΔT – SPECIMEN TEMP. DROP

Figure 9

POWDER INSULATION

AUXILLIARY GUARD

WATER-COOLED SHROUD CONTAINS STACK

8 JUNCTION THERMOPILE

MAIN GUARD CONTROLLER: GUARD RING TO MAIN HEATER

TEMP CONTROLLER: OUTER GUARD TO SAMPLE EDGE

H_2O

TOP SPECIMEN
GUARD HEAT – MAIN HEATER (D.C.) ER RING (A.C.)
BOTTOM SPECIMEN
BOTTOM COLD FACE HEATER

SCALE, METERS (FROM MAIN HEATER)

D.C. AMPS D.C. VOLTS
DIGITAL VOLT METER
VXI = WATTS

D.C. VOLTS METER

COOLING H_2O

SET-POINT TEMPERATURE CONTROLLERS

FIBROUS INSULATIONS $P = 10^3 \, N/m^2$ $(10^{-2} \, atm)$

k/k_0

$922 \, ^{\circ}K \, (1200 \, ^{\circ}F)$

$533 \, ^{\circ}K \, (500 \, ^{\circ}F)$

$\frac{T_M - T_G}{\Delta T}$

245

MOD-1B REI-MULLITE SURFACE COATING DESIGN

(Figure 10)

The SR-2 type filled glaze surface coating is a multicomponent material with each component selected for a primary function as listed in the figure. The coating is chemically compatible with the REI-Mullite insulation substrate at the temperatures and mission environments encountered by the shuttle TPS.

The pigment component for the Mod-1B REI-Mullite has been designed to meet both the orbital and re-entry optical requirements.

MOD 1B REI-MULLITE SURFACE COATING DESIGN

COMPONENT	COMPOSITION	PRIMARY FUNCTION
KYANITE	$3Al_2O_3 \cdot 3SiO_2$	STABLE FILLER
PETALITE	$Li_2O \cdot Al_2O_3 \cdot 8SiO_2$	THERMAL EXPANSION CONTROL
GLASS	$SiO_2 - Al_2O_3 - MgO - CaO$	STRENGTH, H_2O REPELLENCY, NON CATALYCITY
PIGMENT	H_fO_2	THERMAL RADIATIVE PROPERTY CONTROL

Figure 10

247

ORIGIN OF ORBITAL AND ENTRY THERMAL RADIATIVE REQUIREMENTS

(Figure 11)

The forcing functions for both the orbital and entry thermal radiative requirements are graphically illustrated in Figure 11(a) and (b). During orbit, the REI equilibrium temperatures are proportional to the fourth root of the solar absorptance/emittance ratio (α_S/ϵ_H), as plotted in Figure 11(a). Current NR/SD* design requirements have established an α_S/ϵ_H ratio of 0.40-0.50 as an optimum goal for orbital temperature control. The criticality of achieving this goal is illustrated from one point of view in Figure 11(b) where normalized basic insulation thickness is plotted as a function of initial entry temperature (or α_S/ϵ_H ratio). The thickness relationship holds true for the entire TPS surface area and, therefore, has significant systems weight impact.

Also of equal importance is the simultaneous achievement of a high temperature emittance during re-entry as illustrated by the surface boundary condition in Figure 11(b). The systems weight impact of high temperature emissivity, although significant, is less than that of α/ϵ control, primarily because its effect decreases with peak surface temperature.

It should be noted that recent plasma arc experiments conducted by NASA-Ames have indicated that an effective emittance, which includes the beneficial effects of the noncatalytic nature of the SR-series coatings, is a more realistic parameter for expressing this boundary condition.

---

*North American Rockwell Corporation, Space Division (NR/SD)

ORIGIN OF ORBITAL AND ENTRY
THERMAL RADIATIVE REQUIREMENTS

ORBITAL PHASE

RE-ENTRY PHASE

- NON CATALYTICITY EFFECTS

$$(\epsilon_H)EFF = \frac{\epsilon_H}{q} \text{ WHERE } q = q \text{ (ACTUAL)}/q \text{ (FULLY CATALYTIC)}$$

$$q_{NET} \approx q_{CONV} \cdot \epsilon_H \sigma T_s^4$$

$$T_s \approx \left[\left(\frac{\alpha_s}{\epsilon_H} \right) \frac{S}{\sigma} \right]^{1/4}$$

Figure 11

249
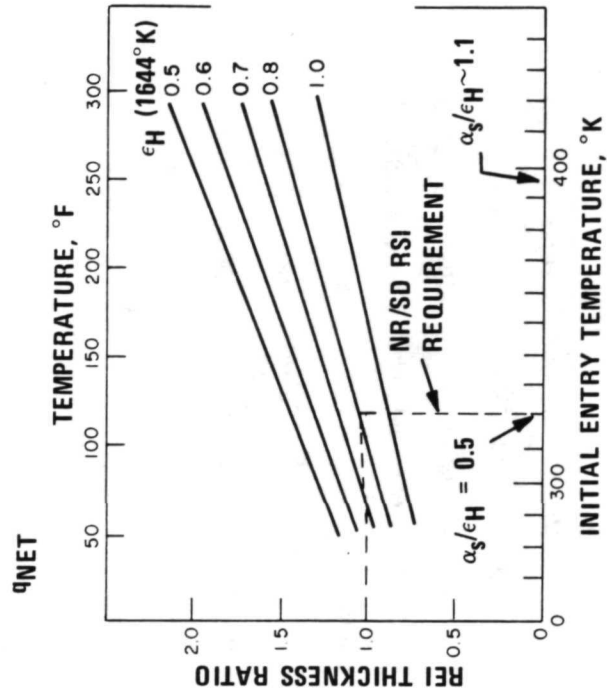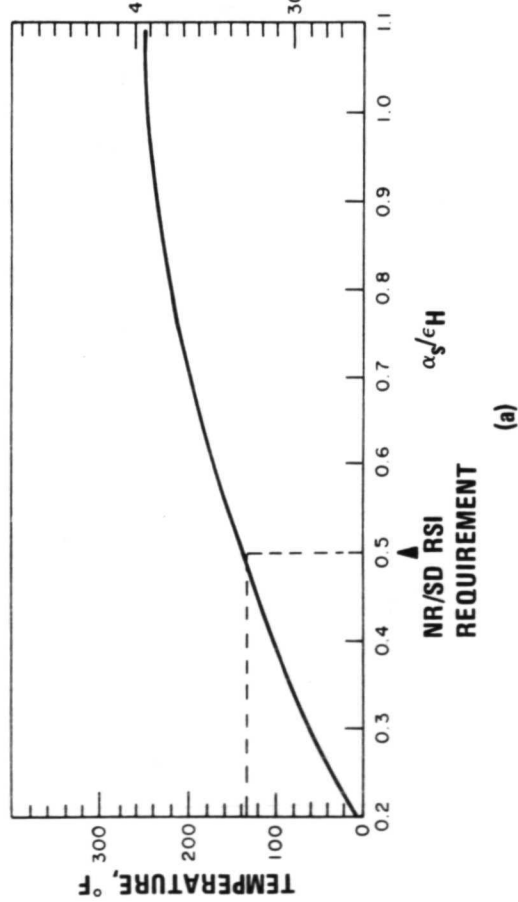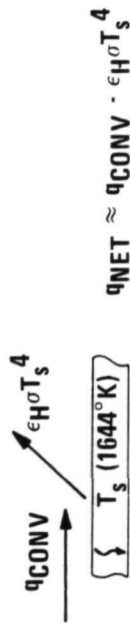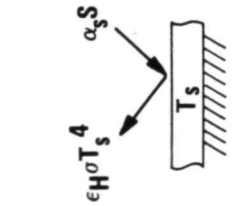
SELECTION OF AN OPTIMIZED THERMAL RADIATIVE COATING SYSTEM

(Figure 12)

The experimental approach taken focused initially upon meeting the orbital requirement. A hypothetical "ideal" coating was defined that exceeded the NR/SD on orbit requirements. This served as a basis for screening candidate coating systems. Figure 12 (a) and (b) shows the nature of this "ideal" coating in terms of its spectral reflectance distribution over the range of pertinent wavelengths, which are used for estimating solar absorptance and both low and high temperature emittance. Figure 12(c) lists the equations used for evaluating these functions numerically. As a point of reference, the peaks of the respective black-body energy distributions are listed. Thus, in order to meet the solar absorptance goal, a high reflectance is required between 0.4 and 1 micron. The low temperature emittance requirement is achieved with a coating which has a low reflectance in the 2 to 25 micron region. The more difficult to achieve high temperature emittance property requires low spectral reflectance down to 1.5 microns, at which point an abrupt rise in reflectance is required to maintain the spectral reflectance required for optimum solar absorptance.

A comparison of spectral reflectance functions for several candidates, SR-2 (NiO pigment), SR-2 (without pigment), and the SR-2 HF1 (HfO$_2$ pigment) are shown in Figure 12(a) and (b), together with integrated values of their respective solar absorptance and emittance. The hafnia pigmented SR-2 coating is seen to most closely approach the ideal function and meets the current NR/SD orbital requirement for a solar absorptance/emittance ratio of 0.4-0.5.

250

SELECTION OF AN OPTIMIZED
THERMAL RADIATIVE COATING SYSTEM

- **SOLAR ABSORPTANCE**

$$\alpha_s = \frac{\sum\limits_{0.3\mu}^{3\mu} (1 - R_\lambda) \, S_\lambda \; \Delta\lambda}{\sum\limits_{0.3\mu}^{3\mu} S_\lambda \; \Delta\lambda} \qquad \text{(PEAK AT 0.5}\mu\text{)}$$

CODE	PIGMENT	α_s
-----	OPTIMUM	0.32
--·--·--	$H_f O_2$	0.38
--·--·--	NONE	0.48
———	NiO	0.72

- **EMITTANCE AT 311°K (100°F)**

$$\epsilon_H = \frac{\sum\limits_{1\mu}^{25\mu} (1 - R_\lambda) \, E_{b\lambda} \, (311°K) \; \Delta\lambda}{\sum\limits_{1\mu}^{25\mu} E_{b\lambda} \, (311°K) \; \Delta\lambda} \qquad \text{(PEAK AT 9}\mu\text{)}$$

CODE	PIGMENT	$\epsilon_H \left[311°K \; (100°F) \right]$
--·--·--	NONE	0.61
———	NiO	0.67
--·--·--	$H_f O_2$	0.79
-----	OPTIMUM	0.90

- **EMITTANCE AT 1644°K (2500°F)**

$$\epsilon_H = \frac{\sum\limits_{1\mu}^{10\mu} (1 - R_\lambda) \, E_{b\lambda} \, (1644°K) \; \Delta\lambda}{\sum\limits_{1\mu}^{10\mu} E_{b\lambda} \, (1644°K) \; \Delta\lambda} \qquad \text{(PEAK AT 1.8}\mu\text{)}$$

Figure 12

251
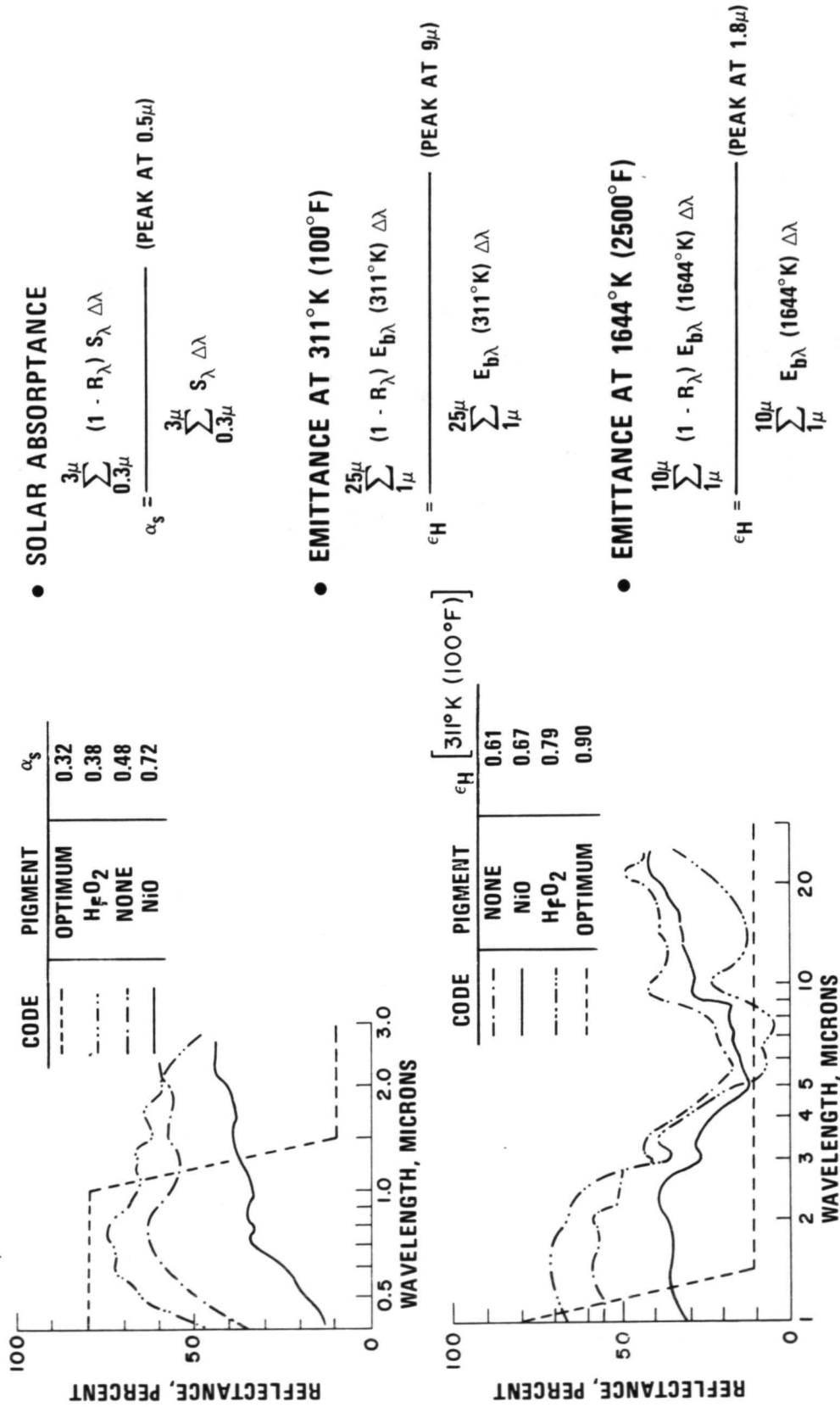
SUMMARY OF THERMAL RADIATIVE PROPERTY DATA
(Figure 13)

The SR-2 HF-1 coating system meets the NR/SD orbital α_S/ϵ_H requirement of 0.4-0.5, and also exceeds the entry emittance requirement of 0.80 at 1644°K (2500°F) as a result of its fully noncatalytic surface characteristics. A summary of the current status of the thermal radiative temperature control developments is given in Figure 13. It should be noted that the good agreement in the computed and measured high temperature emittance data indicates that only a slight shift in the composite coating absorption edge occurs as a function of temperature for the candidates screened.

252

SUMMARY
OF THERMAL RADIATIVE PROPERTY DATA

MAJOR PIGMENT	α_S	ϵ_H (311°K)	α_S/ϵ_H (311°K)	COMPUTED (1) ϵ_H (1644°K)	COMPUTED (1) ϵ_H (1366°K)	ϵ_H (T > 1366°K) LAB MEAS. (2) ϵ_H (1366°K)	ϵ_H (T > 1366°K) AIR ARC MEAS. (3) $\epsilon_{EFF} = \epsilon_H/\bar{q}$ (T > 1366°K)
NR/SD REQUIREMENT	NA	NA	0.40-0.50 / 0.48	> 0.80	NA	NA	NA
H_fO_2 (SR-2 HF1)	0.38	0.79	0.48	0.52	0.60	0.56	> 1.00
NONE	0.48	0.61	0.79	0.53	0.58	0.65	TBM
NiO (SR-2)	0.72	0.67	1.10	0.68	0.67	0.70	> 1.00

(1) COMPUTED FROM ROOM TEMPERATURE SPECTRAL DATA

(2) DEDUCED FROM DIRECT TOTAL NORMAL EMITTANCE MEASUREMENTS

(3) DEDUCED FROM NASA-AMES ARC TESTS

NOTE: COATINGS ARE FULLY NON CATALYTIC, I.E., $\epsilon_{EFF} = \dfrac{\epsilon_H}{\bar{q}} > 1.00$

WHERE $\bar{q} = \dot{q}$ (ACTUAL)/$\dot{q}$ (FULLY CATALYTIC)

Figure 13

253

MICROSTRUCTURE OF SR-2 TYPE FILLED GLAZE SURFACE COATINGS

(Figure 14)

Typical microstructure for the SR-2 HF1 coating (HfO_2 pigment) used on the Mod-1B REI-Mullite is shown on Figure 14(a). In addition to providing both the orbital and re-entry thermal radiative property requirements in a single fully reusable coating, the hafnia pigment has imparted a virtually pore-free structure when compared with the earlier version of the SR-2 coating shown in Figure 14(b). The hafnia modification has also imparted improved mechanical strength to the coating.

MICROSTRUCTURE OF SR-2 TYPE
FILLED GLAZE SURFACE COATINGS

SR-2
COATING
(NiO PIGMENT)

(b)

SURFACE COATING

RIGIDIZED MULLITE
FIBER INSULATION

SR-2 HFI
COATING
(HfO₂ PIGMENT)

(a)

100 μm

100 μm

Figure 14

X-RAY DIFFRACTION PATTERNS OF THE SR-2 HF1 COATING

(Figure 15)

Figure 15 illustrates a typical x-ray diffraction pattern for the current hafnia modified (SR-2 HF-1) coating system. The major phases include mullite, hafnium silicate, hafnium oxide, and an amorphous glass phase. The current system retains its phase stability after extended high-temperature exposures, which is a requirement for system effectiveness.

256

X-RAY DIFFRACTION PATTERN
OF THE SR-2 HF1 COATING

M = MULLITE

– – – = COMBINATION

HAFNIUM SILICATE

HAFNIUM OXIDE

2θ
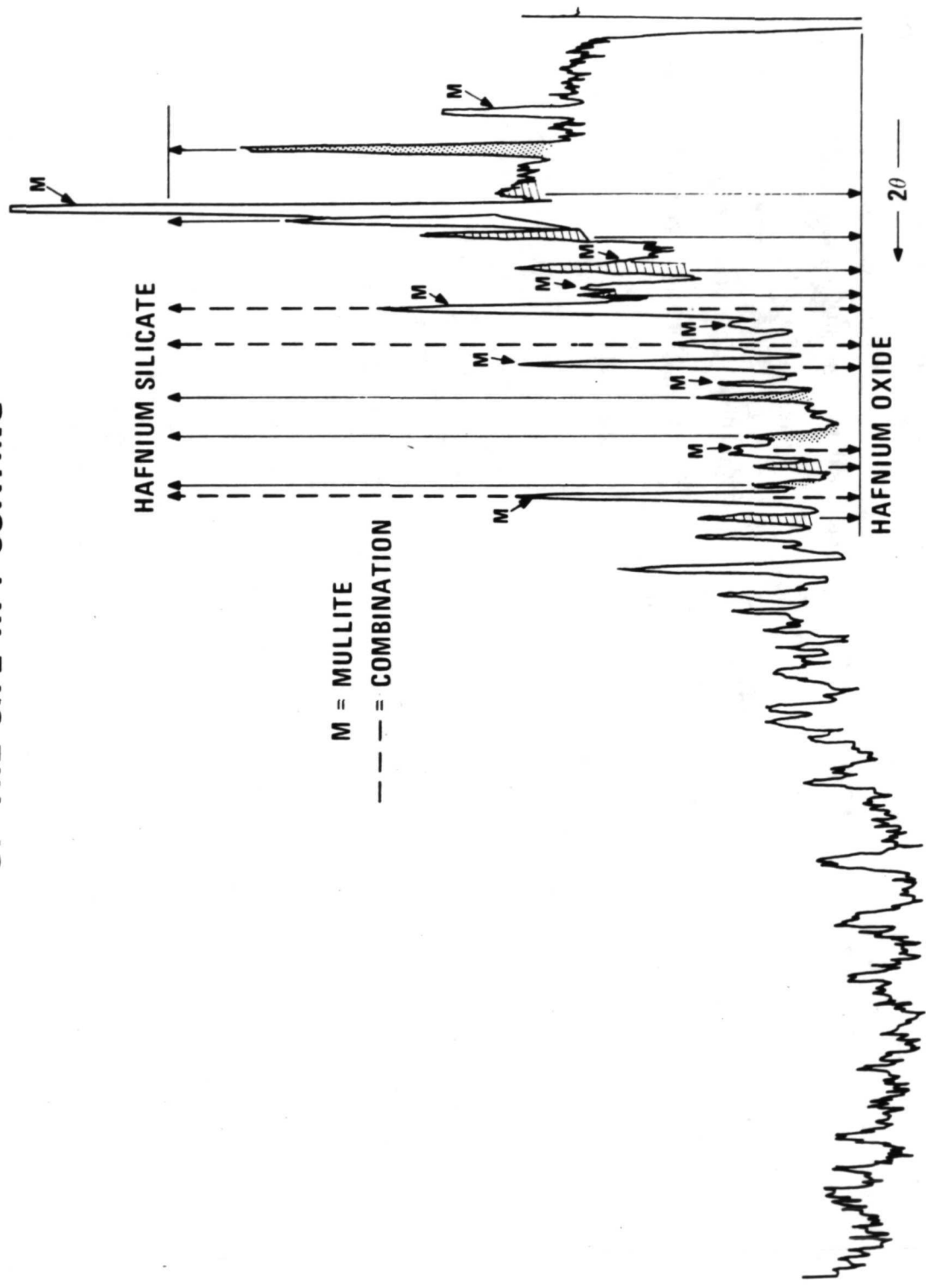
Figure 15

SUMMARY
(Figure 16)

The current Mod 1-B REI-Mullite system, using the B&W mullite fiber and the SBA-10 binder, has been found to be the only fiber-binder combination that satisfies the phase and dimensional stability requirements for continuous reuse at 1644° K (2500°F). In addition, projected reductions in basic insulation weight by a factor of two can be achieved through the use of small diameter fibers (1-2 μm) and fiber/void volume opacification.

Recent improvements in the SR-2 series coating by the incorporation of a hafnia pigment has enabled the total thermal radiative property requirements for orbit and re-entry to be satisfied with a single reusable coating system. Continued refinements in the mechanical and thermal properties of the SR-2 HF-1 coating are foreseen for this highly tailorable coating system.

SUMMARY

- REI-MULLITE IS THE ONLY SYSTEM CAPABLE OF SHUTTLE TPS REUSE TO 1644°K (2500°F).

- HAFNIA PIGMENTED SR-2 SURFACE COATING MEETS BOTH ORBITAL AND RE-ENTRY THERMAL RADIATIVE REQUIREMENTS FOR REUSE WITHOUT REFURBISHMENT.

- THERMAL AND MECHANICAL MODELS HAVE BEEN DEVELOPED WHICH SHOW FURTHER GROWTH POTENTIAL ASSOCIATED WITH THE REI-MULLITE SYSTEM:

  - FACTOR OF 2 IMPROVEMENT IN MECHANICAL PROPERTIES

  - FACTOR OF 2-3 REDUCTION IN THERMAL CONDUCTIVITY

259

Figure 16

REFERENCES

1. R. N. Fetterolf, "Development of High Strength, High Modulus Fibers," AFML TR-70-197, August 1970.

2. R. A. Tanzilli (Editor), "Development of an External Ceramic Insulation for the Space Shuttle Orbiter," NASA CR-112038, April 1972.

3. B. K. Larkin and S. W. Churchill, A.I. Ch. E. Journal, Vol. 5, p. 467, 1959.

260

9

SILICA RSI MORPHOLOGY AND PROPERTIES

R. M. Beasley and J. C. Robinson
LOCKHEED MISSILES & SPACE COMPANY. INC.

SILICA RSI SELECTION
(Figure 1)

In considering materials for Shuttle TPS it was noted that most inorganics, particularly those available for fibrous RSI, exhibit many possible polymorphs. As indicated by the density variations noted in the figure, any polymorphic transformations would be accompanied by volumetric changes. Also, in the case of the crystalline phases, a further disruptive change-in-state, described as "grain growth," would probably occur within the Shuttle environmental envelope, primarily as a function of time, temperature, and minor mineralizing constituents.

These factors were considered along with possible mechanisms for their control, and the property characteristics of the polymorphs as related to the specific material dispositions required and influenced by the predicted Shuttle TPS envelope. It was found that transformation to crystalline silica generally involved heterogeneous surface nucleation and thus could be influenced by materials and processes. Further, this analysis readily identified that silica — in particular, amorphous silica, unquestionably offered the superior characteristics basic to the Shuttle TPS application, including

- Lowest theoretical density
- Lowest thermal expansion
- Lowest thermal conductivity
- Highest thermal shock resistance

262

SILICA RSI SELECTION

	COMPOSITION	NAME	DENSITY (gm/cc)	FORM
SILICA	SiO_2	QUARTZ	2.65	HEXAGONAL
	SiO_2	CRISTOBALITE	2.32	TETRAGONAL
	SiO_2	TRIDYMITE	2.26	RHOMBIC
	SiO_2	GLASS	2.20	AMORPHOUS
ALUMINUM SILICATE	$Al_2O_3 \cdot SiO_2$	KYANITE	3.6	TRICLINIC
	$Al_2O_3 \cdot SiO_2$	SILLIMANITE	3.25	RHOMBIC
	$Al_2O_3 \cdot SiO_2$	ANDALUSITE	3.20	RHOMBIC
	$3\,Al_2O_3 \cdot 2\,SiO_2$	MULLITE	3.16	RHOMBIC
	$3\,Al_2O_3 \cdot 2\,SiO_2$	GLASS	2.54	AMORPHOUS
MULLITE $(Al_2O_3 - SiO_2 - P_2O_5 - B_2O_3)$	$Al_2O_3 \cdot SiO_2$	KYANITE	3.6	TRICLINIC
	$Al_2O_3 \cdot SiO_2$	SILLIMANITE	3.25	RHOMBIC
	$Al_2O_3 \cdot SiO_2$	ANDALUSITE	3.20	RHOMBIC
	$3\,Al_2O_3 \cdot 2\,SiO_2$	MULLITE	3.16	RHOMBIC
	$3\,Al_2O_3 \cdot B_2O_3$	ALUMINUM BORATE	3.0	RHOMBIC
	$B_2O_3 \cdot P_2O_5$	BORON PHOSPHATE	2.80	TETRAGONAL
	$Al_2O_3 \cdot P_2O_5$	ALUMINUM PHOSPHATES	ISOMORPHOUS WITH FORMS OF SiO_2 AND 17 SPECIES	
	SiO_2	GLASS AND CRYSTALLINE FORMS	—	
	$B_2O_3 \cdot SiO_2$	BOROSILICATE GLASSES		AMORPHOUS
	$Al_2O_3 \cdot B_2O_3 \cdot SiO_2$	ALUMINUM BOROSILICATE	VARIOUS GLASSES AND CRYSTALLINE SPECIES	

SOURCE: BULLETIN OF NATIONAL RESEARCH COUNCIL NO. 118, NATIONAL ACADEMY OF SCIENCES

Figure 1

263

HOT STAGE X-RAY DIFFRACTION EVALUATION PROCEDURES
(Figure 2)

The potential variability of the morphology of inorganic materials was recognized from the beginning of development of LMSC's reusable insulation systems. An analytical method for assessing and characterizing this phenomena in relation to expected Shuttle heating was needed to guide material selection and RSI development activities – particularly those addressed to attaining phase stability.

Techniques were developed for X-ray diffraction evaluations under transient heating to attain plotable curves indicating change-of-state against temperature. The main elements established for hot stage X-ray diffraction are indicated in the figure. At best, the resulting data were considered to be roughly semiquantitative. No attempt was made to arrive at quantitative cristobalite values from this type of data, since variations in specimen densities and thicknesses were uncontrollable. Temperature gradients in the specimen were considered to be insignificant in the observation of devitrification, since the specimen thickness was such that greater than 99 percent of the diffracted intensity could be detected.

While the data were semiquantitative, this analytical tool was of great value in indicating initiation of devitrification and variation in morphology characteristics.

HOT STAGE X-RAY DIFFRACTION EVALUATION PROCEDURES

SAMPLE PREPARATION

- MATERIAL SAMPLE GROUND
- FORMED INTO .254 mm (10 mil) THICK SPECIMEN BETWEEN STAINLESS STEEL DIE FACES
- MOISTENED WITH DISTILLED WATER TO FORM ONTO HEATING ELEMENT

X-RAY EQUIPMENT

- NORELCO WIDE ANGLE X-RAY DIFFRACTOMETER
- Ni FILTERED Cu Kα RADIATION AT 40 KV AND 20 MA
- HOT STAGE, MATERIALS RESEARCH CORPORATION MODEL X-86-N-11
- HEATING ELEMENT, 40 PERCENT Rh-Pt RIBBON WITH 13 PERCENT Rh-Pt THERMOCOUPLE

X-RAY MEASUREMENT

- SCAN FROM 36 DEG 2θ TO 15 DEG 2θ AT ROOM AND ELEVATED TEMPERATURES UNTIL CRISTOBALITE 101 DIFFRACTION LINE STOPS INCREASING IN INTENSITY OR TO 1589°K (2400°F)

DATA

- AREAS UNDER CRISTOBALITE 101 AND QUARTZ 1011 LINES ARE PRODUCTS OF PEAK INTENSITY MINUS BACKGROUND AND WIDTH AT HALF MAXIMUM
- PLOT PRODUCTS AGAINST TEMPERATURE TO PRODUCE SEMI-QUANTITATIVE MATERIAL DEVITRIFICATION CURVE

Figure 2

HOT STAGE X-RAY DIFFRACTION EVALUATION AND SELECTION —
PHASE I MATERIALS
(Figure 3)

Hot stage X-ray diffraction analysis was used in the evaluation and selection of fibrous

materials for Phase I NASA Contract. The extremes of data encountered during the

selection process are presented in the figure. The final selection criterion was based

upon identifying materials that resided along the right side of the curves. Only materials

that indicated initiation of crystallation above $1338°$ K ($1950°$ F) were considered for use.

HOT STAGE X-RAY DIFFRACTION
EVALUATION AND SELECTION
PHASE I MATERIALS
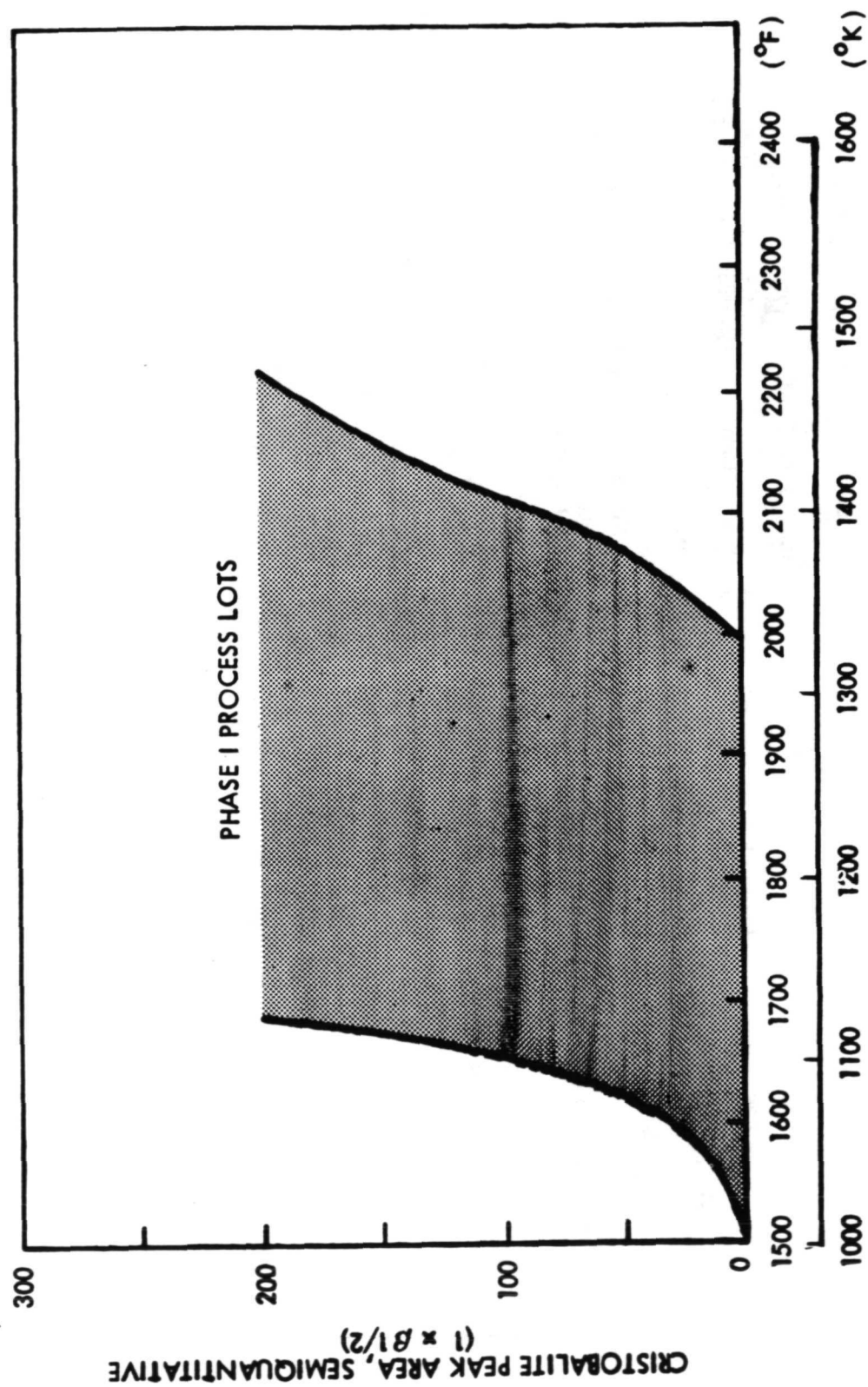
TEMPERATURE
Figure 3

HOT STAGE X-RAY DIFFRACTION EVALUATION AND SELECTION –
PHASE II MATERIALS
(Figure 4)

The curve family represents the hot stage X-ray diffraction data recorded for Phase II materials. These data display the misleading information that this analytical method can present for materials exhibiting high orders of phase stability. Quantitative analysis showed all Phase II materials to be noncrystalline. Because of this limitation, hot stage X-ray diffraction was dropped in favor of the newly developed quantitative analysis methods for establishing material morphological characteristics.

HOT STAGE X-RAY DIFFRACTION EVALUATION AND SELECTION

PHASE II MATERIALS
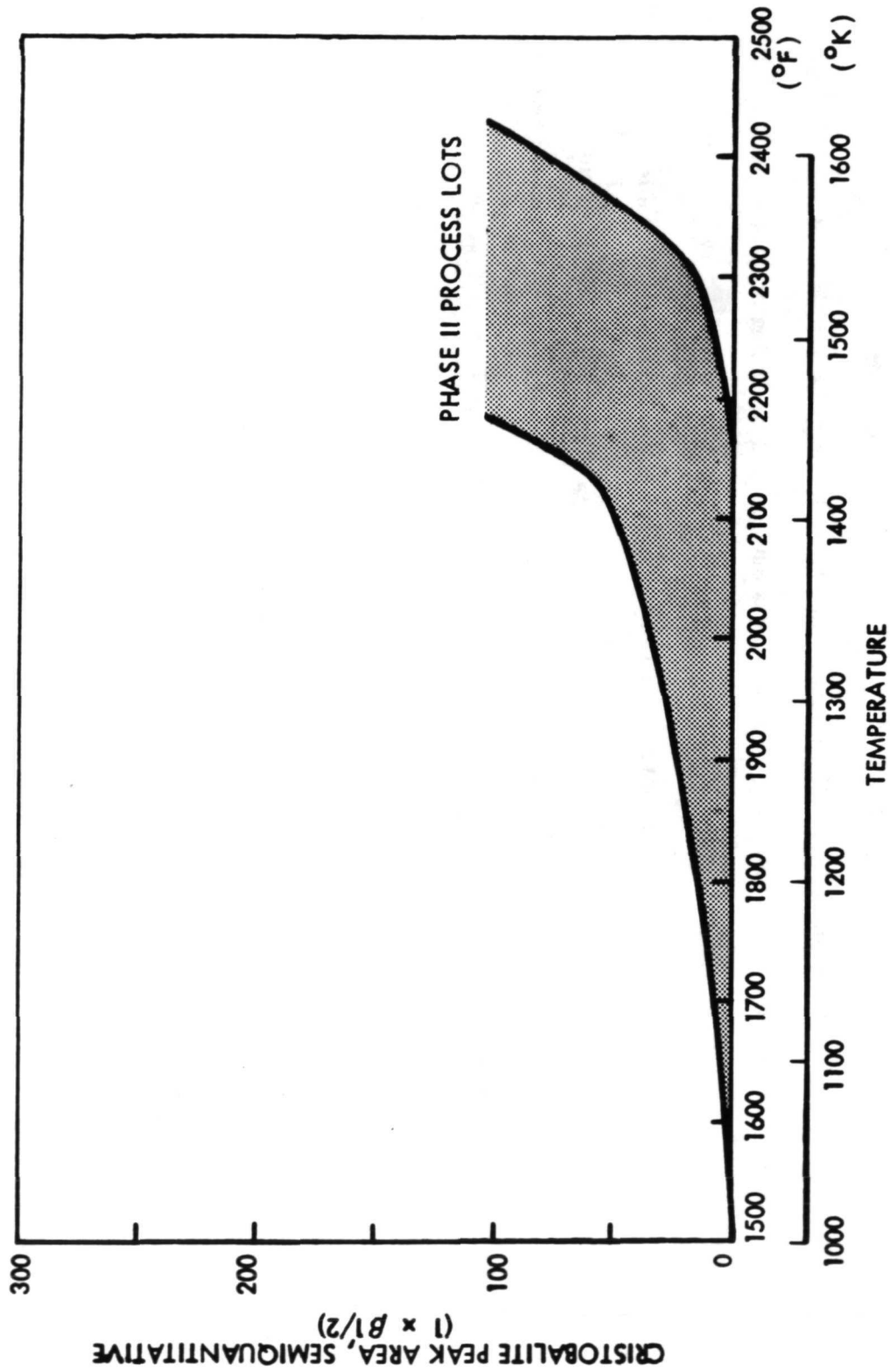
Figure 4

QUANTITATIVE X-RAY DIFFRACTION PROCEDURES
(Figure 5)

The main elements involved in performing quantitative evaluations of the morphology of silica materials are summarized in the figure. Standards taken to be 100 percent cristobalite and quartz have been prepared for the reduction and reporting of data.

For evaluations of the influence of thermal treatements upon silica materials, samples are heat treated under the desired conditions in closed amorphous silica crucibles prior to X-ray diffraction analysis. The use of crucibles during treatments aids in obtaining high reproducibility of data, even for slight phase transformations.

QUANTITATIVE X-RAY DIFFRACTION PROCEDURES

SAMPLE PREPARATION

- MATERIAL SAMPLE GROUND IN SHAPPHIRE MORTAR

- POWDERED MATERIAL PRESSED INTO SAMPLE HOLDER WITH MICROSCOPE
  SLIDE TO PROVIDE SMOOTH FACE

X-RAY EQUIPMENT

- GENERAL ELECTRIC XRD-5, OR NORELCO WIDE RANGE DIFFRACTOMETER
  WITH V-FILTERED Cr Kα RADIATION

X-RAY MEASUREMENT

- SCAN FROM 42 DEG 2θ TO BELOW 32 DEG 2θ AT 0.2 DEG 2θ PER MINUTE
  AND CHART SPEEDS OF 31 cm (12 in.) PER HOUR

- INTEGRATE INTENSITIES DIRECTLY FROM CHART BY MEASURING PEAK INTENSITY
  ABOVE BACKGROUND AND MULTIPLYING BY WIDTH AT ONE-HALF MAXIMUM

DATA

- COMPARE INTEGRATED INTENSITIES TO THOSE OF STANDARD MATERIAL
  MEASURED UNDER SAME CONDITIONS

Figure 5

QUANTITATIVE X-RAY DIFFRACTION EVALUATION OF LI-1500 MATERIAL

(Figure 6)

The data show the significant change in the silica morphological stability obtained through LMSC in-house studies of the influence of material and process parameters upon transformation characteristics. The Phase I materials displayed rather rapid increases in crystallinity with heating (starting from typical 20 percent content as processed). Phase II materials were noncrystalline and displayed an extreme resistance to the development of crystalline phases. It should be noted that while hot stage X-ray diffraction results might indicate significant crystallization at temperatures as low as $1533^{\circ}K$ ($2300^{\circ}F$), quantitative results established that a maximum of 2 percent change might result after heating for two days at that temperature. It is interesting to contemplate the duration of heating that would be required just to reach the content displayed by "as processed" Phase I materials that performed well in extensive thermal tests at NASA facility.

QUANTITATIVE X-RAY DIFFRACTION EVALUATION OF LI-1500 MATERIAL

Figure 6

273
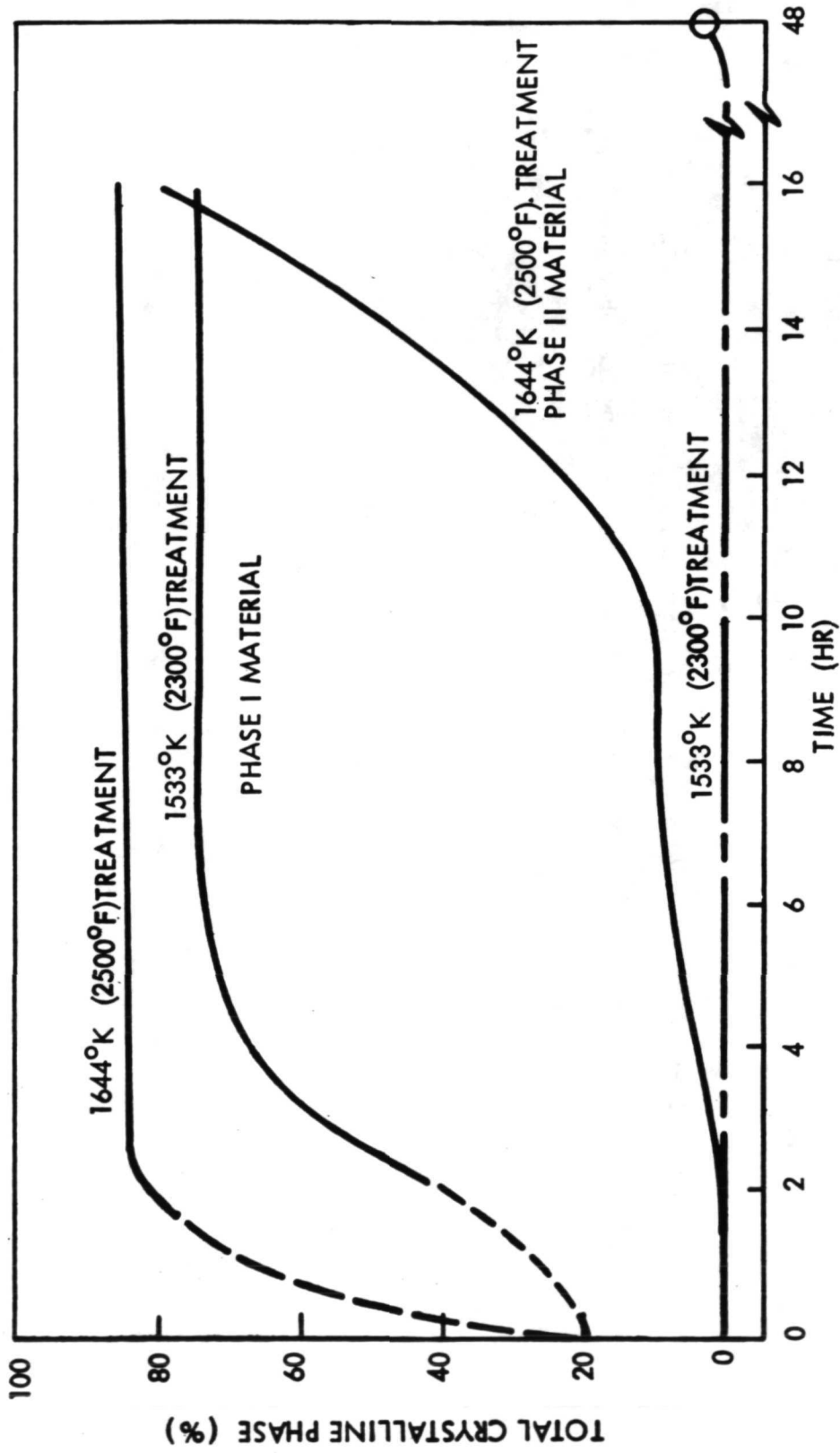
LMSC SILICA RSI MORPHOLOGY

The morphology of all LMSC silica materials produced during the past 18 months has been noncrystalline and resistant to any phase transformations upon subsequent thermal testing representative of the Shuttle environment envelope.

LMSC's ability to control material state as well as processes has resulted in the development of an extremely dependable RSI material family offering the inherently superior characteristics of amorphous silica for Shuttle.

10

EVALUATIONS OF RSI MATERIALS

by

C. W. Kistler, D. E. Niesz, and E. L. Foster

BATTELLE
Columbus Laboratories
505 King Avenue
Columbus, Ohio 43201

SUMMARY OF EVALUATIONS CONDUCTED
(Figure 1)

Battelle's Columbus Laboratories has evaluated nonmetallic materials for the manned space shuttle through a contract with NASA-MSC for approximately two years. In general, each task generated screening data and characterization information on materials obtained by NASA from development contracts. The current paper presents the results obtained from an evaluation of RSI materials obtained from General Electric, Lockheed, and McDonnell-Douglas under Contracts NAS9-12084, 12083, and 12082, respectively. The materials evaluated were believed to represent the state of development as of about January, 1972.

The objective of this program was to obtain valid mechanical and thermophysical property data on RSI insulation materials and on their respective coatings. To aid in the interpretation of data and identify features unique to each material, a limited amount of physical characterization was conducted. However, the present paper emphasizes unique mechanical and thermophysical testing techniques developed at Battelle specifically for evaluating separate properties of the insulations and coatings. Plasma-arc evaluations conducted on the coated materials are discussed in another paper presented at this Symposium.

SUMMARY OF EVALUATIONS CONDUCTED

MATERIAL CHARACTERIZATIONS
   ROUTINE METHODS
   EXPERIMENTAL TECHNIQUES

RESPONSE TO ENVIRONMENTS
   FURNACE TESTS
   ARC TESTS

MECHANICAL PROPERTIES
   TENSILE (TO 1370°K)
   COMPRESSIVE (TO 1370°K)
   SHEAR (ROOM TEMPERATURE)

THERMOPHYSICAL PROPERTIES
   EXPANSION
   CONDUCTIVITY
   EMITTANCE
   SPECIFIC HEAT

Figure 1

MATERIAL CHARACTERIZATIONS
(Figure 2)

This figure summarizes conventional and experimental characterization performed on each material. Radiographic examination was conducted prior to cutting each panel. After cutting, the bulk densities of uncoated bars were determined, and the density gradient through each panel was checked by slicing up a small sample. The GE mullite evaluated in this report had an uncoated bulk density between 183 and 202 kg/m^3 (11.4 to 12.6 lb/ft^3), the Lockheed silica panel ranged from 232 to 271 kg/m^3 (14.5 to 16.9 lb/ft^3), while the MDAC mullite ranged from 234 to 295 kg/m^3 (14.6 to 18.4 lb/ft^3).

Scanning electron microscopy was used to evaluate coating damage done by various cutting and grinding techniques and revealed that edge damage was minor compared to irregularities inherent in the coatings. Coatings were also examined by this technique to determine microstructural changes accompanying thermal exposure in a furnace. The MDAC coating appeared to be more affected by exposure than either of the other two coatings. X-ray diffraction examination revealed that the as-received GE insulation was predominately mullite with some cristobalite (peak ratios about six), the Lockheed material was amorphous, and the MDAC insulation was predominately cristobalite with some mullite (peak ratios about one). After furnace cycling to 1644°K (2500°F) for a total of 2-1/2 hours at this temperature, the GE material was unchanged, the LMSC material contained some cristobalite, and the MDAC insulation now contained more mullite than cristobalite (peak ratios about eight). Moisture adsorption at room temperature and 95 percent relative humidity was negligible for all materials both as-received and after furnace cycling to 1532°K (2300°F). Thermal gravimetric analyses indicated the LMSC and MDAC coatings contained volatile matter believed to be water-repellent additives.

Three experimental evaluation techniques were briefly evaluated as possible methods of detecting irregularities. The infrared inspection technique indicated differences in the radiation characteristics of two coatings from one material measured in the 1 to 4 micron range. A cursory examination of the coatings revealed no apparent microstructural or thickness differences which could account for the observed difference. Neither of the other NDT methods appeared promising.

278

MATERIAL CHARACTERIZATIONS

CONVENTIONAL

- PHOTOGRAPHY
- RADIOGRAPHY
- BULK DENSITY
- SCANNING ELECTRON MICROSCOPY
- X–RAY DIFFRACTION
- MOISTURE ADSORPTION
- THERMAL GRAVIMETRIC ANALYSIS

EXPERIMENTAL

- HOLOGRAPHY
- INFRARED INSPECTION
- MICROWAVE TRANSMISSION

279

Figure 2

TOP VIEW OF TYPICAL CUTTING FORMAT SHOWING SAMPLE UTILIZATION PLAN
(Figure 3)

In order to assess the panel-to-panel uniformity of each type of material and ensure that all the mechanical property data generated were representative, a cutting plan was designed to provide one sample for each test condition from each of three panels provided for each material. No attempt was made to be selective in material utilization unless radiographic examination revealed areas of gross irregularities or specimens were damaged in handling. Some minor exceptions to the general utilization plan were also made to provide, for example, thermal conductivity samples. Because the test plan called for an evaluation of the effects of thermal exposure on tensile and compressive properties, 12 bars from each panel were furnace cycled before machining to the final specimen configuration.

All cutting was done dry with a metal-bonded diamond wheel. After numbering the cut bars, those to be used for shear, compressive or cross-plane tensile tests were ground so that the loaded faces were flat and parallel. In-plane compressive specimens were taken from the lower half of each numbered bar, while the upper half was used for tensile specimens. Because two coatings were required to fabricate a coating tensile sample, two bars had to be allocated for each test condition even though the insulation beneath the second bar was not required for testing purposes. Coatings were removed from the as-received or heat-treated insulation with a diamond wheel _after_ a reduced gage section had been ground in the coated sample. A 100-grit frit-bonded grinding wheel was found suitable for grinding the coatings without chipping the edges. After the coatings were removed, they were positioned upside down on a magnetic table, shimmed at each edge with steel shim stock, and the residual insulation ground off to within 0.25 to 0.50 mm (0.01 to 0.02 inch) of the glassy zone.

280

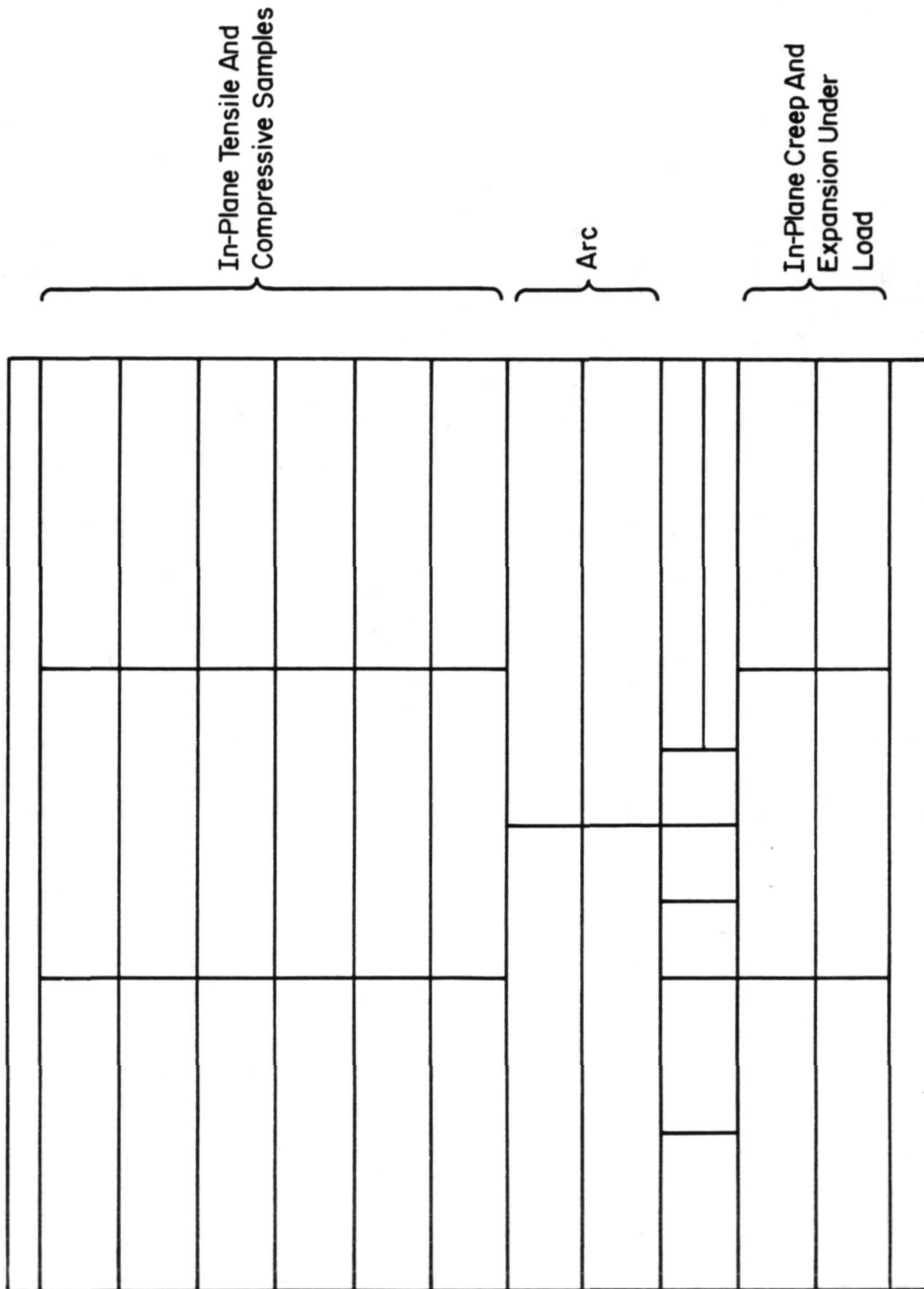TOP VIEW OF TYPICAL CUTTING FORMAT SHOWING SAMPLE UTILIZATION PLAN

In-Plane Tensile And Compressive Samples

Arc

In-Plane Creep And Expansion Under Load

Figure 3

SHEAR TEST TECHNIQUE
(Figure 4)

The shear fixture shown in this figure was used to determine the cross-plane shear properties of both coated and uncoated RSI. For clarity, the orientation of the specimens relative to the shear planes is also shown. The 2.3 x 2.5 x 4.8-cm (0.9 x 1 x 1.9 inch) samples were epoxied to flat regions of the solid steel bar passing freely through each end of the frame for alignment purposes. Strain was monitored from the extensometer attached to the movable and stationary portions of the frame. The epoxy bond and any coating thickness were ignored in calculating the shear moduli.

Average shear properties, determined from four samples of each material, are compiled below, where English units are given in parentheses.

	General Electric	Lockheed	McDonnell-Douglas
Strength, 10^4 N/m^2 (psi)	18 (26)	23 (33)	29 (42)
Modulus, 10^7 N/m^2 (10^3 psi)	5.0 (7.3)	7.6 (11)	6.2 (9)
Strain to Failure, percent	0.45	0.44	0.55

The strengths appear to be in line with the data available from the respective material suppliers, but the moduli are from two to ten times higher. The "increased" stiffness of the materials means that stresses in a TPS panel could be higher than those predicted on the basis of other data. Consequently, designers may want to consider these new data in sizing of panels. Future plans call for both in-plane and cross-plane shear properties to be determined up to 1144°K (1600°F) on more recent lots of material. While there seems to be no difference in properties between coated and uncoated samples, many of the samples failed near the face that corresponded to the center part of the original panel. The implication that the center portions of the RSI panels were weak, however, was not confirmed in cross-plane tensile tests. Stress-strain curves began deviating from linearity at about one-third the fracture stress at an elastic strain limit of between 0.10 and 0.20 percent.

SHEAR TEST TECHNIQUE
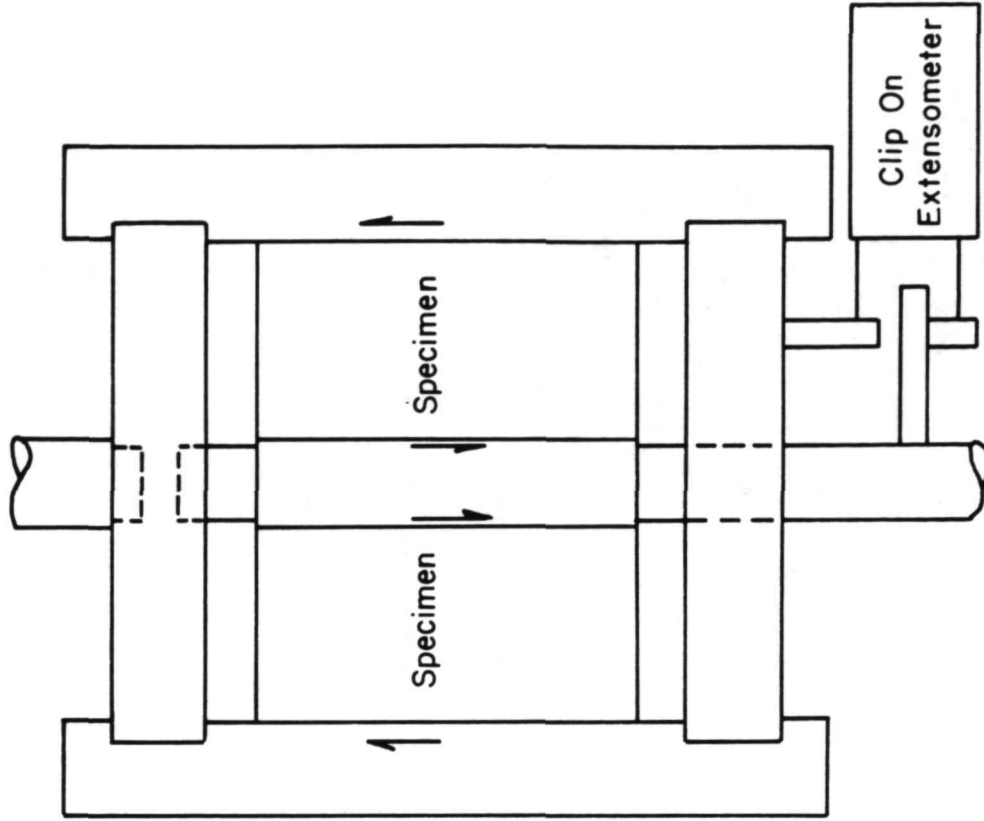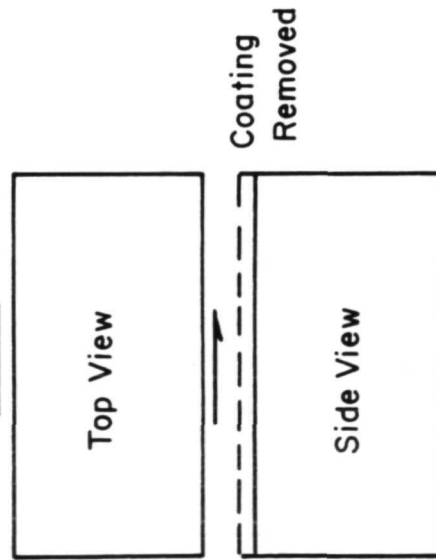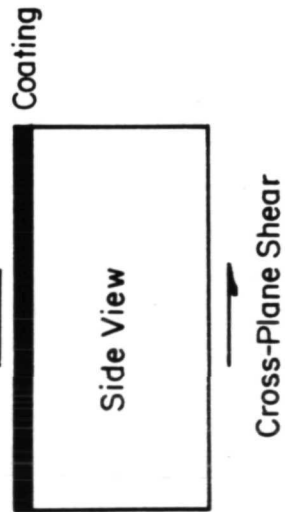
Shear Fixture

Figure 4

DUAL-COATING TENSILE SPECIMEN
(Figure 5)

This figure illustrates the method used to determine the tensile properties of coatings up to 1367°K (2000°F), and to determine the "softening point" of the coatings under load. Two coatings were cast in refractory cement caps to form a single specimen. The coatings were held in the proper position in the molds by foam rubber pads slipped between the two coatings. The actual thickness of each coating was about twice the thickness of the glassy layer on which the property data were calculated. Bending stresses were minimized through the use of knife-edge alumina links which pivoted on alumina pins slipped through each cap. The refractory cement caps consisted of 80 percent minus-48-mesh fused silica or mullite aggregate bonded with 20 percent calcium aluminate cement.

In-plane insulation specimens were tested at elevated temperature by capping a solid insulation sample instead of the coatings. The insulation samples were 1.25 cm (0.5 inch) square in the reduced gage section and 1.25 cm (0.5 inch) by 2.5 cm (1.0 inch) in the caps, being reduced in only one direction. Room-temperature specimens were also this size but were epoxied to aluminum blocks for convenience. A lever-arm extensometer was used to measure strain in the gage section of both the coating and in-plane insulation samples.

Cross-plane insulation samples were only tested at room temperature and consisted of 2.5-cm (1-inch)-square, 4.8-cm (1.9-inch)-long samples epoxied to aluminum blocks. Because the gage sections were not reduced, strain was monitored with an extensometer clipped to the loading blocks. Techniques for measuring the cross-plane tensile properties at elevated temperatures are currently being developed.

DUAL−COATING TENSILE SPECIMEN
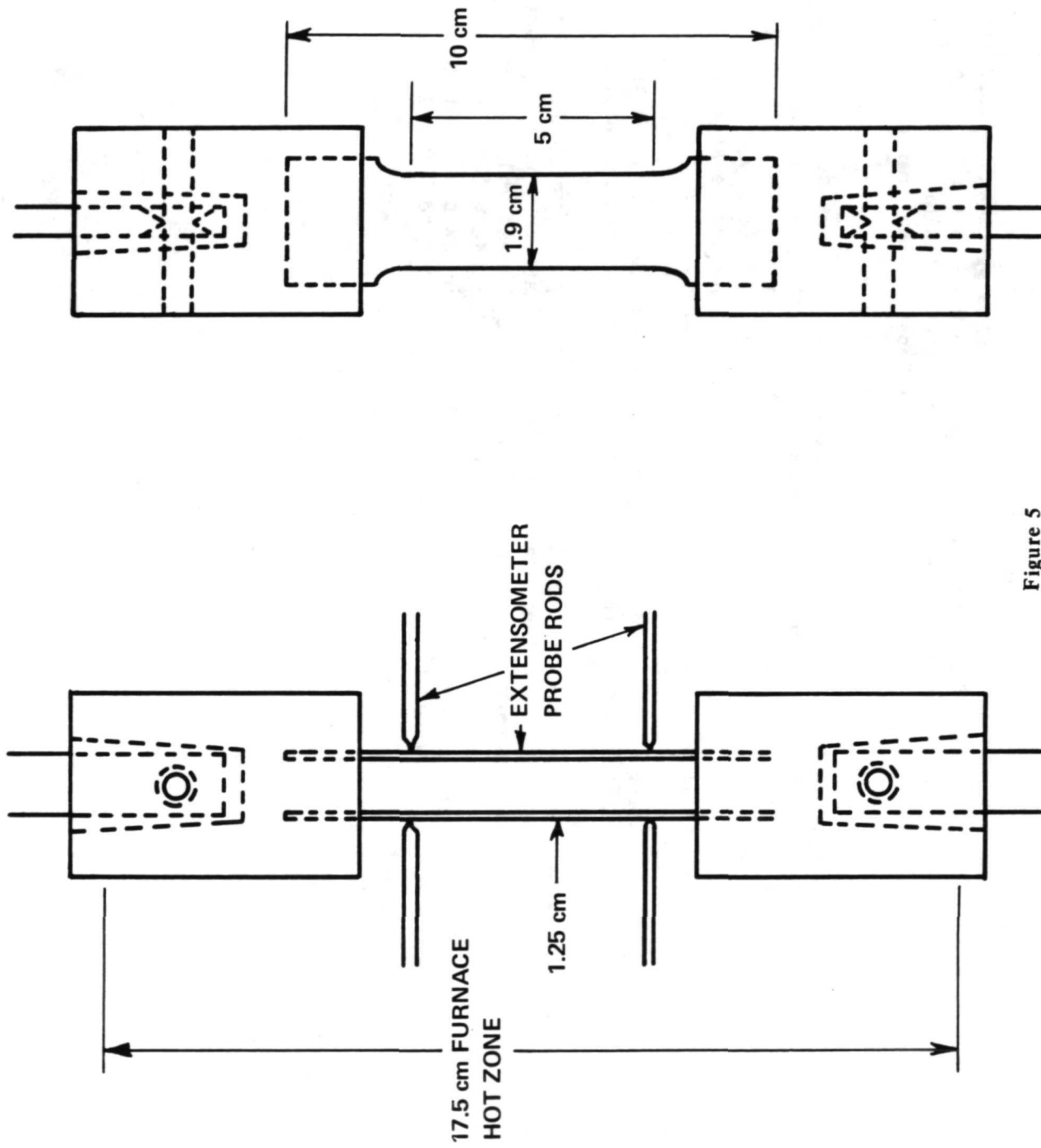
10 cm

5 cm

1.9 cm

EXTENSOMETER
PROBE RODS

17.5 cm FURNACE
HOT ZONE

1.25 cm

Figure 5

285

This figure is a schematic diagram of one of two extensometers designed and built to obtain valid strain data from opposite sides of in-plane tensile specimens, particularly at elevated temperature. It was also used to obtain comparative data on compressive samples at room temperature and to measure the thermal-expansion characteristics of dual coating specimens under a tensile load of 5 to 8 x 10^5 N/m^2 (80 to 120 psi) to determine their softening points.

The arms of the extensometer pivot at mid-length on leaf springs attached to an Invar bar to minimize thermal effects. Pointed alumina rods are positioned against the specimen with an axial thrust of 12 grams maintained through a counter weight. The rods pass through holes in a split silicon carbide resistance furnace, which is moved into position after the extensometers have been suitably positioned on the sample at room temperature. The entire assembly is balanced so that the lever arms remain horizontal and exert no upward or downward thrust on the sample. The 12-gram thrust needed to prevent slippage of the rods on coating samples had a negligible effect on the insulation samples, generally leaving no visible marks unless the sample falls against the rod on failure.

A novel feature of the extensometers is that the gage length is set automatically on each specimen by positioning the aluminum frame on a thin ledge attached to a gage-setting post, then pushing the entire assembly against the specimen until the assembly swings off the ledge and free of the post. A bar fastened in position on the table holding the extensometers provides a stop to prevent damage to the specimen. The extensometer has a sensitivity better than ± 50 x 10^6 cm (± 20 x 10^6 inches) corresponding to ± 0.001 percent strain in a 5-cm (2-inch) gage length.

SCHEMATIC DIAGRAM OF LEVER–ARM EXTENSOMETER USED FOR STRAIN MEASUREMENTS

Assembly Shown Pushed Free of Gage Setting Post

WIRE HARNESS

LEAF SPRING

INVAR BAR

LVDT

ADJUSTABLE LEDGE

GAGE SETTING POST

BASE PLATE

PULLEY

WEIGHT

ALUMINA PROBE RODS

WATER COOLED SUPPORT SHIELD
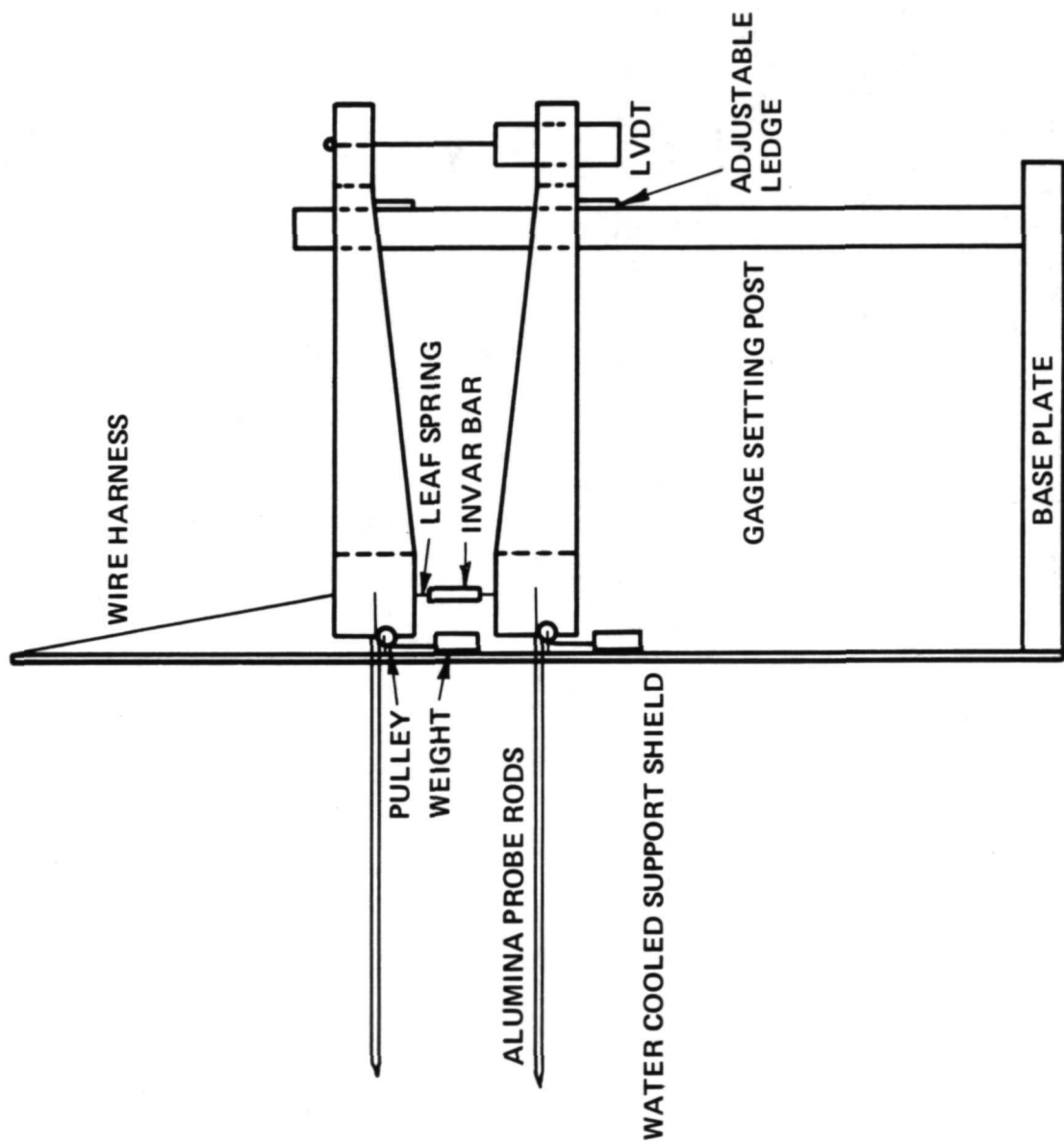
Figure 6

COMPRESSIVE TEST TECHNIQUES

(Figure 7)

This figure illustrates three methods used to determine in-plane compressive property data at room temperature. All samples were nominally 2.5 cm square (1 inch square) with no reduced gage section. Method A was also used to obtain elevated temperature data since the loading fixtures were alumina. Method B was also used to obtain room-temperature cross-plane compressive data and cross-plane tensile data by replacing the steel balls with universal joints. The extensometer used to eliminate "end effects" in Method C is described in figure 6.

Results shown in figure 8 varied significantly with technique, with only Method B giving both "good" strength and "good" modulus values. At this time, it is not known whether the high strengths obtained with Method B are due to a constraint effect or from improved loading uniformity. Because none of the techniques described is entirely suitable for obtaining valid strength and modulus data at elevated temperatures, modifications are being considered so as to obtain both strength and strain data from each specimen tested in the future.

288

COMPRESSIVE TEST TECHNIQUES

Method A

Method B

Method C

Blotter Paper

Extensometer Probe Rods

Epoxy Bond

Clip On Extensometer

Extensometer Probe Rods

Figure 7

289
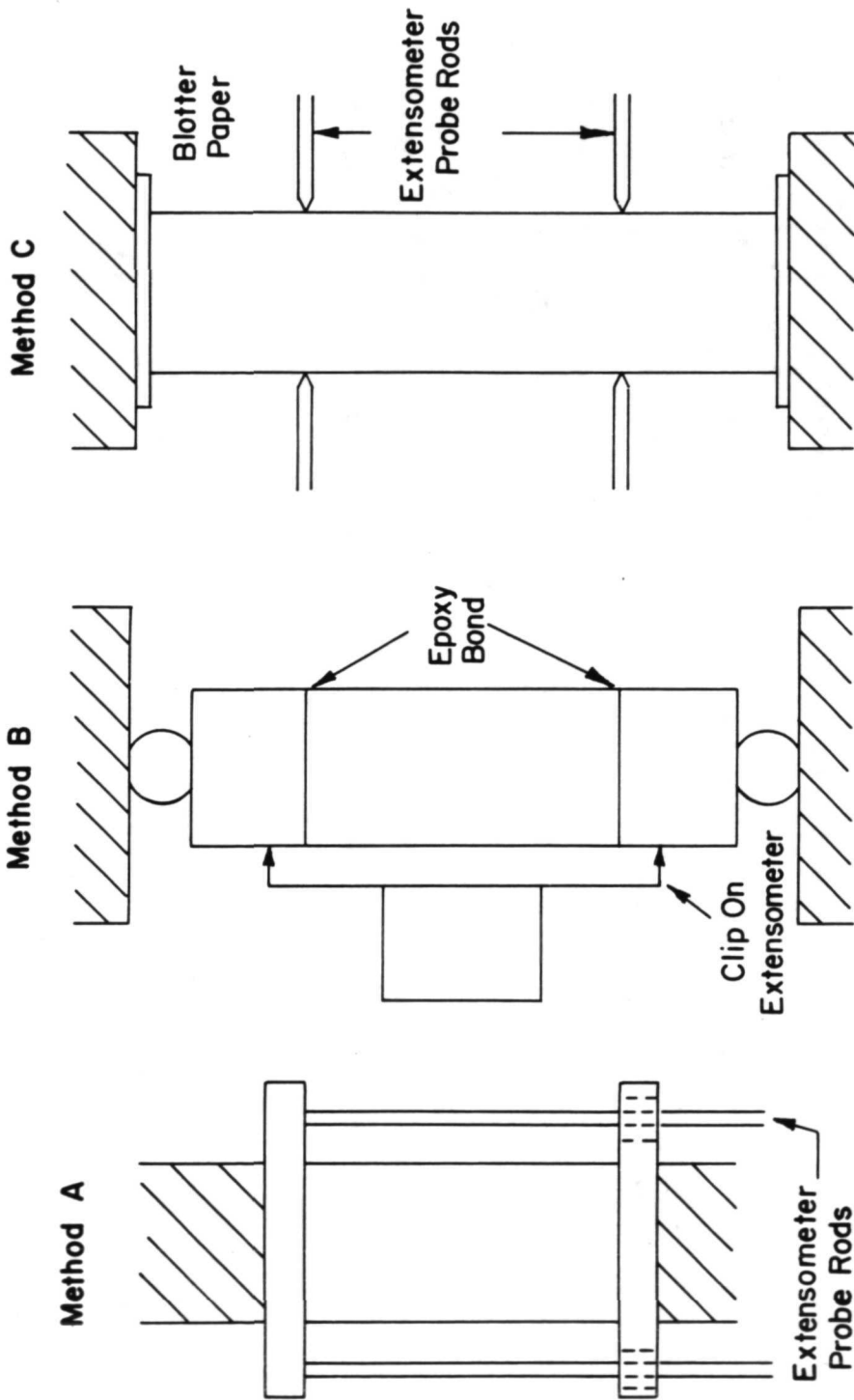
COMPRESSIVE PROPERTIES VERSUS TEST METHOD
(Figure 8)

Compressive properties of three RSI materials determined by three techniques at room temperature are shown in this figure. The results indicate that modulus data obtained from loading plate travel can be an order of magnitude below the "true" property value unless the samples are rigidly bonded to the plate (Method B). Bonding the samples to the plates increases the measured strength by about 30 percent for all materials, possibly by eliminating premature failure at the ends or by constraint of the specimen. Data obtained with Method B were considered more indicative of "true" properties and were therefore used in a subsequent compilation of average properties.

Material anisotrophy is evident by the difference between the in-plane and cross-plane data obtained by Method B. The MDAC material appears to be the most isotrophic material while the LMSC material shows strong anisotrophy. The range of data shown are from three specimens tested at each condition. While the strength data agree with that obtained by other investigators for material of comparable density, the moduli may be higher.

The GE data was obtained from material with an uncoated bulk density of 192 kg per m^3 (12 lb per ft^3) while the other materials had densities of 240 kg per m^3 (15 lb per ft^3).

COMPRESSIVE PROPERTIES VERSUS TEST METHOD

Figure 8

291
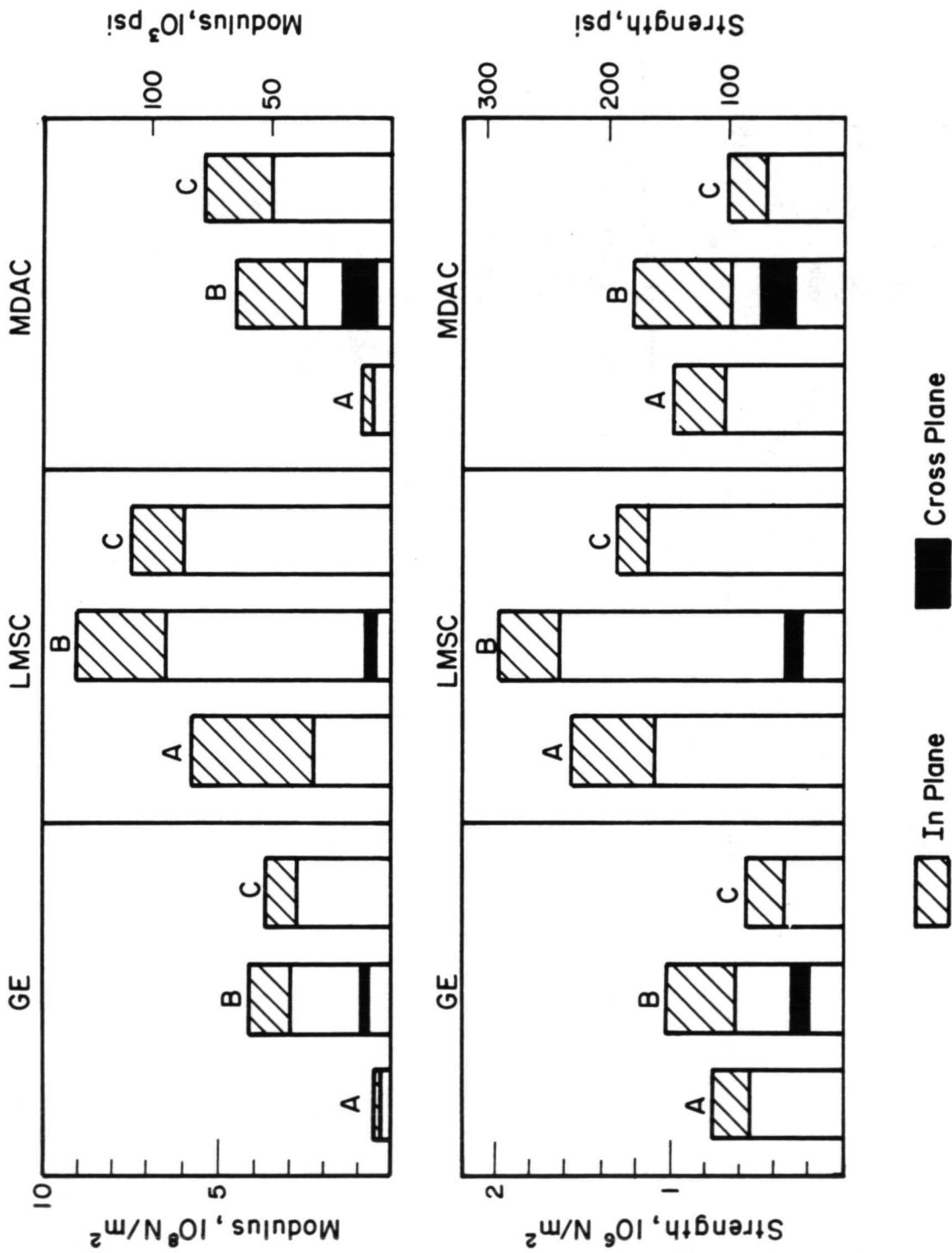
<u>AVERAGE ROOM-TEMPERATURE PROPERTIES OF INSULATORS</u>
(Figure 9)

This figure is a compilation of tensile and compressive property data obtained on as-received insulation tested at room temperature. In-plane tensile and in-plane and cross-plane compressive data are "good" data obtained from specimens bonded to aluminum loading blocks. Considering that the data are an average of three specimens per condition, there is good agreement between the compressive and tensile elastic moduli for both orientations, a correlation often lacking in other data sources. The compressive stress-strain curves were linear up to about half the ultimate strengths at strains between 0.10 and 0.25 percent. Thus, the estimated elastic strain limit in compression closely approximates the failure strains measured in tension.

In addition to relatively low elastic strain limits in both tension and compression, the materials have elastic moduli more than double the values commonly reported to date. Both factors are of particular concern as they affect TPS panel design criteria. Room-temperature cross-plane shear data given earlier are also of interest. All tests were conducted in an Instron at a cross head speed of 0.13 mm per minute (0.005 inch per minute).

AVERAGE ROOM TEMPERATURE PROPERTIES OF INSULATORS

TESTS	GE	LMSC	MDAC
IN PLANE TENSILE			
STRENGTH, 10^4 N/M^2	40	79	68
MODULUS, 10^7 N/M^2	30	69	51
STRAIN TO FAILURE, PERCENT	0.14	0.12	0.14
CROSS PLANE TENSILE			
STRENGTH, 10^4 N/M^2	17	12	23
MODULUS, 10^7 N/M^2	7	7	10
STRAIN TO FAILURE, PERCENT	0.30	0.24	0.30
IN PLANE COMPRESSION			
STRENGTH, 10^4 N/M^2	78	186	100
MODULUS, 10^7 N/Mi^2	37	77	39
STRAIN TO FAILURE, PERCENT	0.25	0.25	0.31
CROSS PLANE COMPRESSION			
STRENGTH, 10^4 N/M^2	25	32	37
MODULUS, 10^7 N/M^2	8	7	8
STRAIN TO FAILURE, PERCENT	0.41	0.61	0.51

Figure 9

<u>TENSILE PROPERTIES OF COATINGS</u>
(Figure 10)

Room-temperature properties of coatings provided in this figure are based on an average of three to five measurements for each material. These data are consistent with those presented by Goldstein, et al.[1], from material contractor sources, except that the 0.12 percent failure strains they reported for a silica coating are about twice as high as our results. This discrepancy may be due to differences in testing techniques, which were not reported in the referenced work. The low failure strain of the coatings compared to the insulations places a restriction on design of a TPS panel.

Some property data were obtained on these coatings at elevated temperature, but only the LMSC coating "survived" testing at 1367°K (2000°F), where an average strength of 1420×10^4 N/m^2 and failure strain of 0.15 percent were obtained. Viscous flow observed at this temperature resulted in a "modulus" of about 1×10^{10} N/m^2. Softening of the MDAC coating near 1089°K (1800°F) and consistent brittle fracture of the GE coatings near 520°K (500°F) on heat-up restricted elevated temperature measurements on these materials. Limited data obtained for the MDAC coatings between 867°K (1100°F) and 1089°K (1500°F) indicated they were sensitive to creep failure at stresses less than half their room-temperature strength. Failure of the GE coatings appeared to be related to erratic thermal expansion characteristics of the coatings.

294

ROOM TEMPERATURE TENSILE PROPERTIES OF COATINGS

	GE	LMSC	MDAC
STRENGTH, 10^4 N/M^2	1690	1520	1450
MODULUS, 10^{10} N/M^2	7.6	3.5	8.3
FAILURE STRAIN, PERCENT	0.023	0.047	0.018
COATING DESIGNATION	SR2	0042	$M5_{23}A7P_{700}$
GLASSY LAYER THICKNESS, MM	0.25 (0.33*)	0.38	0.25

*One panel had a thicker coating designated SR2 – XSR2 which had properties similar to the SR2 coating.

Figure 10

IN-PLANE PROPERTIES OF INSULATORS AT 1367°K (2000°F)

(Figure 11)

Average in-plane tensile and compressive properties of the insulators measured at 1367°K (2000°F) are given in this figure. The GE and MDAC insulations have tensile and compressive strengths only about half their corresponding room-temperature values, while the LMSC insulation strength is increased by about 50 percent. Significant creep observed at this temperature resulted in the nonlinear stress-strain curves, high failure strains, and low elastic moduli compared to corresponding room-temperature data. The apparent discrepancy between the tensile and compressive moduli is due to the compressive moduli being obtained from a zero load; whereas, the tensile moduli were calculated at a stress of about 0.5×10^5 N/m^2 (7.5 psi) due to linkage in the load train. Because the compressive moduli were based on loading plate movement, they may be somewhat lower than the "true" value. However, because creep was observed in all the materials at this temperature, the "elastic" data shown are of questionable value regardless of measurement technique.

IN–PLANE PROPERTIES OF INSULATORS AT 1367°K (2000°F)

	GE	LMSC	MDAC
TENSION			
STRENGTH, 10^4 N/M^2	14	115	17
MODULUS, 10^7 N/M^2	>5	71	>2
STRAIN TO FAILURE, PERCENT	0.37	0.55	1.0
COMPRESSION (METHOD A)			
STRENGTH, 10^4 N/M^2	44	238	43
MODULUS, 10^7 N/M^2	14	65	5.5

Figure 11

TYPICAL CREEP BEHAVIOR OF INSULATORS AT 1370°K
(Figure 12)

This figure illustrates typical creep behavior observed at 1370°K (2000°F) when strain was plotted versus time. The creep behavior of the LMSC insulation was quite predictable, doubling when the load was doubled up to a high stress level. However, the creep rate of both mullite insulators showed a strong stress dependence, becoming quite high when the load was doubled. When the data were plotted on a log-log plot, both mullite materials had stress exponents approaching four in the vicinity of 1370°K, while that of the LMSC insulation was very close to one, which is typical of viscous flow behavior. The high stress dependence of the mullite insulators may indicate that creep is controlled by grain boundary sliding at fiber-to-fiber contact points, since high stress exponents observed in creep of dense ceramic materials normally is attributed to grain boundary sliding and/or diffusion controlled behavior.

While the stress dependence of creep is of interest from an academic viewpoint, the temperature dependence of creep is of more importance with regard to the shuttle application, since any creep that occurs to relieve stress can affect results predicted from an elastic stress analysis. Creep may be beneficial in relieving stress due to thermal or mechanical stains at elevated temperatures but can result in stress reversal when mechanical stresses or thermal gradients disappear. Consequently, creep characteristics may have to be considered in design of thermal protection systems.

298

TYPICAL CREEP STRAIN VERSUS TIME CURVES OBTAINED FOR
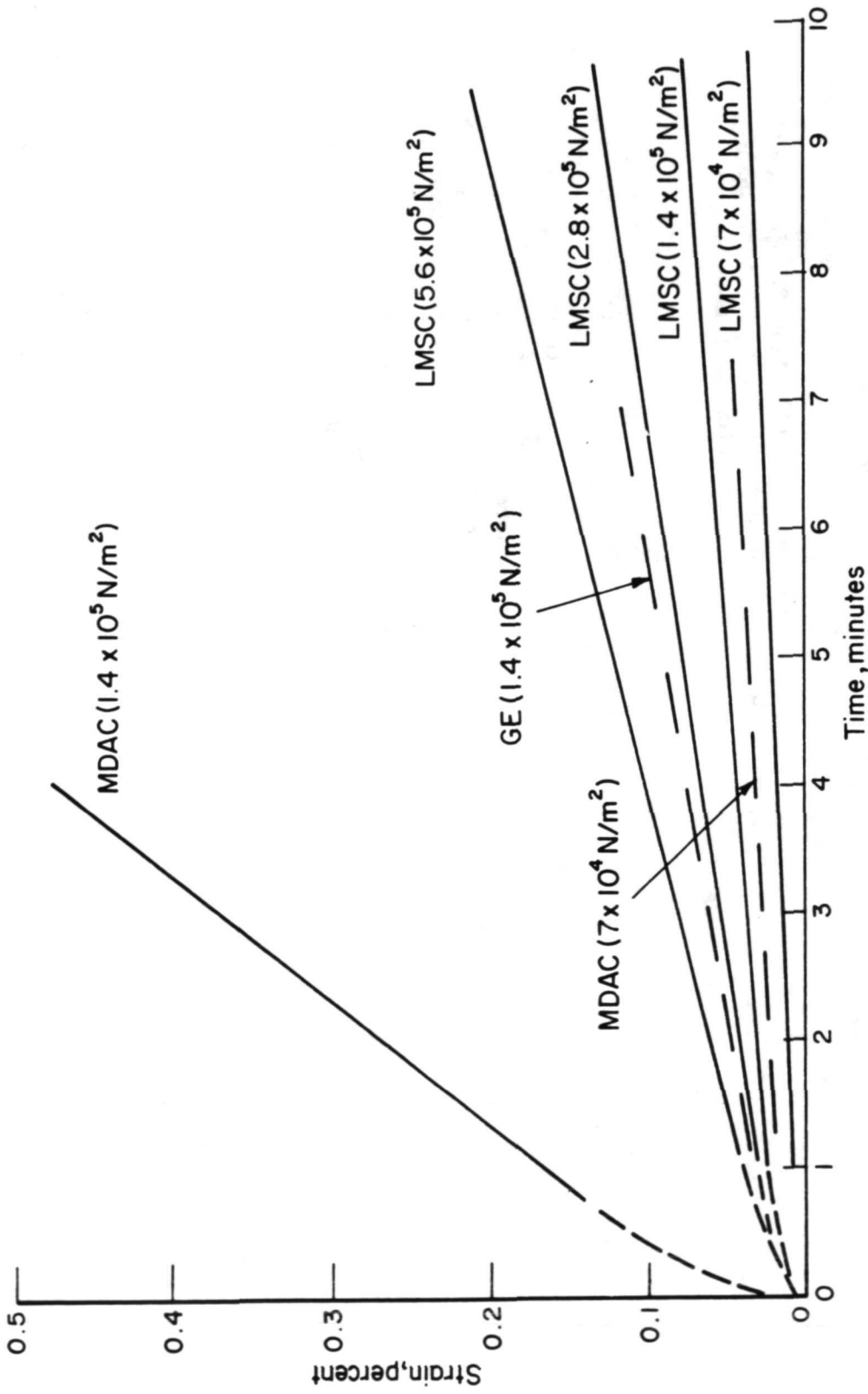EXTERNAL INSULATORS AT 1370°K

Figure 12

299

This figure illustrates the in-plane tensile and compressive creep of three insulators at a stress of 10^5 N/m^2 (15 psi) versus the reciprocal of absolute temperature. This stress is from one-fourth to one-eighth of the ultimate room-temperature tensile strength of these materials. As would be expected, there are specimen-to-specimen differences evident in the data, and these differences are generally larger than differences between tensile and compressive data obtained by two entirely different measuring techniques. Creep rates become significant (0.001 percent per minute) above 1090°K (1500°F) for the mullite insulators at this stress, but the fused silica material does not begin creeping until about 1250°K (1800°F). These temperatures give some indication of the temperature limits over which elastic stress analyses are appropriate.

Because the figure is an Arrhenius plot, activation energies for creep can be estimated from the slope of the creep curves. The activation energy measured for the LMSC insulation approaches 419 x 10^3 joules/mole (100 Kcal/mole) above 1367°K (2000°F), which is somewhat below a typical value of 590 x 10^3 joules/mole (140 Kcal/mole) reported for viscous flow of fused silica. The activation energy for creep of the GE and MDAC insulators is in the vicinity of 210 x 10^3 joules/mole (50 Kcal/mole), considerably below the 712 x 10^3 joules/mole (170 Kcal/mole) value typical of refractory bricks with a mullite matrix, perhaps indicating the presence of impurities that may be concentrated at fiber-to-fiber contact points. Although the mullite materials show creep rates higher than those of the fused silica material below 1367°K (2000°F), there is some indication that they are more creep resistant at higher temperatures. However, creep below this temperature is of more concern, perhaps being due to the lower tensile strength of these materials compared to the fused silica insulation.

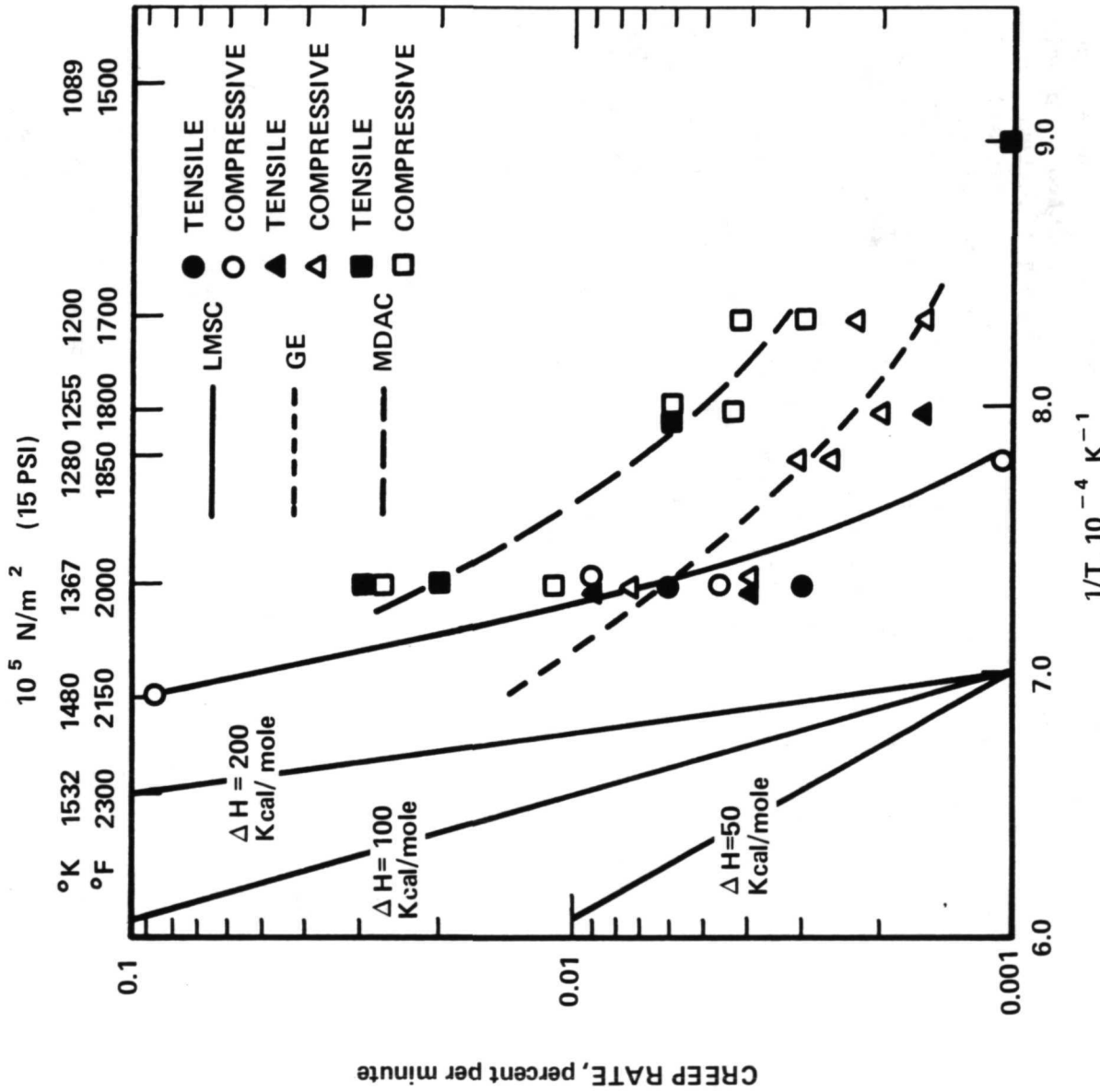TENSILE AND COMPRESSIVE CREEP OF THREE EXTERNAL INSULATORS AT STRESS OF 10^5 N/m^2 (15 PSI)

Figure 13

301

EFFECT OF FURNACE CYCLING ON MECHANICAL PROPERTIES

(Figure 14)

This figure summarizes room-temperature properties of as-received and thermally cycled measured insulation materials. The heat treatments were conducted by placing samples on fused silica shelves in a 23-cm (9-inch)-diameter fused silica muffle tube extending through the walls of a furnace preheated to the test temperature. A fused silica fork was used to transfer specimens to and from the furnace so that all samples were subjected to five 30-minute soak periods at the test temperature. The muffle was used to protect uncontaminated specimens from impurities in the furnace and then protect the furnace from salt when sea water-contaminated specimens were run at the conclusion of these tests. Although sea water was sprayed on only the coated surface of those specimens used for tensile tests, uncoated compressive specimens were saturated and dried to evaluate gross effects.

By itself, the compressive data would seem to indicate that thermal cycling does not degrade any of the materials and, in fact, strengthens the LMSC insulation. This trend is confirmed by the tensile data for the LMSC material, but not for the mullite insulators, which were very weak in tension after cycling. Transverse cracks were noted in some of the MDAC material cycled to 1530°K, but no cracks were visible in the GE insulation after similar cycling. No data were obtained on the GE insulation cycled to 1420°K (2100°F) because the samples were broken when grinding reduced gage sections in the bars. These results indicate that thermal stress microcracking may occur in the mullite materials which can reduce their tensile strength. However, this would only be expected to occur near the coated surface of the insulation in a TPS panel.

EFFECT OF FURNACE CYCLING ON MECHANICAL PROPERTIES

ROOM TEMPERATURE STRENGTH, 10^4 N/M^2*	GE	LMSC	MDAC
IN-PLANE COMPRESSIVE			
AS RECEIVED	65	136	89
5 CYCLES TO 1420°K	73	207	79
5 CYCLES TO 1530°K	55	260	101
5 CYCLES TO 1420°K CONTAMINATED	94	CRACKED	91
IN-PLANE TENSILE			
AS RECEIVED	40	79	67
5 CYCLES TO 1420°K	—	105	~3
5 CYCLES TO 1530°K	~5	143	~3

*69 X 10^4 N/M^2 = 100 psi.

Figure 14

THERMAL EXPANSION MEASUREMENT TECHNIQUES
(Figure 15)

This figure is a schematic diagram of a lever-arm extensometer used to measure the expansion characteristics of surface insulators and their coatings. Two 0.32-cm (1/8-inch) holes 10 cm (4 inches) apart on center were drilled through each 12.7-cm (5-inch)-long specimen so that it slipped over the ends of the alumina rods. The arms of the extensometer were then counterbalanced so that a 3-gram tensile load was imposed on the sample. Insulation samples were 0.6 by 1.27 cm (1/4 by 1/2 inch) across, while single coating specimens were 1.27 cm (1/2 inch) wide and 0.7 to 1.0 mm (0.03 to 0.04 inch) thick.

The output of linearly variable differential transformer (LVDT) was continuously plotted with an X-Y recorder while the specimen was heated and cooled at a linear rate of 111°K (200°F) per hour in a silicon carbide resistance heated furnace. Because the specimens did not fit tightly on the alumina rods, the measured expansion had to be corrected for diametral expansion of the rods, which amounted to about 5 percent of the recorded expansion for the mullite-based insulators or their coatings, and about 50 percent for the fused silica materials. Because of the large corrections required for the latter materials, a calibration curve was obtained by running a fused silica block in the apparatus.

Two other methods were used to characterize the expansion characteristics of these materials. Insulation samples of each material were also run in an optical dilatometer under a helium atmosphere. Optical data obtained for the two mullite materials fell on the respective curves obtained from the lever-arm dilatometer, but the optical data from the fused silica sample did not.

Thermal expansion characteristics of coatings were also determined from dual-coating tensile specimens subjected to .5 to 8 x 10^5 N/m^2 (80 to 120 psi) tensile load. Because the two coatings were capped at either end, bowing effects noted with a single specimen were minimized. In addition, no corrections were necessary for diametral expansion of the extensometer rods because pointed rods positioned on the surface of the coatings were self-centering throughout the run.
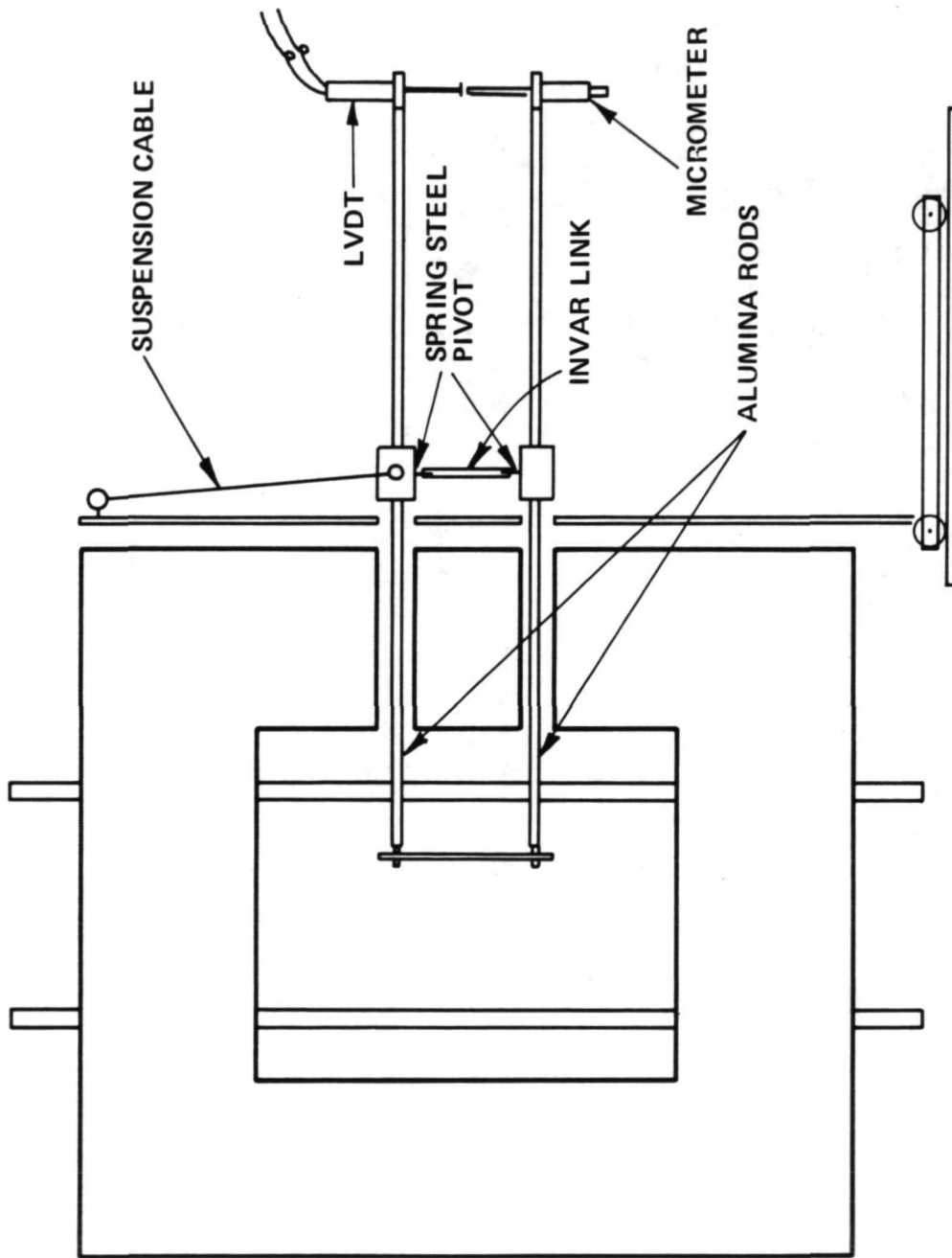
NO–LOAD THERMAL EXPANSION MEASUREMENT TECHNIQUE

SUSPENSION CABLE

LVDT

SPRING STEEL
PIVOT

INVAR LINK

MICROMETER

ALUMINA RODS

Figure 15

305

THERMAL EXPANSION CHARACTERISTICS OF REI MATERIALS
(Figure 16)

The data shown in this figure were compiled from expansion curves obtained with lever-arm dilatometers on as-received material. Expansion coefficients shown for the insulations are typical of mullite or fused silica bodies. Expansion coefficients of the coatings are difficult to characterize because warping characteristics affect the measurements. However, the LMSC and MDAC coatings had expansion coefficients close to those of the respective insulation samples, while the GE coating had expansion characteristics somewhat lower than the GE insulation. Because bowing was not eliminated with either technique used with the coatings, the coating data may not represent "true" bulk expansion behavior. The "loaded" expansion data are considered more indicative of the "true" expansion behavior, especially for characterizing a "softening point" above which elastic analyses are not appropriate. The large difference between the softening points of the MDAC coating is attributed to residual insulation supporting the unloaded coating up to 1530°K (2300°F). Even though the glassy layer had become soft about 1260°K (1810°F). The cooling curve of the MDAC coating was quite linear and parallel to the heating curve, while those of the LMSC and GE coatings exhibited irregular behavior, with a GE coating exhibiting a sharp inversion near 450°K (350°F).

None of the insulation materials exhibited any inversions on cooling from one cycle to 1530°K (2300°F). However, the LMSC and MDAC insulations began shrinking above the peak temperatures indicated in the figure, while the GE insulation began to creep above 1530°K (2300°F), resulting in a residual growth rather than shrinkage on cooling to room temperature. The LMSC insulation shrunk 2.6 percent in one cycle to 1530°K.

Expansion behavior of the insulation was also determined for samples that had been given five half-hour furnace cycles to 1530°K (2300°F). An expansion coefficient of $4.6 \times 10^{-6}/°K$ measured for both the GE and MDAC heat-treated samples is slightly different than that of the as-received materials. However, an expansion coefficient of $1.1 \times 10^{-6}/°K$ for the heat-treated LMSC insulation is about double that of as-received material. Although the coefficient was increased, the expansion curve was linear on heating, and only 0.01 percent length change occurred at an inversion near 500°K (450°F) on cooling.

306

THERMAL EXPANSION CHARACTERISTICS OF REI MATERIALS

	GE	LMSC	MDAC
COEFFICIENT, 10^{-6} $\degree$K^{-1}			
INSULATION	5.2	0.44	6.6
COATING	4.4	0.28	8.4
COATING UNDER LOAD	2.7	nil	3.9
INSULATION			
PEAK TEMPERATURE, $\degree$K($\degree$F)	None	1350 (1960$\degree$F)	1600 (2420$\degree$F)
PEAK EXPANSION, PERCENT	None	0.05	+0.79
DIMENSIONAL CHANGE IN ONE			
CYCLE TO 1530$\degree$K, PERCENT	Nil	-2.6	Nil
INVERSIONS ON COOLING	None	None	None
COATING SOFTENING POINT, $\degree$K($\degree$F)			
LOADED	>1440 (>2140$\degree$F)	1480 (2200$\degree$F)	1260 (1810$\degree$F)
UNLOADED	1530 (2300$\degree$F)	1530 (2300$\degree$F)	1530 (2300$\degree$F)

Figure 16

307

CONCLUDING REMARKS

Novel attachment and strain-measuring techniques were developed to obtain valid mechanical and thermophysical property data to above 1530°K (2300°F) in air on the RSI insulators and their coatings. While much of the data verify properties reported by the material manufacturers, additional data have been generated that had not previously been available, especially those for the insulators at elevated temperatures and coatings separated from them.

Comparative tests have demonstrated that "end effects" can lead to erroneous strain and modulus data in compression tests. Attempts have been made to minimize these effects as much as possible by cementing specimens to loading blocks or monitoring strain directly in the gage length. Good agreement observed between the tensile and "good" compressive moduli of each material in both in-plane and cross-plane tests substantiate the validity of the data. Generally, the data obtained on each material agree with those obtained by the material contractors, except that the Battelle moduli may be higher and failure strains lower.

The lever-arm extensometer developed for measuring strain does not require any electrical or manual corrections for temperature and thus can be used for measuring thermal and/or mechanical strain. Consequently, thermal expansion measurements could be made on coating specimens subjected to a tensile load to define their softening points. Creep characteristics of the insulators were monitored at elevated temperatures and found to become significant above 1090°K (1500°F).

Because the strain measurement equipment is versatile, it can be modified to measure strain on shear specimens as well as tensile and compressive specimens. Currently, techniques are being developed to obtain shear strength and strain data and cross-plane tensile strength and strain data at elevated temperatures. These data are needed for three-dimensional stress analyses in TPS panels.

308

REFERENCE

1. Goldstein, H.E., Buckley, J.D., King, H.M., Probst, H.B., and Spiker, I.K.: "Reusable Surface Insulation Materials Research and Development", paper presented at NASA Space Shuttle Technology Conference held in San Antonio, Texas, April 12-14, 1972. Proceedings published in NASA TM X-2570, July 1972.

309

11

PORE STRUCTURE ANALYSIS OF RSI TILE

By

O. J. Whittemore, Jr. and L. W. Smiser

The Method

Mercury porosimetry is the most generally used method of quantitatively measuring pore size distributions of open-pored solids. Mercury is an unusual liquid in that it does not wet most solids and pressure must be applied to force it into pores. Washburn[1] first suggested using mercury intrusion and proposed the relationship:

$$P = \frac{-2\,\gamma\cos\theta}{r}$$

where r is the radius of the pore being intruded by mercury under pressure P, γ is the surface tension of mercury, and θ is the contact or wetting angle of mercury with the solid. Since γ and θ can be considered constants, only pressure need be measured to determine pore size.

Ritter and Drake[2,3] first developed the method and published experimental data on several materials. Excellent agreement between mercury porosimetry and isothermal nitrogen desorption in determining fine pore sizes was demonstrated by Joyner et al.[4] In the past two decades, the method has been applied to studies of many materials and several designs of equipment have evolved, differing mainly in technique of measuring the intruded volume.

Many of the applications have been devoted to ceramics. Watson et al.[5] demonstrated the relation of pore dimensions to properties of structural products such as brick and building stone. Ulmer et al.[6] studied the pore structure of several steel plant refractories. Thompson et al.[7] found by mercury porosimetry that the porosity and pore size of plasma-sprayed alumina increased because of crystal inversion when the material was reheated.

The factors contributing to errors in mercury porosimetry are discussed by Rootare et al.[8] Some of these are:

312

(1) The surface tension of mercury. Reported to be from 473 to 485 dynes/cm., it also can vary slightly with temperature.

(2) The contact or wetting angle for mercury with the solid. Most workers assume either 130° or 140°, but it may vary from 120° to 160°.

(3) Compressibility of mercury. This cause of error is accentuated by high pressure and by the ratio of the volume of mercury used in the test to the volume of the sample.

(4) The "ink-bottle" pore with an opening smaller than the pore itself. This method determines the size of the opening.

(5) Thermal expansion. Mercury has a higher coefficient of thermal expansion than a borosilicate glass sample holder so errors may occur if the equipment heats during the test.

Surface areas can also be calculated from mercury intrusion data by integrating the intrusion curve. Usually a cylindrical pore shape is assumed, but Rootare et al.[9] have shown that a model of pore shape is unnecessary if the curves are integrated with regard to work.

Mercury Porosimetry as Applied to RSI

A study of the structure of RSI is an excellent application of mercury porosimetry. The factors leading to error are all minimized. Because of the high porosity (~90%), no error can be expected due to "ink bottle" pores since any pore has several openings, the largest of which would allow intrusion. Most pores are larger than 12 μm in diameter so that atmospheric pressure is sufficient for their characterization, thus simplifying the experimental apparatus. Little error is caused by compressibility at these low pressures. Since no additional pressurization is needed, no heating would occur so errors due to thermal expansion would be absent.

Ormiston et al.[10] studied the sintering of silica RSI by mercury porosimetry. Surface areas were calculated at 12.64 m²/g, agreeing within 2% of areas determined by nitrogen adsorption, 12.85 m²/g. The

average fiber diameter was calculated by finding the diameter of a single fiber of the same surface area and was found to be 1.44 μm as compared with an average diameter of 1.56 μm measured on SEM photomicrographs. They estimated that not over 4% of the total surface area of RSI would be in the intersections of fibers. Therefore, a sintering model should consider a cylindrical rod rather than the conventional intersection of two spheres.

In their study, Ormiston et al. derived the interesting relationship that the rate of change of fiber radius equals the surface tension of the fiber divided by three times the viscosity. They measured the fiber growth at four temperatures and, assuming a value for surface tension, calculated viscosities that agreed well with published values for fused silica. It should be noted that this analysis can be used only for glass fibers; crystalline fibers do not sinter by viscous flow.

Computations of physical properties of the RSI for which the pore volume has been measured may be made according to the following formulas:

Porosity:

$$P = \frac{V_p \rho t}{V_p \rho t + 1} \quad (100\%) \tag{2}$$

Bulk Density:

$$\rho_b = \frac{\rho t}{V_p \rho t + 1} = \frac{P}{100 V_p} \tag{3}$$

Surface Area:

$$A_s = \frac{1}{\gamma \cos \theta} \sum_{i=1}^{i=n} \bar{P}_i \, \Delta V_i \tag{4}$$

Mean Fiber Diameter:

$$\bar{D}_f = \frac{4}{\rho t \, A_s} \tag{5}$$

Mean Pore Diameter:

$$\bar{D}_p = \sqrt{\frac{V_p}{\sum_{i=1}^{i=n} \left(\frac{\Delta V_i}{\bar{D}_i^2} \right)}} \tag{6}$$

314

SYMBOLS

P	=	porosity
V_p	=	volume of pores per unit weight of RSI
t	=	true density of fibers in RSI
b	=	bulk density of RSI
A_s	=	specific surface area of RSI
γ	=	surface tension of mercury
θ	=	wetting angle of mercury on fibers
$\bar{P}_i$	=	mean pressure of i'th pressure interval
ΔV_i	=	change in mercury penetration volume at i'th pressure step
$\bar{D}_f$	=	mean fiber diameter
$\bar{D}_p$	=	mean pore diameter
$\bar{D}_i$	=	mean pore diameter at i'th pressure step

315

PORE SIZE OF SOME RSI TILES BY MERCURY POROSIMETRY

(Figure 1)

One silica tile LI-1542 and three mullite tiles MDAC MOD I, MDAC MOD III, and GE MOD 1A were examined by mercury porosimetry. The pore volume V_p, porosity P, and the calculated bulk density ρ_b and bulk densitites from direct measurements are given in figure 1. The pore size distributions vary with the tile manufacturer. The Lockheed tile appears to have a log-normal distribution and shows a mean diameter of 16 microns and a geometric standard deviation of 1.8. McDonnell-Douglas tiles have a complex distribution of pore sizes that deviates somewhat from a normal distribution at both ends. The General Electric tile shows a normal distribution of pore sizes with a mean of 91 microns and a standard deviation of 23 microns.

The total pore volume V_p is shown in column 3. This is a directly measured quantity and is the volume of open pores. Porosity is determined by equation (2) assuming that there are no closed pores. The last two columns compare the bulk densities calculated from equation (3) and by the direct method of specimen measurement. With the exception of LMSC LI-1542, the porosimetry figure is higher than the direct measurement figure. This is likely a result of the conformity of mercury to the surface roughness of the tile giving an effectively smaller bulk volume than does external dimensions. Because of the small specimen size (about 0.04 g), a surface layer 90 microns thick (or about the mean pore diameter of three of the test tiles) would contain about 10% of the specimen volume. The porosity is about 90%. Mercury could be expected to fill a large part of this surface volume when the sample is only immersed. Better agreement is expected with larger samples in the order of one gram weight, and suitable equipment is being designed.

MDAC MOD I tile contains a considerable concentration of hollow glass spheres, which contribute a closed porosity accounting for the apparently too high bulk density. An addition of 0.71 x 10⁻³ m³/kg of closed pore volume would be necessary to yield a bulk density of 277 (kg/m³) for this tile. The closed porosity then accounts for about 11% of the total porosity.

PORE SIZE OF SOME RSI TILES BY MERCURY POROSIMETRY

TILE	PORE SIZE DISTRIBUTION	V_p (m^3/kg)	P (%)	ρ_b POROSIMETRY (kg/m^3)	ρ_b DIRECT
LMSC LI-1542	Log-Normal $\bar{D}_p = 16$ μm $\sigma_g = 1.8$	3.5×10^{-3}	89.1	255.2 (15.9)	259.5 (16.2)
MDAC MOD I	Complex $\bar{D}_p = 86$ μm	2.6×10^{-3}	89.1	342.8 (21.4)	277.1 (17.3)
MDAC MOD III	Complex $\bar{D}_p = 65$ μm	3.0×10^{-3}	90.4	301.1 (18.8)	297.9 (18.6)
GE MOD IA	Normal $\bar{D}_p = 91$ μm $\sigma_g = 23$ μm	4.3×10^{-3}	93.2	216.2 (13.5)	200.2 (12.5)

ρ_b values in parentheses are in lb/ft^3

Figure 1

EFFECTS OF HEAT TREATMENT ON RSI

(Figure 2)

This figure shows the effects of heat treatment on the pore structures of these tiles. The silica tile was heat treated at 1260°C (2300°F) for 2 and 16 hours and the mullite tiles were heat treated at 1427°C (2600°F) for 16 and 64 hours. The pore size distributions do not appear to change character with heat treatment. In the case of the Lockheed LI-1542, the mean pore size decreased while the dispersion σg remains nearly constant at 1.8. The mullite tiles, on the other hand, show an increase in mean pore size. The McDonnell-Douglas tiles first show an increase in mean pore size at 16 hours followed by a smaller increase after 64 hours. The pore volume, however, does not appear to increase. On the other hand, the GE tile after 16 hours shows an increase in bulk volume of about 8% with the increase in mean pore size. Porosity and bulk densities reflect these changes in the pore structure.

Shrinkages with respect to the as-received bulk volume are given in the last two columns, and are examples of the use of mercury porosimetry data as a means of calculating such quantities.

EFFECTS OF HEAT TREATMENT ON RSI

TILE	HEAT TREATMENT	PORE SIZE DISTRIBUTION	V_p (m^3/kg)	P (%)	ρ_p (kg/m^3)	Volume Shrinkage (%)	Linear Shrinkage (%)
LMSC	1260°C 2 hrs.	Log-Normal $\bar{D}_p$ - 13 µm	2.2×10^{-3}	83.7	382.7	33.1	12.5
LI·1542	1260°C 16 hrs.	Log-Normal $\bar{D}_p$ - 10 µm	0.8×10^{-3}	65.1	816.9	68.7	32.1
MDAC	1427°C 16 hrs.	Complex $\bar{D}_p$ - 100 µm	2.4×10^{-3}	88.3	369.8	6.9	2.4
MOD I	1427°C 64 hrs.	Complex $\bar{D}_p$ - 98 µm	1.5×10^{-3}	82.5	553.1	37.7	14.6
MDAC	1427°C 16 hrs.	Complex $\bar{D}_p$ - 77 µm	2.8×10^{-3}	89.8	321.6	6.0	2.0
MOD III	1427°C 64 hrs.	Complex $\bar{D}_p$ - 67 µm	2.9×10^{-3}	90.1	311.9	3.0	1.0
GE	1427°C 16 hrs.	Normal $\bar{D}_p$ - 105 µm	4.7×10^{-3}	93.6	199.4	-8.7	-3.0
MOD I-A	1427°C 64 hrs.	Normal $\bar{D}_p$ - 105 µm	3.7×10^{-3}	92.1	249.2	13.0	4.5

Figure 2

BULK DENSITY MAP OF GE MOD 1A TILE AT MID-LEVEL

(Figure 3)

Density variations within a 30.5 x 30.5 x 53.4 cm (12 x 12 x 21 inch) GE REI mullite tile were measured by mercury porosimetry. Samples were taken 2.54 cm (one inch) below the coated surface at 5.08 cm (two inch) or 10.2 cm (four inch) intervals. The average of three samples was used at each point to make the bulk density map shown in figure 3. The map indicates a density gradient toward the center. This may be the result of firing behavior since the same tile indicated an expansion upon firing at 1427°C (2600°F) for 16 hours. Thus it is conceivable that the firing of the tile produced this gradient due to more severe heating conditions at the edges than near the center. These contours could then be a reflection of the thermal coutours during firing.

Bulk Density Map of GE MOD IA Tile
at Mid-Level

kg/m³ (lb/ft³)

(10.50)
168.2

(11.00)
176.2

(11.50)
184.2

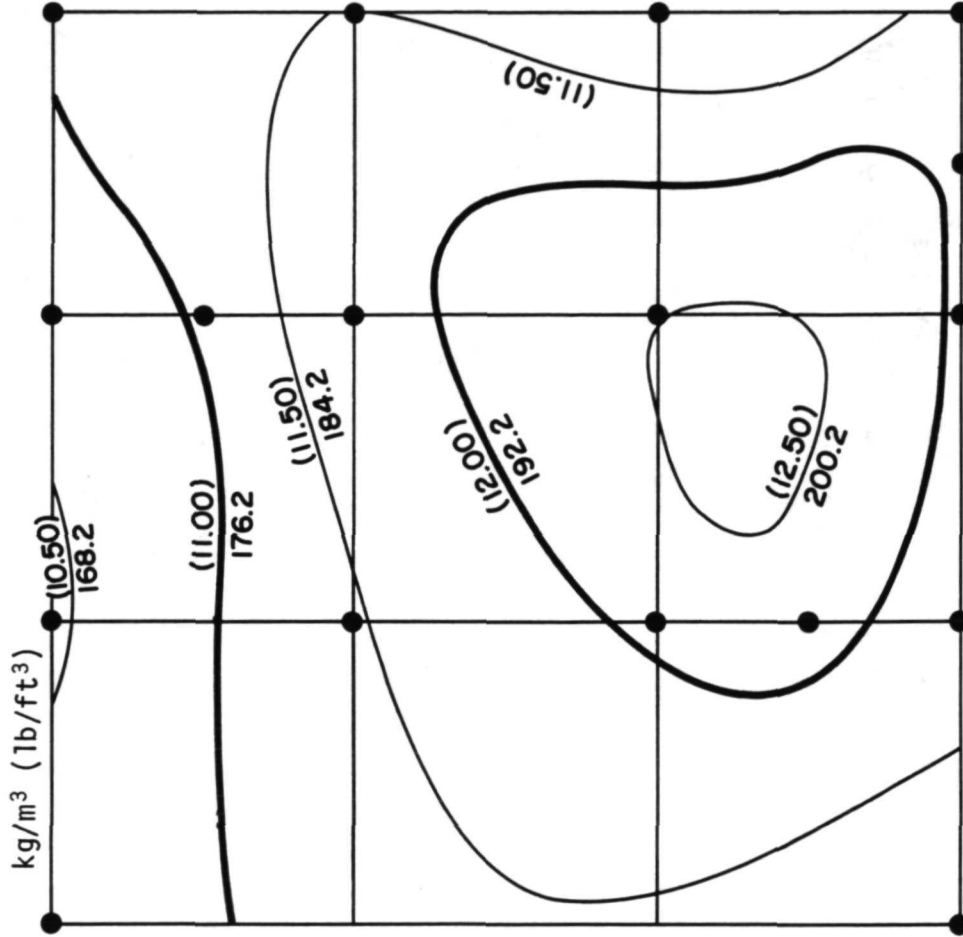(12.00)
192.2

(12.50)
200.2

(11.50)

Figure 3

A COMPARISON OF BULK DENSITIES FROM POROSIMETRY AND

DIRECT MEASUREMENTS ON AN RSI TILE

(Figure 4)

Several specimens were checked by measuring their dimensions and weighing to determine their bulk densities. Figure 4 shows the results for six specimens. The differences are fairly constant at about 48 kg/m³ (3 lb/ft³). The regression equation shows that there is a good correlation between the two methods. The values reported on the density map in figure 3 are mercury porosimetry bulk densities adjusted according to the regression equation.

A COMPARISON OF BULK DENSITIES FROM POROSIMETRY AND DIRECT MEASUREMENTS ON AN RSI TILE

SECTION NUMBER	ρ_1 (kg/m^3) POROSIMETRY	ρ_2 DIRECT	$(\rho_1 - \rho_2)$	$\hat{\rho}_2$
1	226.82	176.04	50.77	181.39
5	252.93	198.47	54.46	199.95
16	249.41	196.39	53.02	197.45
9	241.40	195.43	45.97	191.75
19	219.62	176.37	43.25	176.27
4	229.39	187.42	41.97	183.22
AVERAGES	236.60	188.38	48.22	188.34

REGRESSION EQUATION: $\hat{\rho}_2 = 0.711\rho_1 + 20.119$

CORRELATION COEFFICIENT: $R = 0.937$

MEAN DEVIATION: $\dfrac{\Sigma|\rho_2 - \hat{\rho}_2|}{(6)\,(188.38)}\,(100\%) = 1.4\%$

Figure 4

323

CONCLUSIONS

Mercury porosimetry gives a means of characterizing RSI tile pore structure in terms of porosity, pore size distribution, bulk density, specific surface area, mean pore diameter, and mean fiber diameter. It also allows the determination of the effects of heat treatment on these parameters. It is limited in application to open-pored structures, however, since any closed pore volume is ignored.

Porosimetry devices are inherently simple, and when pores are all larger than about 12 microns, atmospheric pressure is adequate for determination of pore size distributions.

REFERENCES

1. Washburn, E.W.: "Note on a Method of Determining the Distribution of Pore Sizes in a Porous Material," Proc. Nat. Acad. Sci. 7: 115-116, 1921.

2. Ritter, H.L. and Drake, L.C.: "Pore-Size Distribution in Porous Materials; Pressure Porosimeter and Determinations of Complete Macropore-Size Distribution," Ind. Eng. Chem. Anal. Ed., 17: 782-6, December 1945.

3. Drake, L.C. and Ritter, H.L.: "Macropore-Size Distribution in Some Typical Porous Substances," Ind. Eng. Chem. Anal. Ed., 17: 787-91, December 1945.

4. Joyner, L.G., Barrett, E.P. and Skold, R.: "The Determination of Pore Volume and Area Distributions in Porous Substances. II. Comparison between Nitrogen Isotherm and Mercury Porosimeter Methods," J.Am. Chem. Soc. 73: 3155-8, July 1951.

5. Watson, S., May, J.O. and Butterworth, B.: "Studies of Pore Size Distribution," Trans. Brit. Ceramic Soc. 56: 5, 37-52, 1957.

6. Ulmer, G.C. and Smothers, W.J.: "Application of Mercury Porosimetry to Refractory Materials," Am. Cer. Soc. Bul. 46: 7, 649-52, 1967.

7. Thompson, V.S. and Whittemore, O.J., Jr.: "Structural Changes on Reheating Plasma-Sprayed Alumina," Am. Cer. Soc. Bul. 47: 7, 637-41, 1968.

8. Rootare, H.M. and Nyce, A.C.: "The Use of Porosimetry in the Measurement of Pore Size Distribution in Porous Materials," Inst. Jour. Powder Met., 7: 1,3-11, 1971.

9. Rootare, H.M. and Prenzlow, C.F.: "Surface Areas from Mercury Porosimeter Measurements," J. Phys. Chem., 71: 2734-36, July 1967.

10. Ormiston, T.J. and Whittemore, O.J., Jr.: "Sintering of Silica Fiber Compacts," accepted for publication in the Amer. Cer. Soc. Bulletin.

325

12

SPECTRAL AND TOTAL NORMAL EMITTANCE OF REUSABLE SURFACE INSULATION MATERIALS

Andronicos G. Kantsios, S. Franklin Edwards, and Dennis L. Dicus

SUMMARY

Measurements of spectral and total normal emittance have been made on three types of reusable external insulation materials proposed for space shuttle. The types measured were manufactured by General Electric, McDonnell Douglas, and Lockheed. Emittances were measured in the spectral range 1 to 15 μm at temperatures of 800°K and 1100°K and 1300°K using a radiometric measurement technique. Values were determined by a comparison method to a National Bureau of Standards inconel specimen. Results indicate that the total normal emittance of these materials is less than 0.8 between 800°K and 1300°K. The total normal emittance decreases with increasing temperature. Considerable variation in measured emittance was found in measurements taken on several virgin samples of each material indicating a possible non-uniformity in the coating thickness or composition. The three candidate materials exhibited a similar spectral emittance distribution.

INTRODUCTION

One of the most important thermal properties of the materials proposed as reusable surface insulation (RSI) is the emittance. Since reradiation is the principle heat rejection mode for surface insulation, the emittance should be optimized at the operating temperature anticipated for the materials. Since the low density ceramic heat-shield materials have low emittance and may be partially transparent, high emittance coatings must provide heat rejection capacity while ensuring opacity.

The three main techniques used for measuring emittance are calorimetric, reflectance, and radiometric, whose working equations are:

Calorimetric:
$$\varepsilon = \frac{P}{\sigma (T_s^4 - T_o^4)}$$

Reflectance:
$$\varepsilon_\lambda = 1 - \rho_\lambda$$

Radiometric:
$$\varepsilon_\lambda = \frac{W_\lambda (T)}{W_{b\lambda} (T)} \qquad \text{where } W_{b\lambda} (T) = \frac{C_1}{\lambda^5 (e^{C_2/\lambda T} - 1)}$$

The calorimetric technique equates input power into a material to radiative heat loss by the material, since conduction and convection losses are minimized by design. This technique gives total hemispherical emittance. For the reflectance technique, energy of a specified wavelength band at a specified angle is impressed on the test material's surface and the amount reflected is measured. Assuming that the material is opaque and that Kirchoff's laws hold, the spectral emittance can be calculated from the reflectance. Finally, the radiometric technique compares energy radiated by a material to the energy radiated by a black body at the same temperature and wavelength. The emittance values reported in this paper were obtained from measurements using a radiometric technique. The spectral and total normal emittances of RSI materials heated in air from 800 to 1300°K over the wavelength range from 1 to 15 μm are reported.

328

SYMBOLS

C_1 —   radiation constant
C_2 —   radiation constant
P —   power input
T —   temperature
V —   thermopile output voltage
W —   Planck distribution function
ε —   emittance
λ —   wavelength
ρ —   reflectance
σ —   Stefan-Boltzmann constant

Subscripts

b —   black body
n —   normal
o —   surrounding environment
Ref   —   NBS reference specimen
s —   sample
t —   total
λ —   spectral

HIGH TEMPERATURE EMITTANCE APPARATUS

(Figure 1)

A schematic representation of the radiometric technique used to make emittance measurements is shown in figure 1. The test specimen and reference specimen are suspended side by side on a rotating holder mounted within a high temperature furnace (ref. 3). A typical specimen is 3 by 3 by 2.5 cm. The test specimen is backed by platinum foil to avoid transmission of energy from the rear of the furnace. The reference specimen is a 2.5-cm diameter oxidized inconel disk procured from the National Bureau of Standards (NBS) (ref. 4). Values of normal spectral emittance of the reference specimen are given by NBS for 155 discrete wavelengths over the range of 1 to 15 μm for temperatures of 800, 1100, and 1300°K.

The holder is rotated from the position in the upper part of the furnace, past a water-cooled aperture located in the lower part of the furnace, and then back to the top of the furnace in 12 seconds. Energy from the specimens as they pass the aperture is dispersed by an NaCl prism spectrometer and measured by a thermopile detector. The detector output is recorded on a strip chart potentiometer. After each measurement (at each wavelength) the specimens are held in the upper part of the furnace for at least 60 seconds. Temperatures of the specimens are assumed to be that of the furnace. Platinum-platinum-13% rhodium thermocouples are used to measure and control the furnace temperature.

330
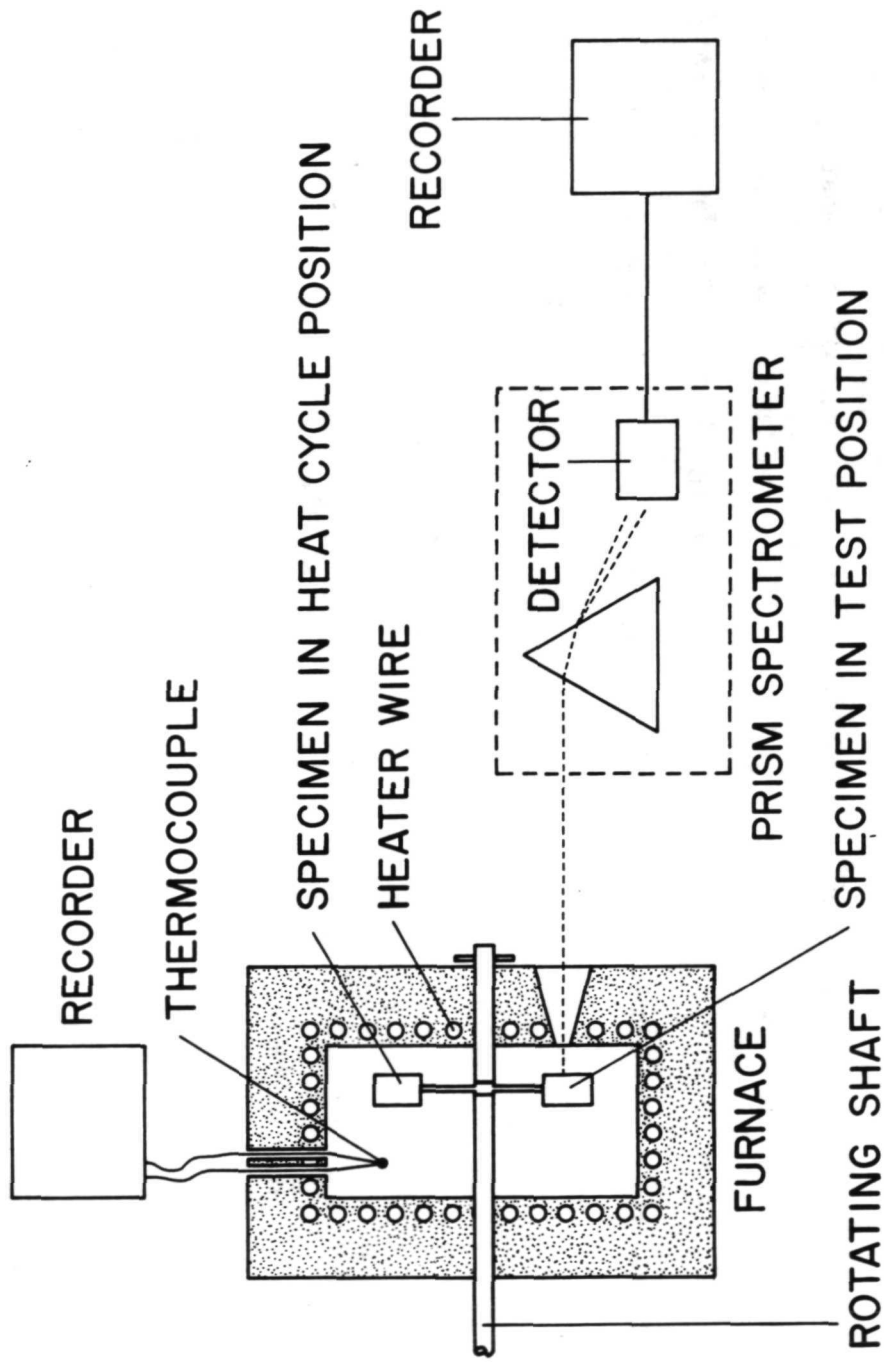
HIGH TEMPERATURE EMITTANCE APPARATUS

Figure 1

EQUATIONS GOVERNING CALCULATIONS

(Figure 2)

Values of emittance are determined at discrete wavelengths by equations described in

figure 2. The ratio of the thermopile output voltage generated by the test specimen to the

thermopile output voltage generated by the reference specimen is directly proportional to the

ratio of the test specimen spectral emittance to the reference spectral emittance. Substitut-

ing the two measured voltages and the known emittance in equation (1) the test specimen

spectral emittance is calculated. For temperatures between 800 and 1300°K at least 95% of the

energy radiated by the test specimen is located in the 1 to 15 μm band. Therefore, a reasonably

accurate value of total normal emittance can be calculated using equation (2). The indicated

integration was performed numerically, using the trapezoidal rule, as shown in equation (3).

EQUATIONS GOVERNING CALCULATIONS

$$\epsilon_n(\lambda, T) = \frac{V_s(\lambda, T)}{V_{Ref}(\lambda, T)} \, \epsilon_{Ref}(\lambda, T) \qquad (1)$$

$$\epsilon_{tn}(T) = \frac{\int_1^{15} \epsilon_s(\lambda, T) \, W_b(\lambda, T) \, d\lambda}{\int_1^{15} W_b(\lambda, T) \, d\lambda} \qquad (2)$$

$$\epsilon_{tn}(T) = \frac{\sum\limits_{i=1}^{15} \left\{ \frac{\epsilon_s(i+1, T) \, W_b(i+1, T) + \epsilon(i, T) \, W_b(i, T)}{2} \right\} \left\{ \lambda(i+1) - \lambda(i) \right\}}{\sum\limits_{i=1}^{15} \left\{ \frac{W_b(i+1, T) + W_b(i, T)}{2} \right\} \left\{ \lambda(i+1) - \lambda(i) \right\}} \qquad (3)$$

Figure 2

RSI MATERIALS

(Figure 3)

The commercial designation for the RSI materials examined in this study are shown in figure 3. Each consists of a low density ceramic insulator that is coated to increase its emittance and make it waterproof. The General Electric coating is a multiphase glass containing kyanite, petalite, and a nickel oxide emittance agent. The insulator is composed of mullite fibers with an $Al_2O_3-SiO_2-B_2O_3$ glass binder. The coating on the Lockheed (LMSC) material is a borosilicate glass containing silicon carbide as an emittance agent. The coating on the insulation is composed of silica fibers with a colloidal silica binder. The coating on the McDonnell Douglas (MDAC) material is multi-layered. The outer layer enhances the emittance. It is a black ceramic oxide stain containing a mixture of iron, chromium, and cobalt oxides. The insulation is composed of mullite fibers with silica microspheres and a silica binder. The materials were supplied in large tiles. All the test samples for each material were taken from the same tile. In later figures the materials are referenced by company name only.

RSI MATERIALS

COMPANY	COATING TYPE	INSULATION TYPE
G.E.	SR-2	REI-MULLITE MOD IA
LMSC	LI-0042	LI-1500
MDAC	$M_{23}A_7P_{700}$	MULLITE-HCF MOD III

Figure 3

SPECTRAL NORMAL EMITTANCE OF RSI MATERIALS AT 800°K

(Figure 4)

The next three figures show normal emittance of the three candidate materials as a function of wavelength for three temperatures. The values shown represent the average of runs on three virgin specimens of the G.E. and MDAC material and five virgin specimens of the LMSC material. Data were taken at 0.5 μm intervals from 1 to 3 μm and at 1 μm intervals from 3 to 15 μm. The 1 to 3 μm region was examined more closely in anticipation of more rapid emittance changes in this region.

At 800°K (figure 4) for these materials as a group, the emittance tended to decrease from 1 to 2.5 μm, increased from 2.5 to 8 μm, and remained relatively constant out to 14 μm where it decreased again. Values of emittance ranged from 0.85 to 0.53 over the spectral range. The G.E. material had the highest emittance over most of the region with the significant difference occurring in the 5 to 8 μm region. The LMSC material's emittance very closely followed the G.E. material except in the 5 to 8 μm region. The MDAC material had the lowest emittance of the three throughout most of the region, although the difference was slight beyond 9 μm.

SPECTRAL NORMAL EMITTANCE OF RSI MATERIALS AT 800°K
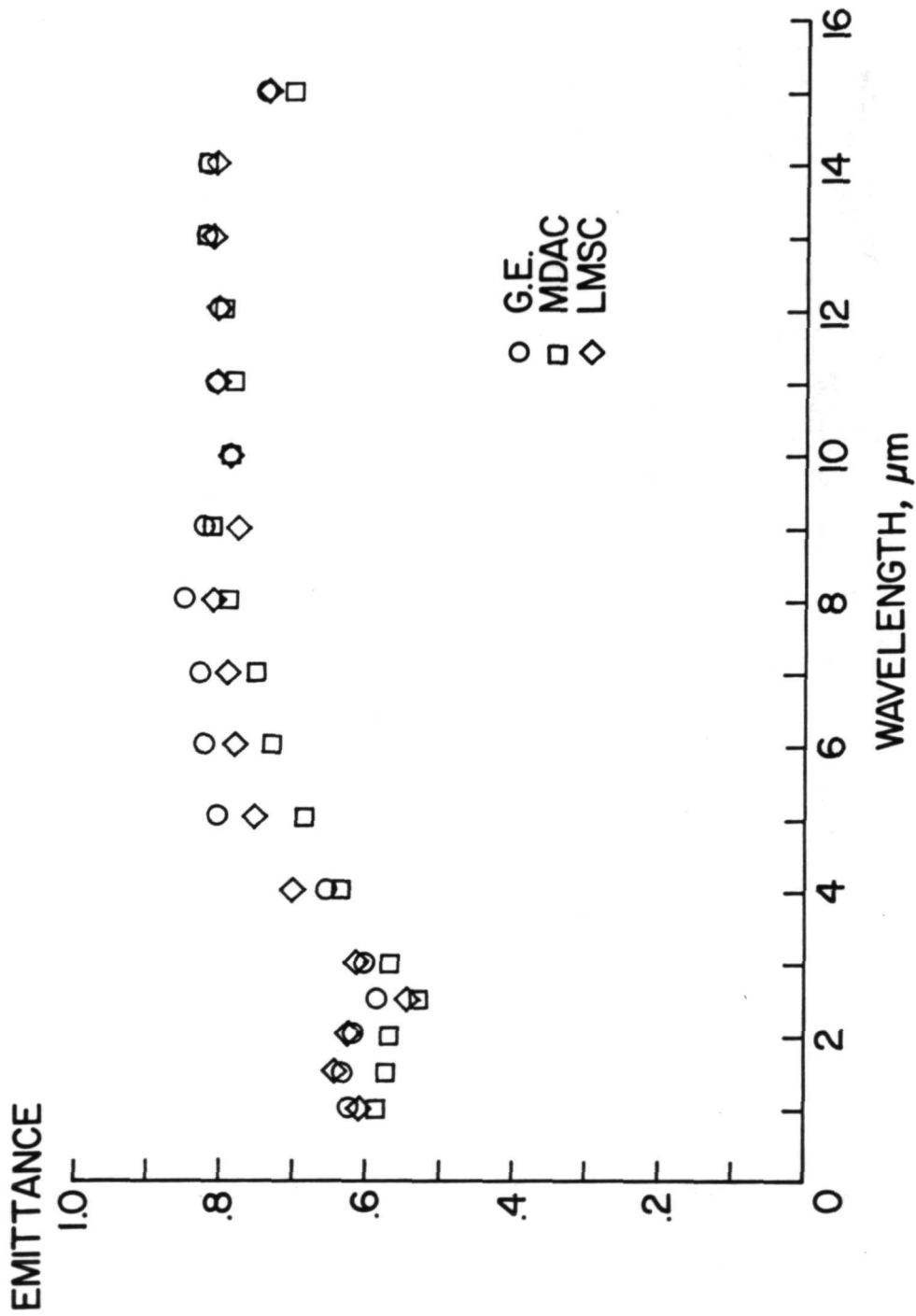
Figure 4

SPECTRAL NORMAL EMITTANCE OF RSI MATERIALS AT 1100°K

(Figure 5)

Figure 5 shows the spectral emittance of the three materials at 1100°K. Trends in the relative magnitudes were similar to those at 800°K. Values of emittance ranged from 0.86 to 0.49 over the spectral range. Comparing this data to the 800°K values, the G.E. and LMSC values were lower between 1 and 2.5 μm. The emittance of the G.E. material was higher beyond 2.5 μm, while the emittance of the LMSC material remained essentially the same. The emittance of the MDAC material remained essentially the same up to 2 μm and beyond 5 μm with some increase in emittance in the 2.5 to 5 μm region.

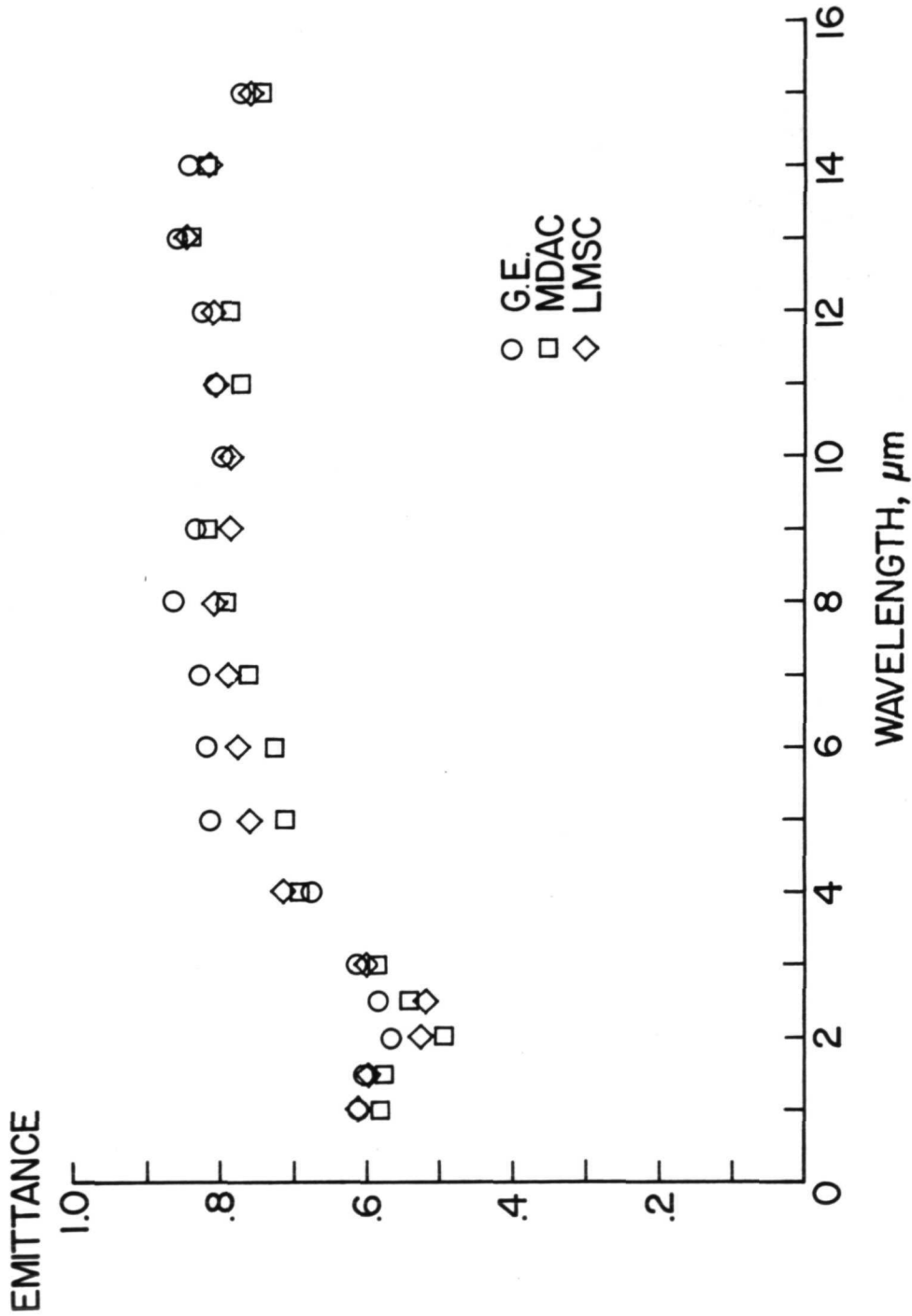SPECTRAL NORMAL EMITTANCE OF RSI MATERIALS AT 1100°K

Figure 5

SPECTRAL NORMAL EMITTANCE OF RSI MATERIALS AT 1300°K

(Figure 6)

The spectral emittance of the three materials at 1300°K is shown in figure 6. Values of emittance ranged from 0.82 to 0.48 over the spectral range. Trends in the relative magnitudes were similar to those at the two lower temperatures except in the 1 to 3 μm region where the emittance of the MDAC material was slightly higher than that of the LMSC material. Comparing these data to the values at 1100°K from 1 to 3 μm, the emittance of the G.E. material was slightly lower and that of the MDAC material was somewhat higher. Beyond 3 μm, the emittance of the G.E. material was slightly higher while the MDAC material exhibited very little change. The emittance of the LMSC material was lower between 1 and 2 μm and was virtually unchanged beyond 2 μm.

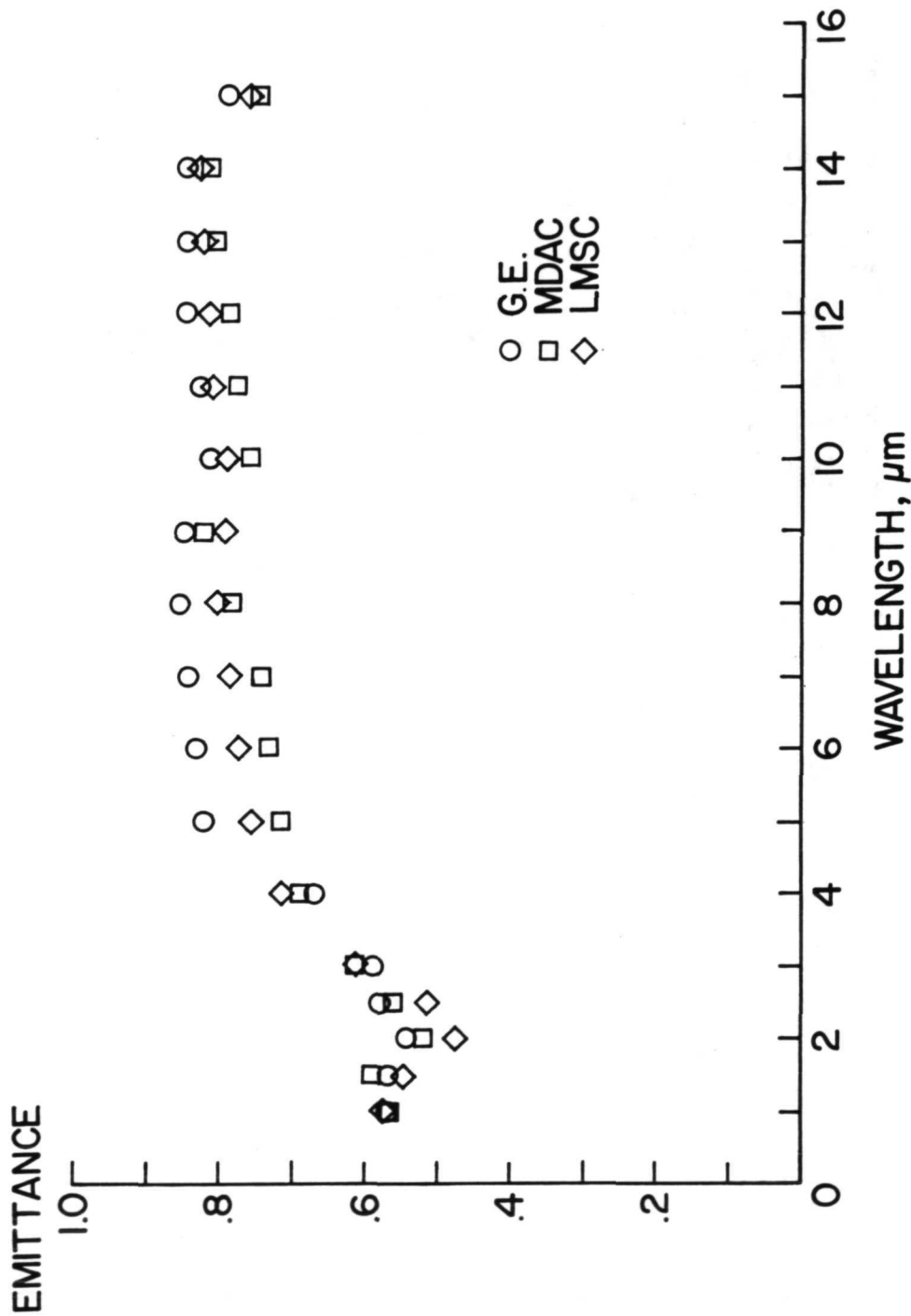# SPECTRAL NORMAL EMITTANCE OF RSI MATERIALS AT 1300°K

Figure 6

TOTAL NORMAL EMITTANCE OF RSI MATERIALS AS A FUNCTION OF TEMPERATURE

(Figure 7)

The total normal emittance of the three materials as a function of temperature is shown in figure 7. The data were calculated from the average spectral emittance values. Over all temperatures, total normal emittance values ranged from 0.74 to 0.63. The G.E. material exhibited the highest total normal emittance at each temperature. The LMSC material had the next highest emittance at 800 and 1100°K, but it exhibited a slightly lower emittance than the MDAC material at 1300°K. The emittance of the G.E. and LMSC materials decreased rapidly and nearly linearly with increasing temperature. The MDAC material showed a much more gradual nonlinear decrease in emittance with increasing temperature.

TOTAL NORMAL EMITTANCE OF RSI MATERIALS
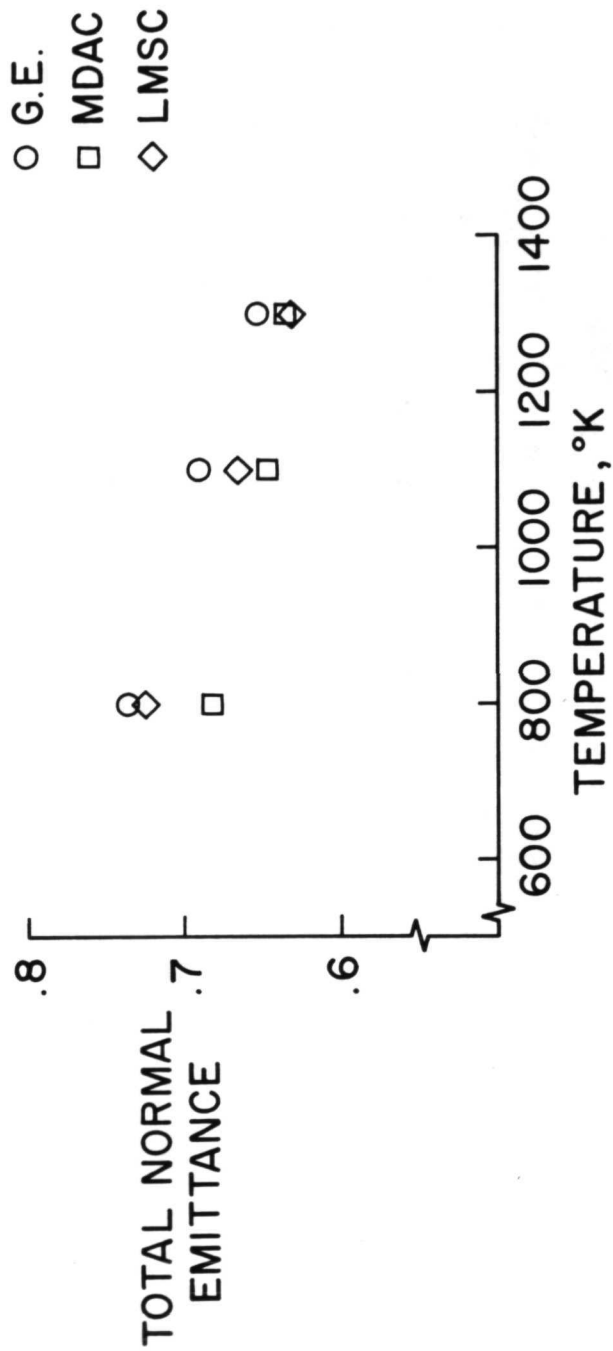AS A FUNCTION OF TEMPERATURE

Figure 7

343

VARIATION IN TOTAL NORMAL EMITTANCE OF VIRGIN RSI MATERIALS

(Figure 8)

Measurements were made on several virgin samples of each material to assess their consistency. The spread in the total normal emittance from all runs on each material is shown in figure 8. The average values shown in the previous figure are superimposed. The G.E. and MDAC materials exhibited considerably less scatter than the LMSC material at 800 and 1100°K. At 1300°K the scatter was comparable for all three materials. It should be noted again that the LMSC data covered measurements on five specimens while G.E. and MDAC data covers measurements on three specimens each. The samples for each of these sets of materials were taken from a single tile. The scatter in the data may indicate a variation in either coating thickness or coating composition. It is difficult to make a conclusive statement about the scatter with the limited number of tests completed to date.

344
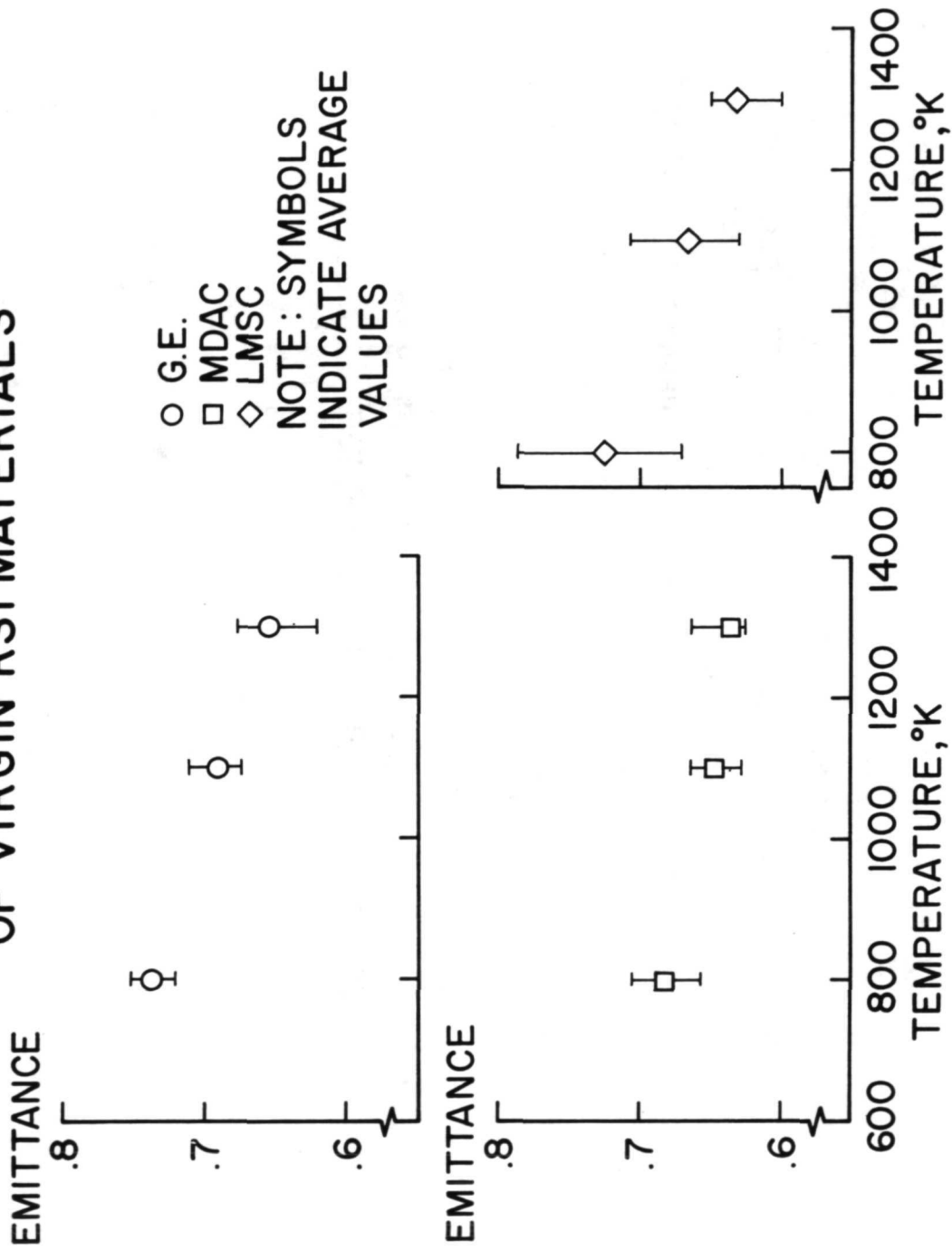
VARIATION IN TOTAL NORMAL EMITTANCE
OF VIRGIN RSI MATERIALS

Figure 8

345

CONCLUDING REMARKS

BETWEEN TEMPERATURES OF 800°K AND 1300°K

TOTAL NORMAL EMITTANCE

- LESS THAN 0.8
- DECREASED WITH INCREASING TEMPERATURE
- CONSIDERABLE VARIATION IN MEASUREMENTS OF SEVERAL VIRGIN SAMPLES OF EACH MATERIAL
- EMITTANCE OF THREE MATERIALS CONVERGED TO NEARLY SAME VALUE AT 1300°K

SPECTRAL EMITTANCE

- SIMILAR DISTRIBUTION
- LOWEST EMITTANCE BETWEEN 1 AND 4 µm
- GREATEST DIFFERENCE BETWEEN 5 AND 8 µm
- RELATIVELY WAVELENGTH INDEPENDENT BEYOND 8 µm

346

REFERENCES

1. Wiebelt, J.A.: Engineering Radiation Heat Transfer, Holt, Rinehart, and Winston, 1966.

2. Harrison, T.R.: Radiation Pyrometry and its Underlying Principles of Radiant Heat Transfer, John Wiley and Sons, 1960.

3. Slemp, W.S. and Wade, W.R.: A Method for Measuring the Spectral Normal Emittance in Air of a Variety of Materials Having Stable Emittance Characteristics. Measurement of Thermal Radiation Properties of Solids, NASA SP-31, pp. 433-439, 1963.

4. Richmond, J.C. Harrison, W.N. and Shorten F.J.: An Approach to Thermal Emittance Standards. Measurement of Thermal Radiation Properties of Solids, NASA SP-31, pp. 403-423, 1963.

347

N73-33474

13

AN EXPLORATORY STUDY OF THE MICROSTRUCTURE

OF MULLITE FIBERS

G. Santoro, H. B. Probst and B. Buzek

NASA-Lewis Research Center

INTRODUCTION

Although considerable effort has been directed to the consolidation of mullite fibers into rigidized tiles, little work has been directed toward the characterization of the microstructure of mullite fibers either alone or in the rigidized tiles. It would seem that microstructural features would certainly control the properties of the fibers, which in turn should to some degree affect the properties of the finished tiles. Thus, it was the purpose of this investigation to examine methods that could more fully reveal the microstructure of mullite fibers. The methods found effective during this study will be used in an investigation relating microstructural features to mechanical behavior. The ultimate goal is to define means of improving the mechanical behavior of mullite fibers.

The approach taken in this phase of the effort was to examine a number of mullite-composition fibers and their precursor solution in the as-prepared condition and after subjecting them to a range of thermal exposures, primarily near the maximum end of their useful temperature range. The idea was to ascertain how well various transmission electron microscopy (TEM) techniques could identify microstructural features associated with compositional differences, variations in heat treatments and differences in material preparation. The experimental techniques used for this purpose included TEM examinations of microtomed sections of mounted fibers and of replicas of polished, chemically etched and cathodically etched fibers. In addition to the electron microscopy effort, X-ray diffraction analyses were used to identify crystalline phases and to determine crystallite size.

MATERIAL PROPERTIES

(Figure 1)

The materials studied in this investigation are given in Figure 1. Both the spun fibers and monofilaments were supplied by the manufacturer producing the mullite fibers which are currently being used in the preparation of RSI. The handmade fibers and the cast solution were prepared at Lewis Research Center from the manufacturer's precursor solution (standard composition). Of the three spun fibers the standard fiber is being used for making RSI tiles of mullite. The handmade fibers were produced by evenly distributing a few drops of the precursor solution between two glass slides and then pulling the slides apart in rapid motions in front of an electric fan. The cast material was prepared by spreading the precursor solution into a thin film, drying and heating at 1065°C for 10 minutes. The heat treatment was to convert the hydrous ingredients into the oxides.

The only crystalline phase detected in the as-received standard spun fiber and in the Al_2O_3-rich spun fiber was $\gamma-Al_2O_3$. In the other materials only mullite was detected. The mean diameter values were determined from measurements on 100 fibers from each of the three compositions. The data were fitted on probability paper and the log-normal distribution was found to give the best fit in each case.

350

MATERIAL PROPERTIES

MATERIALS	COMPOSITION, MOL % (WT %)				CRYSTALLINE PHASES	MEAN FIBER DIAM LOG-NORMAL DISTRIBUTION
	Al_2O_3	SiO_2	B_2O_3	P_2O_5		
STANDARD SPUN FIBER	67.7 (77.0)	25.5 (17.0)	5.8 (4.5)	1.0 (1.6)	γ-Al_2O_3	6.8±4.0 μm
Al_2O_3-RICH SPUN FIBER	77.4 (84.0)	15.8 (10.1)	5.8 (4.3)	1.0 (1.5)	γ-Al_2O_3	9.5±2.1 μm
SiO_2-RICH SPUN FIBER	53.2 (64.8)	40.0 (28.7)	5.8 (4.9)	1.0 (1.7)	MULLITE	8.0±2.5 μm
MONOFILAMENT	STANDARD COMPOSITION				MULLITE	6.8*
HAND-MADE FIBER	STANDARD COMPOSITION				MULLITE	-------
CAST PRECURSOR SOLUTION	STANDARD COMPOSITION				MULLITE	-------

*MANUFACTURER'S DATA - NORMAL AVG OF 10 MEASUREMENTS

Figure 1

CRYSTALLITE SIZE

(Figure 2)

The materials studied in this investigation were subjected to various isothermal exposures at 1205°C and at 1426°C. The specimens were heated on platinum foil in a platinum wound furnace and then cooled in air. The times at temperature for the various samples are listed in Figure 2.

The TEM crystallite size value was determined by measuring and averaging the widths of about 100 images of the crystallites appearing in the transmission photos. In many cases ten to twelve photographs were required to provide enough sufficiently clear images. The crystallite widths were measured so as to be able to compare this data with sizes calculated from XRD. The latter was determined from diffraction line broadening using a quartz sample to correct for instrumental broadening introduced by the diffractometer (ref. 1). The diffraction profiles measured are the (400) reflection of γ-Al_2O_3 along with the (201) quartz reflection and the (110) reflection of mullite along with the (100) quartz reflection. This procedure yielded the average crystallite width. The TEM and XRD size data are in good agreement, except for the TEM replica value of 2300 Å compared to microtome size of 1022 Å and an XRD size of 1350 Å. This apparent discrepancy will be discussed later.

Both sets of size values (TEM and XRD) show that with the standard spun fibers and the Al_2O_3-rich spun fibers the average size increased until the 16 hour - 1426°C exposure where the average size then decreased. For the SiO_2-rich spun fiber the size at first increased and then remained more or less constant at the one hour - 1205°C and the one hour - 1426°C exposures and then it increased again. The nature of these observed discontinuities in the growth of the crystallites is described later along with experimental verification.

CRYSTALLITE SIZE

MATERIALS	THERMAL TREATMENT	TEM		XRD	
		TECHNIQUE	SIZE (WIDTH), Å	SIZE, Å	PHASE,
STANDARD SPUN FIBER	AS-RECEIVED	MICROTOME	ABOUT 100-200	61	γ-Al$_2$O$_3$
	1 HR AT 1205° C	----------	----------	423	MULLITE
	1 HR AT 1426° C	MICROTOME	663	765	MULLITE
	16 HR AT 1426° C	MICROTOME	480	378	MULLITE
	116 HR AT 1426° C*	MICROTOME	1022	1350	MULLITE
	116 HR AT 1426° C*	REPLICA	2300	1350	MULLITE
Al$_2$O$_3$-RICH SPUN FIBER	AS-RECEIVED	MICROTOME	ABOUT 100-200	73	γ-Al$_2$O$_3$
	1 HR AT 1205° C	----------	----------	345	MULLITE
	1 HR AT 1426° C	MICROTOME	950	1000	MULLITE
	16 HR AT 1426° C	MICROTOME	520	838	MULLITE
SiO$_2$-RICH SPUN FIBER	AS-RECEIVED	MICROTOME	ABOUT 100-200	213	MULLITE
	1 HR AT 1205° C	----------	----------	408	MULLITE
	1 HR AT 1426° C	MICROTOME	350	325	MULLITE
	16 HR AT 1426° C	MICROTOME	519	623	MULLITE
CAST SOLUTION	AS-PREPARED	----------	----------	440	MULLITE
	16 HR AT 1426° C	----------	----------	1380	MULLITE

*16 HR AT 1426° C, COOLED TO ROOM TEMP & 100 HR AT 1426° C.

Figure 2

MICROTOMED SECTIONS OF STANDARD SPUN FIBERS

(Figure 3)

Fibers which had been vacuum encapsulated in epoxy resin were sectioned with an ultramicrotome. The cut sections were 0.3 to 1.5 μm thick. Microtomed sections were prepared of the three spun fibers only. All three of the as-received fibers were found to consist of extremely small crystallites (about 100 to 200 Å) dispersed in a large amount of an amorphous phase. The structure shown in Figure 3 is representative of all three compositions. The small dark shapes with sharp edges are the crystallites and the formless grey area surrounding them is the amorphous material. Because of their small size the γ-Al_2O_3 crystallites in the as-received standard and in the as-received Al_2O_3-rich fibers could not be distinguished from the mullite crystallites in the as-received SiO_2-rich fibers.

During thermal exposure the crystallites grew larger and the amount of amorphous material decreased. In the most extreme case studied (116 hours at 1146°C) the crystals appear contiguous. The average crystal size was 1022 Å (TEM) and 1350 Å (XRD), i.e., much less than the mean fiber diameter of 6.8 μm. Thus, the degradation of mechanical properties observed in these fibers after being exposed to temperatures of 1350°C and above (ref. 2) is not the result of crystallites growing to the dimension of the fiber diameter as has been proposed in the case of Y_2O_3-stabilized ZrO_2 fibers (ref. 3). The situation between the two extremes shown here is discussed next using the SiO_2-rich fibers as representative of the microstructure of all three compositions.

354

MICROTOMED SECTIONS OF STANDARD SPUN FIBERS

AS-RECEIVED

0.1 μm

AFTER 116 HOURS AT 1426° C

0.1 μm

Figure 3

MICROTOMED SECTIONS OF SiO$_2$-RICH SPUN FIBERS

(Figure 4)

After heating the fibers at 1426°C for one and for 16 hours the crystallites grew and the amount of amorphous phase decreased. The grey area between the crystallites in Figure 4 is the amorphous phase. Mullite was the only crystalline phase detected by X-ray diffraction in all three compositions. Thus the crystallites shown are assumed to be all mullite. These crystallites are elongated polyhedra, some of which are orientated such that their short axes are in the plane of the photo giving them a square appearance. A prismatic crystalline habit is expected since this mullite was produced essentially from sintering the component oxides. The more common acicular morphology is present only when the mullite is formed in the presence of a liquid phase such as in the solidification from the melt (ref. 4).

The observed discontinuity in growth of the crystallites can be explained by assuming that during the series of thermal exposures new crystallites were nucleated from the amorphous phase while those already present continued to grow. The smaller, more recently nucleated crystallite, eventually became sufficient in number so as to bias the average to a lower value despite the increase in size of the original crystallites. The temperature at which this concurrent nucleation and growth process caused a discontinuity in the average growth rate was found to be higher for the standard and for the Al$_2$O$_3$-rich fiber than for the SiO$_2$-rich fibers. This temperature relationship is probably due to the fact that the homologous temperature of the standard and the Al$_2$O$_3$-rich fibers is higher than that of the SiO$_2$-rich fibers.

The concurrent nucleation and growth process should result in a rather large range of crystallite sizes in the thermally exposed samples. Such a size range was evident in measurements from the TEM photos. For example, after one hour at 1426°C the SiO$_2$-rich fibers with an average size of 350 Å had a size range from about 200 to 800 Å.

Further experimental proof of the concurrent nucleation and growth phenomenon was sought. Standard spun fibers were heated to 1426°C for one hour, then leached in hydrofluoric acid for about 10 minutes. The purpose of the acid treatment was to preferentially dissolve the amorphous phase and thereby decrease the amount of nucleation possible thereafter. The fibers were then reheated at 1426°C for an additional 15 hours and then subjected to X-ray diffraction analysis. Again mullite was the only phase detected in this specimen and the average crystallite size was beyond the limits of detection by the X-ray line broadening technique, i.e., > 2000 Å.

356

MICROTOMED SECTIONS OF SiO$_2$-RICH SPUN FIBERS
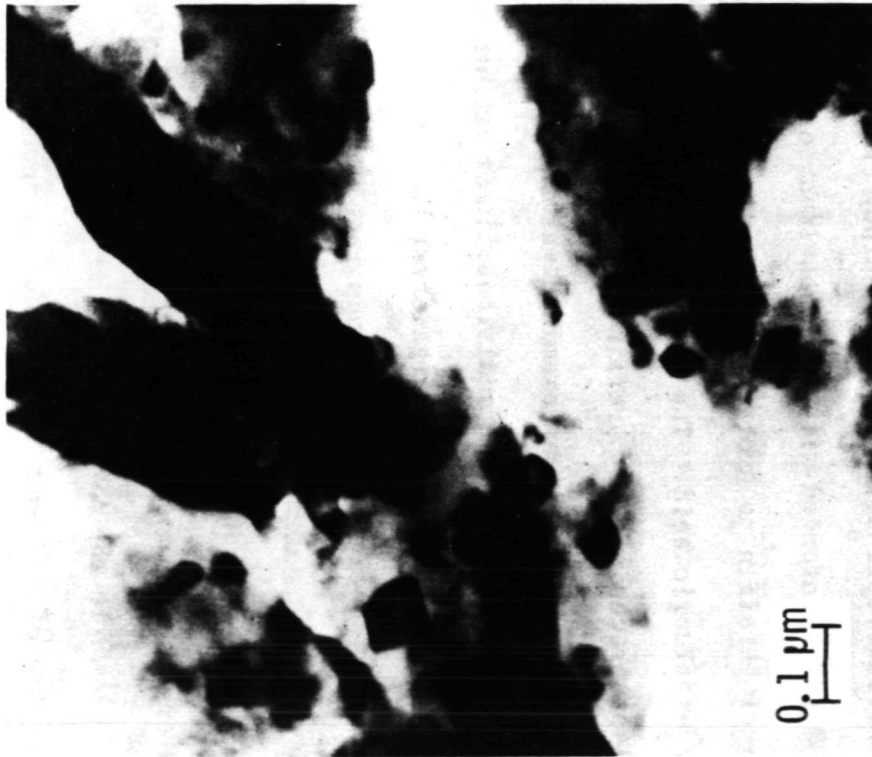
AFTER ONE HOUR AT 1426° C
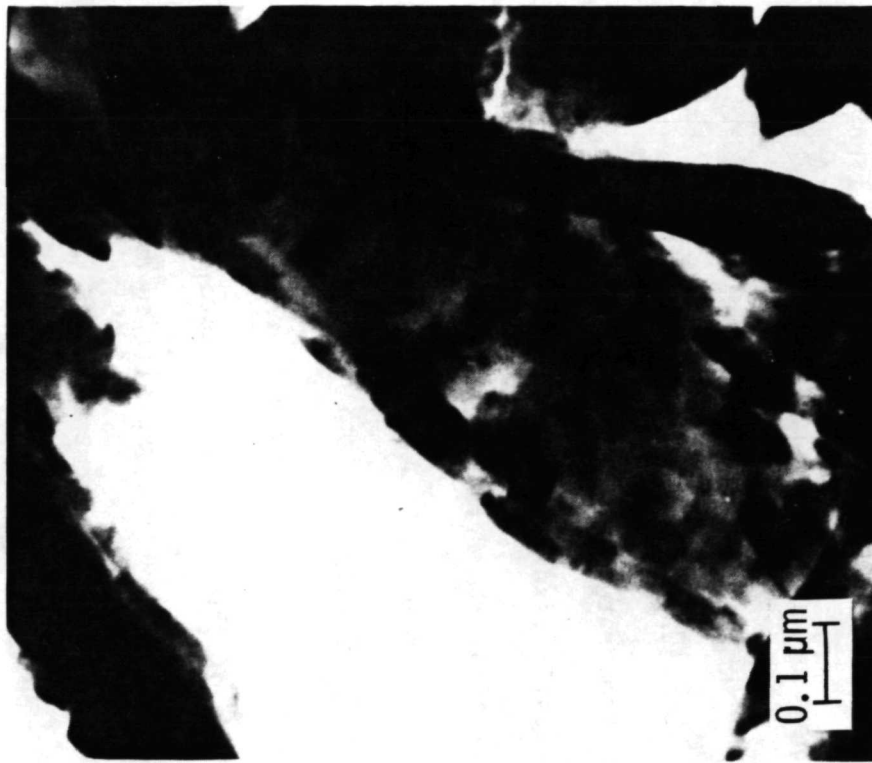
AFTER 16 HOURS AT 1426° C

Figure 4

REPLICA OF UNETCHED STANDARD SPUN FIBER

(Figure 5)

A limited number of replicas of unetched fibers were examined. The replicas were made by a one-step carbon replication process whereby unmounted fibers were shadowed with platinum-carbon at an angle of 23° and reinforced with a carbon layer of about 200 Å. The coated sample was covered with a thin layer of paraffin to protect the brittle carbon film during the chemical dissolution of the fibers in 30% hydrofluoric acid. The paraffin was then removed by heating in distilled water at about 60°C. The last traces of the paraffin were removed by a toluene wash.

One of the specimens examined was the standard spun fiber, which was exposed for 16 hours at 1426°C and then heated an additional 100 hours at the same temperature. Its surface microstructure as seen in Figure 5 contains large crystallites with facets clearly resolved. The crystallites are essentially contiguous with no apparent amorphous phase. The X-ray diffraction pattern contains mullite lines as expected and a few unidentified lines. The average surface grain width as measured from the electron photomicrographs is 2300 Å compared to an X-ray value of 1350 Å and to 1022 Å from measurements from the photos of microtomed sections. The replica shows essentially the surface structure while the microtomed section is more representative of the internal structure. Thus after an exposure of at least 116 hours at 1426°C it is concluded that the outer crystallites are larger than the internal crystallites. The nature of this development and its effect upon the mechanical properties of the fibers are subjects under consideration in our current program.

358

REPLICA OF UNETCHED STANDARD SPUN FIBER

0.3 μm

EXPOSED FOR 16 HOURS AT 1426° C COOLED TO ROOM TEMPERATURE AND HEATED AN
ADDITIONAL 100 HOURS AT 1426° C

Figure 5

359

REPLICAS OF CROSS-SECTIONS OF FIBERS

(Figure 6)

The amount of internal porosity is an important factor in the fiber's strength. For this reason it was important to see if the amount of internal porosity could be observed in these small diameter fibers. For this purpose as-received, and thermally exposed fibers were mounted, polished, and in a few cases chemically etched. The mounting, polishing, and etching procedures were as follows.

A bundle of fibers (spun or monofilament) was lined up in more or less one direction and placed on a flat metallic surface. A mixture of epoxy resin and a small amount of red dye was poured over the fibers. The dye was used to facilitate detection of the colorless fibers. The resin cured into a flat button shape which was then cut in half, perpendicular to the fibers' axes. The imbedded fibers were again mounted such that the cross-section of the fibers were exposed for polishing and etching. The mounted fibers were ground and polished by using wet abrasive papers and 3 μm and 0.5 μm diamond polishing compounds. Some of the polished fibers were then chemically etched. The etchant consisted of 90 parts lactic acid, 10 parts nitric acid, and 5 parts of hydrofluoric acid.

Representative cross-sections of these fibers are shown in Figure 6. The first photo shows the as-received standard spun fiber. There is no indication of porosity although there is a faint indication of some structure. The middle photo shows the monofilament (standard composition) after a moderate thermal exposure. The lack of porosity seen here was also observed in the as-received monofilament (not shown). These observations are in direct contrast to those in reference 5 where 10 to 20 volume percent porosity was reported. The technique used in reference 5 was the replication of fractured fiber surfaces. Beyond showing features related to fracture, such replicas are difficult to interpret. It would appear that the examination of a replica of a polished surface is more informative for porosity determinations.
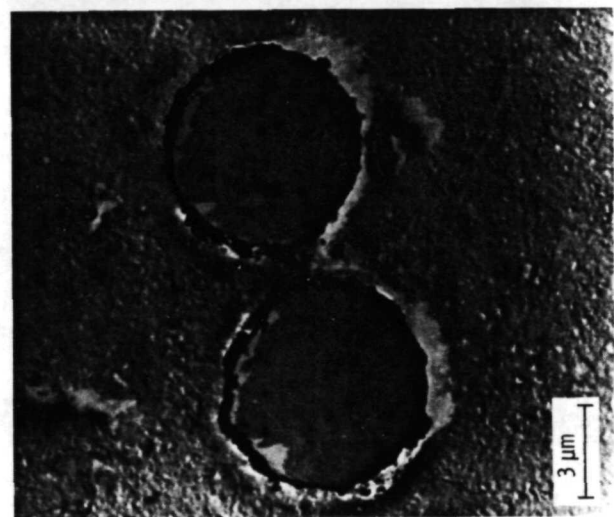
An important observation here is that it was possible to obtain polished surfaces of good quality even though the size of the abrasive used (0.5 μm diamond) was large compared to the diameter of the fiber (6.8 μm).

Chemical etching of the cross-section of the polished, as-received fibers revealed no useful metallographic information. The only features seen are the many small areas that have been preferentially attacked by the etchant. (In negative replicas the depressions appear as mounds when viewed from the direction of the shadowing.) These etched out areas roughly range in size from 400 to 2000 Å. Although their appearance is similar to etch pits they are not believed to be etch pits since they are much larger than the crystallites (100 to 200 Å). No attempt was made to chemically etch thermally exposed fibers since the feasibility of obtaining information by chemically etching mullite fibers when they contain sufficiently large crystallites (about 1000 Å and larger) has already been demonstrated in reference 5.

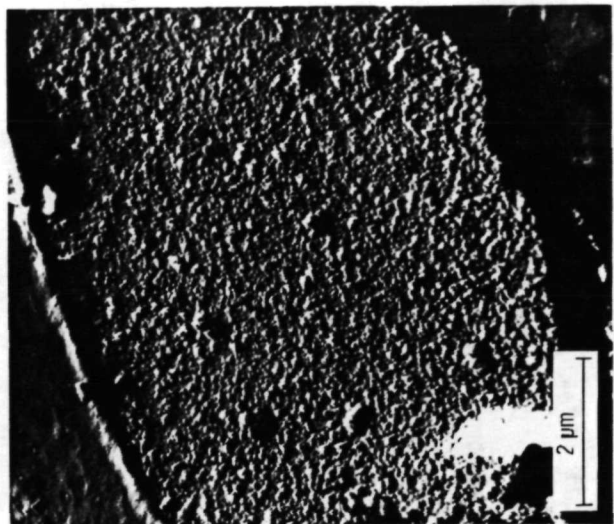360

REPLICAS OF CROSS-SECTIONS OF FIBERS

AS-RECEIVED STANDARD SPUN FIBER – CHEMICALLY ETCHED

2 μm

MONOFILAMENTS AFTER 1/2 HOUR AT 1205° C POLISHED, UNETCHED

3 μm

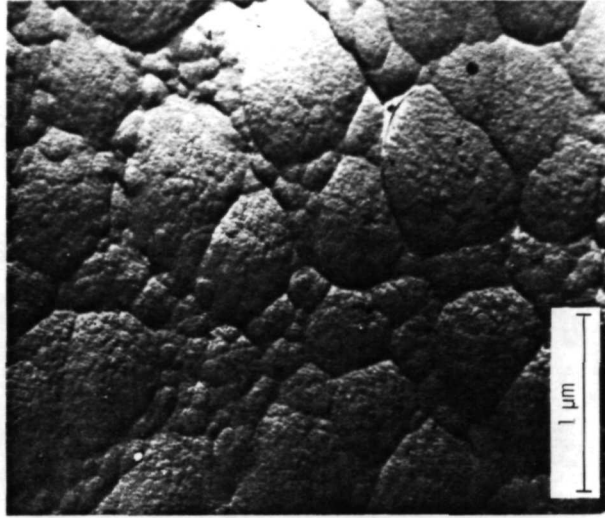AS-RECEIVED STANDARD SPUN FIBER – POLISHED UNETCHED

2 μm

Figure 6

REPLICAS OF CATHODICALLY ETCHED FIBERS

(Figure 7)

Samples from all the materials studied during this investigation (as-prepared and thermally exposed) were cathodically etched and replicated. The etching procedure consisted of individually separating and placing the fibers on aluminum foil which covered an aluminum block in a cathodic etching apparatus. The aluminum block (and the foil) served as the cathode and the walls of the cathodic etcher served as the anode. The chamber was evacuated to less than 0.66 N/m^2 (5×10^{-3} torr) and flushed twice with argon. Then the argon flow and pumping speed were regulated until a steady pressure of 19.95 N/m^2 (0.15 torr) was obtained. A potential of 2000 volts (5 milliamperes) was applied and held for five minutes. The sample was then allowed to cool for five minutes after which the potential was reapplied. This cycle was repeated six times for a total etching time of 30 minutes. This sequence achieved the required sample etch without excessive heating of the fibers or of the aluminum backing. The replication of the cathodically etched fibers was accomplished by the one-step carbon replication process previously described in connection with the examination of unetched fibers.

The major findings from the examination of replicas of the cathodically etched spun fibers are as follows. The standard composition fibers and the Al_2O_3-rich fibers displayed similar features which consisted of cellular structures and striations. Within any fiber the structure was inhomogeneous with cells and striations sometimes appearing together and with cell size varying along the fiber. Curiously the features revealed by cathodic etching seems unaffected by thermal exposure or phases present (crystalline or noncrystalline). Thus, as seen in Figure 7 the as-received fiber cannot be readily distinguished from the heat treated fiber. Further, the dimensions of the structural features of the cathodically etched fibers cannot be correlated with the crystal size calculated from XRD or measured from TEM photos of microtomed sections.
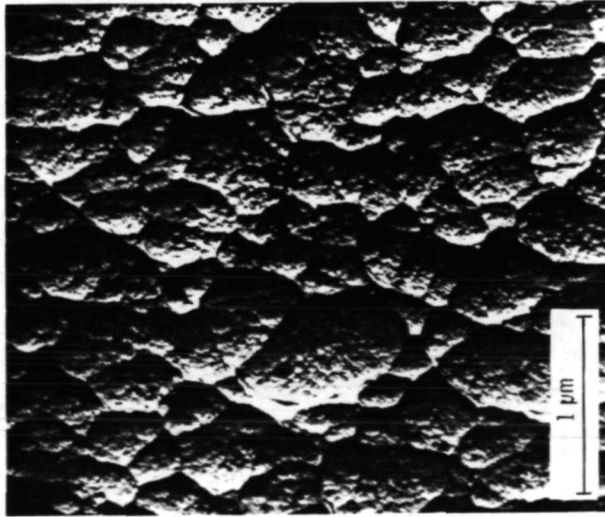
362

REPLICAS OF CATHODICALLY ETCHED FIBERS

STANDARD SPUN FIBER AFTER
16 HOURS AT 1426°C
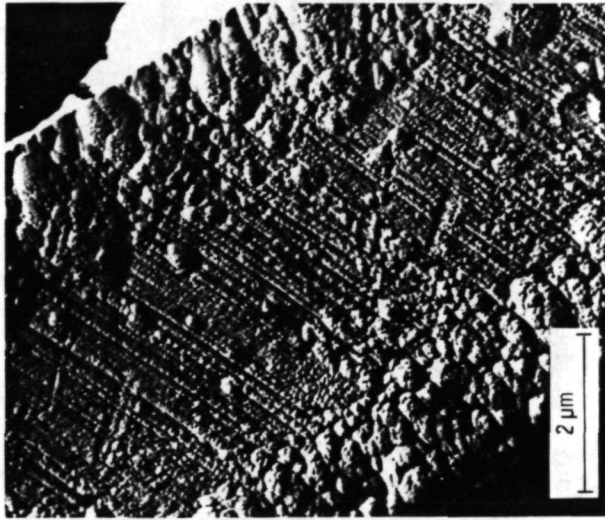
AS-RECEIVED STANDARD SPUN
FIBER WITH STRIATED STRUC-
TURE

AS-RECEIVED STANDARD SPUN
FIBER WITH CELLULAR STRUC-
TURE

Figure 7

CATHODICALLY ETCHED SiO$_2$-RICH FIBERS

(Figure 8)

After cathodic etching the SiO$_2$-rich fibers were also observed to contain the cellular structure, but striations were never observed. The SiO$_2$-rich fibers differed from the standard and the Al$_2$O$_3$-rich fibers in two other respects. One is the frequent appearance of a tiered structure as seen in Figure 8. The other is the occasional appearance of a structure in the thermally exposed fibers that looks as if it had been molten at temperature.

The distinctive features revealed by cathodic etching appear real but they cannot be related for the most part to composition or exposure. It is possible then that this technique is not revealing structure on the scale of the crystallite size, but it may be revealing features of a larger scale. These larger features may be caused by fiber processing and thus reflect processing history. For example, the observed striations in the standard and Al$_2$O$_3$-rich fibers may be related to the shearing that must be present when the precursor solution is forced through the spinnerette orifice and rapidly dried. Such striations were also observed in monofilaments and the handmade fibers, again suggesting the action of shearing forces during processing. Of course, this raises the intriguing question of why striations were not observed in the SiO$_2$-rich fibers, for which there is no obvious answer.

364

CATHODICALLY ETCHED SiO$_2$-RICH FIBERS

SiO$_2$-RICH SPUN FIBER AFTER ONE HOUR AT 1426°C

1 μm
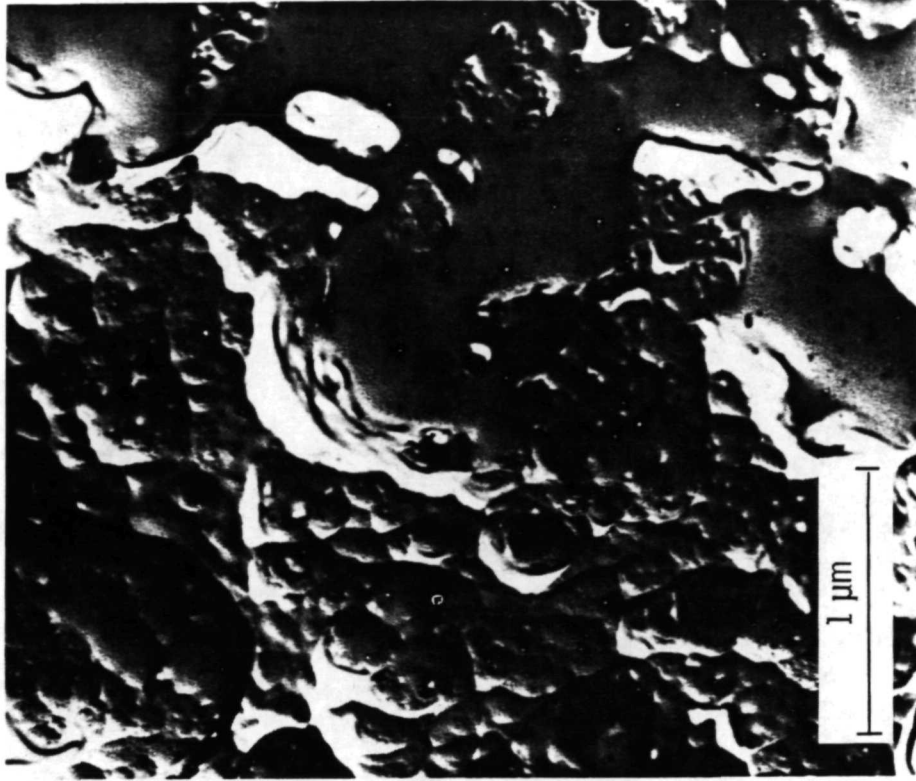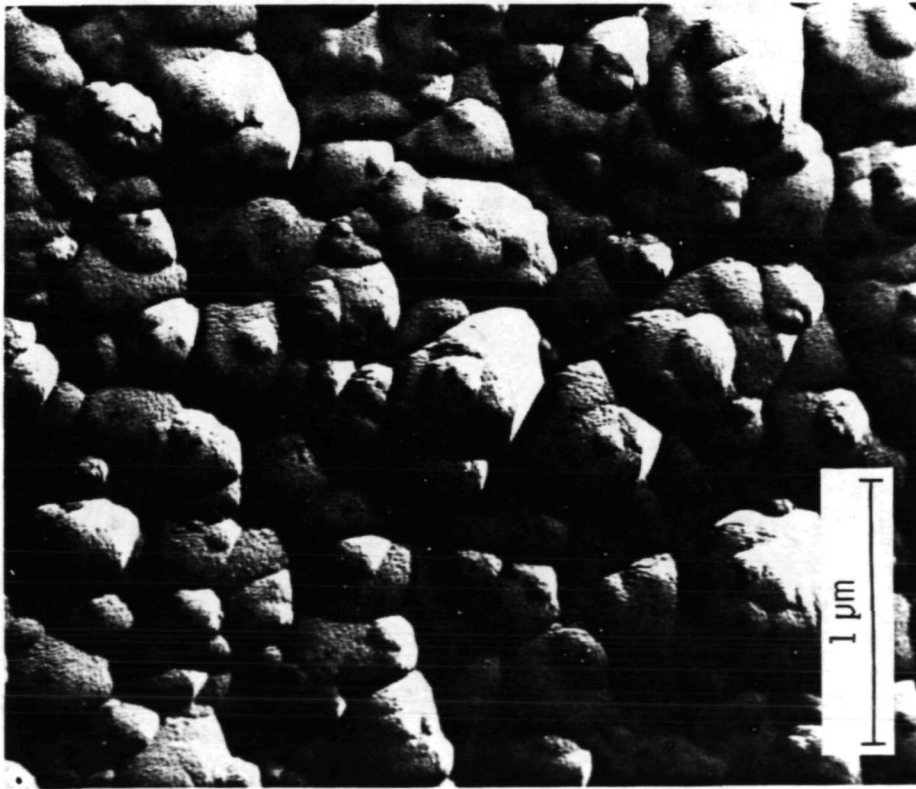
AS-RECEIVED SiO$_2$-RICH SPUN FIBER WITH TIERED STRUCTURE

1 μm

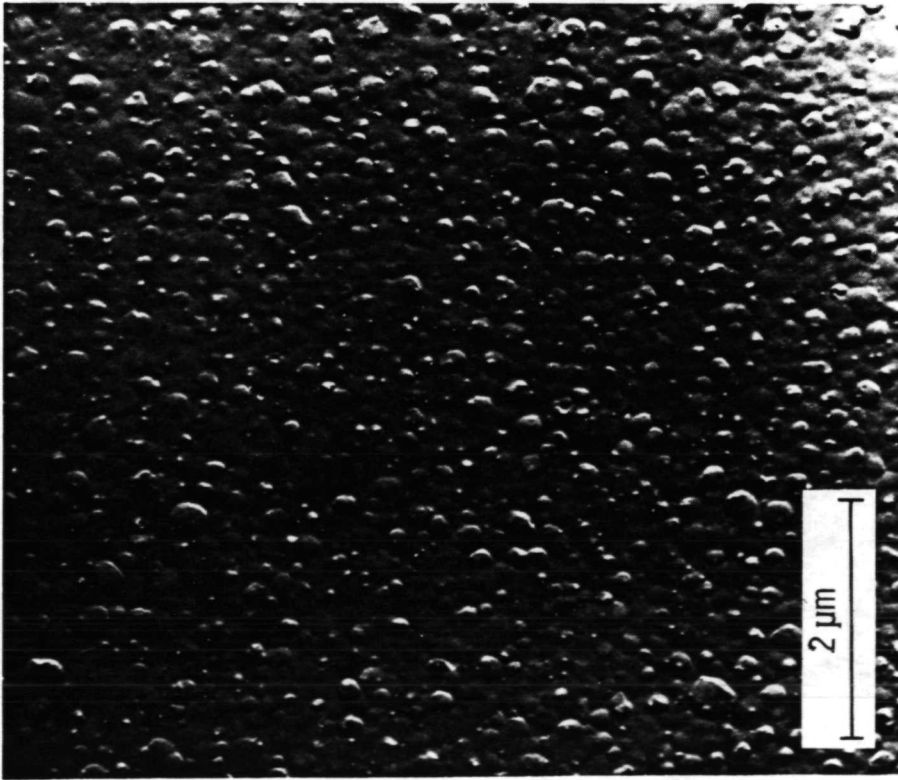Figure 8

365

CATHODICALLY ETCHED PRECURSOR SOLUTION

(Figure 9)

An effort was made to see if the microstructural features resulting from cathodic etching could be related to processing differences. For this purpose the three spun fibers, the monofilament, the hand-made fibers, and the cast precursor solution were tested. The preparation of these materials differed with respect to many of the important processing parameters such as the basic forming mode (drawn, spun, or cast), humidity, drying method, collection mode and firing schedule, etc.
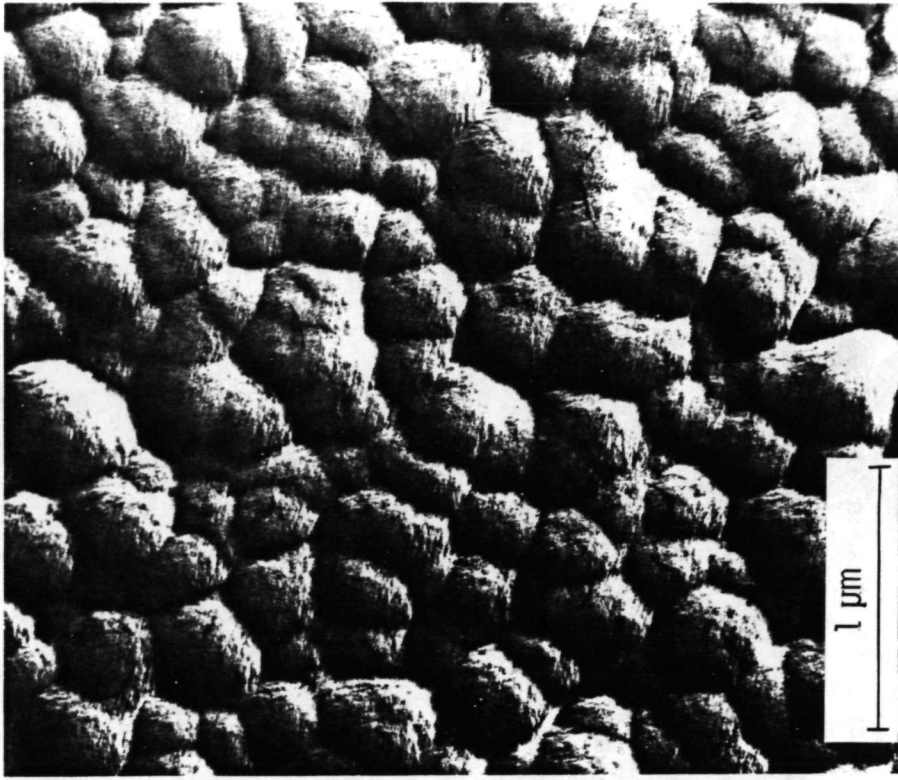
The as-prepared cast precursor solution (fired for ten minutes at 1065°C during its preparation) did indeed have a unique structure as seen in Figure 9. However, after a thermal exposure at 1426°C the cast material developed cellular structures similar to those of the spun fibers. The cathodically etched monofilament and the handmade fibers could not be distinguished from the spun fibers either in the as-prepared condition or after thermal exposure.

Thus this cursory examination did not demonstrate the ability of cathodic etching to differentiate processing parameter differences among the fibers. Nevertheless, the very distinctive features revealed by this etching method must be associated with some aspect of the microstructure of these fibers. Perhaps a more systematic study with well-controlled processing parameters may reveal a relationship between the features exposed by cathodic etching and the processing parameters. If indeed it does then cathodic etching would prove to be a useful tool for studying the effects of processing variables upon fiber properties.

CATHODICALLY ETCHED CAST PRECURSOR SOLUTION

CAST SOLUTION OF STANDARD COMPOSITION AFTER 16 HOURS AT 1426° C

1 µm

AS-PREPARED CAST SOLUTION OF STANDARD COMPOSITION

2 µm

Figure 9

SUMMARY OF RESULTS

In this investigation the microstructures of mullite-composition fibers were examined by a number of TEM techniques and by XRD. The major findings are as follows:

The as-received fibers of standard compositions, both the spun and the monofilament, contained little if any porosity. Nor did the degree of porosity change after heating the monofilament for a half hour at 1205°C. Prior to the thermal exposures the crystallites in all three of the spun fibers were very small (about 100 to 200 Å) and were dispersed in a large amount of an amorphous phase. When thermally exposed, these crystallites grew and simultaneously new crystallites were nucleated from the amorphous phase. After 116 hours at 1426°C the crystallites of the standard spun fibers became contiguous. At this juncture the average crystallite size was less than 0.2 μm, relatively small compared to the mean fiber diameter of 6.8 μm. In addition, the surface crystallites of these fibers were found to be more than twice as large as the interior crystallites. It is concluded that by the proper combination of a number of TEM techniques a valuable description of the microstructure of mullite fibers can be obtained. The potential for such a microstructural description is, of course, to ultimately relate fiber microstructure to mechanical behavior.

368

REFERENCES

1. P. Klug and E. Alexander, X-Ray Diffraction Procedures for Polycrystalline and Amorphous Materials, John Wiley and Sons, 1954.

2. R.N. Fetterolf, NASA CR-120929, 1971.

3. R.A. Tanzilli, Ed. NASA CR-112038, 1972.

4. R.F. Davis and J.A. Pask, Mullite Ch.3. of High Temperature Oxides Part IV Refractory Glasses, Glass-Ceramics, and Ceramics, A.M. Alper, Ed., Academic Press, 1971.

5. R.N. Fetterolf, AFML-TR-70-197, 1970.